Driver Steering Support Interfaces Near the Vehicle's Handling Limits

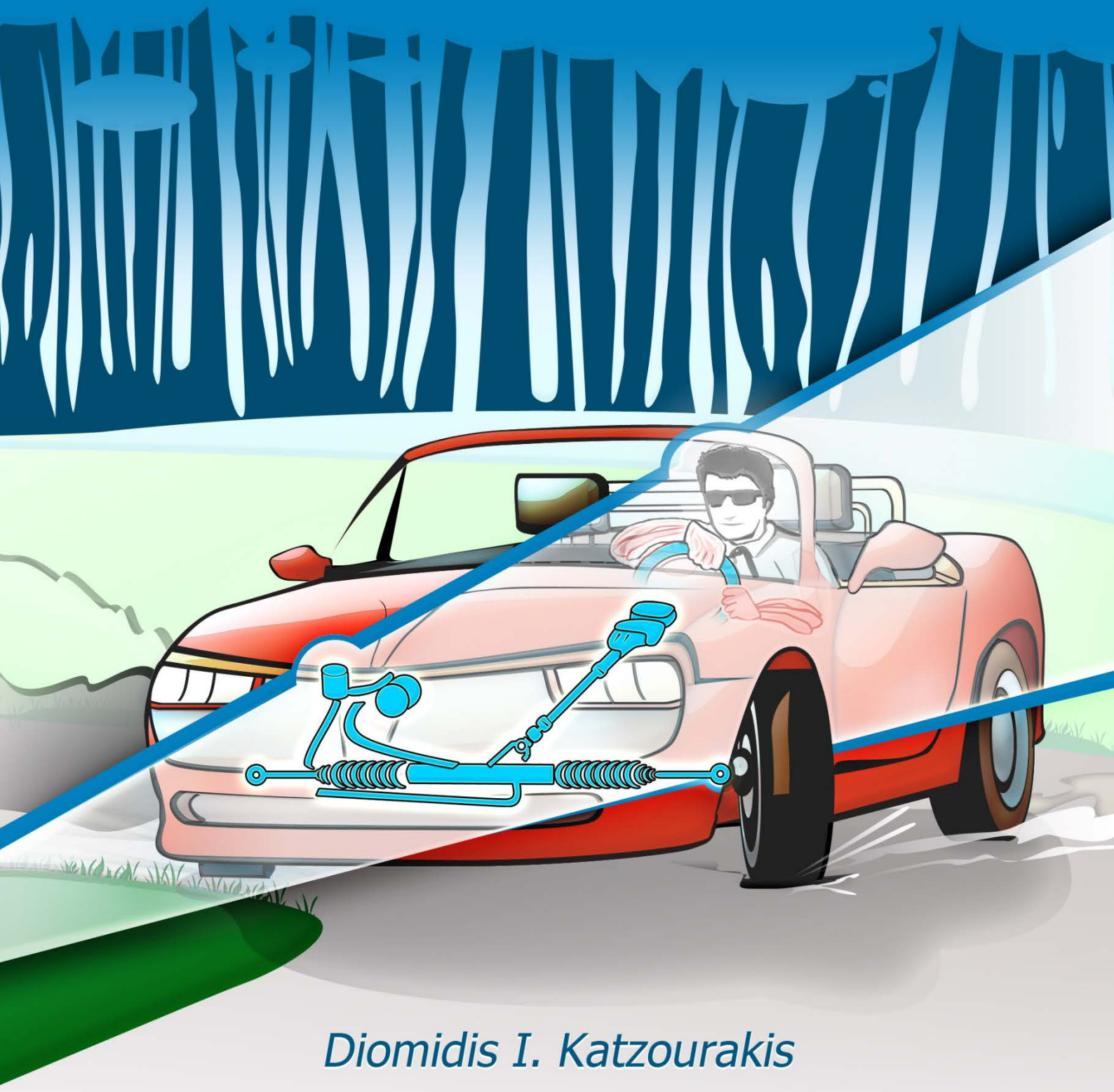

Diomidis I. Katzourakis

Driver Steering Support Interfaces Near the Vehicle's Handling Limits

Diomidis I. KATZOURAKIS

Στην οικογένεια μου

To my family

Driver Steering Support Interfaces Near the Vehicle's Handling Limits

Proefschrift

ter verkrijging van de graad van doctor
aan de Technische Universiteit Delft,
op gezag van de Rector Magnificus prof. ir. K.C.A.M. Luyben,
voorzitter van het College voor Promoties,
in het openbaar te verdedigen op woensdag 6 Juni 2012 om 12:30 uur

door Diomidis I. KATZOURAKIS
Master of Science in Electronic and Computer Engineering
Technical University of Crete
Geboren te Chania, Kreta, Griekenland

Dit proefschrift is goedgekeurd door de promotoren:
Prof. dr. F.C.T. van der Helm
Prof. dr. ir. E.G.M. Holweg
Copromotor dr. ir. R. Happee

Samenstelling promotiecommissie:

Rector Magnificus,	voorzitter
Prof. dr. F.C.T. van der Helm,	Technische Universiteit Delft, promotor
Prof. dr. ir. E.G.M. Holweg,	Technische Universiteit Delft, promotor
Dr. ir. R. Happee,	Technische Universiteit Delft, copromotor
Prof. dr. B.J.H. Jacobson,	Chalmers U. of Technology, Zweden
Prof. dr. ir. B. van Arem,	Technische Universiteit Delft
Dr. G. Mavros,	Loughborough U., Groot-Brittannië
Dr. ir. I.J.M. Besselink,	Technische Universiteit Eindhoven
Prof. dr. ir. M. Verhaegen,	Technische Universiteit Delft, reservelid

This research was funded by the Automotive Development Centre of SKF under the project:
Mobility Intelligence Using Load-Based Lateral Stability (MILLS)

ISBN/EAN: 978-94-6203-063-3

Front cover: Antonis Katzourakis, tonykatz@gmail.com
Printed in the Netherlands: CPI Koninklijke Wöhrmann.

“Δει γαρ την μεν τέχνην χρήσθαι τοις οργάνοις, την δε ψυχήν τω σώματι.”
Αριστοτέλης, 384-322 π.Χ.

“The art should utilize tools, the soul the body.”
Aristotle, 384-322 B.C.

CONTENTS

Summary

“Μελέτη δέ τοι έργον οφελλεί.”
Ησίοδος, μεταξύ 750 και 650 π.Χ.

“Studying avails every project.”
Hesiod, between 750 and 650 B.C.

Driver Steering Support Interfaces Near the Vehicle's Handling Limits; Summary

The goal of this thesis is to propose steering support systems that can reduce the driver's control effort, mental load and promote safety. The driver dictates the vehicle's motion and the support should centralize him/her in the control loop; thus our design philosophy is to increase driver's responsibility and support him/her in the sense of information rather than automation. Incarnating such an abstract theme into a concrete problem which can be methodologically solved in terms of engineering science, necessitates a milestone-oriented work approach. Thus, the path to realize this development is to systematically sub-divide the concept into distinct milestones allowing to embody this high-level idea into objectively assessed steering interfaces.

This milestone-oriented approach can be divided into seven steps: i) Study the state-of-the-art driver support systems and identify the potential space for improvement. ii) Develop the means (driving simulators, vehicular instrumentation and data analysis methods) to aid the driver steering support interface research. iii) Study the driver steering interface without any support. iv) Utilize the gathered knowledge to develop steering support interfaces, assess them in simulation level, v) and adapt the simulation support controllers into real vehicles and test them. vi) Evaluate the influence of the support interface with the real vehicle results. vii) Based upon the assessment, make a road-map for the commercial implementation of the support interface; if it is fruitful promote its further development with ultimate goal the adoption into production vehicles.

Fig. S 1. TUDelft moving base simulator.

The aforementioned milestone-oriented approach has been followed for the development of the driver steering support interfaces presented in this thesis. The current summary substantiates the milestones into the distinct goal addressed in Chapters 2 – 7.

The goal to develop the hardware and performance evaluation-control methods in order to engineer realistic haptic cues on the steering wheel of our driving simulator (c.f. Fig. S 1) is addressed in

Chapter 2. A relatively low-cost solution for hardware is deployed, consisting of a velocity-controlled three-phase brushless servomotor, whose high bandwidth control allows for a realistic representation of forces. To test the system, different inertia-spring-damper systems were simulated and evaluated in time and frequency domain. We concluded, that the designed system allowed reproduction of a large range of steering wheel dynamics and forces, comparable to those found in actual cars.

Our target to systematically adjust the steering systems properties of the driving simulator so that it matches the steering feedback and vehicle response of a certain vehicle is addressed in Chapter 3. To do so, we employed the steering sensitivity and steering torque gradient, which are two important metrics describing on-centre vehicle dynamics response and steering feedback. We acquired the steering metrics of real cars during double-lane change tests and indicated the key parameters of the vehicle that determine these steering metrics (c.f. Fig. S 2 instrumentation for steering indices measurement). We instrumented and tested five modern passenger cars, and used a vehicle dynamics model to extract the metrics for multiple vehicular parameterizations (steering ratio, power assist level, etc.) and test speeds. Sensitivity analysis showed that steering sensitivity was mainly influenced by the components that determine the steering ratio whereas the steering torque gradient was also affected by power assist steering settings. By completing this work, we had the foundation to easily assess the realism of our simulated vehicles' response as well as to easily adapt the vehicular settings to achieve a realistic steering feedback in our driving simulator.

Fig. S 2. Steering indices measurement for different vehicle's in Prodrive, UK. Mazda Rx-8 (left), Jaguar XF (right).

Lane departure appears relevant in 179,000 crashes per year and is related to the greatest number of fatal crashes; up to 7,500 fatal crashes per year in the United States. Infiniti predicts that if lane departure prevention (LDP) were fitted to all vehicles, some 12% of all road fatalities could be prevented annually. The problem is that although numerous studies have shown the potential of lane keeping and LDP systems, there are few studies related to their effects during emergency manoeuvres. Thus, Chapter 4 aims to investigate a road-departure prevention (RDP) system during an emergency manoeuvre. We present a driving-simulator experiment which evaluated various steering interfaces of a road-departure prevention (RDP) system in an emergency situation. The interfaces were: 1) haptic-feedback (HF) where the RDP provided advisory steering torque; 2) drive-by-wire (DBW) where the RDP automatically corrected the front-wheel angle; and 3) DBW & HF, which combined both setups. The RDP system intervenes by applying haptic (guidance) feedback torque and/or correcting the angle of the front wheels (drive-by-wire) when road departure is likely to occur. Thirty test drivers tried to avoid an obstacle (a pylon-confined area) while keeping the vehicle on the road. The results showed that HF without DBW had a significant impact on the measured steering torque, but no significant effect on steering-wheel angle or vehicle path. DBW prevented road departure and reduced mental

workload, but lead to inadvertent human-initiated counter-steering. It was concluded that a low level of automation, in the form of HF, does not prevent road departures in an emergency situation. A high level of automation, on the other hand, is highly effective in preventing road departures.

Chapter 5 has been divided into three parts (A, B, C), all related to real vehicle testing. Our goal to construct a versatile low-cost instrumentation suitable to be fitted on race cars (c.f. Fig. S 3, Fig. S 4) and develop the methods for processing from raw measurements to user-friendly data suitable for driver behaviour studies is addressed in part A. Through a case study on driving behaviour, during the execution of high speed skid-pad manoeuvres, we could easily notice the markedly different driving behaviours between an expert and a novice driver. The experienced driver could learn quickly how to perform repeatable trajectories, unlike the novice driver. The consistently high performance of the expert driver was realized by relatively small correcting inputs (steering wheel angle, throttle). The experienced driver was able to quickly learn how to generate the correct inputs to the vehicle, to yield repeatable vehicle behaviour and consistently perform well.

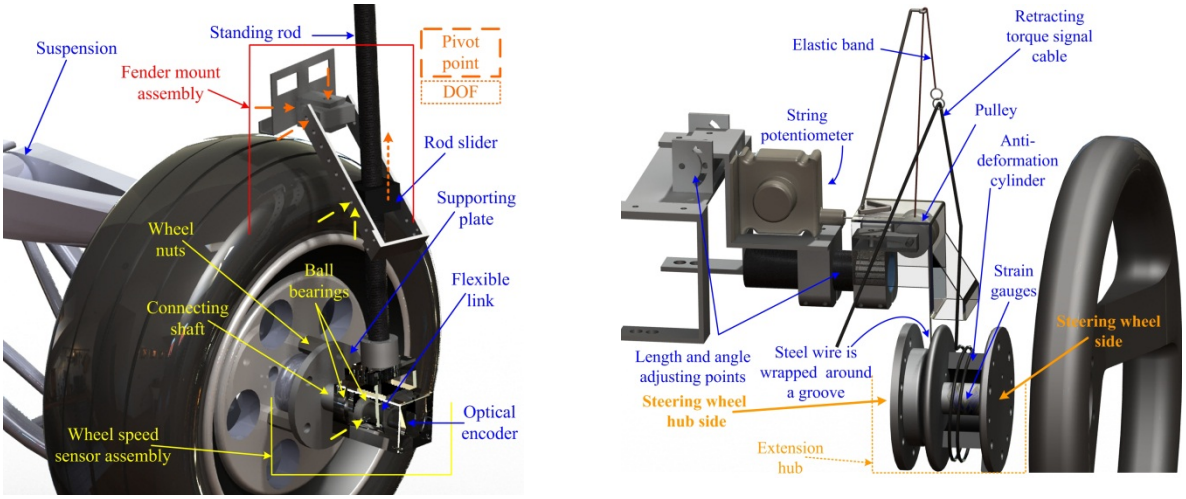

Fig. S 3. Externally fitted wheel speed sensor and steering system measurement assembly (c.f. Chapter 5, part A).

Our aim to investigate driver control actions during high speed cornering with a rear wheel drive vehicle is depicted in Chapter 5, part B. Six drivers were instructed to perform the fastest manoeuvres possible around a marked circle, while trying to retain control of the vehicle and constant turning radius. The data reveal that stabilization of the vehicle is achieved with a combination of steering and throttle regulation. The results show that the drivers used steering control to compensate for disturbances in yaw rate and sideslip angle. Vehicle accustomed drivers had the most consistent performance resulting in reduced variance of task metrics and control inputs.

Our target to design controllers that can stabilize the vehicle as an expert driver would is approached in part C of Chapter 5. There, we present data of driver control commands and vehicle response during the execution of cornering manoeuvres at high sideslip angles (drifting) by an expert driver using a RWD vehicle (c.f. Fig. S 4; bottom left). The data reveal that stabilization of the vehicle with respect to such cornering equilibria requires a combination of steering and throttle regulation. A four wheel vehicle model with nonlinear tire characteristics is introduced and the steady-state drifting conditions are solved numerically to derive the corresponding control inputs. A sliding mode control is proposed to stabilize the vehicle model with respect to steady-state drifting, using steering angle and drive torque inputs. The performance of the controller is validated in a high fidelity simulation environment; the controller can stabilize the vehicle similarly to an expert driver. We also conceptually describe how the proposed controller can motivate a driver steering support drifting interface in the by-wire sense.

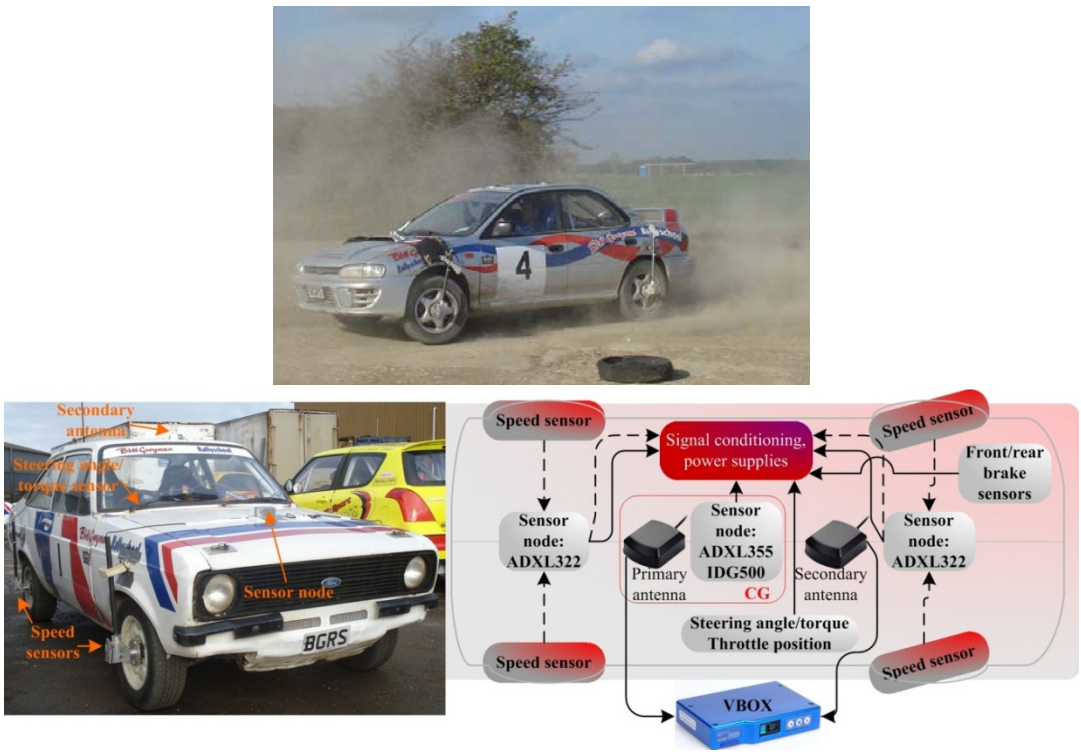

Fig. S 4. An instrumented 4WD Subaru Impreza GT (top) and Ford Escort mk II (bellow) with the developed equipment described in Chapter 5, part A.

Our goal to objectively evaluate vehicular steering systems through detailed driver models is substantiated in Chapter 6. It presents a driver model that consists of a preview controller part that responds to visual feedback and a neuromuscular component that reacts to force-feedback. The developed model is sensitive to steering wheel systems with different dynamics, and can predict both goal-directed steering wheel movements, as well as neuromuscular feedback. To provide evidence, we simulated different parameterizations of a steering system and tested them in conjunction with the developed driver model. We concluded that the developed model could predict the expected response for different steering setups.

Our milestone goal to propose haptic steering wheel support when driving near the vehicle's handling limit (Haptic Support Near the Limits: HSNL) is addressed in Chapter 7. The rationale behind the HSNL, derives from the vehicle's property to reduce the steering "stiffness" (the steering feedback torque as a function of the steering wheel angle) before the vehicle reaches its handling limits and starts to understeer. The HSNL exaggerates the reduction of the steering "stiffness" and makes it profound to the driver, so he/she avoids excessive steering angle inputs which will result in increased tire slip and consequently lateral force loss.

Chapter 7 is divided into two parts (A, B). Part A of Chapter 7 studies the influence of the HSNL in (a) driver-in-the-loop simulation and in (b) real track testing with a vehicle (Opel Astra G/B) equipped with a variable steering feedback torque system (c.f. Fig. S 5). In the simulator study (a) 25 drivers attempted to achieve maximum velocity, on a dry skid-pad while trying to retain control of the simulated vehicle parameterized as the Astra. In (b) 17 drivers attempted to achieve maximum velocity, around a wet skid-pad while trying to retain control of the Astra. Driving aids (ABS and traction control) were disabled during testing. Both the driving simulator and the real vehicle tests led to the conclusion that HSNL assisted the test subjects to drive closer to the designated path while achieving effectively the same speed. In the presence of HSNL, the drivers operated the tires in smaller slip

angles and hence avoided saturation the front wheels' lateral forces and excessive understeer. Finally, the support reduced their mental and physical demand.

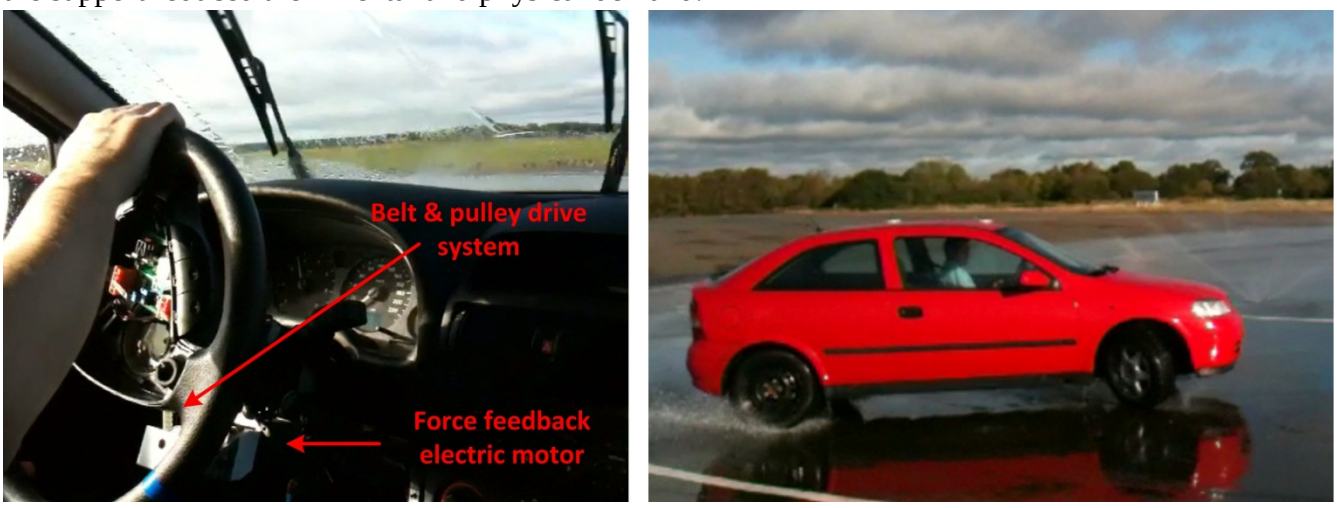

Fig. S 5. Force-feedback Opel Astra in wet skid-pad testing.

Part B of Chapter 7, studies the influence of HSNL during high speed cornering in a test-track. 17 test subjects drove around a narrow-twisting tarmac circuit, the aforementioned Opel Astra equipped with a variable steering feedback torque system (c.f. Fig. S 6; left). The drivers were instructed to achieve maximum velocity through corners, while receiving haptic steering feedback cues related to the vehicle's cornering potentials. Driving aids (ABS and traction control) were disabled during testing. The test-track tests led to the conclusion that HSNL reduced drivers' mental and physical demand.

Fig. S 6. Force-feedback Opel Astra in Prodrive's UK adverse handling test-track (left) and circuit park Zandvoort NL (right).

One of the primal goals of automotive manufacturers is to reduce the driver's mental and control effort (c.f. Chapter 7); the work that will be presented in this thesis revealed that steering support near the vehicle's handling limits can reduce the drivers' mental and physical demand and can potentially promote safety. We can therefore conclude that certain of the developed support interfaces can be implemented into production vehicles.

Chapter 1. Introduction

"There is nothing more difficult to take in hand, more perilous to conduct, or more uncertain in its success, than to take the lead in the introduction of a new order of things."
Niccolo Machiavelli, 1469-1527 A.D.

Driver Steering Support Interfaces Near the Vehicle's Handling Limits; Introduction

Abstract—The current introductory Chapter 1 discusses this thesis' problem statement, research goals, and the corresponding research approach described in Chapters 2 – 8.

I. Problem statement

A. Road safety and state-of-the-art driver support systems

Vehicle dynamics technology related to cornering started to become a main stream of research in the mid-1980s [172]. This control technology has evolved through various phases from simple chassis control with mechanical four wheel steering, to the current modern era cars which are equipped with advanced driving assist systems such as the electronic stability control (ESC), active front steering (AFS) and lane-departure warning/prevention (LDW/P) systems. Several studies since 1998 have showed the ESC's effectiveness [71], depicting that the global installation of ESC could reduce skidding accidents by even 80% [127]. Similarly, active steering systems have been credited to improve the handling characteristics of the car and increase the driving comfort [166][167].

The global adoption of new sensor technologies (GPS, cameras radar, etc.) has enabled driver support system beyond the concepts applied to chassis control. Systems for example designed to mitigate collisions and apply the brake if they detect an imminent collision [101]. Considering now systems designed to operate in less dynamic driving, LDW/P systems have also proven to promote safety [70][45] even in emergency situations (c.f. Chapter 4; [41]). The utilization of cameras to detect the lane markings has enabled steering control to maintain the vehicle's intended path [153]. Collision mitigation and LDW/P systems, do not aim to improve the vehicle's physical dynamical performance, but do effectively reduce driving effort; and diminishing the driver's load is one of the primal goals of the current and future vehicles for automotive manufacturers [172].

Steering support in low acceleration curve negotiation, has exposed that haptic support is an efficient way to improve the driver-car interaction [119][131][122], improving curve negotiation performance and decreasing driving effort. Support systems for moderate driving conditions, often share control with the driver in the "haptic shared control" sense, operating under the principle that the driver should be aware of the system's activity by force information on the control interface (e.g. the steering wheel in a LDW/P system).

Haptic steering support in a wider dynamic range near the vehicle's handling limits where, where for instance the ESC and AFS would intervene would constitute a new field of support applications. In fact, systems that provide force information to the driver in order to promote his/her understanding of the vehicle's cornering potentials, have only recently been studied [38][35] (c.f. Chapter 7) and displayed significant positive effects on the vehicle's lateral control performance [35] and reduction of the driving effort (mental and physical demand) [38][35]. The driver though dictates the vehicle's motion, and centralizing him/her in the control loop is hypothesized to promote safety and driving pleasure.

Continuing upon road safety, lane-departure is a factor in a large proportion of accidents involving fatal or serious injuries, and is usually induced by the driver's inattention, fatigue, impairment and distraction or improper control inputs in an emergency situation. Jermakian [100] estimated the potential of lane-departure warning (LDW) and asserts that lane-departure appears relevant in 179,000

crashes per year and is related to the greatest number of fatal crashes; up to 7,500 fatal crashes per year in the United States.

Since 2001, Nissan motors in Japan has been offering a lane-keeping support system [25], with audible feedback that sounds if the vehicle begins crossing the lane markings/limits. In 2002 and 2003, Toyota and Honda launched their lane- keeping assist systems that apply steering-wheel torque to help drivers to keep the vehicle in the lane. Nowadays (2012), most high-end automobile manufacturers (Mercedes, Volvo, BMW, Nissan-Infiniti, Honda, etc.) offer similar assist systems in their top-class models. Most LDW systems utilize a camera to track road markings and estimate the vehicle position relative to the road. The feedback to the driver varies from audible, visual, and/or vibro-tactile signals, to haptic steering-wheel feedback. Nissan (Infiniti) was the first to offer lane-departure prevention (LDP), an extension of LDW [103]. In addition to the warning system (automatically enabled when the vehicle is started), LDP brakes slightly to help prevent unintended departure from the travelling lane.

Although some studies tend to favour human-centred automation, where the driver has final control of the vehicle, solely receiving feedback guidance on the steering wheel [119][122], the literature is still arguing the optimal level of automation for a given task. Giving drivers control and authority for safety-critical actions may not always be the best solution [158][159] because of human limitations in speed and decision-making [22]. An example of driver-assist technology deviating from the principle of human-centred automation (in the sense that it can act autonomously in emergencies and completely overrule the driver) is a collision-mitigation system that can apply the brakes if the driver does not act in time. If such a system was not entirely effective in all circumstances, it would worsen the potential for collision when operated by an ineffective driver (due to misunderstanding its functions). Research related to adaptive cruise control (ACC) [20] agrees with the former argument: although ACC is acknowledged to reduce mental workload, it has also been blamed for provoking false reliance on the system. According to Seppelt *et al*. [20], reliance on ACC disengaged drivers from their primary task, driving, and increased their response time to vehicles braking ahead. Summarizing, advanced driver-assistance systems can lead to false reliance that could reduce the benefits under certain conditions, suggesting that careful design and rigorous testing is essential for emergency situations (additional to normal driving); see, for instance, the study by Itoh *et al*. [115] presenting a pedestrian collision-avoidance system in emergency situations.

Substantiating the above statements, we derive to two milestones that have to be attained: i) the development of haptic steering support to driver, near the vehicle's handling limits (c.f. Chapter 7) and ii) the development of a steering support interface for an RDP system in an emergency situation (c.f. Chapter 4).

B. Driving behaviour and modelling studies; promoting the steering support concept

Driver car interaction studies were initiated in the 1960's [55]. The goal has always been the system's optimization for streamlining the driving experience. However, optimizing a vehicle with a real human in the loop is challenging due to the variation in the behaviour of different drivers. Consistency for the automotive refinement process is commonly sought by careful design of the test procedures [120][104], but is not always achieved [95]. Vehicular development can be aided with vehicle modelling and driver behaviour modelling at computer simulation level. Early driver models were simple with error-compensating behaviour [55] but their complexity and potentials have considerably increased over time [16][23][145]. The dominant approach in the design of human-like driver controllers is to decouple the anticipatory and compensatory actions [83] since the driving task can be divided into a feedforward and a compensation action. Drivers primarily apply steering in an anticipatory feedforward manner to an estimated future path; in addition, drivers employ a closed-loop adaptive-control strategy to compensate for deviations of the vehicle from the demanded trajectory

[56]. The full understanding of human driving in terms of compensation to steering disturbances [31] remains an open issue. The majority of driver-car interaction studies dealing with the driver's compensatory behaviour are performed in a simulation environment (e.g. [15]) since real in-field extreme driving tests can be difficult to interpret [95].

Models describing extreme steering behaviour incorporating variable preview times have already been proposed [24]. Experiments have shown how to measure the neuromuscular system (NMS) response to force-feedback [50]. NMS driver models have recently been proposed for objective assessment of the lateral stability induced by the car's steering system configuration [31]. The vast majority of the existing driver models have been developed by human-in-the-loop (HIL) testing in driving simulators. As discussed in the earlier paragraphs drivers are quite diverse; certain vehicular evaluation methods like the "moose test," normally used for handling rating, can be characterized unsuitable for objective assessment of the vehicle's handling. Objectivity can be ensured by examining solely the vehicle's behaviour, but the total performance is always realized in conjunction with the driver. If both the vehicle and the driver are replaced by a computer model the optimal steering system can be sought through traditional optimization methods. Traditionally, driving is seen as a visually dominant task [96][24] and most driver models are limited to describing responses to visual feedback (e.g. preview driver models [145]). However, drivers also rely on neuromuscular (NMS) and vestibular feedback [2], especially in more extreme manoeuvres. Only recently, kinesthetic features on driver modelling have been proposed [2][49][11], that recognize that a driver responds to steering wheel forces not only cognitively, but also instantaneously (through limb inertia and visco-elasticity from co-contracted muscles) as well reflexively (with fast responses from proprioceptive sensors in the muscles).

The knowledge acquired from driving behaviour and modelling can be utilized in the development of new generation of active safety systems. Those are envisioned to employ expert driving skills, instead of restricting the vehicle's response within the predictable linear region of operation of the tires, to actively manoeuvre vehicles away from accidents. For instance, mathematical analysis of expert driving techniques [67][68][69] revealed operation of the vehicle outside the stable operation envelope enforced by current active safety/stability systems.

The aforementioned problem statements, evoke two scientific milestones: i) the design of controllers that can stabilize the vehicle as a race driver would (c.f. Chapter 5, part C) and ii) the development of a driver model for objective assessment of steering systems (c.f. Chapter 6).

C. The means to investigate steering support interfaces

Human-in-the-loop (HIL) driving simulators are widely utilized by automotive manufacturers [47] and researchers to reduce prototyping time and cost. Successful applications range from driver behaviour and perception research, vehicle development, steering systems prototyping, and driver training [92][114][32][3] to Human-Machine-Interface (HMI) system design for automotive control applications [119]. Compared to real vehicle experiments, driving simulation provides enhanced repeatability, safety, unlimited parameterization for the vehicle and the environment and relatively lower cost.

The validity of the acquired research data and the effectiveness of driver training dependσ on the fidelity of the simulator. Designing a high-fidelity HIL simulator able to provide realistic cues to the driver is challenging. It requires sophisticated vehicle dynamics modelling, high-fidelity visualization and sensor/actuation mechanisms [76].

Force-feedback steering wheels (FFSW) are popular within driving game simulators. Usually they are cost effective solutions for the wide market (e.g., Logitech Momo [108]). Although some low-cost FFSW can already increase simulation realism, they are not suited for high-fidelity haptic research. The

weak motors used, offer little force-feedback (FF) power while the reduction gearing imposes a noticeable high inertia. The steering angle is commonly determined through plain potentiometers achieving moderate angular resolution. Still, some researchers have used low-fidelity FFSW when studying the effect of FF [160], in cases where fidelity is of secondary importance. High-end steering wheels also exist, but at a considerable higher price (FrexGP, ECCI etc. [108]). More sophisticated commercial FFSW are also available for HIL automotive research. Their enhanced performance is accompanied with a cost surpassing the price of an average automobile (Moog FCS ECoL-8000 S actuator [49]).

Assuming now that we have a steering force-feedback device which can successfully realize the forces we command it; we still have to derive the steering feedback forces from a suitably parameterized vehicle dynamics model. As discussed earlier, steering feedback is an important aspect of neuromuscular [31] and psychological [8] perception during driving. Studies have shown that changes in steering feedback have an important effect on driver performance and behaviour [144][47]. Not surprisingly, steering feedback plays a crucial role in the automotive design process [113][124].

Simulator fidelity can be evaluated physically, for example by comparing objective handling test performance data in the simulator with those obtained in the real vehicle [169]. One of the difficulties in assessing the physical fidelity of the steering system in a simulator is the scarcity of comparison data from real cars. A number of studies have measured steering torques and angles for deriving certain steering indices during handling tests [151][104][135][13].

Although simulators can be fairly realistic [32], the development of a driver models-controllers reacting to fully realistic vestibular and tactile stimuli (as those described in the previous subsection), as-well-as the evaluation of steering support systems, would require real vehicle in-field tests. To enable real vehicle tests, the vehicles should be fully instrumented. Normally, automotive researchers use externally attached test equipment which are mainly off-the-shelf commercial products [102][150], with a considerably high price tag. Low-cost open source solutions for scaled vehicle instrumentation exist [44] but limited information on full scale vehicle instrumentation is available in the literature.

Substantiating the above paragraphs, we derive three scientific milestones: i) the method to engineer a steering force-feedback system and evaluate its fidelity (c.f. Chapter 2), ii) the employment of steering indices metrics to easily parameterize a driving simulator and assess its steering fidelity (c.f. Chapter 3), iii) the instrumentation of a vehicle and the data processing methods enabling driver behaviour studies (c.f. Chapter 5).

II. Goal of the thesis

The goal of this thesis is to propose steering support interfaces that reduce the driving load and can promote safety. The driver dictates the vehicle's motion and the support should centralize him/her in the control loop; thus our design philosophy is to increase driver's responsibility and support him/her in the sense of information rather than automation.

To incarnate this into reality, we sub-divided the goal into three scientific milestone classes that would help us realize our goal:

i) Develop the means (driving simulators, vehicular instrumentation and data analysis methods) to aid the driver steering support interface research, addressed in Chapters 2, 3, 5 and 6.

ii) Study the driver steering interaction without any support, addressed in Chapter 5.

iii) Utilize the gathered knowledge to develop steering support interfaces-controllers and assess them in driving simulators, addressed in Chapters 4, Chapter 5 (part C) and Chapter 7 (part A). Adopt the support interfaces into real vehicles and test them, addressed in the milestone Chapter 7.

The realization of our goal is therefore presented within Chapters 2 – 7. Each Chapter though is self-contained and has a central scientific milestone theme as described in the next paragraphs.

Firstly, we required a driving simulator with an efficient haptic device to use in the steering system interface design process; thus our first milestone, achieved in Chapter 2, was to propose a method to engineer a steering force-feedback system and evaluate its fidelity. We also had to develop a method to parameterize driving simulators and easily assess the realism, as well as to easily adapt the vehicular settings to achieve the response we wanted. This constituted our second milestone, described in Chapter 3.

The global adoption of new sensor technologies (GPS, cameras radar, etc.) has enabled driver support system beyond the concepts applied to chassis control. We therefore developed and evaluated steering support interfaces for a road-departure prevention (RDP) in an emergency situation system. We investigated which of 1) no support, 2) haptic feedback support (where the RDP provided advisory steering torque) 3) drive-by-wire support (where the RDP automatically corrects the front-wheels angle) or 4) the combination of the previous two supports, had the best interface results. This embodied our third milestone, presented in Chapter 4.

We needed to study the relationship between driver's sensory inputs and compensatory control-actions outside the stable operation envelope and investigate how to design controllers that can stabilize the vehicle as a race driver. To do so, we had to devise the means to easily instrument a vehicle with low-cost and the methods for processing raw measurements to user-friendly data suitable for driver behaviour studies, appointing this to our fourth milestone, addressed in Chapter 5. Given the huge diversity of drivers and driver input variance we realized the need to develop a driver model sensitive to automotive steering systems with different dynamics employing neuromuscular features. This model development would enable the objective assessment of steering interfaces and represents our fifth milestone, appearing in Chapter 6.

Finally, given the adoption of haptic solutions in modern vehicles we sympathized the idea of haptic support in dynamic driving. We hypothesized that with haptic support, a driver can better distinguish the grip limit of the front wheels' and can improve the vehicle's lateral control performance. Proving this hypothesis constituted our final milestone, presented in Chapter 7.

The aggregation of the aforementioned milestones together, constitutes the goal of the thesis; individual Chapter deals with the scientific milestones in the order presented here.

III. Research approach

The research approach to realize our goal is presented within Chapters 2 – 7, which derive from their original journal and/or conference proceedings articles. Each Chapter is self-contained; this thesis can therefore be read in random order.

Chapter 2: "Steering Force-Feedback for Human Machine Interface Automotive Experiments"

In Chapter 2 [32] we present a framework to engineer a high-quality Force-Feedback (FF) steering system. Inspiration was drawn from similar haptic device design in automotive implementations [76] and biomechanical applications [9]. Goal of this work is to establish the apparatus for providing realistic steering force-feedback for human-in-the-loop automotive experiments. The Force-Feedback Steering Wheel (FFSW) has been integrated into the moving base simulator of the Intelligent Automotive Systems Group (IAS). The implementation surpasses the limitations of realizing accurately inertia and damping by: employing a torque sensing element, avoiding the steering angle differentiation and by applying speed control for the feedback motor.

Chapter 3: “Driving Simulator Parameterization using Double-Lane Change Steering Metrics as Recorded on Five Modern Cars”

The objective of the work that will be presented in Chapter 3 [40] is twofold: a) assess the on-centre related steering metrics of real cars during lane-change tests, b) identify the key parameters of the vehicle that determine these steering metrics. To achieve these goals we measured vehicle speed, lateral acceleration, steering wheel torque, and steering wheel angle in five modern passenger cars during double-lane change tests. Using these data, we quantified the steering sensitivity and steering torque gradient metrics. Then we simulated the same manoeuvres using a single-track vehicle dynamics model. We evaluated the relationships between the model parameters and steering metrics to investigate which physical characteristics of the vehicle affect the metrics. As proof of concept: a) we present an example where we parameterized the single-track vehicle dynamics model so that its on-centre dynamical response was similar to the one of the tested cars, and b) we adapted and ported the former parameterization to a high-fidelity driving simulator, so as to evaluate its realism for driver in the loop tests.

Chapter 4: “Road-Departure Prevention in an Emergency Obstacle Avoidance Situation”

In Chapter 4 [41], we present a road-departure prevention system we developed and tested in an emergency scenario, with 30 test drivers in our driving simulator. This RDP system utilizes look-ahead information to derive the future lateral position of the vehicle with respect to the road. The RDP system intervenes by applying haptic (guidance) feedback torque and/or correcting the angle of the front wheels (drive-by-wire) when road departure is likely to occur.

Chapter 5: “Race Car Instrumentation for Driving Behaviour Studies”

In part A of Chapter 5 [34] we provide information on how to instrument real race cars with a limited budget and to enable data-acquisition required for studying driving behaviour. Part A condenses issues related to the building of electro-mechanical equipment, where all the developed solutions, mechanical-electronic designs and software are made freely available online in [33]. Raw measurement processing and data interpretation is presented and the Simple-Driver-Model (SDM) is introduced to analyse driver behaviour. A case study in circular manoeuvring is presented comparing an expert and a novice driver. The novel SDM-based driving analysis is used to identify distinct driving behaviour characteristics of drivers with varying skill levels.

In part B of Chapter 5 [39] we present a pilot study we commenced to investigate the relationship between driver’s sensory inputs and compensatory control-actions. The sensory inputs can be visual, kinesthetic (steering torque) or vestibular (lateral acceleration, yaw rate and slip angle) feedback. Six drivers with varying driving skill level were instructed to execute high-speed circular manoeuvres on a loose surface (dirt), aiming at maintaining approximately a constant sideslip angle and distance from the centre of the tire-marked circular path (with 7.5 m radius). For the test, we used a rally prepared purpose instrumented RWD vehicle. By analysing the driver control actions and the vehicle response, we studied the cross-correlation of the sensory inputs and the corresponding control actions (steering, throttle). In part C of Chapter 5 [63] we present a controller to stabilize a RWD vehicle with respect to drifting equilibria.

Chapter 6: “Driver Model with Visual and Neuromuscular Feedback for Objective Assessment of Automotive Steering Systems”

Chapter 6 [31] will introduce a force-feedback driver model based on previous NMS models developed at TU Delft [51][9][168]. This model will be used to evaluate the driver-car interaction with various steering systems settings, under different test scenarios that involve response to forces. This required the combination of existing NMS models with a preview driver model leading to a coherent structure proposed earlier by Pick and Cole [11].

Chapter 7:"Haptic Steering Support for Driving Close to the Vehicle's Handling Limits"

Part A of Chapter 7 [36][38][35] will elaborate the concept of a haptic steering support when driving near the vehicle's handling limits (Haptic Support Near the Limits; HSNL). The goal of the support is to promote the driver's vehicle internal model (vehicle behaviour and handling capacity) by providing haptic cues on the steering wheel. The haptic controller was initially tested in a driving simulator and was later adapted-improved to be tested in a 1.8L Opel Astra, which can provide variable steering feedback torque. The rationale behind the HSNL, derives from the vehicle's property to reduce the steering "stiffness" (the steering feedback torque as a function of the steering wheel angle) before the vehicle reaches its handling limits and starts to understeer.

Part B of Chapter 7 [37] will evaluate HSNL performance, on high-speed real track testing The principle to assess the HSNL into two fundamentally different conditions derives from prior driver behaviour research. Studies related to driving that had set off in the 1930's [96] manifest that drivers primarily steer in an anticipatory feed-forward manner to an estimated future path while they use an adaptive-control strategy to compensate for deviations of the vehicle from the demanded trajectory [56].

Continuing upon the aforementioned statements, the drivers in the skid-pad testing (Chapter 7 part A)[36] were expected to mainly employ feedback control to compensate for disturbances (e.g. friction coefficient changes) or driver's perception mismatch [56][105]. On the contrary in the test-track driving (Chapter 7 part B), drivers were expected to mainly employ feedforward steering control, due to the repetitive test-track driving test, where drivers would try to memorize and re-apply the same control inputs. Therefore, the two experiments were aiming to stimulate the two different parts of the human controller facilitating the analysis.

Chapter 8: "Conclusions"

Chapter 8 distils Chapter 2 –7, discussing the results and gives recommendations for future research on human-machine-interface near the vehicle's handling limits.

IV. Publications

The publications that each Chapter has derived from are given in the following list, below individual Chapter's title.

This thesis includes 8 Chapters. Chapter 1 is the current introduction. Chapters 2 – 7 derive from their original journal and/or conference proceedings articles.

Chapter 2: "Steering Force-Feedback for Human Machine Interface Automotive Experiments," derived from:

D. Katzourakis, D. Abbink, R. Happee, E. Holweg, "Steering Force-Feedback for Human Machine Interface Automotive Experiments," *IEEE Transactions on Instrumentation and Measurement*, vol. 60, no. 1, pp. 32-43, Jan. 2011.

Diomidis Katzourakis, Mathieu Gerard, Edward Holweg, Riender Happee, "Design Issues for Haptic Steering Force Feedback on an Automotive Simulator," *Proc. of the IEEE International Workshop on Haptic-Audio Visual Environments and Games*, pp.1-6, 2009.

Chapter 3: "Driving simulator parameterization using double-lane change steering metrics as recorded on five modern cars," derived from:

D. Katzourakis, J. C. F. de Winter, S. de Groot, R. Happee, "Driving simulator parameterization using double-lane change steering metrics as recorded on five modern cars," *Simulation Modeling Practice and Theory*, vol. 26, pp. 96-112, 2012.

Chapter 4: "Road Departure Prevention in an Emergency Obstacle Avoidance," derived from:

D. Katzourakis, M. Alirezaei, J. C. F. de Winter, M. Corno, R. Happee, A. Ghaffari, R. Kazemi, "Shared Control for Road Departure Prevention," *Proc. of the 2011 IEEE System, Mans and Cybernetics Conference*, pp. 1037-1043, 2011.

D. Katzourakis, J. C. F. de Winter, M. Alirezaei, M. Corno, R. Happee, "Road Departure Prevention in an Emergency Obstacle Avoidance Situation," submitted for review, 2012.

M. Alirezaei, M. Corno, D. Katzourakis, A. Ghaffari, R. Kazemi, "Robust Driver Steering Assistance for Road Departure Avoidance," *IEEE Transactions on Vehicular Technology*, 2012.

Chapter 5: "Race Car Instrumentation for Driving Behaviour Studies," derived from:

D. Katzourakis, E. Velenis, D. Abbink, R. Happee, E. Holweg, "Race Car Instrumentation for Driving Behaviour Studies," *IEEE Transactions on Instrumentation and Measurement*, vol. 61, no. 2, pp. 462-474, 2012 (Chapter 5, part A).

D. Katzourakis, E. Velenis, R. Happee, "Driver Control Actions in High Speed Circular Driving," *Proc. of the 6th International Driving Symposium on Human Factors, Driving Assessment, Training and Vehicle Design*, 2011 (Chapter 5, part B).

E. Velenis, D. Katzourakis, E. Frazzoli, P. Tsiotras, R. Happee, "Steady-State Drifting Stabilization for RWD Vehicles," *Control Engineering Practice Journal*, vol. 19, no. 11, Nov. 2011, pp. 1363-1376, 2011.

E. Velenis, D. Katzourakis, E. Frazzoli, P. Tsiotras, R. Happee, "Stabilization of Steady-State Drifting for a RWD vehicle," *10th International Symposium on Advanced Vehicle Control 2010*, pp. 820-825, 2010 (Chapter 5, part C).

Chapter 6: "Force-Feedback Driver Model for Steering Systems Development," derived from:

D. Katzourakis, C. Droogendijk, D. Abbink, R. Happee, E. Holweg, "Force-Feedback Driver Model for Objective Assessment of Automotive Steering Systems," *10th International Symposium on Advanced Vehicle Control 2010*, pp. 381-386, 2010.

Chapter 7: "Haptic Steering Support for Driving Near the Vehicle's Handling Limits," derived from:

D. Katzourakis, E. Velenis, E. Holweg, R. Happee, "Haptic Steering Support in High Speed Cornering," *Proc. of the 1st International Conference on Human Factors in Transportation*, to be presented, Jul. 2012 (Chapter 7, part A).

D. Katzourakis, E. Velenis, E. Holweg, R. Happee, "Haptic Steering Support when Driving at the Tires' Cornering Limits," *Proc. of the 11th International Symposium on Advanced Vehicle Control, AVEC12*, to be presented, Sept. 2012 (Chapter 7, part B).

D. Katzourakis, E. Velenis, E. Holweg, R. Happee, "Haptic Steering Support for Driving Near the Vehicle's Handling Limits; Skid-pad case," submitted for review, 2012 (Chapter 7, part A).

D. Katzourakis, E. Velenis, E. Holweg, R. Happee, "Haptic Steering Support for Driving Near the Vehicle's Handling Limits; Test-track case," submitted for review, 2012 (Chapter 7, part B).

Diomidis Katzourakis, "Haptic Steering Support when Driving Close to the Front Tire's Grip Limits." Patent filled with SKF, 2012.

Chapter 8: "Conclusions"

Chapter 2. Steering Force-Feedback for Human Machine Interface Automotive Experiments

“The driver of a racing car is a component. When I first began, I used to grip the steering wheel firmly, and I changed gear so hard that I damaged my hand.”
Juan Manuel Fangio, 1911-1995 A.D.

Steering Force-Feedback for Human Machine Interface Automotive Experiments

Abstract—Driving simulator fidelity is usually defined by the quality of its visual and motion cueing system. However, the quality of its haptic cues is also very important, and determined by both hardware and control properties. Most experiments with haptic steering systems employ commercially available systems, and do not address the system's fidelity. The goal of this Chapter is to offer guidelines for the development of hardware, performance evaluation and system's control in order to engineer realistic haptic cues on the steering wheel. A relatively low-cost solution for hardware is deployed, consisting of a velocity-controlled three-phase brushless servomotor, whose high bandwidth control allows for a realistic representation of forces. A method is presented to overcome electromagnetic interference produced by the industrial servomotor and the controller, through careful amplification and filtering. To test the system, different inertia-spring-damper systems were simulated and evaluated in time and frequency domain. In conclusion, the designed system allowed reproduction of a large range of steering wheel dynamics and forces. As a result, the developed system constitutes an efficient haptic device for human-machine-interface automotive experiments.

I. Introduction

Human-In-the-Loop (HIL) driving simulators are widely utilized by automotive manufacturers [47] and researchers to reduce prototyping time and cost. Successful applications range from driver training [92] to Human-Machine-Interface (HMI) system design for automotive control applications [55][119]. Compared to real vehicle experiments, driving simulation provides enhanced repeatability, safety, unlimited parameterization for the vehicle and the environment and relatively lower cost. Nevertheless, designing a high-fidelity HIL simulator able to provide realistic cues to the driver is challenging. It requires sophisticated vehicle dynamics modelling, high-fidelity visualization and sensor/actuation mechanisms [76].

Motion during driving is sensed through vestibular, audio-visual and kinesthetic-haptic stimulants [2]. Poor quality of any of the simulated cues can make difficult or even impossible to perform easy driving tasks, such as lane following [76]. A fundamental haptic cue is the feedback force at the steering wheel. It renders the vehicle-road interaction and is considered very important for driving a vehicle [5][46]. For example, the reduction of the self-aligning moment at the steering wheel, when the front tires approach their lateral force peak, is a valuable feedback to the driver [142] (pp. 408).

This Chapter presents a framework to engineer a high-quality Force-Feedback (FF) steering system. Inspiration was drawn from similar haptic device design in automotive implementations [76] and biomechanical applications [9]. Goal of this work was to establish the apparatus for providing realistic steering FF for HIL automotive experiments. The Force-Feedback Steering Wheel (FFSW) has been integrated into the moving base simulator (Fig. 2.1) of the Intelligent Automotive Systems Group (IAS).

The rest of the Chapter is organized as follows: Section II summarizes related work while Section III describes briefly the architecture of the system. Section IV focuses on the FF hardware and electronics whereas Section V is dedicated to FF motor control. Section VI is occupied with the fidelity

analysis of the system. Section VII addresses automotive steering system modelling and HIL testing. Finally Section VIII concludes the Chapter.

Fig. 2.1. TUDelft moving base simulator.

A. Related work in force-feedback steering wheels

FFSW are popular within driving game simulators. Usually they are cost effective solutions for the wide market (e.g., Logitech Momo [108]). Although some low-cost FFSW can already increase simulation realism, they are not suited for high-fidelity haptic research. The weak motors used, offer little FF power while the reduction gearing imposes a noticeable high inertia. The steering angle is commonly determined through plain potentiometers achieving moderate angular resolution. Still, some researchers have used low-fidelity FFSW when studying the effect of FF [160], in cases where fidelity is of secondary importance. High-end steering wheels also exist, but at a considerable higher price (FrexGP, ECCI etc. [108]). More sophisticated commercial FFSW are also available for HIL automotive research. Their enhanced performance is accompanied with a cost surpassing the price of an average automobile (Moog FCS ECoL-8000 S actuator [49]).

Custom-made FFSW have also been presented in the literature regarding automotive simulation [76][136] or drive-by-wire applications [133][98][1]. Griffiths and Gillespie [136] explore the benefits of augmented FF to share control between the driver and automated steering, to support lane keeping. They use low-complexity vehicle dynamics and a current-controlled haptic wheel. Mohelbi *et al.* [76] propose a method that calculates the feedback force for driving simulators and haptic augmentation to overcome the simulation latencies. The DC motor feedback torque can simulate the stiffness and damping of the steering column.

An exceptional steer-by-wire conversion on a 1997 Chevrolet Corvette has been presented from Yih and Gerdes [133] (Stanford Dynamic Design Lab). This study aimed to improve the handling characteristics of the Corvette through steer-by-wire. Using closed-loop system identification they

estimated the properties of the steering system (rack mass and damping) and derived a controller with minimal steering lag. Another publication for the same vehicle from Switkes *et al*. [98] describes in detail the FFSW system and the control method. They present a realistic steering system model for determining the feedback torque. The brushless DC motor they used has a reduction ratio of 5:1 and the system's properties were experimentally identified. For creating an additional sense of damping and inertia they use the first and second derivative of the steering angle. Further, they evaluate the design of the drive-by-wire system for stability during lane keeping. Another haptic interface for steer-by-wire technology has been presented by Baviskar *et al.* [1]. They propose an adaptive steer-by-wire controller with torque observers eliminating the needs for torque measurement. Their experimental setup of the FFSW involves a steering wheel in direct drive from a torque-controlled switched reluctance motor. The characteristics of the FF device were identified by torque tests. Note that in the majority of this related work, the representation of virtual inertia and damping is accomplished by differentiating the steering angle; a method which introduces noise. Although the mentioned studies address FFSW, they mostly focus on the effects of FF on the driver, and neither on the device itself nor its fidelity.

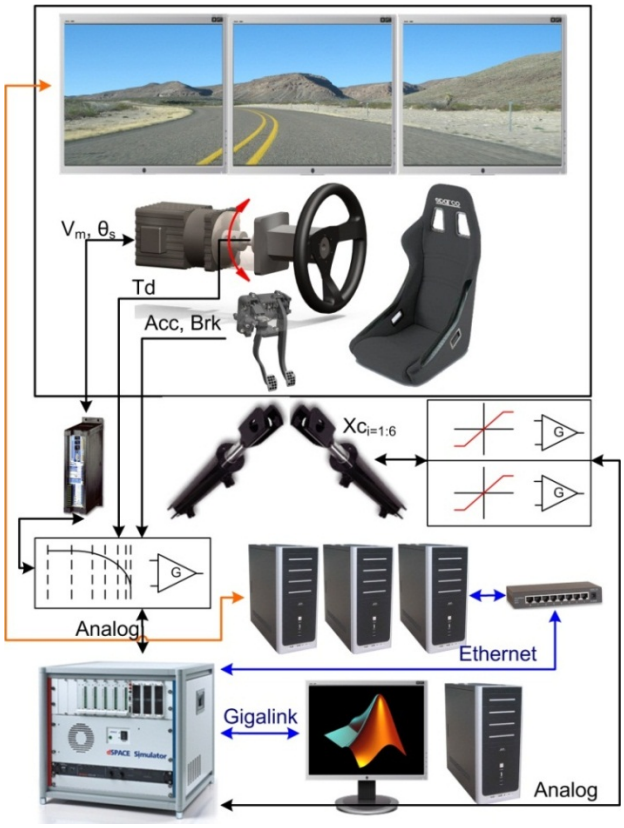

Fig. 2.2. Moving base simulator components.

This Chapter presents an implementation which surpasses the aforementioned limitations of realizing accurately inertia and damping by: employing a torque sensing element, avoiding the steering angle differentiation and by applying speed control for the feedback motor. It provides a framework for realizing a high fidelity FFSW based on innovative concepts, summarized as:

(a) Architecture of an automotive simulator with FFSW.
(b) Feedback motor velocity control.
(c) FFSW experimental fidelity analysis.
(d) Automotive steering system modelling.

(e) Noise tolerant FFSW control method.
(f) Simulation test analysis on the proposed methods.

II. Architecture of the automotive simulator

This subsection portrays briefly the simulator's architecture. A detailed description can be found in Ref. [43]. The simulator is based on a dSPACE Real-Time (RT) computer. It executes a commercial RT Vehicle Dynamics Model (VDM), developed on an open Matlab®/Simulink® block, from the dSPACE *Automotive Simulation Model* (ASM) package. An overview of the simulator is illustrated in Fig. 2.2.

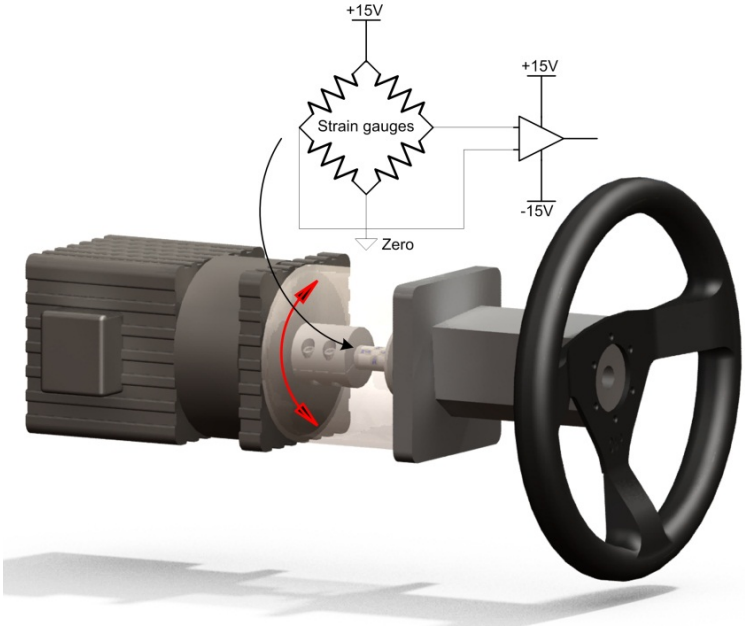

Fig. 2.3. Force-feedback motor with torque sensing on the drive shaft.

A. Computing components

The simulator consists of a mid-size dSPACE computer with two DS1005 boards in master-slave topology. dSPACE interfaces with the environment via Analog-to-Digital (A/D, DS2002) and Digital-to-Analog (D/A, DS2102) boards. One desktop PC constitutes the user station providing the interface to the simulator. It also hosts the Matlab®/Simulink® suite where the VDM and control algorithms are being developed. The dSPACE simulator transmits the animation data over an Ethernet connection to three desktop PCs handling the graphics. Finally, three TFT monitors compose a viewing angle of 135^{o} (Fig. 2.1).

B. Software for the simulator

Software from Matlab®/ Simulink® and dSPACE is used for the operation of the simulator. The dSPACE *Test and Experiments* software suite and the ASM VDM are used for: RT parameter handling, RT 3-D animation and RT parameterization of the virtual vehicle components (drivetrain or chassis). The vehicle is an open Matlab®/ Simulink® model with 24 degrees-of-freedom (DOF). It incorporates semi-empirical tire models, suspension dynamics, steering system model etc. The VDM model is being executed at 1 kHz at the "slave" DS1005 board. Communication with the environment through the D/A and A/D boards is performed through the "master" board at 5 kHz.

C. Motion hardware

The simulator can render inertial and haptic cues through the motion of the platform and the FFSW respectively.

The cockpit on top of the platform (driver's seat, FFSW etc.) is mounted on a hydraulically controlled Stewart platform, constructed at the Faculty of 3mE, TUDelft. The signals controlling the movement pass through an electronic array where inappropriate signals are limited by saturation. The cockpit was originally a commercial driving simulator, which was modified for the HMI-HIL experimental needs.

The FF steering motor (Fig. 2.3) is an Ultract II, type 708303, high response AC Brushless Servo Motor. The motor shaft is connected in direct-drive fashion to the steering wheel, through an adjustable clamp mechanism. The steering torque at the shaft is measured by four symmetrically glued active strain gauges forming a Wheatstone bridge circuit. When the shaft is strained, the resistive changes of the bonded gauges unbalance the bridge resulting to a few mVs voltage deviation. The Wheatstone bridge offers temperature compensation and linearity between strain and voltage measurements [14]. The torque signal requires further conditioning (filtering-amplification) to become practical for usage, as explained in the next section. The FF motor is controlled by a DSP based AX-V brushless motor servo controller from Phase Motion Control. The default Speed-V software is uploaded in the AX-V, transforming the steering motor to a speed controlled servo drive. The current loop for the motor is updated at 16 kHz and the position loop at 4 kHz. The AX-V supplies the absolute angular position of the shaft through a continuous analog signal with a range 0-10 V (representing 0-360^o). The analog position signal after being conditioned is supplied to the dSPACE A/D board. The AX-V platform was developed specifically as a controller for the Ultract II motor for optimal performance. Nonetheless, despite the good specifications, the noisy nature of the motor-controller imposes difficulties for connecting it to the simulator. The challenge for achieving high accuracy in the measurements and stability for control is addressed in the following sections.

III. Force-feedback hardware equipment

Realistic representation of haptic steering forces requires a mechanism for adjusting the feedback torque. While direct motor torque control is commonly utilized [76][136], it is not accurate enough for frequencies below 0.5 Hz [17]. A popular solution for high fidelity haptic applications is to apply velocity controlled motors [9]. The Ultract II motor employed for the FF is powered by a three-phase source of alternating voltage. The speed can be adjusted by powering the motor through inverters. Inverters convert DC voltage to AC at a specific amplitude and frequency. The 3-phase voltage waves are produced with Pulse Width Modulation (PWM) [84] at 16 kHz. The PWM drive evokes noise lines at frequencies linked to the switching frequency of the IGBTs [138]. This excites parasitic capacitive couplings at the components of the system, spreading EMI currents to other components of the driving simulator [4]. Overall, when the system is in operation it creates noise to all circulation paths, including the ground and the power supply.

The electric noise sampled from the A/D board with the FF motor enabled can be easily identified in Fig. 2.4. It illustrates the unfiltered voltage from the throttle sensor, a simple variable resistor. The noise when the motor is enabled at time equals 2.55 sec is illustrated at the top subplot. The same sensor, with the motor disabled exhibited noise only at 50 Hz and its harmonics, as displayed at the bottom subplot (frequency of the main power line). The 16 kHz PWM (f_{pwm}) signal is responsible for the peaks around 1 kHz (and their harmonics), as displayed in the middle subplot. The 1 kHz peak is frequency folded because of aliasing. The sampling frequency f_s is at 5 kHz, thus the aliased frequency f_a is expected to be present at $f_a = f_{pwm} - f_s \cdot C \Rightarrow f_a = 16$ kHz $- 5 \cdot 3$ kHz $= 1$ kHz (C integer multiples of the f_s) [94].

The initial approach to reduce the noise was to apply second order low-pass Butterworth active filtering (Appendix, Fig. 2.17, right) for all the sensors and to isolate the connections from and towards

the motor controller, using two ISO-122 isolation amplifiers. Although this approach improved the noise over the dSPACE lines, it did not sufficiently reduce the noise in the torque measurements (motor's shaft, Fig. 2.3).

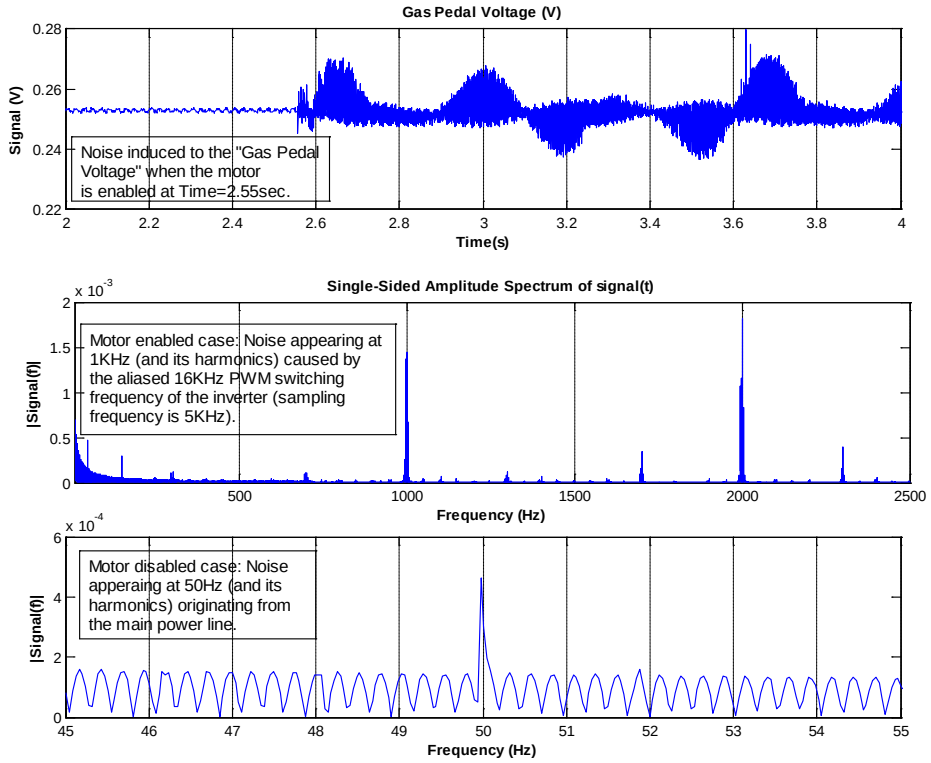

Fig. 2.4. Noisy sampled data from the A/D boards prior to system's redesign, recorded with a variable resistor used as throttle pedal position sensor.

Spectral analysis revealed that the motor EMI was affecting the strain gauges at frequencies above the bandwidth of the op-amp (1.5 MHz maximum) of the active filter. This resulted in the non-linear operation of the op-amp, ruining the filter's properties.

Best results were finally achieved by simple analog RC filters between the connections of the A/D board and the sensors. Concerning the torque sensor, individual output of the bridge was RC-filtered and fed through a voltage follower (G = 1) to the difference amplifier (G = 470) (Fig. 2.5). A design guide from Texas Instruments [19] was used for designing the difference amplifier.

The system performed best with the torque conditioning circuit as close as possible to the motor shaft. Also all the shieldings from the cables that carried analog signals were connected to the ground of the A/D board. The filters' components are shown in Fig. 2.5 along with their resulting bandwidths (**F_b(Hz)**; bold letters, inside dashed boxes). The conditioned torque is a fairly linear function of the measured voltage as displayed in Fig. 2.6). The estimated torque from voltage follows closely the first degree polynomial fitted with the *polyfit* function from Matlab®.

Two RC filters in series constitute a second order low-pass filter for the steering angle (Fig. 2.5). This filter has the low bandwidth of 12.77 Hz. Nonetheless, driver's steering inputs are expected to be lower than the cut-off frequency of the filter. Von Groll *et al.* [124] denote that torque steering inputs from a driver are expected to be less than 4 Hz. Therefore, position inputs are expected in even lower frequencies, since they derive from the second integration of the driver's torque. Yet, steering FF above 4 Hz will provide useful haptic information to the driver about the vehicle's state; thus a high bandwidth actuator is always desired.

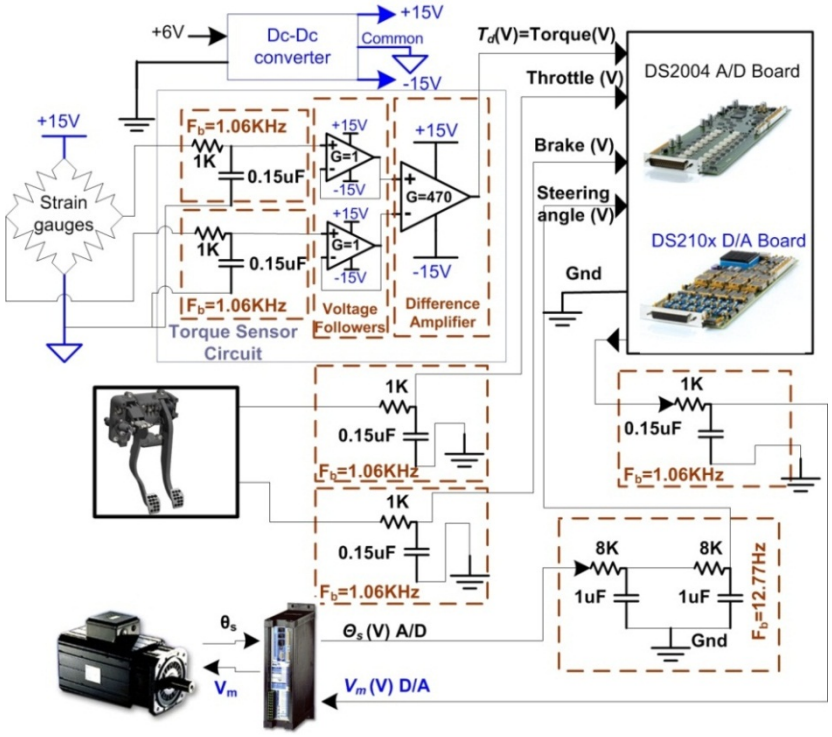

Fig. 2.5. Optimal topology for dSPACE-sensors- motor.

IV. Feedback motor control

This part of the Chapter explains the velocity control concept for the feedback motor. The Force-Feedback-Device (FFD) was for simplicity initially tested independently of the VDM. It was programmed to simulate a virtual Inertia-Spring-Damper (ISD) system (dotted sketch in Fig. 2.7) coupled to the motor and externally stimulated by the driver's torque T_d. The virtual model consists of: the torsion stiffness K_s, the moment of inertia J_s and the rotational damping b_s. Assuming a physical implementation of the system inside the dotted box of Fig. 2.7 and applying Newton's second law, one can derive the following dynamical equation:

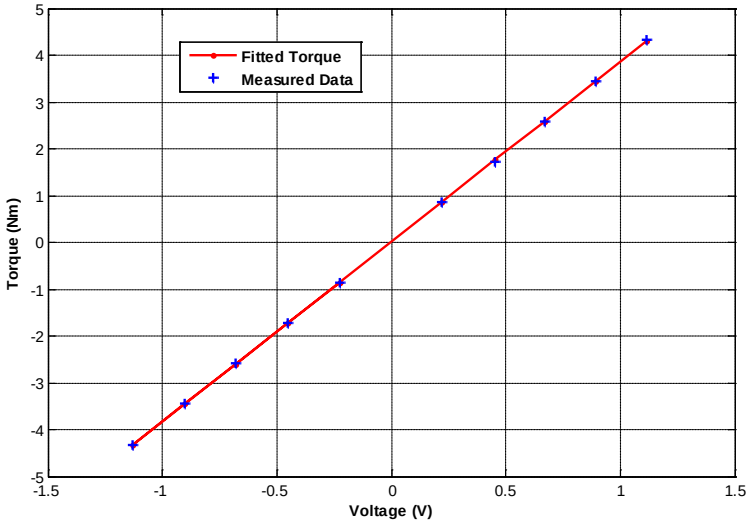

Fig. 2.6. Steering torque vs. output voltage of the torque sensor.

$$J_s\ddot{\theta}_s = T_d - K_s\theta_s - b_s\dot{\theta}_s \quad (2.1)$$

The actual simulated system though, is described inside the dashed rectangle of Fig. 2.7. The *Resultant torque* is the subtraction of the *Driver's torque* T_d and the *Model's torque*. T_d is measured from the torque sensor on the shaft (Fig. 2.3). Dividing the *Resultant torque* by the virtual inertia results in the *Desired angular acceleration* $d^2\theta_{des}/dt^2$. Its integral, the *Desired angular velocity* $d\theta_{des}/dt$ is used as the velocity command for the feedback motor. The damping force is calculated as the product of b_s and the *Desired angular velocity*; not the derivative of the steering wheel angle θ_s that other researchers use [98]. The dynamical equation of the simulated system is depicted in (2.2).

$$J_s\ddot{\theta}_{des} = T_d - K_s\theta_s - b_s\dot{\theta}_{des} \quad (2.2)$$

The rationale behind this is that the steering angle is an analog signal with a noise ripple of 0.1° (after being analog and digitally filtered). The differentiation of the noisy steering angle signal results in large errors, which when multiplied with a high damping value, can lead to system instability. At the same time, the integration of the *Desired angular acceleration* (Fig. 2.7) for obtaining the *Desired angular velocity* filters out the torque noise ripple, which has a magnitude of 0.02 Nm. The usage of the *Motor velocity command* as the actual steering velocity also coheres with the haptic controller design guide of Schouten *et al.* [9].

If the virtual inertia J_s (Fig. 2.7) is set below 0.001 kg·m^{2}and at the same time the steering wheel is grasped extremely strongly by the driver (thus rigidly coupling arm inertia to the virtual dynamics), then an effect named "contact instability" [9] occurs provoking the system to become unstable. Nonetheless, the system is still safe for the subject since it will become stable as soon as the grasp becomes less stiff.

Both the steering angle θ_s *(V)* and the torque T_d *(V)* voltages (Fig. 2.5) are software conditioned before being utilized in the virtual model. This includes: second order filtering with a bandwidth of 195.5 Hz for the torque and 19.5 Hz for the steering angle and further conversion from voltages to actual values.

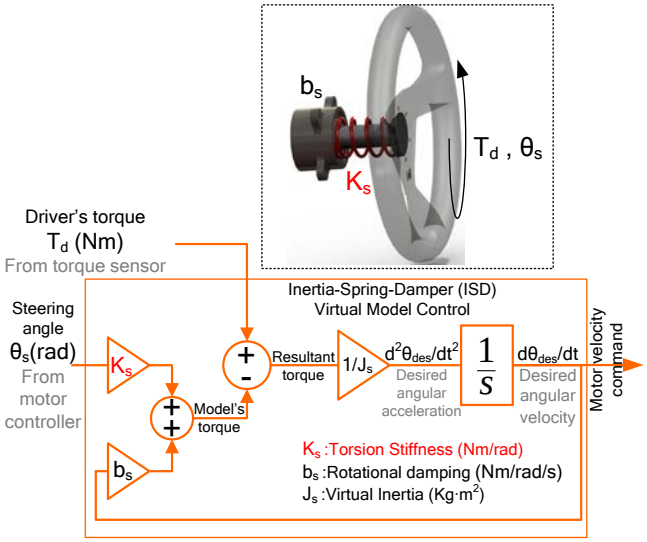

Fig. 2.7. Inertia-spring-damper virtual model for force-feedback testing. The physical model is sketched in the dotted square and the actual simulated system in the dashed rectangle.

V. Force-feedback device fidelity

The performance of the designed hardware and controller of the FFD was evaluated by simulating several virtual models (i.e. changing parameters for inertia, damping and stiffness). The response of the steering wheel system to torque perturbations was measured, and validated in two ways. First, the measured signals were compared in the time-domain to simulated signals which describe the response of

the virtual system to the torque perturbation. Second, the virtual models were estimated back using closed-loop system identification techniques [140][107][60].

Fig. 2.8 illustrates the system identification scheme. The virtual dynamics of several inertia-spring-damper systems without load (i.e., no subject holding the steering wheel) were perturbed by multi-sine torque disturbances. The virtual stiffness was realized using the steering angle signal $\theta_{realized}$ from the motor controller. Although the experiments were conducted with no human load, the measured torque was also included in the simulated model. That is because in practice an external torque is caused by the combined inertia of the steering wheel and the motor's shaft; damping is also introduced by the supporting ball bearing (Fig. 2.8, *Load* block).

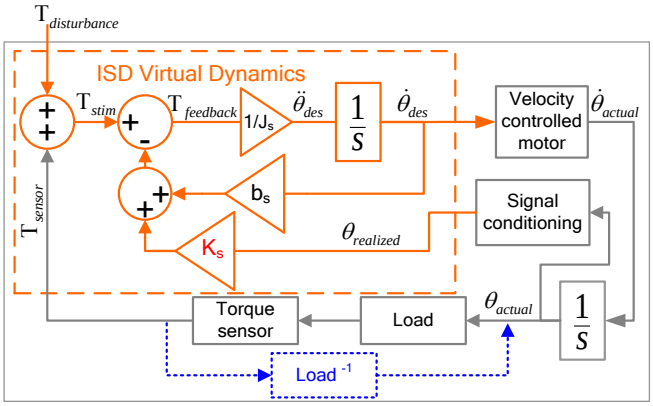

Fig. 2.8. System identification scheme.

To enable accurate system identification, the torque disturbance signal was designed in the frequency domain as a multi-sine signal with optimized crest factor, so as not to introduce bias or variance in the estimated spectral densities [140]. Furthermore, for an improved Signal-to-Noise Ratio (SNR) the power of the disturbance signal was distributed over a limited number of frequencies within the bandwidth. The disturbance signal consisted of 30 logarithmically spaced clusters of frequency points (a cluster contained two adjacent frequencies for averaging) in a bandwidth of 0.65-20 Hz. Fig. 2.9 shows the time and frequency domain representation of the designed torque perturbation signal.

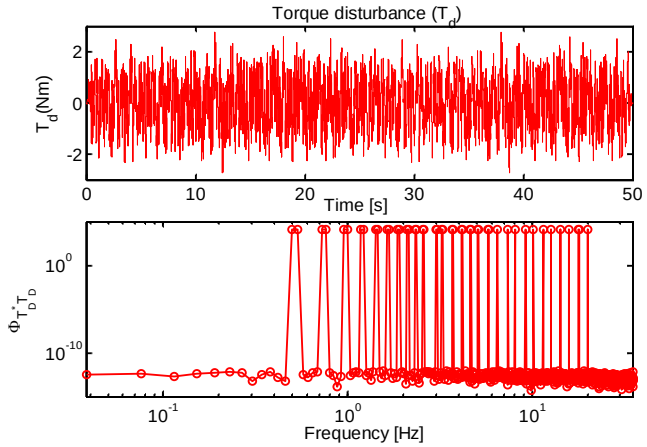

Fig. 2.9. Torque disturbance (upper subplot) and corresponding spectral power (lower subplot). It consists upon 30 logarithmically spaced clusters of frequency points starting from 0.65 Hz.

A. Time response analysis

The most simple fidelity analysis can be done by comparing the time response of the steering angle $\theta_{realized}$, (Fig. 2.8) of the real system and the simulated system, when both are excited with the same torque disturbance. An example of time domain analysis is illustrated in Fig. 2.10.

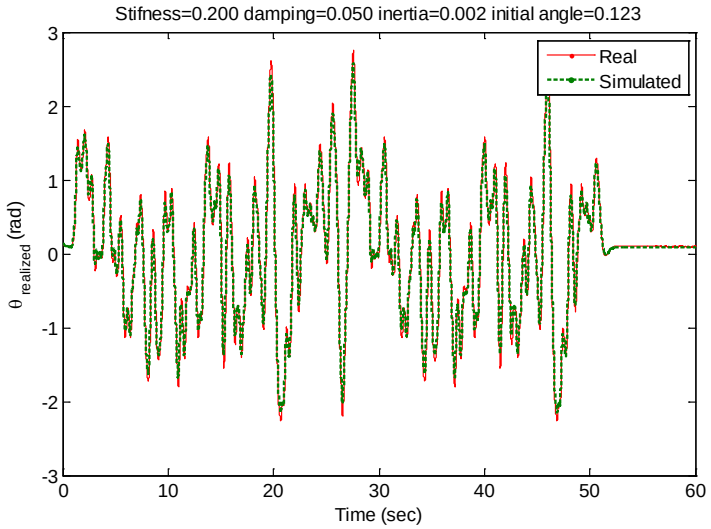

Fig. 2.10. Time response of the actual force-feedback device ("Real") response and a simulated inertia-spring-damper system ("Simulated") with the same parameter settings and initial conditions.

Multiple parameter settings (inertia, damping, stiffness) were tested and the Root Mean Square (RMS) between the "Real" and "Simulated" angle of the ISD system was obtained. The normalized RMS is shown in Fig. 2.11. The radius of the sphere representing the error's magnitude is the square of the RMS error (for better visualization). The minimum and maximum RMS errors were 0.03 and 0.2 rad respectively. Overall, it can be concluded that the required dynamics were realized accurately over a large range of parameters. Notice that the error increases for small damping values. Definitely, the time domain analysis can give an insight for the dynamic performance of the FFD. Yet, high frequency responses cannot be evaluated solely from a time domain evaluation. Thus, frequency domain analysis was the second stage in the fidelity assessment process.

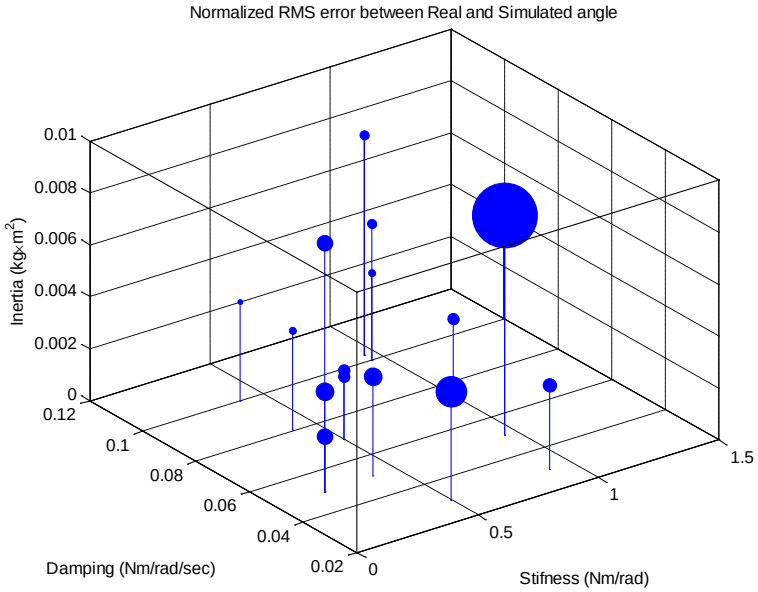

Fig. 2.11. Normalized RMS angle error between the actual response from the force-feedback device and that of a simulated inertia-spring-damper system. Plotted for multiple parameter settings. The radius of the sphere is the square of the RMS error (for better visualization).

B. Frequency domain analysis

Another way to visualize the developed system's ability to accurately emulate the desired stiffness, damping and inertia, is to estimate the realized dynamics from the measured signals, and to compare them to the desired dynamics. This visualization has an advantage over the time-domain in that it also shows the performance to simulate dynamics at higher frequencies (where damping and inertia dominate).

To achieve the aforementioned comparison an identification process described by Schouten *et al.* [9] and de Vlugt *et al.* [60] was adjusted to the particularities of the current system. During individual experiments, the measured torque T_{sensor}, the torque disturbance $T_{disturbance}$, the realized angle $\theta_{realized}$ (steering angle realized after the signal conditioning) and the perturbation torque signals T_{stim} (T_{stim} = $T_{disturbance}$ + T_{sensor}) were sampled at 500 Hz for 60 sec (the names of the signals correspond to Fig. 2.8). Two Frequency-Response-Functions (FRF) were estimated: the admittance of the programmed ISD (*ISD(f)*), resulting from T_{stim} to θ_{actual} signal, and the admittance $Load(f)^{-1}$ resulting from T_{sensor} to θ_{actual} signal. Note that the $Load(f)^{-1}$ is the inverse FRF of the Load's impedance, so that the causal admittance is shown. In the estimation process the actual steering angle θ_{actual} was not available, thus it was taken to be equal to the realized steering angle $\theta_{realized}$.

The sampled signals $T_{sensor}(t)$, $T_{disturbance}(t)$, $T_{stim}(t)$ and $\theta_{realized}(t)$ were transformed with the Fast Fourier Transform (FFT) to the frequency domain signals of $T_{Sensor}(f)$, $T_{Disturbance}(f)$, $T_{Stim}(f)$ and $\Theta_{Realized}(f)$ respectively. The frequency signals were used to estimate the cross spectral densities (2.3)-(2.5).

$$\hat{\Phi}_{T_{Disturbance}\Theta_{Realized}} = T^{*}_{Disturbance}(f)\cdot\Theta_{Realized}(f) \tag{2.3}$$

$$\hat{\Phi}_{T_{Disturbance}T_{Sensor}} = T^{*}_{Disturbance}(f)\cdot T_{Sensor}(f) \tag{2.4}$$

$$\hat{\Phi}_{T_{Disturbance}T_{Stim}} = T^{*}_{Disturbance}(f)\cdot T_{Stim}(f) \tag{2.5}$$

The hat (^) denotes estimate and the asterisk (*) denotes complex conjugate. The FRFs of the *ISD(f)* and the $Load^{-1}(f)$ can be estimated by dividing the appropriate cross-spectral densities [9][60]:

$$ISD(f) = \frac{\Theta_{Realized}(f)}{T_{Stim}(f)} = \frac{\hat{\Phi}_{T_{Disturbance}\Theta_{Realized}}}{\hat{\Phi}_{T_{Disturbance}T_{Stim}}} \tag{2.6}$$

$$Load^{-1}(f) = \frac{\Theta_{Realized}(f)}{T_{Sensor}(f)} = \frac{\hat{\Phi}_{T_{Disturbance}\Theta_{Realized}}}{\hat{\Phi}_{T_{Disturbance}T_{Sensor}}} \tag{2.7}$$

The FRFs of (2.6) and (2.7) without any further processing will be referred as "measured data" in the rest of this section. Only frequencies with expected high SNR from the FRFs were used for the model estimation. Those were the frequencies containing more than half of the maximum power of the power spectral density of the disturbance signal (2.8). In (2.8), *f* denotes the frequency vector and *k* the index of that vector.

$$\begin{aligned} &\hat{\Phi}_{TT} = T^{*}_{Disturbance}\cdot T_{Disturbance} = \left|T_{Disturbance}\right|^{2} \\ &f_k : \hat{\Phi}_{TT}(f_k) \geq 0.5\cdot Max\left(\hat{\Phi}_{TT}\right) \end{aligned} \tag{2.8}$$

The outliers from the resulting FRF were also removed for better performance. An outlier was considered to be more than three standard deviations away from the mean [125]. Finally, the resulting FRF was fitted to a second order system (ISD) system with the *invfreqs* function from the Matlab®'s *Signal Processing Toolbox*. This function is suitable for identifying continuous-time filter parameters from frequency responses.

Fig. 2.12 shows an example of such frequency domain plot based on closed-loop system identification, for one of the tested dynamics: an under-damped ISD with inertia = 0.01 kg·m^2, stiffness = 0.2 Nm/rad and damping = 0.05 Nm/rad/sec. The desired, programmed dynamics (cyan line) are compared to the measured data (magenta asterisks). To further substantiate the findings, an ISD model was fitted to the measured data in the frequency domain, according to the process described above, which yielded nice fits (blue circles). The figure shows that the estimated model resembles closely the programmed one. This was true for all tested conditions.

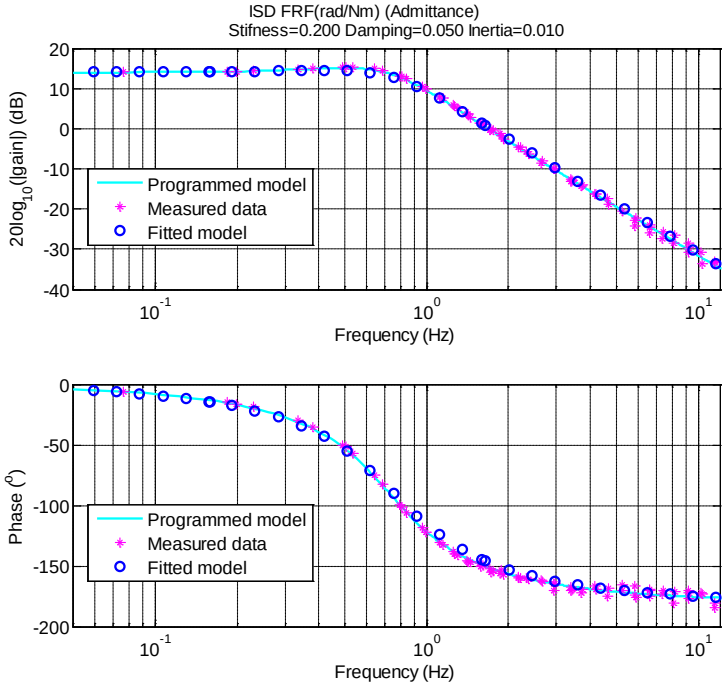

Fig. 2.12. FRFs of the admittance (rad/Nm) from an under-damped system setting (inertia = 0.01 kg·m2, stiffness = 0.2 Nm/rad and damping = 0.05 Nm/rad/sec). The gain (upper subplot) and phase (lower subplot) are shown for the FRFs for the desired dynamics (cyan line), the measured data (magenta asterisks) and an estimated (blue circles) inertia-spring-damper model fitted to the measured data.

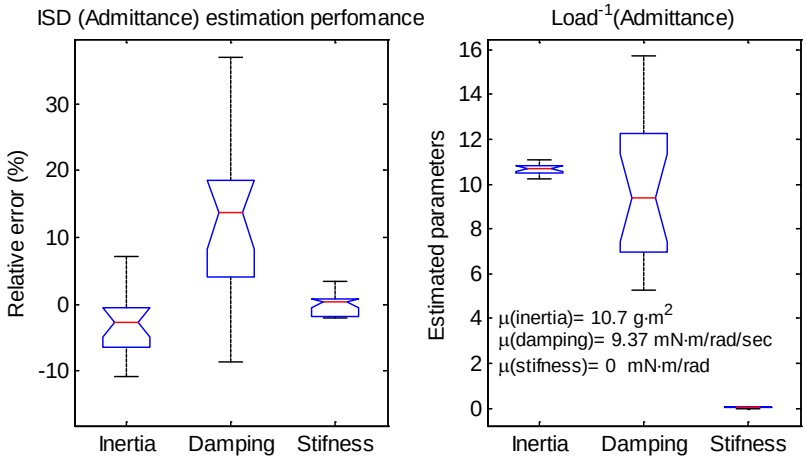

Fig. 2.13. Left boxplot displays the relative error between the programmed and the fitted model parameters for the ISD FRF. Right boxplot exposes the estimated parameters from the Load(f)$^{-1}$ FRF.

The estimated parameters were compared to the simulated parameters (same parameters as in Fig. 2.11). In the left boxplot of Fig. 2.13 one can see the relative error between the programmed and the

fitted model parameters for the *ISD* FRF. The process exhibited satisfying results, given the sensitive nature of the described method. The stiffness demonstrates the smallest relative error compared to damping and inertia. Its effect is dominant in low frequencies and thus can be easily both simulated and estimated.

As mentioned earlier, the experiments where performed with no external load on the system. However, the steering wheel assembly is expected to introduce dynamics estimated by the $Load^{-1}(f)$ FRF. This is illustrated in Fig. 2.14 and resembles a second order system with inertia and damping with a gain drop of 40 dB/dec. The estimation process yielded realistic values with medians of: μ(inertia) = 0.017 kg·m^2, μ(damping) = 0.0937 Nm/rad/sec and μ(stiffness) = 0 Nm/rad, presented at the right boxplot of Fig. 2.13.

VI. Automotive steering system modelling

After assuring that the designed system could accurately simulate a wide variety of linear inertia-spring-damper models, the final challenge to enable realistic FF on the steering wheel was addressed; to couple the FFD to the ASM Vehicle Dynamics Model (VDM). However, realizing the dynamical connection of real measured data (steering angle and driving torque) with a virtual model is a difficult process. For example, the ASM VDM assumes noise free values of the state variables, which is improbable when real measurements are being involved.

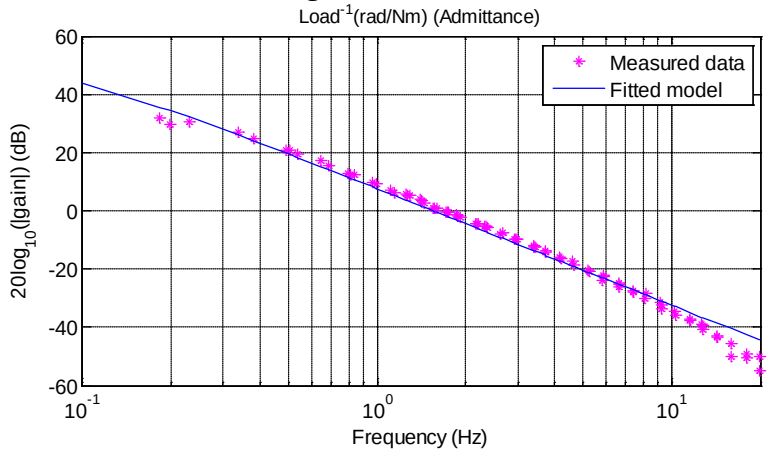

Fig. 2.14. FRFs of the Load^{-1} denoting the load's admittance (Nm/rad). It shows the gain from the measured data (magenta asterisks) and the estimated (blue line) second order system fitted to the measured data.

Both time and frequency domain analyses showed that the developed system can accurately simulate a large range of linear dynamics. Thus, the performance of the FFD system can be characterized as suitable for high fidelity FF HMI experiments.

A. Classical steering system dynamic model

To model the steering system, a power assist steering system is chosen, as illustrated in Fig. 2.15. It is composed of: steering column, rack with gearing and a power assist motor ([7]). Its dynamic behaviour is described by the following equations (the parameters are described in Table 2.1):

$$J_s\ddot{\theta}_s = T_d - K_{tb}(\theta_s - \theta_{sc}) - b_s\dot{\theta}_s \tag{2.9}$$

$$J_{sc}\ddot{\theta}_{sc} = K_{tb}(\theta_{sc} - x/R_s) + T_{assist} \tag{2.10}$$

$$m_r\ddot{x} = \frac{(K_{tb}(\theta_{sc} - x/R_s) + T_{assist})}{R_s} - b_r\dot{x} - F_r \tag{2.11}$$

$$T_{assist} = G_a(\theta_s - \theta_{sc}) = -T_m \tag{2.12}$$

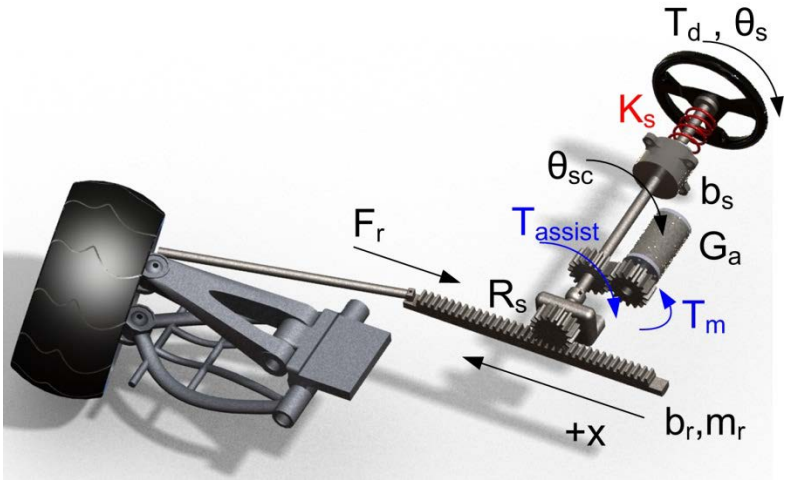

Fig. 2.15. Overview of relevant elements in the steering system model.

This particular model involves the majority of the important parts that can be found on most real steering system. Equation (2.12) describes the assist torque T_{assist} as a function of the strain (θ_s - θ_{sc}) on the torsion bar multiplied by an assist gain G_a. The resulting torque from the torsion bar as well as the assist torque act directly on the steering rack through a gear with radius R_s. Two equal size frictionless gears are assumed to deliver the motor's torque T_m directly to the steering column. The ASM steering system model that was employed, assumes that the force F_r acting to the rack through the tie rod is realized through the vehicle's suspension. F_r is derived from 6 DOF torques and forces from the tires.

Using the same principle which was described in Section V, "Feedback Motor Control," the FF can be realized by integrating the right hand side of (2.9) divided by the steering wheel moment of inertia. The resulting *Desired angular velocity* $d\theta_{des}/dt$ in (2.13) (in correspondence with Fig. 2.7) will constitute the feedback motor command. Again, for the damping estimation the $d\theta_{des}/dt$ should be used.

$$\dot{\theta}_{des}(t) = \int_0^t \frac{T_d - K_{tb}(\theta_s - \theta_{sc}) - b_s\dot{\theta}_{des}}{J_s} d\tau \tag{2.13}$$

Utilizing the above principle with a realistic stiffness value for the torsion bar, which would be in kN·m/rad scale, creates numerical challenges. A 0.1^o ripple error in the steering angle measurement multiplied by a stiffness of 1 kN·m/rad results in a 0.1·(pi/180)·1000 = 1.75 Nm fluctuation in the *Resultant torque* (Fig. 2.7). The initial attempt to overcome this issue was to increase the damping and to use smaller values for the torsion bar stiffness (values from 50-200 N·m/rad). This approach, besides deteriorating the steering feel, failed to achieve satisfactory results. Hence, a new steering system model with reduced dynamics was developed, where the feedback control was less vulnerable to the noise and at the same time it was safer for the driver holding the steering wheel.

B. New simulator steering system model

A new steering system model with reduced dynamics was implemented into the system; appropriate for being adopted at the simulator and to operate with the velocity controlled motor. The system, although simple, achieves realistic FF. The dynamical equations are the following (2.14)-(2.17):

$$J_s\ddot{\theta}_{des} = T_d - R_sF_r + T_{assist} - K_{s\_d}(V_X)\cdot\theta_s - b_{s\_d}(V_X)\cdot\dot{\theta}_{des} - (1/(|T_d|+0.2))\cdot b_{high\_damp}\cdot\dot{\theta}_{des} \tag{2.14}$$

$$x = \theta_s R_s \tag{2.15}$$

$$\dot{x} = \dot{\theta}_{des}R_s \quad (\dot{\theta}_{des}\text{: motor velocity command}) \tag{2.16}$$

$$T_{assist} = G_{a\_d}\cdot T_d \tag{2.17}$$

Equation (2.14) is the backbone of the system and consists of multiple terms including rack forces $R_s \cdot F_r$, the power assist force T_{assist}, stiffness and damping terms both functions of the longitudinal velocity and an optional "safety" term. The innovation of this model lies to the fact that the high stiffness at the torsion bar has been by-passed; the feedback stiffness component derives now from the tires' forces through the $R_s \cdot F_r$ term. The former promotes stability because the steering rack displacement is calculated as the product of the steering angle θ_s times the pinion gear radius R_s (2.15). This allows for the fluctuation error at the steering angle to be damped through the tire dynamics without creating artefacts in the feedback forces. Additionally, the J_s in (2.14) is higher compared to (2.9) since it renders the augmented inertia of the steering wheel, the steering column and the rack mass. The higher inertia reduces the magnitude of the high frequency FF noise caused by the steering angle ripple.

Table 2.1.Steering System Parameters.

Name	*Description*	*Name*	*Description*
K_{tb}	Torsion bar stiffness (Nm/rad)	R_s	Pinion gear radius (m)
J_s	Steering wheel moment of inertia (kg·m^2)	T_{assist}	Assist torque (Nm)
θ_s	Steering wheel angle (rad)	x	Rack displacement (m)
θ_{sc}	Steering column angle (rad)	b_r	Rack damping (N/m/s)
J_{sc}	Steering column moment of inertia (kg·m^2)	F_r	Rack force from tie rod (N)
b_s	Steering column damping (Nm/rad/sec)	G_a	Power assist gain
T_m	Motor's torque (Nm)	m_r	Rack mass (kg)

Equation (2.14) also includes the stiffness term $K_{s\_d}(V_X)$ which increases with the longitudinal velocity V_X. It serves as a firm aligning component to the steering wheel to improve the on-centre feel on high velocities. The damping term $b_{s\_d}(V_X)$ also increases with V_X so as to compensate for the increasing stiffness. The power assist torque T_{assist} is determined as the measured driver's torque T_d times the gain G_{a_d} (2.17). Thus, the actual strain on the shaft of the FFSW is used and not a simulated strain originating from the noisy signal of the steering angle as in (2.12). Finally, the steering rack velocity *dx/dt*, necessary for the vehicle's suspension dynamics, derives from the feedback motor *Desired velocity command* $d\theta_{des}/dt$ times the R_s (2.16).

Regarding the "safety" term $(1/(|T_d|+0.2))\cdot b_{high\_damp}$: suppose that the parameters of the steering system have been adjusted for high magnitude FF (e.g. small assist gain G_{a_d} or large R_s). If the driver releases the steering wheel, $|T_d|$ drops to zero. Thus, the safety term can inhibit any extreme motion of the steering wheel by increasing the feedback damping. However, when the driver is holding the steering wheel this term has limited effect.

C. Full system evaluation with human driver

This subsection presents an application example of the proposed system. A double lane change manoeuvre with a driver-in-the-loop utilizing the proposed feedback model was performed at 68 km/h. The final FFSW system was perceived as to feel like a real car. Results are plotted in Fig. 2.16 where the trajectory of the vehicle is illustrated at the top subplot (solid line). The dashed line represents the centre of the lane. The time t and the yaw angle $YA(^o)$ are also displayed. In the bottom subplot of Fig. 2.16, dynamical states of the steering system are being displayed in correspondence with the top subplot. The state *Model_Torque* is defined in (2.18) and is the right hand side of (2.14) when $T_d = 0$ (*Model_Torque*'s numeric negative has been plotted). The phase differences between the coupled state variables can be discerned from the sequence of the dynamic events.

$$Model\_Torque = -R_s F_r + T_{assist} - K_{s\_d}(V_X)\cdot\theta_s - b_{s\_d}(V_X)\cdot\dot{\theta}_{des} - (1/(|T_d|+0.2))\cdot b_{high\_damp}\cdot\dot{\theta}_{des} \quad (2.18)$$

The driver initially applies a torque T_d. The resultant torque (T_d - *Model_Torque*) results in a steering angular velocity and steering angle; first and second integral respectively of the resultant torque divided with the inertia J_s. The above plots of the feedback torque, the steering angle and the model torque (which represents the human-tire-road interaction) resemble the results obtained from real vehicle double lane change experiments conducted from Velenis *et al*. [63]. By altering the constant parameters values of the steering system in (2.14)-(2.17), one can achieve a virtually infinite number of different steering feelings.

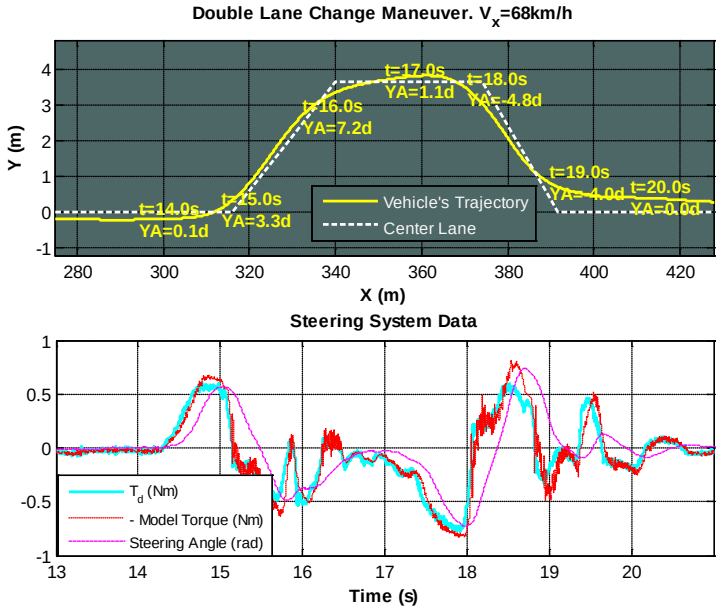

Fig. 2.16. Driver-in-the-loop double lane change manoeuvre.

VII. Conclusions

This Chapter describes the development of a high fidelity force-feedback (FF) steering device, aimed to enable human-in-the-loop automotive simulations. The developed system allows FF to be delivered to the driver through a speed-controlled three-phase brushless servomotor with a torque sensor on the motor's shaft. The developed system was able to simulate a wide range of virtual dynamics, allowing realistic FF from a large variety of steering systems. The system's performance was investigated by frequency and time domain techniques, and was found to be reliable and accurate.

The system was connected to a dynamical model of a steering system developed to achieve smooth FF with an accuracy of 0.02 Nm.

Chapter 2, extends this work by involving a more sophisticated steering system model, parameterized using real vehicular data. A video with the FF device in operation is available online [162].

VIII. Appendix

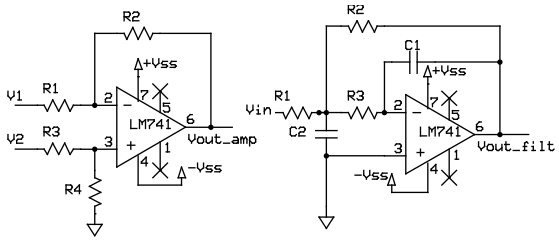

Fig. 2.17. Difference amplifier (left) and 2nd order low-pass filter (right).

The transfer functions for the difference amplifier and for the filter (Fig. 2.17) are respectively (A.1) and (A.2):

Difference amplifier

$$Vout\_amp(s) = \left(\frac{R1+R2}{R3+R4}\right)\frac{R4}{R1}V2(s) - \frac{R2}{R1}V1(s) \qquad (A.1)$$

$$\xrightarrow{\begin{matrix}R1=R3\\R2=R4\end{matrix}} Vout\_amp(s) = \frac{R2}{R1}\left(V2(s) - V1(s)\right)$$

Filter

$$Vout\_filt(s) = -\frac{R2/R1}{s^2 R2R3C1C2 + s\left(R3C1 + R2C1 + \left(R3R2C1/R1\right)\right) + 1}Vin(s) \qquad (A.2)$$

IX. Acknowledgment

The author is grateful to Dr. Frans van der Helm, Mr Cas Droogendijk and Mr Mathieu Gerard. The project was supported by the Biomechanical Eng. and the Intelligent Automotive Systems research groups, 3mE, TUDelft, and the Automotive Development Center of SKF.

Chapter 3. Driving Simulator Parameterization Using Double-Lane Change Steering Metrics as Recorded on Five Modern Cars

“And suddenly I realised that I was no longer driving the car consciously. I was driving it by a kind of instinct, only I was in a different dimension.”
Ayrton Senna, 1960-1994 A.D.

Driving Simulator Parameterization Using Double-Lane Change Steering Metrics as Recorded on Five Modern Cars

Abstract—Steering sensitivity and steering torque gradient are two important metrics describing on-centre vehicle dynamics response and steering feedback. The objective of this work is to acquire the steering metrics of real cars during double-lane change tests and indicate the key parameters of the vehicle that determine these steering metrics. Harnessing the reported findings, driving simulator users can swiftly adjust key parameters to achieve a realistic on-centre response. We instrumented and tested five modern passenger cars, and used a vehicle dynamics model to extract the metrics for multiple vehicular parameterizations (steering ratio, power assist gain, etc.) and test speeds. Sensitivity analysis showed that steering sensitivity was mainly influenced by the components that determine the steering ratio whereas the steering torque gradient was also affected by power assist steering settings. An example study indicated how vehicular parameterization could be adapted to achieve realistic on-centre vehicle steering response and steering feedback in a driving simulator.

I. Introduction

Steering feedback is an important aspect of neuromuscular [31] and psychological [8] perception during driving. Studies have shown that changes in steering feedback have an important effect on driver performance and behaviour [5][144][47]. Not surprisingly, steering feedback plays a crucial role in the automotive design process [113][124]. Although the driver-steering wheel interface has to conform to certain rules (e.g. force-feedback torque levels, steering ratio etc.), the optimal haptic sense is subjective and debatable. Humans usually express perceptions and feelings in words, while engineering science calculates critical metrics through physical variables by performing standardized tests [121].

Driving simulators are widely used for applications such as driver behaviour and perception research, vehicle development, steering systems prototyping, and driver training [152][114][32][3]. The advantages of simulators are that they enable us to present virtual environments and scenarios in a controlled manner, assess driving performance accurately, and evaluate hazardous situations without actual risk. The validity of the acquired research data and the effectiveness of driver training depend on the fidelity of the simulator. Simulator fidelity can be evaluated behaviourally, for example by statistically comparing performance scores in the simulator with driving test performance on the road [93][129], or physically, for example by comparing objective handling test performance data in the simulator with those obtained in the real vehicle [169]. One of the difficulties in assessing the physical fidelity of the steering system in a simulator is the scarcity of comparison data from real cars. Although a number of studies have measured steering torques and angles during handling tests [104][151][135][13], data for low speeds (i.e. < 50 km/h) were unavailable.

The objective of this work is twofold: a) assess the on-centre related steering metrics of real cars during lane-change tests, b) identify the key parameters of the vehicle that determine these steering metrics. To achieve these goals we measured vehicle speed, lateral acceleration, steering wheel torque, and steering wheel angle in five modern passenger cars during double-lane change tests. Using these

data, we quantified the steering sensitivity and steering torque gradient metrics. Then we simulated the same manoeuvres using a single-track vehicle dynamics model. We evaluated the relationships between the model parameters and steering metrics to investigate which physical characteristics of the vehicle affect the metrics. As proof of concept: a) we present an example where we parameterized the single-track vehicle dynamics model so that its on-centre dynamical response was similar to the one of the tested cars, b) we adapted and ported the former parameterization to a high-fidelity driving simulator, so as to evaluate its realism for driver in the loop tests. Using the present results, simulator users will be able to judge whether their simulator provides steering feedback that corresponds to real cars.

II. Real vehicle tests

Table 3.1. Cars used in the experiment.

Car model	Engine	Tires (front/rear pressure bar)	Power Steering	Kerb mass (kg)
BMW 116i E81	1.6L 90 kW	Continental Premium Contact SSR 195/55R16 (2.4/ 2.6)	Electric	1,330
Ford Fiesta MK VI	1.6L Ti-VCT 88KW	Bridgestone Potenza 205/40R17 (2.3/1.9)	Electric	970
Peugeot 3008	1.6L THP 125 kW	Michelin Primacy HP 225/50R17 (2.4/2.4)	Electro-hydraulic	1,374
Dodge Journey JC49	2.4L 129 kW	Kumho Solus KH16 225/55R19 (2.5/2.6)	Hydraulic	1,730
Toyota Avensis T27	1.8L VVTi 90 kW	Bridgestone ER30 205/60R16 (2.5/2.6)	Electric	1,405

Table 3.2. Double lane change test conditions.

Test order	*a* (m)	*b* (m)	Speed (km/h)
1, 12	3	35	3
2, 11	3	35	25
3, 10	3	35	50
4, 9	3	55	3
5, 8	3	55	25
6, 7	3	55	50

A. Test vehicles

Five passenger cars (Table 3.1) were admitted for testing from a car testing association (www.autogetest.nl). All cars were built in 2009 and had a mileage of less than 15,000 km. Tire pressures were set to the recommended factory settings.

B. Double-lane change manoeuvre

Six conditions were tested twice (Table 3.2). The double-lane change tests were performed by driving around three traffic cones, as illustrated in Fig. 3.1. The variables *a* and *b* represent the distances between the cones. The driver was instructed on the corresponding test speed (Table 3.2).

C. Procedure

Measurements were conducted on a uniform piece of dry asphalt in the paddock area of the Circuit Park Zandvoort in the Netherlands. Tests were conducted on the same day by Stefan de Groot, an experienced driver previously active in European car-racing series. The cars were controlled manually

without automated speed or lateral stability control systems. The Electronic Stability Control (ESC), if present, was left in its default settings.

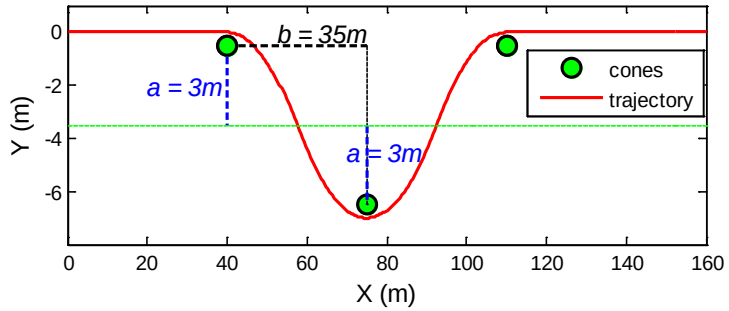

Fig. 3.1.Illustration of the double lane change trajectory. Three traffic cones were spaced with distances *a* and *b* between them (illustrated for *a* = 3 m and *b* = 35 m).

Recorded variables

The following variables were measured:

1) Steering wheel torque (Nm) was measured using a self-developed secondary steering wheel (Fig. 3.2, top left) instrumented with strain gauges measuring the stress of the steel rods. The strain gauges were symmetrically glued at the top and bottom of individual rod and were arranged in a Wheatstone-bridge configuration. When the rods were stressed, the resistive changes of the bonded gauges unbalanced the bridge, resulting in voltage deviation of a few millivolts. The millivolt deviation was boosted *G* times with an operation amplifier (a common design for an amplifier is given in [32]) to become the V_{torque} voltage (Fig. 3.2, bottom left) representing the net force between the rods. The net force between the two rods was converted to torque by multiplying with the moment-arm of 0.19 m.
2) Steering wheel angle (^{o}) was measured optically with an absolute-position black-white codewheel mounted on the back of the secondary steering wheel. The non-contact optical sensor used three OPB745 phototransistors from Optek consisting of an infrared (IR) emitting diode and an NPN photodarlington mounted side by side on converging optical axes. Two phototransistors in conjunction with a codewheel having two concentric rings of overlapping black and white sectors (each sector spaced in 2^o increments) allowed for incremental determination of the position (angle and direction). Using a third phototransistor and a corresponding ring having four black and four white sectors (spaced in 45^o) allows for position correction in case of drift (missed state). The angle was resolved by accounting for all possible black-white transitions of Opt1 and Opt2 from the four possible states (see state transition diagram in the top-right subfigure of Fig. 3.2). Each of these can transfer into another state, giving information about the direction of change. The resulting steering angle resolution was 1^o. Each photodarlington was connected in an open-collector fashion and the voltage, representing reflected light, was measured through a pull-down resistor (c.f. Fig. 3.2, bottom middle). The three optical channels were converted and interpolated offline, to a continuous steering wheel angle signal, using a self-developed code.
3) Lateral acceleration (g) was measured using a ± 1.5 g ADXL320 accelerometer from Analog Devices on a practical breakout board positioned close to the estimated centre-of-gravity (CG). The accelerometer contains provisions for low-pass filtering to avoid anti-aliasing (50 Hz cut-off frequency). The output of the sensor is an analog voltage (± V_{acc}) proportional to the lateral acceleration.
4) Speed (km/h) was measured with an MXL Pro data acquisition system from AiM Sports through a global positioning system (GPS). All the aforementioned analog signals were recorded using the

analog inputs of the same data logger. A schematic diagram of the sensor system is displayed in Fig. 3.2, bottom right.

A detailed description for engineering the necessary sensors and a low cost data acquisition system, for capturing the aforementioned variables, is given in [34].

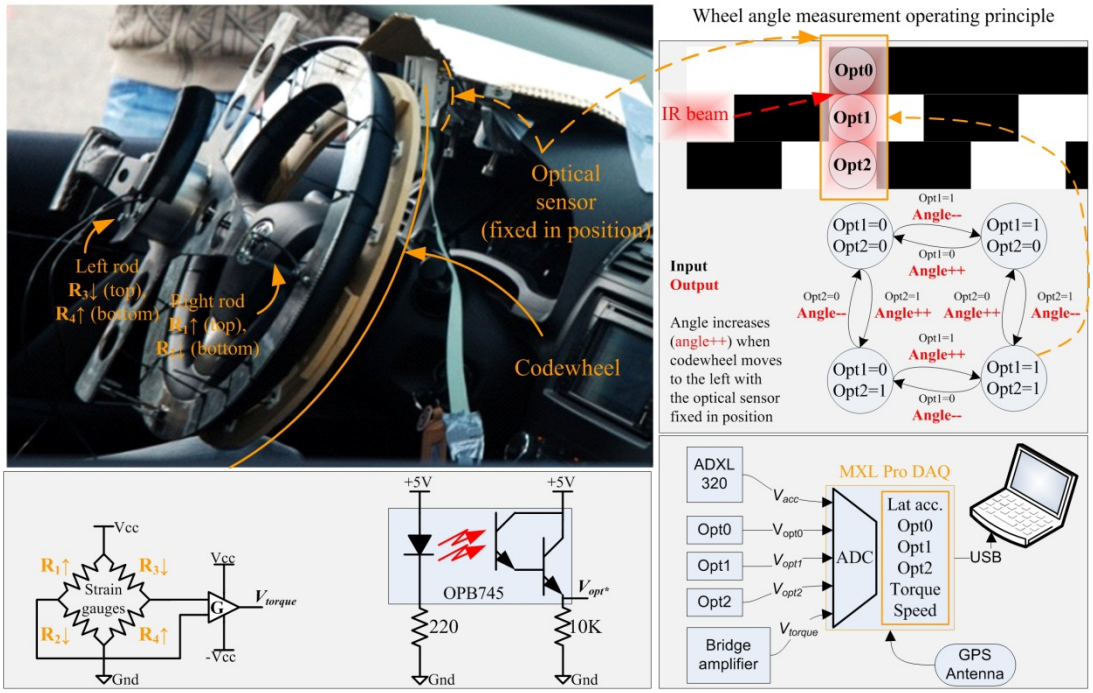

Fig. 3.2. The measurement setup (top left); the secondary steering wheel was attached with steel rods to a ring which in turn was attached to the primary steering wheel. The rods were instrumented with strain gauges in a Wheatstone bridge configuration (bottom left) measuring the shear forces. The optical sensor (bottom left, circuit OPB745) was attached to the dashboard. It reads a codewheel mounted on the back of the steering wheel. The states' transition of the 3 optical encoders (Opt0, Opt1, Opt2) determined the angle value (top right). All the resulting analog signals were recorded using an MXL Pro data logger (bottom right).

D. Steering metrics

Based on the recorded data, the steering sensitivity, the steering torque gradient and the lateral acceleration (lat. acc.) range metrics were calculated. The first two constitute the steering metrics; the third is an additional measure describing the overall severity of the manoeuvre. The choice of these metrics was inspired by steering handling evaluations reported by [104]. The steering sensitivity was defined as the gradient of the lateral acceleration per 100 degrees (^{o}) of steering angle (3.1). The steering torque gradient was defined as the gradient of the steering torque per lateral acceleration (3.2); the gradients of equations (3.1) and (3.2) were obtained by fitting the sampled data with robust regression using the MATLAB® function *robustfit*. The lateral acceleration range was defined as in (3.3).

- Steering sensitivity (3.1), indicating the vehicle's lateral acceleration induced by the steering wheel angle.

$$\text{Steering sensitivity}\left(g/100^o\right)=\frac{\partial\text{lat. acc.}\left(g\right)}{\partial\text{steering angle}\left(^o\right)}\cdot 100 \tag{3.1}$$

- Steering torque gradient (3.2), indicating the required steering torque to accelerate the car laterally.

$$\text{Steering torque gradient}\left(Nm/g\right)=\frac{\partial\text{steering torque}\left(Nm\right)}{\partial\text{lat. acc.}\left(g\right)} \tag{3.2}$$

- Lateral acceleration range (3.3), the difference between maximum and minimum lateral acceleration during the double-lane change manoeuvres.

$$\text{Lat. acc. range}\left(\text{g}\right)=\max\left(\text{lat. acc.}\left(\text{g}\right)\right)-\min\left(\text{lat. acc.}\left(\text{g}\right)\right) \tag{3.3}$$

Fig. 3.3 illustrates the BMW 116i hysteresis loops of the steering angle (top) and the steering torque (bottom) versus the lateral acceleration for a double-lane change manoeuvre with 50 km/h. The steering sensitivity (top) and the steering torque gradient (bottom) are represented with dashed lines. Both fits were determined by linear fit using robust regression.

E. Results

The lateral acceleration and steering torque signals were digitally low-pass filtered at 2 Hz, using a zero-phase second-order Butterworth filter to filter out road and sensor irregularities, while keeping the dynamics response of the vehicle. The steering wheel angle and lateral acceleration correlated strongly, which means that these two variables had a close-to-linear relationship (Fig. 3.3). This was true for all five cars, with a mean correlation for all cars and all speeds > 10 km/h of .98 (median = .99). The correlation between lateral acceleration and steering torque was considerably smaller with a mean correlation for all cars and all speeds > 10 km/h of .85 (Fig. 3.3). The relatively low correlation was caused by hysteresis; that is, for a particular lateral acceleration, different torque levels were obtained depending on the position and velocity of the steering wheel.

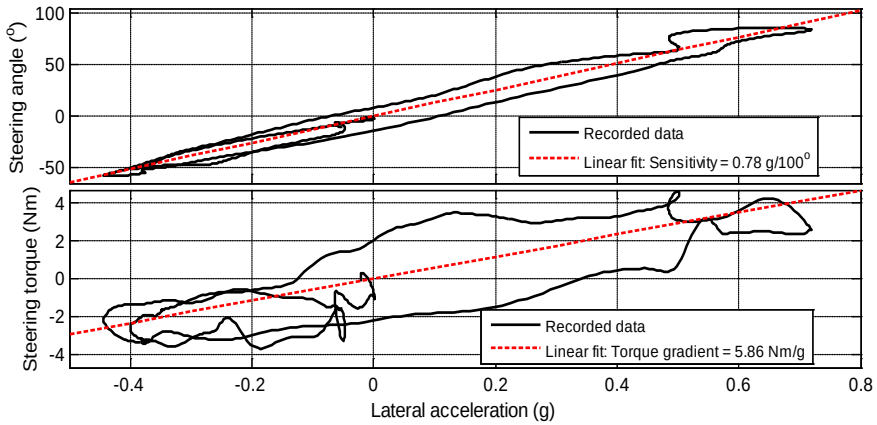

Fig. 3.3. Hysteresis loops (HL) of the steering angle (top) and the steering torque (bottom) versus the lateral acceleration for the BMW 116i; double-lane change test with *b* = 35 m and 50 km/h instructed speed. The steering sensitivity represented by the dashed line (top) was 0.78 g/100° (correlation = 0.99). The steering torque gradient represented by the dashed line (bottom) was 5.86 Nm/g (correlation = 0.84). Both fits were determined by a linear fit using robust regression.

Fig. 3.4 illustrates a) steering sensitivity, b) steering torque gradient and c) lateral acceleration range, all versus mean speed. The low lateral acceleration from tests with instructed speed of 3 km/h obscured the distinction between noise (mechanical vibrations, road bank, uneven road, etc.) and actual acceleration due to vehicular motion. Therefore, these tests were excluded from both the illustration and fits of steering sensitivity and steering torque gradient.

Steering sensitivity (Fig. 3.4; top) was closely related to mean speed. The Dodge, the car with the highest steering ratio, had the lowest steering sensitivity, whereas the Ford had the highest sensitivity and lowest steering ratio (based on online car specifications).

Required acceleration to complete the double-lane change manoeuvre increased quadratically with speed and was relatively independent of the type of car (Fig. 3.4; bottom). Note that manoeuvres were dynamically moderate and did not activate the ESC, which might have influenced the results. The lines in Fig. 3.4 represent quadratic fits per car for steering sensitivity and lateral acceleration range, and linear fits for steering torque gradient.

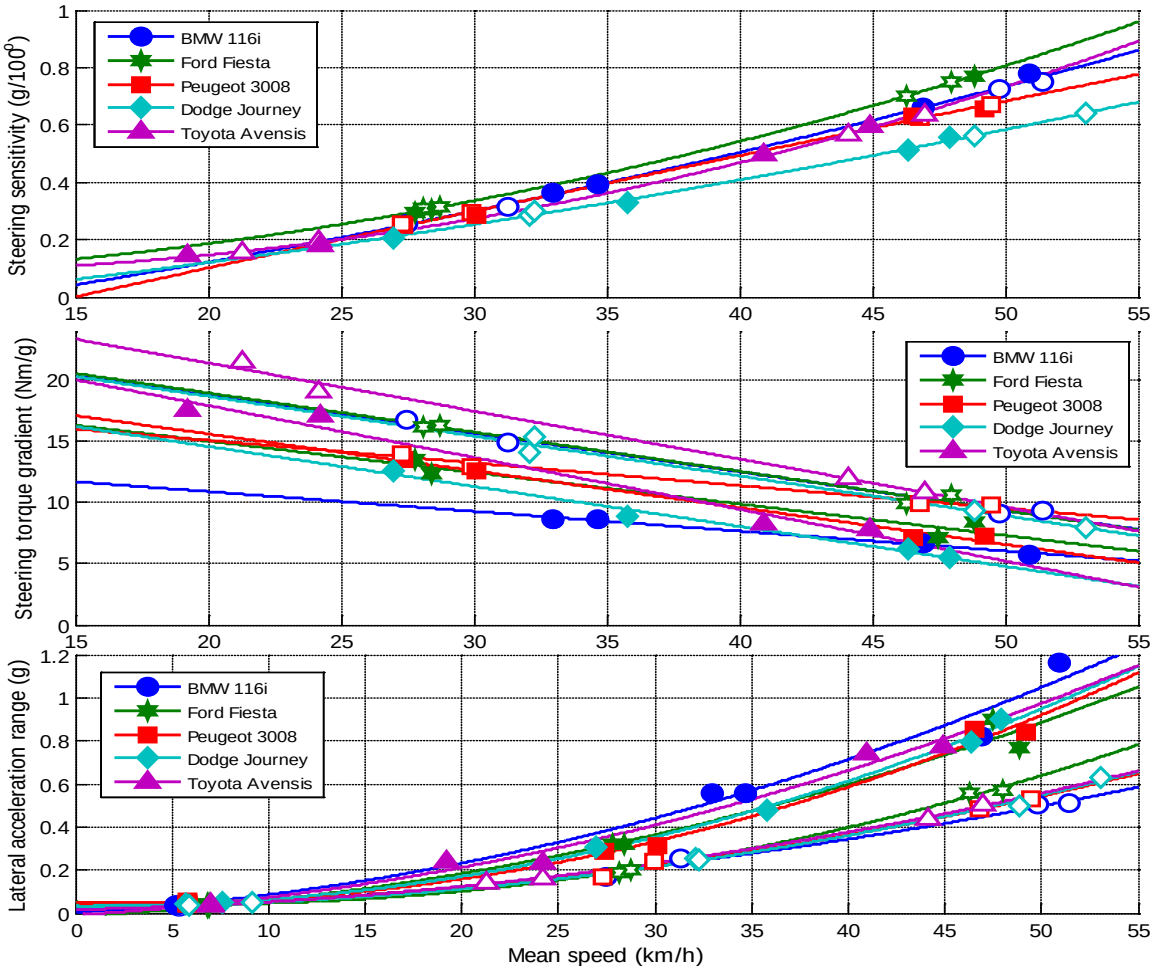

Fig. 3.4. Top: Steering sensitivity versus mean speed. Middle: Steering torque gradient versus mean speed. Bottom: Lateral acceleration range versus mean speed. The filled markers correspond to traffic cone distance b = 35 m, the white-filled markers correspond to b = 55 m. The lines represent quadratic fits per car for steering sensitivity and lateral acceleration range, and linear fit for steering torque gradient.

III. Vehicle dynamics model

A. Longitudinal and lateral dynamics

Here we introduce the simulation models used to compute the steering metrics under the same manoeuvres as in section II.B. The planar dynamics of the vehicle were simulated using a single-track vehicle dynamics model (Fig. 3.5). Friction coefficients for the front and rear axles μ_f and μ_r (for lumped left and right tire) were calculated using Pacejka's Magic Formula [59] as in (3.4). The α_f and α_r are the front and rear axle slip angles (the angle between the longitudinal axis of the wheel and its velocity vector; c.f. Fig. 3.5). Assuming a linear relationship between tire friction force and tire normal force (3.5), the front F_{fy} and rear F_{ry} axle lateral tire forces can be obtained as in (3.6). The vehicle dynamics model parameters and variables are summarized in Table 3.3.

$$\mu_{f,r} = MF(a_{f,r}) = D_{pac} \cdot \sin(C_{pac} \cdot \operatorname{atan}(B_{pac} \cdot a_{f,r})) \tag{3.4}$$

$$F_{fz} = \frac{M \cdot g \cdot l_r}{l_f + l_r} \qquad F_{rz} = \frac{M \cdot g \cdot l_f}{l_f + l_r} \tag{3.5}$$

$$F_{fy}(\alpha_f) = \mu_f \cdot F_{fz},\ F_{ry}(\alpha_r) = \mu_r \cdot F_{rz} \tag{3.6}$$

$$C_f = F_{fy}(\alpha_f)/\alpha_f,\ C_r = F_{ry}(\alpha_r)/\alpha_r \tag{3.7}$$

$$F_{fy} = \alpha_f \cdot C_f\,|_{\alpha_f=0.1},\ F_{ry} = \alpha_r \cdot C_r\,|_{\alpha_r=0.1} \tag{3.8}$$

$$\alpha_f = \delta - \tan^{-1}\left(\frac{\dot{y} + l_f\dot{\psi}}{\dot{x}}\right),\ \alpha_r = -\tan^{-1}\left(\frac{\dot{y} - l_r\dot{\psi}}{\dot{x}}\right) \tag{3.9}$$

The tires' cornering stiffness C_f and C_r can be calculated as a function of the slip angle by the slope of the line connecting the origin and the tires' lateral force for a given slip angle (3.7). In the current implementation, cornering stiffness was assumed to be constant with $\alpha_{f,r}$ = 0.1 rad and lateral tire forces were estimated as the product of the tire slip angle, and lumped left and right tire cornering stiffness as in (3.8). The slip angles were calculated as in (3.9) [142] (pp. 15-49).

$$acc_x = \ddot{x} - \dot{\psi} \cdot \dot{y} \tag{3.10}$$

$$acc_y = \ddot{y} + \dot{\psi} \cdot \dot{x} \tag{3.11}$$

$$m \cdot acc_y = F_{fy} \cdot \cos(\delta) + F_{ry} \tag{3.12}$$

$$I \cdot \ddot{\psi} = l_f \cdot F_{fy} - l_r \cdot F_{ry} \tag{3.13}$$

$$\frac{d}{dt}\begin{Bmatrix}\dot{y}\\ \dot{\psi}\end{Bmatrix} = \begin{bmatrix} -\dfrac{C_f + C_r}{m\dot{x}} & \dfrac{C_r l_r - C_f l_f}{m\dot{x}} - \dot{x} \\ \dfrac{C_r l_r - C_f l_f}{I_z \dot{x}} & -\dfrac{C_f l_f^2 + C_r l_r^2}{I_z \dot{x}} \end{bmatrix} \cdot \begin{bmatrix}\dot{y}\\ \dot{\psi}\end{bmatrix} + \begin{bmatrix} C_f / m \\ C_f l_f / I_z \end{bmatrix} \delta \tag{3.14}$$

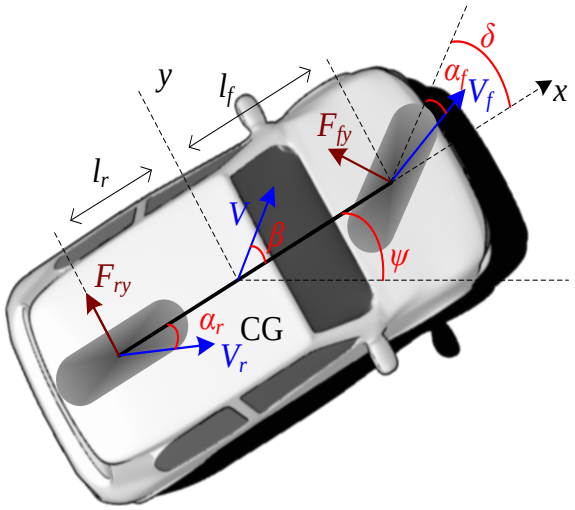

Fig. 3.5. The single track vehicle dynamics model.

Longitudinal acc_x and lateral acc_y acceleration for the vehicle dynamics model are given by (3.10) and (3.11), which contain the induced acceleration component generated from the yaw motion of the vehicle [142]. Applying Newton's second law along the lateral axis *y* and the vertical axis *z* around the CG results in (3.12) and (3.13). Substituting from equations (3.8) and (3.9) to (3.12) and (3.13) and assuming small angles ($tan^{-1}(\alpha) \approx \alpha$, $cos(\delta) \approx 1$), the state space model form of (3.14) can be obtained

[142]. The vehicle's longitudinal velocity $\dot{x}$ (*dx/dt*) in (3.14) was considered an input to the system. The vehicle's states were translated to the global *X*, *Y* and yaw angle ψ coordinates with (3.15):

$$\begin{aligned} X(t+T) &= \int_t^{t+T} \left(\dot{x}\cos\psi - \dot{y}\sin\psi\right)d\tau + X(t) \\ Y(t+T) &= \int_t^{t+T} \left(\dot{x}\sin\psi + \dot{y}\cos\psi\right)d\tau + Y(t) \\ \psi(t+T) &= \int_t^{t+T} \dot{\psi}\,d\tau \end{aligned} \tag{3.15}$$

B. Steering system model

Fig. 3.6 illustrates the steering system model that was coupled to the vehicle dynamics model. It is a quasi-realistic representation of an electronic power-steering system (EPS) found in modern vehicles, consisting of a steering column, a torque sensing element, an assist motor and a rack-pinion assembly. The system equations are described in (3.16)–(3.23). The parameters and variables are summarized in Table 3.4.

Table 3.3.Vehicle dynamics model parameters and variables. The displayed values were either fitted (◊) to the Peugeot 3008 or assigned (□) using literature reports.

Symbol	Description	Value(s)	Fitted ◊ Assigned □	Unit
	Parameters			
m	Mass of the vehicle	1470	□	kg
I_z	Moment of inertia around the Z axis at the CG	1900	◊	kg·m^2
l_f, l_r	Distance of front, rear axle from the CG	1.04, 1.56	◊ (using known wheelbase)	m
D_{pac}, C_{pac}, B_{pac}	Pacejka's Magic Formula coefficients	0.96, 1.7, 6.9	◊	-
C_f, C_r	Cornering stiffness: front, rear axle	71, 47 (at 0.1 rad slip angle)		kN/rad
g	Gravitational acceleration	9.81		m/s^2
	Variables			
α_f, α_r	Slip angles at front, rear axle	-		rad
$\dot{x}$, $\dot{y}$	Longitudinal, lateral velocity on x, y axis	-		m/s
$\ddot{x}$, $\ddot{y}$	Acceleration on x, y axis	-		m/s^2
acc_x, acc_y	Longitudinal, lateral acceleration	-		m/s^2
β	Slip angle at the CG	-		rad
δ	Steering angle at the wheels	-		rad
X, Y	Global vehicle coordinates	-		m
ψ	Yaw angle at the CG	-		rad
$\dot{\psi}$	Angular rate around the Z axis at the CG	-		rad/s
$\ddot{\psi}$	Angular acceleration around Z axis at the CG	-		rad/s^2
V, V_f, V_r	Velocity vector of vehicle at CG, front axle, rear axle	-		m/s
F_{fy}, F_{ry}	Lateral forces acting on the tires	-		N
F_{fz}, F_{rz}	Normal force at front, rear axle	-		N

The forces acting on the steering system are the driver's torque T_d and rack forces F_r originating from the tie-rod, which connects the steering rack to the upright. The T_{map} constitutes the power-assist map as found in a modern power-steered vehicle [165]. This map is in reality a speed-dependent lookup table [113][165]. However, to simplify the analysis, the power-assist map is only a function of the torsion T_s (3.18). The assist torque is the product of the T_{map} (for the given torsion) times the power-assist gain T_{gain}. The T_{map} design was based on a spline-based curve-map of the torsion at the torsion

bar as in Fig. 3.7. Note that the T_{gain} is also used for the T_{map} design. The values T_{gain}, T_{min}, T_{max} displayed in Fig. 3.7 are the nominal values from Table 3.5.

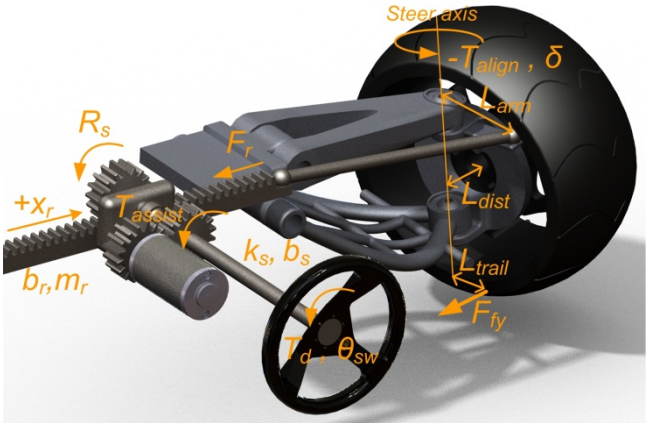

Fig. 3.6. Steering system model.

$$J_s\ddot{\theta}_{sw} = T_d - T_s \tag{3.16}$$

$$T_s = k_s(\theta_{sw} - \frac{x_r}{R_s}) + b_s(\dot{\theta}_{sw} - \frac{\dot{x}_r}{R_s}) \tag{3.17}$$

$$T_{assist} = T_{map}(T_s)\cdot T_{gain} \quad \text{torsion} = T_s \tag{3.18}$$

$$m_r\ddot{x} = \frac{(T_s + T_{assist})}{R_s} - b_r\dot{x}_r - F_r \tag{3.19}$$

$$\delta = \frac{x_r}{L_{arm}} \tag{3.20}$$

$$F_r = \frac{T_{align}}{L_{arm}} \tag{3.21}$$

$$T_{align} = F_{fy}\cdot L_{trail} + T_{lift} \quad (L_{trail} = L_{pt} + L_{mt}) \tag{3.22}$$

$$T_{lift} = L_{lift}\cdot F_{fz}\cdot\sin(\delta) \quad (L_{lift} = L_{dist}\cdot\cos(\theta_c)\cdot\sin(\theta_{king})) \tag{3.23}$$

The resulting rack displacement x_r derives from the application of the T_d and the external forces on the rack F_r. The x_r through the lever arm (with length L_{arm}) connecting the tie-rod to the upright results to the wheels' angle δ (3.20). The aligning moment T_{align} (3.22) at the upright pivot (kingpin steer axis) is composed from a) the moment caused by the lateral wheel forces F_{fy} times the length of steer trail L_{trail} (the sum (3.22) of the mechanical trail L_{mt}, due to the wheel caster angle θ_c and tire pneumatic trail L_{pt}) and b) the aligning moment T_{lift} (3.23) caused by the lift or lowering of the wheel-steer axis when steering. This effect is described in detail in [147]. Three components contribute to the T_{lift}: a) the offset distance L_{dist} of the wheel centre to the steer axis, b) the inclination angle θ_{king} of the kingpin and c) the wheel caster angle θ_c. The lift effect described in (3.23) derives from [147] by nullifying the torque component caused by left and right-wheel normal load difference.

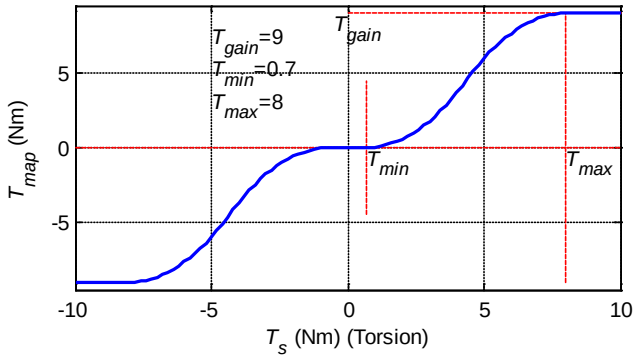

Fig. 3.7. Power-assist map.

C. Vehicle dynamics verification with empirical data

A two degrees-of-freedom (DOF) linear vehicle dynamics model can entail realistic behaviour at moderate manoeuvres [52]. To substantiate the realism of the vehicle dynamics model, recorded data were fitted to the model. At Fig. 3.8 (top), recorded data from the Peugeot 3008 (from a double-lane change test, test speed of 50 km/h and cone distance of 35 m) were superimposed on the simulated data using properly fitted parameters for the vehicle dynamics model and steering system. Mass m and wheelbase $l_f + l_r$ (Table 3.3) were obtained from the vehicle's available specifications. The rest of the parameters were fitted, by simulating a range of parameters values within physical limits and using generic values from the literature as initial guesses [89][134]. The value-fitting process was performed in two steps.

Step A in the fitting process was minimizing the root-mean-square (RMS) error between simulated acc_y 'Open loop' (open loop control) and 'Recorded' acc_y (Fig. 3.8) (acc_y; lateral acceleration). This step is used to estimate unknown parameters related to the lateral response of the vehicle, such as the I_z, Pacejka coefficients and position of the vehicle's CG (l_f, l_r). Input for the simulation was the measured steering wheel angle θ_{sw} 'Recorded' from real test drives and longitudinal velocity dx/dt 'Recorded' as in Fig. 3.8. The θ_{sw} 'Recorded' signal was the input for (3.17). Using a high stiffness value k_s for the torsion bar (multiple kN/rad) resulted in the real θ_{sw} being directly translated as rack displacement x_r and correspondingly to the wheel angle δ. By doing so, the steering system dynamics did not influence the vehicle's lateral response.

Once the previous parameters were fitted, step B involved minimizing the RMS error between the simulated driver's torque T_d 'Open loop' over the 'Recorded' (Fig. 3.8). This estimates parameters related to the steering system (Table 3.4). Inputs for the simulation were the same as in step A. Steering column inertia J_s was set to 0 so as to avoid differentiating the 'Recorded' θ_{sw} twice (which would have inevitably created noise) to get the driver's torque T_d (3.16). The former suggests that T_d becomes equal to the torsion T_s (3.16), introducing the phase lag in the torque seen in Fig. 3.8. We did not use the 'Recorded' T_d as input to the system, because it would only result in a θ_{sw} identical to the 'Recorded' one (the variable we were trying to control for the fitting process), in case that we had a) a perfect dynamical model of the steering system and b) knowledge of the real vehicle's rack forces F_r (3.21). Both not feasible in this study. The complexity of simulating a virtual inertia, justifying our choice to ignore this high frequency mass component, has been earlier discussed in [32]. The RMS errors for acc_y and T_d were 0.052 g and 0.973 Nm, respectively.

The parameter values from this two-step fitting process are given in Table 3.3 and Table 3.4. Note that this section clearly serves only as a paradigm. The combination of vehicle dynamics and steering system model can entail a realistic response resembling a real vehicle. The unique identification of the parameters would necessitate more rigorous tests, involving system identifications techniques

[134][32]. Still, the fitted parameters and simulated vehicle response are within the same range of similar reports from the literature [52][134].

Table 3.4. Steering system parameters and variables. The displayed values were either fitted (◊ see section C) to the Peugeot 3008 or assigned (□) using literature reports.

Symbol	Description	Value	Fitted ◊ Assigned □	Unit
		Parameters		
T_{min}	Minimum torsion where power assist is still 0	2	□	Nm
T_{gain}	Power assist gain	9	◊ (considered as a unitless gain in (3.18))	Nm
T_{max}	Torsion where maximum power assist occurs	8	□	Nm
T_{map}	Power assist map (c.f. Fig. 3.7)	look-up table function of T_s		Nm
R_s	Pinion gear radius	0.01	◊	m
k_s	Torsion bar stiffness	170	□ [134]	Nm/rad
J_s	Steering wheel moment of Inertia	0	□ (thus $T_d = T_s$)	kg·m^2
b_s	Steering column damping	0.07	□ [134]	Nm/rad/s
b_r	Rack damping	0.2	□ [134]	N/m/s
m_r	Rack + suspension + wheels mass	50	□	kg
L_{trail}	Tire steer trail	0.05	□	m
L_{lift}	Torque lift lever length	0.05	◊	m
L_{arm}	Length of the lever connecting the tie-rod to the upright	0.18	□	m
L_{dist}	Offset distance of the wheel centre to the steer axis (m)	Their combined value constitutes the L_{lift} (3.23)		m
θ_c	Caster angle			Rad
θ_{king}	Kingpin inclination angle			Rad
L_{mt}	Mechanical trail	Their combined value constitutes the L_{trail} (3.22)		M
L_{pt}	Pneumatic trail			M
		Variables		
T_d	Driver's torque (Nm)	-		Nm
x_r	Rack displacement	-		M
θ_{sw}	Steering wheel angle	-		Rad
T_{assist}	Assist torque	-		Nm
T_{lift}	Aligning moment because of lifting, lowering the wheel	-		Nm
T_{alliqn}	Aligning moment at the wheel steer axis	-		Nm
F_r	Rack force from tie rod	-		N

IV. Steering metrics during simulated driving

The same steering metrics as in real tests were calculated for the double-lane change manoeuvres with b = 35 m (Table 3.2) to study their influence on the metrics. To control the vehicle during the manoeuvre we used a multi-point preview driver model [31]. This model estimates its future path through an internal vehicle dynamics model (as in [23]) and by using future lateral errors and current yaw error (as in [145]) calculates the steering angle to follow the desired trajectory (c.f. Fig. 3.1). The preview driver model controller [31] and the detailed description for estimating the future and current yaw error are available online [34].

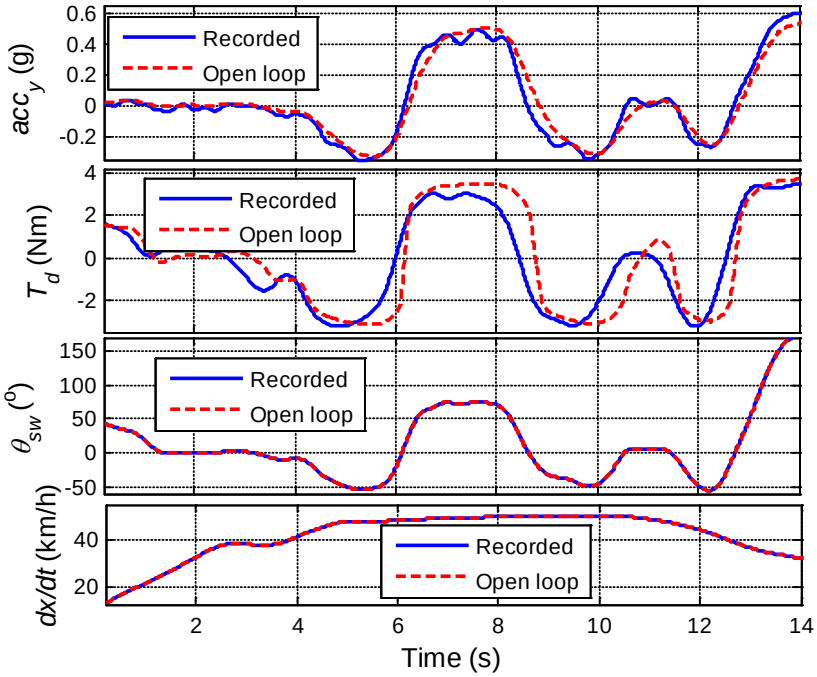

Fig. 3.8. Recorded data superimposed with simulated data. The recorded data correspond to a double-lane change test with the Peugeot 3008. The acc_y 'Recorded' and the T_{driver} 'Recorded' signals are a low-pass filtered (1 Hz) version of the recorded signals. The 'Open loop' signal is the response of the vehicle dynamics model using as input the 'Recorded' θ_{sw} and *dx/dt* signals.

Table 3.5. Parameters values used for generating the steering metrics in simulation.

Parameter	Nominal value	Modifications from nominal value					
		65%	**80%**	**90%**	**110%**	**120%**	**135%**
m	**1300**	845	1040	1170	1430	1560	1755
I_z	**1900**	1235	1520	1710	2090	2280	2565
T_{min}	**0.7000**	0.4550	0.5600	0.6300	0.7700	0.8400	0.9450
T_{max}	**8.0000**	5.2000	6.4000	7.2000	8.8000	9.6000	10.8000
T_{gain}	**9.0000**	5.8500	7.2000	8.1000	9.9000	10.8000	12.1500
L_{arm}	**0.1667**	0.1084	0.1334	0.1500	0.1834	0.2000	0.2250
L_{lift}	**0.0500**	0.0325	0.0400	0.0450	0.0550	0.0600	0.0675
L_{trail}	**0.0500**	0.0325	0.0400	0.0450	0.0550	0.0600	0.0675
R_s	**0.0110**	0.0072	0.0088	0.0099	0.0121	0.0132	0.0149
		Modifications from nominal value					
		85%	**90%**	**95%**	**105%**	**110%**	**115%**
B_{pac}	**6.900**	5.865	6.210	6.555	7.245	7.590	7.935
C_{pac}	**1.700**	1.445	1.530	1.615	1.785	1.870	1.955
D_{pac}	**0.900**	0.765	0.810	0.855	0.945	0.990	1.035

For individual test speeds of 10, 20, 30, 40 and 50 km/h, only one parameter from Table 3.5 was altered while the rest were kept at their nominal values. The vehicle's parameters excluded in Table 3.5 have their values depicted in Table 3.3 and Table 3.4. The tested parameters in Table 3.5 were expected to have greater influence on the metrics compared to the rest. The first nine parameters in Table 3.5 were tested with modified values of ± 35%, ± 20% and ± 10% from their nominal value. The last three (B_{pac}, C_{pac}, D_{pac}), related to tire dynamics, were tested with modified values of ± 15%, ± 10% and ±5%. This discrimination in the modification percentages was done to ensure lateral stability and comparable

trajectories during the double-lane change simulation. Based on the simulations we calculated the steering sensitivity (g/100^o) and steering torque gradient (Nm/g) metrics. We also calculated the lateral acceleration range (g) to investigate whether a manoeuvre-dictated measure can be effectively influenced by certain vehicular parameters. Parameter variations can only affect this measure, if they indirectly affect the trajectory that can be achieved by the preview driver model. The preview driver model is in practice a fixed gain PID controller that tries to regulate the future path error by steering the vehicle. The driver model had good tracking performance, yielding almost identical trajectories (less than 0.1 m lateral difference) for all test cases (Table 3.5); the maximum absolute lateral error from the desired trajectory was 0.6 m.

A. Parameter influence; selected examples

As an illustrative example, the hysteresis loops for steering sensitivity and steering torque gradient are displayed in Fig. 3.9. The m, T_{gain} and L_{arm} were tested for 100%, 65% and 135% of the nominal value of Table 3.5. For each parameterization (subplot), only the noted parameter was altered; the remainder of the parameters were kept at their nominal values.

An example of the impact of the pinion gear radius value R_s on steering sensitivity and steering torque gradient versus test speed is illustrated in Fig. 3.10. A robust regression estimate was made on the data per manoeuvre parameterization. The illustrated fits per parameterization are quadratic.

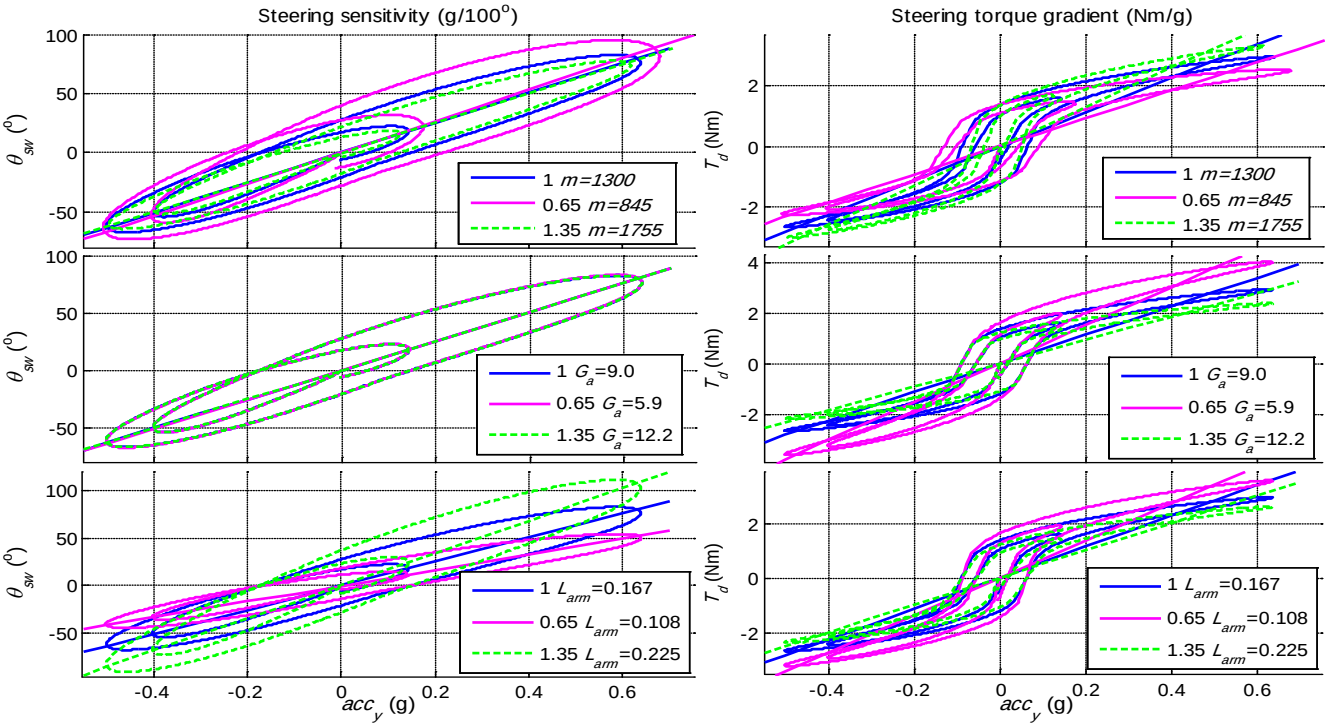

Fig. 3.9. Hysteresis loops (HL) of steering sensitivity plots (left panel) and steering torque gradient (right panel) for 100%, 65% and 135% values of Table 3.5 of the m, G_a and L_{arm}. Double-lane change with cone distance b = 35 m and test speed of 50 km/h. For each parameterization (subplot), only the noted parameter was altered; the rest were kept at their nominal values (Table 3.5).

B. Sensitivity analysis for vehicular parameters

Sensitivity analysis was performed for steering metrics versus test speed for all the parameterizations of Table 3.5. Sensitivity was calculated with (3.24). The metrics were again calculated as in (3.1) and (3.2). For simplicity, Table 3.6 contains the relative changes of steering

sensitivity and steering torque gradient per parameter only for the tests speeds of 10 km/h and 50 km/h and only for relative changes on the parameters values of ± 35% and ± 10%. The entire group of results for sensitivity analysis on all parameterizations and tests speeds is cited in Table 3.8.

The lateral acceleration range has been omitted from Table 3.6 since it remained relatively unaffected by parameter changes since the trajectory to be realized was nearly the same in all simulated conditions. Still, vehicle parameters related to cornering forces, such as inertia or tire properties, are expected to affect the achievable trajectory. Please refer to Table 3.8 for the lateral acceleration range results.

$$Metric_{\text{sensitivity}} = \frac{Metric_{\text{modified}} - Metric_{\text{nominal}}}{Metric_{\text{nominal}}} \tag{3.24}$$

C. Sensitivity analysis; parameter influence

Table 3.6 summarizes the results for minimum (10 km/h) and maximum test speed (50 km/h). The results are consistent and influenced by both test speed and proportional changes of the parameters.

i)Steering sensitivity

Steering sensitivity was mainly affected by parameters determining the steering ratio of the vehicle; the pinion gear radius R_s and length of the lever L_{arm} connecting the tie-rod to the upright (Table 3.4). Steering ratio is defined as L_{arm}/R_s (L_{arm}/R_s = 15.1, for the nominal values of Table 3.5). The relationship between steering sensitivity and R_s is approximately 1:1 for both 10 and 50 km/h (c.f. Fig. 3.10). The length of L_{arm} has the inverse effect of the R_s. For small changes from its nominal value ± 10%, the relation is almost linear; for greater changes the relationship is neither linear nor symmetric. Test speed has no considerable impact on the sensitivity of L_{arm} and R_s.

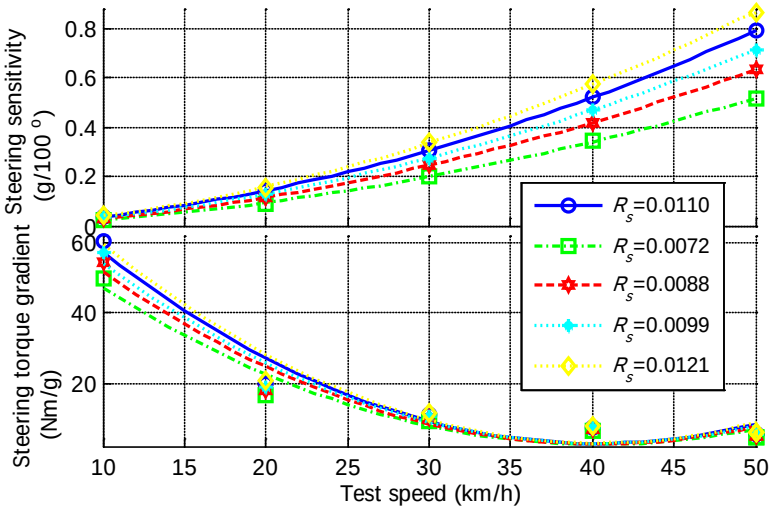

Fig. 3.10. Effect of R_s in steering sensitivity (top) and steering torque gradient versus test speed (bottom); double-lane change manoeuvre with cone distance b = 35 m. Only the R_s parameter was altered while the rest were kept at their nominal values (Table 3.5).

Mass m and inertia around the z-axis I_z, have a moderate impact on steering sensitivity; -5% changes for alterations up to -35%. However, they do affect the shape of the corresponding hysteresis loop (HL). The top-left subplot of Fig. 3.9 shows steering sensitivity HL for 100%, 65% and 135% of the nominal value of the mass m. The hysteresis of the HL increases with decreasing mass. A decrease in mass results in decrease of the lateral tire force F_{fy} that a tire develops during cornering at a certain slip angle. Retaining the nominal value for the inertia I_z forces the tires to develop higher slip angle values

to achieve the required tire forces to negotiate the manoeuvre. Therefore, higher steering inputs should be performed, increasing hysteresis (Fig. 3.9). In contrast, increase in inertia increases hysteresis and vice-versa. Hysteresis is also affected by test speed; the higher the test speed, the greater the hysteresis.

Modification of tire parameters affects corresponding cornering stiffness (3.7). The D_{pac} coefficient has the higher impact on the cornering stiffness, since it represents the tire-road friction coefficient. Cornering stiffness mainly affects hysteresis and not the shape of HL. Still, a high speed manoeuvre (50 km/h) with a low value for the D_{pac} = 0.76 (85% the nominal value) does influence steering sensitivity, since the vehicle has to develop higher slip angles to generate the required tire force compared to the nominal parameterization.

The parameters related to feedback forces have a negligible influence on the steering sensitivity. This influence originates from the dynamics of the steering system that do make it faster or slower according to the settings. The system can be regarded as a fourth-order filter system, from the steering torque input T_d to the wheel angle δ. For example a high power-assist gain T_{gain} is expected to increase the bandwidth from the T_d to δ. If the torsion bar stiffness was assumed to be infinitely stiff, then the steering system parameters related only to feedback forces (T_{gain}, T_{min}, T_{max}, L_{trail}) would have no influence on the steering sensitivity.

Table 3.6. Relative changes of sensitivity analysis for a selection of parameterizations.

	Parameter	Steering sensitivity (%) Nominal: 0.037 g/100°				Steering torque gradient (%) Nominal: 60.5 Nm/g			
	Relative change (%)	**-35**	**-10**	**10**	**35**	**-35**	**-10**	**10**	**35**
10 km/h	m	0	0	0	0	-17	-4	4	12
	I_z	0	0	0	0	0	0	0	0
	B_{pac}		0	0			0	0	
	C_{pac}		0	0			0	0	
	D_{pac}		0	0			0	0	
	T_{min}	0	0	0	0	-14	-5	4	13
	T_{gain}	0	0	0	-1	15	4	-4	-10
	T_{max}	-1	0	0	0	-14	-5	3	12
	L_{arm}	53	11	-9	-26	18	4	-4	-12
	L_{lift}	0	0	0	-1	-12	-3	3	8
	L_{trail}	0	0	0	0	-4	-1	1	3
	R_s	-35	-10	10	35	-18	-6	4	13

	Parameter	Steering sensitivity (%) Nominal: 1.524 g/100°				Steering torque gradient (%) Nominal: 3.68 Nm/g			
	Relative change (%)	**-35**	**-10**	**10**	**35**	**-35**	**-10**	**10**	**35**
50 km/h	m	-5	-1	1	2	-18	-5	5	15
	I_z	3	1	-1	-3	2	0	0	-1
	B_{pac}		-1	1			-1	0	
	C_{pac}		-1	1			-1	1	
	D_{pac}		-1	1			-1	1	
	T_{min}	0	0	0	0	-6	-2	2	6
	T_{gain}	0	0	0	0	34	7	-6	-18
	T_{max}	0	0	0	0	-26	-7	7	25
	L_{arm}	52	11	-9	-26	20	5	-4	-12
	L_{lift}	0	0	0	0	-2	-1	1	2
	L_{trail}	0	0	0	0	-14	-4	4	12
	R_s	-35	-10	10	34	-16	-4	4	14

ii)Steering torque gradient

The steering torque gradient is influenced by the test speed (c.f. Fig. 3.4) and by the majority of the tested parameters of Table 3.5. The R_s and L_{arm} have again the inverse effect: An increase of the L_{arm} decreases the rack feedback force F_r from the tires. The inverse happens with an increase of the R_s. The sensitivities of the L_{arm} and R_s are little affected by the test speed.

The vehicle's inertial properties, the mass m and the inertia around the z-axis I_z have a large influence on the steering torque gradient. Less mass m means less required cornering force to laterally accelerate the vehicle to negotiate the given manoeuvre. The effect of the mass on the steering torque gradient is illustrated in Fig. 3.9 (top right). Lower mass also means less lifting torque T_{lift} (3.23). The T_{lift} is a function of the normal force F_{fz} at the front axle. For the 10 km/h test speed the developed lateral force is low; therefore the T_{lift} constitutes a great portion of the feedback forces. The I_z at 10 km/h does not influence the torque gradient, since the required yaw acceleration is small. At higher speeds though (e.g., 50 km/h) an increase in I_z decreases the torque gradient. This effect is not straightforward in terms of dynamics, since for a lower inertia, smaller tire forces are needed to accelerate the I_z. Still, the final fit is dictated by the whole shape of the HL giving the results of Table 3.6.

The D_{pac} coefficient has the highest effect on the cornering stiffness. The cornering stiffness is not expected to affect the magnitude of the forces generated on the steering wheel for a specific lateral acceleration, since independent of the tire's cornering stiffness, the same tire forces should be developed for the vehicle to negotiate the same manoeuvre. In a high speed manoeuvre (50 km/h) the cornering stiffness affects the hysteresis of the HL. For a smaller cornering stiffness, the hysteresis is expected to grow; higher slip angles are needed for the same manoeuvre, requiring more time to be generated. Therefore all three Pacejka coefficients alterations influence the steering torque gradient, mainly in the hysteresis.

As expected, the power-assist parameters T_{gain}, T_{max}, T_{min} have a great influence on the steering torque gradient; the order of this influence is also related to the test speed. For the test speed of 10 km/h all parameters T_{min}, T_{max} and T_{gain} have approximately the same absolute sensitivity (Table 3.6). The effect of decreasing the T_{min} and T_{max} is similar; if reduced the assist torque becomes greater (Fig. 3.7) for a given T_d. The reverse happens for the power-assist gain T_{gain}; smaller T_{gain} means less power-assist torque, thus higher driver torque. Interestingly, the T_{min} sensitivity is rather high at low speeds (e.g., 10 km/h) where the magnitude of the required steering torque is low (close to the origin of the T_{map}, c.f. Fig. 3.7; the maximum torque for the nominal case of Table 3.5 with 10 km/h is 1.35 Nm). With increasing test speed, the sensitivity of T_{min} drops (the maximum torque for the nominal case of Table 3.5 with 50 km/h is 2.96 Nm). The reverse effect happens with T_{max} and T_{gain} (the sensitivity increases with increasing speed). The tire steer trail L_{trail} has the expected effect on the steering torque; an increase results to higher steering torques and correspondingly to a greater steering torque gradient. The effect is straightforward since the L_{trail} is in practice a lever (3.22) converting the tires' aligning moment to the rack feedback forces F_r without though affecting the kinematics of the tire; the greater the lever length, the higher the feedback forces.

V. Driving simulator parameterization using the steering metrics

A. Single track vehicle model

Using the sensitivity analysis results we tried to iteratively approximate the steering metrics of the Toyota Avensis. In Fig. 3.11 the steering sensitivity and steering torque gradient reconstruction process is illustrated. The 'Recorded' metrics are compared with the simulated 'Sim nominal', which uses the nominal parameters of Table 3.5 and the rest from Table 3.3 and Table 3.4. Initiating from 'Sim

nominal' case and by altering specific parameters (using always the 'Sim nominal' values as reference), we obtain the 'Sim A' and 'Sim B' fits. The test speed used for the simulation was the 'mean speed' from the recorded tests.

The 'Sim nominal' steering sensitivity of Fig. 3.11 has higher values compared to the 'Recorded' case. Consulting Table 3.6, the R_s and L_{arm} can influence the sensitivity. We therefore alter the R_s by -10% resulting to an approximately -10% change in the steering sensitivity and -5% in the steering torque gradient values. The 'Sim nominal' steering torque gradient is also higher from the corresponding 'Recorded' case, especially at low speeds. To correct for the mismatch, we should alter the parameters, which have great influence in the torque gradient in low speeds such as the T_{min} and the L_{lift}. Therefore we modified by -50% the T_{min} and the L_{lift}. To compensate for the decrease that the former alterations would induce to the torque gradient at higher speeds, we altered the T_{max} and the L_{trail} by +20%. The aforementioned changes resulted in the 'Sim A' curve.

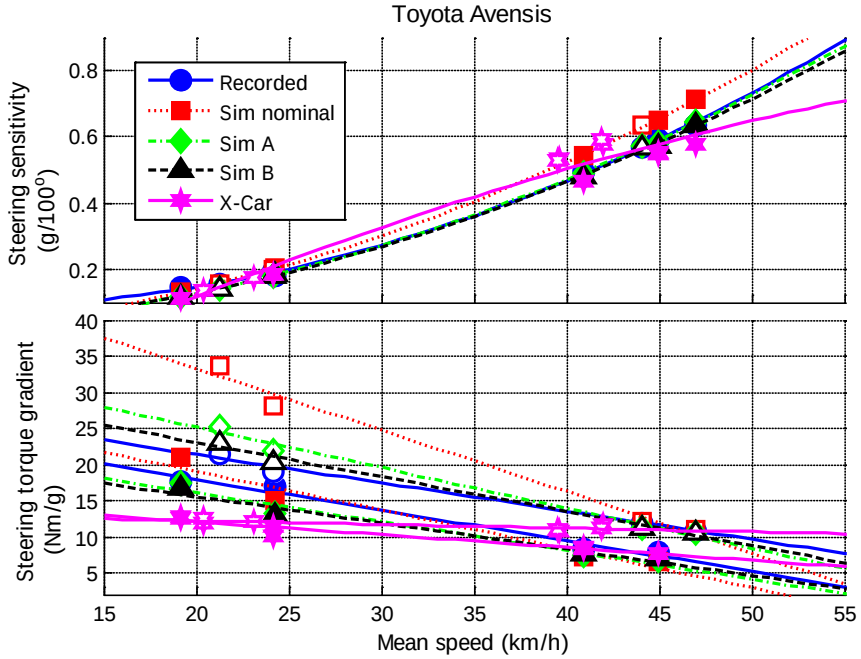

Fig. 3.11. Steering sensitivity and steering torque gradient reconstruction for the Toyota Avensis. The 'Recorded' metrics are compared with the 'Sim nominal' case, having the nominal parameters values of Table 3.5, and two additional cases; 'Sim A' and 'Sim B'. The lines represent quadratic and linear fits for the steering sensitivity and the steering torque gradient correspondingly. The filled markers correspond to b = 35 and the white-filled to b = 55 m tests.

To further elaborate the approximation between the simulated and the 'Recorded' metrics, we retained the R_s, T_{max} and L_{trail} values of the 'Sim A' settings. The torque gradient values for the speeds above 40 km/h were close for the 'Sim A' and the 'Recorded' case. We aimed therefore for changes influencing only the lower speeds. Thus we altered the L_{lift} and the T_{min} by -65%, the I_z by +30% (expected to change the sensitivity by -3% only at higher speeds). We also changed the T_{gain} by -10% (to increase the torque gradient at higher speeds so as to compensate for the decrease imposed by the former changes). Those alterations yielded the 'Sim B' curves. The RMS errors for the steering sensitivity of Fig. 3.11 from 15 to 50 km/h between 'Recorded' on the one hand, and 'Sim nominal', 'Sim A', 'Sim B', on the other, were 0.043, 0.011, and 0.012, respectively. Similarly, the RMS errors for the steering torque gradient for the b = 35 m case, were 1.19, 1.54 and 1.71, respectively. For the b = 55 m case, the RMS errors were 7.51, 2.31 and 1.03. The final parameters used for the 'Sim nominal' case, 'Sim A' and 'Sim B' are summarized in Table 3.7.

Table 3.7. Final parameters used for simulation.

Parameter	Sim nominal	Sim A	Sim B	X-car
M	**1300**	1300	1300	1195
I_z	**1900**	1900	2470	1900
T_{min}	**0.700**	0.350	0.245	0.245
T_{max}	**8.000**	9.600	9.600	9.600
T_{gain}	**9.000**	9.000	8.100	8.100
L_{arm}	**0.167**	0.167	0.167	-
L_{lift}	**0.050**	0.025	0.018	-
L_{trail}	**0.050**	0.060	0.060	-
R_s	**0.011**	0.01	0.01	0.01
B_{pac}	**6.900**	6.900	6.900	-
C_{pac}	**1.700**	1.700	1.700	-
D_{pac}	**0.900**	0.900	0.900	-
t_f	**1.040**	1.040	1.040	0.91
t_r	**1.560**	1.560	1.560	1.7

B. High fidelity driving simulator realism evaluation for driver in the loop testing

To substantiate the findings the resulting 'Sim B' steering system settings were combined with the body-mass settings of a nominally understeering Opel Astra G. This parameterization was employed in the X-Car driving simulator [32], in order to assess its realism in the context of our haptic steering support research needs (the developed haptic controllers would be later ported on an Opel Astra G). The X-Car is based on a dSPACE real-time computer and runs the real-time dSPACE *Automotive Simulation Model* package [58], a commercial 24-DOF vehicle dynamics model. The vehicle is an open *MATLAB®/Simulink®* model and incorporates semi-empirical tire models, suspension dynamics, steering-system models, etc.

Due to the complex vehicle dynamics model used in the X-car, only the parameters shown in the "X-Car" column Table 3.7 could be directly adapted in the simulator. The modelled steering system in the X-car was identical to the steering system model displayed in Section 3 up to equation (3.19). The rack's displacement x_r (3.17) determined the vehicle's left and right wheel angles through a complex suspension setup. The steering ratio was set to average the 16.7 (steering ratio = L_{arm}/R_s) as in the 'Sim B' case, resulting to a relative error of 2.5% compared to the Astra's actual average measured steering ratio of 16.3. We use the term 'average', because the front wheels' angle, is influenced, not only by the steering wheel angle θ_{sw}, but also by the suspension geometric steer originating from the vertical wheel motion coupled with the linkage geometry (bump and/or roll steer), toe-angle, and suspension compliance [89] (pp. 284). The steering ratio derives from the average angles of the left and right wheel, which due to the modelled leverages of the suspension, are neither identical (between them) nor linearly related to the rack's displacement x_r. In the X-car vehicle dynamics model, a generalized rack force F_r (as in (3.21)) incorporated all the components constituting the wheels feedback force; aligning moment due to the pneumatic and mechanical trail, the lifting torque (as in (3.23)) caused by the lift or lowering of the wheel-steer axis when steering, etc. [89].

The same manoeuvres as in Table 3.2 were performed with a human driver in the loop performing the steering through a high fidelity force-feedback system composed of a powerful three-phase brushless motor [32]. The steering task was accomplished by the driver whilst a longitudinal controller was responsible for achieving similar mean speed with the Toyota's Avensis tests presented in Fig. 3.11. The resulting metrics are displayed in Fig. 3.11 ('X-Car'). It can be seen that the metrics are comparable with those acquired from the real vehicle. The differences in the steering torque gradient, besides the modelling errors, are due to additional force-feedback components (besides those in (3.16)

and (3.17)), which aim to promote the driver's safety in the expense of fidelity (c.f. [32]). The powerful motor used for the force-feedback can impose almost any virtual dynamics to the driver; it should therefore remain stable under all circumstances. The understeering setup of the vehicle model resulted, the steering sensitivity to drop with the b = 35 m cone distance. This was because the driver had to steer more to achieve the same lateral force necessary to negotiate the given lane change. Still though, upon this simple test, we could assess the X-Car's on-centre force-feedback and vehicle dynamics response fidelity as suitable for human-in-the-loop testing. Example car specifications (caster angle, pneumatic trail length etc.), can be found in [89] (pp. 508 – 509).

VI. Discussion

The aim of this work was a) to assess the steering metrics of real cars during lane change manoeuvres and b) to investigate how key parameters of the vehicle determine these steering metrics, so that they can be adjusted for a realistic on-centre vehicle response. To reach our objective we measured the relationships between vehicle speed, lateral acceleration, steering wheel torque and steering wheel angle for five modern passenger cars. Through simulation we studied the connection between vehicular parameters and the steering metrics, a) steering sensitivity and b) steering torque gradient.

The empirical results showed that for a given speed, the relationship between lateral acceleration and steering wheel angle was close to linear with an average correlation of .98. The slope of this relationship (i.e., the steering sensitivity) grew slightly with speed. The steering sensitivity was reversely proportional to the steering ratio. Contrary to the steering wheel angle versus lateral acceleration relationship, which was close to linear, the relationships with the steering torque were characterized by considerable hysteresis (c.f. Fig. 3.3). The current results showed that the steering torque depends predominantly on the lateral acceleration. However, because of the complex shape of the hysteresis loop (HL) of the steering torque versus lateral acceleration, we can conclude that further criteria should be studied so as to better capture the steering force-perception (e.g. geometric properties of the HL; height, area etc.).

The same manoeuvres for the real tests were simulated using a vehicle dynamics model. A sensitivity analysis on the simulated results showed clear trends on which parameters influence the steering metrics and how the parameters can be adapted to yield certain steering metrics obtained from real cars. The steering sensitivity was mainly affected by the steering ratio of the vehicle; also supported from the empirical results; the highest the steering ratio, the lowest the steering sensitivity. The steering torque gradient was influenced by the majority of the vehicular parameters and especially those related to the steering system (and in particularly the power assistance system). Through an example, we showed that by using the sensitivity analysis results, a researcher can effectively adjust the settings of the vehicle dynamics model to achieve realistic steering in a driving simulator. Tuning the parameters to approximate the shape of a specific steering metric curve is not a trivial exercise because of the cross-coupled effects of the adjustments. For example, the adaptations we made to improve the large RMS error for the steering torque gradient for the b = 55 m case slightly worsened the RMSE for the b = 35 case in (part A of Section 5). The adaptation process is a trade-off between realism and applicability. For example, due to its inherent limitations, a simulator might be able to offer only a -180 to 180^o of steering wheel angle. The researcher can therefore either adapt the steering ratio to offer full-range steering of the vehicle or to limit the steering range and retain realism around the on-centre steering.

The limitations imposed by a simple vehicle dynamics model that considers the lateral, longitudinal, and vertical dynamics separately are known [52][132]. However, simple models have been established

for a basic understanding of the vehicle behaviour with the emphasis on the overall performance [132], which was the purpose of this study. Our analysis showed that the bicycle model provided a good fit for the relationship between steering wheel angle and lateral acceleration (for moderate lateral acceleration). Tentatively, for many basic research applications using on-centre handling, the bicycle model will be sufficiently accurate. For situations such as skid control and emergency driving, more advanced models will be needed.

Table 3.8. Sensitivity analysis synopsis for all parameterizations and velocities of Table 3.5. The parameters Bpac, Cpac and Dpac were modified with -15%, -10%, -5%, 5%, 10% and 15% (the corresponding columns are -35%, -20%, -10%, 10%, 20% and 35%) from their nominal values.

		Steering sensitivity						Steering torque gradient						Lateral acceleration range					
		-0,4	-0,2	-0,1	0,1	0,2	0,35	-0,4	-0,2	0	0,1	0,2	0,35	-0,4	0	0	0,1	0,2	0,4
10 km/h	Nominal			0,037		g/ 100°				60,521		Nm/ g				0,052		g	
	m	0.0	-0.1	0.0	-0.2	-0.2	-0.3	-16.9	-8.9	-4.5	3.5	6.7	11.6	0.5	0.2	0.1	-0.1	-0.1	-0.2
	I_z	0.1	0.1	0.1	0.0	0.0	-0.1	-0.3	-0.2	-0.1	0.0	0.0	0.2	-0.2	-0.2	-0.1	0.1	0.2	0.4
	B_{pac}	0.0	0.1	0.1	0.0	0.1	0.1	-0.1	-0.1	-0.1	-0.1	0.0	-0.2	0.2	0.1	0.1	0.0	-0.1	-0.1
	C_{pac}	0.0	0.1	0.0	0.1	0.1	0.2	-0.1	-0.1	-0.1	-0.1	-0.1	-0.1	0.2	0.1	0.1	-0.1	-0.1	-0.2
	D_{pac}	-0.1	-0.1	0.0	0.1	0.2	0.1	-0.2	-0.1	-0.1	0.0	0.0	0.0	0.4	0.2	0.1	0.0	-0.2	-0.3
	T_{min}	0.2	0.0	0.0	-0.2	-0.2	-0.1	-13.9	-8.7	-4.6	3.6	7.0	13.3	0.0	-0.1	0.0	0.0	0.0	0.0
	T_{max}	-0.1	-0.1	-0.1	0.0	-0.2	-0.8	15.5	7.9	3.5	-4.2	-7.5	-9.9	0.0	0.1	0.0	-0.1	0.0	0.0
	T_{gain}	-1.0	-0.4	-0.1	-0.1	-0.1	-0.1	-14.4	-8.8	-5.1	3.5	7.0	11.6	0.0	0.0	0.0	0.0	0.0	0.0
	L_{arm}	52.6	24.4	10.8	-9.0	-16.6	-25.9	17.7	8.2	3.9	-4.2	-7.5	-11.8	0.3	0.1	0.0	0.0	-0.1	-0.1
	L_{lift}	0.0	-0.1	0.0	-0.1	-0.4	-0.5	-11.6	-6.5	-3.3	3.0	4.9	8.5	-0.1	0.0	0.0	0.0	0.0	0.0
	L_{trail}	-0.1	-0.1	0.0	0.1	0.0	-0.1	-4.4	-2.5	-1.3	1.1	2.3	3.5	0.0	0.0	0.0	0.0	0.0	0.0
	R_s	-35.1	-20.4	-10.1	9.8	19.7	34.5	-18.1	-9.8	-5.7	4.1	8.0	13.2	-0.1	-0.1	-0.1	0.0	0.1	0.2
20 km/h	Nominal			0.141		g/ 100°				19.783		Nm/ g				0.190		g	
	m	-0.5	-0.1	-0.1	0.0	0.0	0.1	-15.5	-8.6	-3.9	3.8	7.6	12.7	1.6	0.7	0.3	-0.2	-0.4	-0.7
	I_z	0.4	0.2	0.1	-0.1	-0.2	-0.4	0.1	0.1	0.0	0.0	0.0	-0.1	-1.0	-0.6	-0.3	0.3	0.6	1.1
	B_{pac}	-0.2	-0.1	-0.1	0.0	0.1	0.1	-0.2	-0.1	-0.1	0.1	0.1	0.1	0.6	0.4	0.2	-0.1	-0.3	-0.4
	C_{pac}	-0.2	-0.1	0.0	0.1	0.1	0.1	-0.2	-0.1	-0.1	0.1	0.1	0.1	0.8	0.5	0.2	-0.2	-0.4	-0.5
	D_{pac}	-0.3	-0.2	-0.1	0.1	0.2	0.2	-0.3	-0.2	-0.1	0.1	0.1	0.3	1.2	0.8	0.4	-0.3	-0.6	-0.8
	T_{min}	0.1	0.1	0.0	-0.1	0.0	-0.1	-11.7	-6.7	-3.3	3.3	6.7	11.7	0.0	0.0	0.0	0.0	0.0	0.0
	T_{max}	0.0	0.1	0.0	0.0	0.0	0.1	23.4	11.2	5.1	-4.1	-8.1	-12.5	0.1	0.0	0.0	0.0	0.0	0.0
	T_{gain}	0.0	0.1	0.0	0.0	0.0	0.0	-19.0	-10.6	-5.1	5.0	9.9	17.4	0.0	0.0	0.0	0.0	0.0	0.1
	L_{arm}	52.5	24.5	10.9	-9.0	-16.4	-25.6	18.6	9.1	4.2	-3.5	-7.0	-11.1	0.2	0.1	0.0	0.0	0.0	-0.1
	L_{lift}	0.2	0.1	0.1	0.0	-0.1	-0.1	-6.4	-3.5	-1.8	1.8	3.3	5.8	0.0	0.0	0.0	0.0	0.0	0.0
	L_{trail}	0.1	0.0	0.0	0.0	0.0	-0.1	-8.4	-4.5	-2.3	2.1	4.3	7.5	0.0	0.0	0.0	0.0	0.0	0.0
	R_s	-34.8	-19.9	-10.0	10.0	19.8	34.6	-15.8	-8.8	-4.1	4.1	8.6	14.4	-0.1	-0.1	0.0	0.0	0.1	0.2
30 km/h	Nominal			0.306		g/ 100°				11.062		Nm/ g				0.417		g	
	m	-1.8	-0.8	-0.3	0.3	0.5	0.6	-16.3	-8.9	-4.1	4.1	8.1	13.3	2.9	1.3	0.6	-0.5	-0.9	-1.4
	I_z	1.1	0.6	0.3	-0.3	-0.7	-1.3	0.5	0.3	0.2	-0.1	-0.3	-0.4	-1.9	-1.1	-0.5	0.5	1.1	1.9
	B_{pac}	-0.4	-0.3	-0.1	0.1	0.2	0.3	-0.4	-0.2	-0.1	0.1	0.2	0.3	1.1	0.7	0.3	-0.3	-0.5	-0.7
	C_{pac}	-0.6	-0.4	-0.2	0.1	0.3	0.4	-0.5	-0.3	-0.2	0.1	0.2	0.4	1.5	0.9	0.4	-0.4	-0.7	-0.9
	D_{pac}	-0.9	-0.5	-0.3	0.2	0.4	0.6	-0.8	-0.5	-0.2	0.2	0.4	0.6	2.3	1.4	0.7	-0.6	-1.1	-1.6
	T_{min}	0.1	0.1	0.0	0.0	-0.1	-0.1	-9.6	-5.4	-2.6	2.7	5.6	9.6	0.0	0.0	0.0	0.0	0.0	0.0
	T_{max}	-0.3	-0.2	-0.1	0.1	0.1	0.2	28.0	13.4	6.2	-5.0	-9.4	-14.6	0.1	0.0	0.0	0.0	0.0	0.0
	T_{gain}	0.3	0.2	0.1	-0.1	-0.1	-0.2	-22.0	-12.2	-6.0	6.1	11.7	20.2	0.0	0.0	0.0	0.0	0.0	0.0
	L_{arm}	52.4	24.5	10.9	-8.9	-16.4	-25.6	19.1	9.5	4.4	-3.6	-7.0	-11.2	0.2	0.1	0.0	0.0	-0.1	-0.1
	L_{lift}	0.1	0.0	0.0	0.0	0.0	0.0	-3.7	-2.1	-1.0	1.0	2.1	3.7	0.0	0.0	0.0	0.0	0.0	0.0
	L_{trail}	0.1	0.1	0.0	0.0	-0.1	-0.1	-11.1	-6.1	-2.8	2.9	5.8	9.7	0.0	0.0	0.0	0.0	0.0	0.0
	R_s	-34.7	-19.7	-9.8	9.8	19.6	34.2	-15.9	-8.7	-4.1	4.1	8.1	13.8	-0.1	-0.1	0.0	0.0	0.1	0.1
40 km/h	Nominal			0.522		g/ 100°				7.519		Nm/ g				0.730		g	
	m	-3.3	-1.4	-0.6	0.5	0.8	1.2	-16.9	-9.3	-4.4	4.3	8.3	14.2	3.4	1.7	0.8	-0.6	-1.2	-1.9
	I_z	1.9	1.1	0.6	-0.6	-1.2	-2.2	1.0	0.6	0.3	-0.2	-0.5	-0.7	-2.6	-1.5	-0.7	0.7	1.4	2.4
	B_{pac}	-0.7	-0.5	-0.2	0.2	0.3	0.5	-0.6	-0.4	-0.2	0.2	0.3	0.5	1.5	0.9	0.4	-0.4	-0.7	-1.0
	C_{pac}	-0.9	-0.6	-0.2	0.2	0.4	0.6	-0.8	-0.5	-0.2	0.2	0.4	0.6	2.0	1.2	0.6	-0.5	-0.9	-1.3
	D_{pac}	-1.4	-0.9	-0.4	0.4	0.7	1.1	-1.2	-0.8	-0.4	0.4	0.7	1.0	3.0	1.9	0.9	-0.8	-1.5	-2.2
	T_{min}	0.1	0.1	0.0	0.0	-0.1	-0.1	-7.9	-4.4	-2.3	2.3	4.7	7.9	0.0	0.0	0.0	0.0	0.0	0.0
	T_{max}	-0.2	-0.2	-0.1	0.1	0.2	0.2	31.6	15.0	6.7	-5.5	-10.2	-16.3	0.1	0.0	0.0	0.0	0.0	0.0
	T_{gain}	0.4	0.2	0.1	-0.1	-0.2	-0.3	-24.3	-13.6	-6.6	6.6	13.1	22.7	0.0	0.0	0.0	0.0	0.0	0.0
	L_{arm}	52.2	24.4	10.9	-8.9	-16.4	-25.6	19.7	9.8	4.4	-3.7	-7.1	-11.4	0.2	0.1	0.0	0.0	0.0	-0.1
	L_{lift}	0.1	0.0	0.0	0.0	0.0	0.0	-2.6	-1.4	-0.7	0.7	1.5	2.5	0.0	0.0	0.0	0.0	0.0	0.0
	L_{trail}	0.1	0.1	0.0	0.0	-0.1	-0.1	-12.9	-7.0	-3.4	3.4	6.5	11.3	0.0	0.0	0.0	0.0	0.0	0.0
	R_s	-34.6	-19.7	-9.8	9.8	19.6	34.2	-15.9	-8.6	-4.0	4.1	8.0	13.6	-0.1	0.0	0.0	0.0	0.1	0.1
50 km/h	Nominal			0.788		g/ 100°				5.655		Nm/ g				1.138		g	
	m	-4.7	-2.1	-0.8	0.7	1.2	1.8	-17.9	-9.7	-4.7	4.5	8.8	14.8	4.2	2.1	0.9	-0.8	-1.5	-2.4
	I_z	2.6	1.6	0.9	-0.9	-1.8	-3.2	1.5	0.8	0.3	-0.3	-0.6	-1.2	-3.4	-1.9	-0.9	0.9	1.7	2.8
	B_{pac}	-1.1	-0.6	-0.3	0.2	0.5	0.7	-0.8	-0.5	-0.2	0.2	0.4	0.6	1.8	1.1	0.5	-0.5	-0.9	-1.2
	C_{pac}	-1.3	-0.8	-0.3	0.3	0.6	0.9	-1.0	-0.6	-0.3	0.2	0.5	0.7	2.3	1.5	0.7	-0.6	-1.1	-1.5
	D_{pac}	-1.9	-1.3	-0.5	0.6	1.1	1.4	-1.8	-1.0	-0.5	0.4	0.9	1.3	3.5	2.2	1.1	-1.0	-1.9	-2.7
	T_{min}	0.1	0.1	0.0	0.0	0.0	-0.1	-6.4	-3.7	-1.9	1.9	3.7	6.4	0.0	0.0	0.0	0.0	0.0	0.0
	T_{max}	-0.3	-0.2	-0.1	0.1	0.2	0.3	34.1	16.2	7.4	-6.0	-11.1	-17.5	0.1	0.0	0.0	0.0	0.0	0.0
	T_{gain}	0.5	0.2	0.1	-0.1	-0.1	-0.2	-26.2	-14.8	-7.3	7.3	14.2	24.6	0.0	0.0	0.0	0.0	0.0	0.0
	L_{arm}	52.1	24.4	10.9	-8.9	-16.4	-25.5	20.0	9.8	4.6	-3.9	-7.3	-11.7	0.1	0.1	0.0	0.0	0.0	-0.1
	L_{lift}	0.1	0.1	0.0	0.0	-0.1	-0.1	-1.9	-1.1	-0.5	0.6	1.1	1.8	0.0	0.0	0.0	0.0	0.0	0.0
	L_{trail}	0.1	0.1	0.1	0.0	0.0	0.0	-14.3	-7.8	-3.8	3.6	7.1	12.0	0.0	0.0	0.0	0.0	0.0	0.0
	R_s	-34.5	-19.7	-9.8	9.8	19.6	34.2	-16.3	-8.8	-4.3	4.0	8.0	13.5	-0.1	0.0	0.0	0.0	0.0	0.1

How can the present results be used in the development of driving simulators for training and research? Simulator users and vehicle dynamics theorists can potentially use the reported steering metrics, combined with the sensitivity analysis, for adjusting key driving simulator parameters. Improved fidelity of the simulation will usually enhance transfer of training and data validity. The present study dealt with the analysis of on-centre behaviour. On-centre behaviour is usually of interest for most driving simulator applications; for example, in driver training or highway driving, where participants normally do not seek the limits of the car. For more exclusive driving simulator applications, such as emergency vehicle driving, more sophisticated validation studies will be required.

We recommend future research that will study the relationship between the steering metrics and driver's objective performance (e.g., lane maintenance performance, cornering speeds) and subjective criteria (e.g., feeling perception, [13]) so as to promote driver-oriented steering systems design.

VII. Acknowledgements

The research was supported by the Automotive Development Center of SKF as part of the Mobility Intelligence using Loadbased Lateral Stability (MILLS) project. Research by J.C.F. de Winter was supported by the Stichting voor de Technische Wetenschappen (STW, Dutch Technology Foundation), Applied Science Division of the Nederlandse Organisatie voor Wetenschappelijk Onderzoek (NWO, Netherlands Organisation for Scientific Research) and the Technology Program of the Ministry of Economic Affairs.

Chapter 4. Road Departure Prevention in an Emergency Obstacle Avoidance Situation

“The greater the obstacle, the more glory in overcoming it.”
Molière, 1622-1673 A.D.

Road-Departure Prevention in an Emergency Obstacle Avoidance Situation

Abstract—This Chapter presents a driving simulator experiment which evaluated a road-departure prevention (RDP) system in an emergency situation. Two levels of automation were evaluated: 1) haptic-feedback (HF) where the RDP provided advisory steering torque such that the human and the machine carry out the manoeuvre cooperatively, and 2) drive-by-wire (DBW) where the RDP automatically corrected the front-wheels angle, overriding the steering-wheel input provided by the human. Thirty participants were instructed to avoid an obstacle in a pylon-confined area while keeping the vehicle on the road. The results showed that HF had a significant impact on the measured steering torque, but no significant effect on steering-wheel angle or vehicle path. DBW prevented road-departure and reduced mental workload, but led to inadvertent human-initiated counter-steering. It is concluded that a low level of automation, in the form of HF, does not prevent road-departures in an emergency situation. A high level of automation, on the other hand, is highly effective in preventing road-departures. However, more research may have to be done on the human response while driving with systems that alter the relationship between steering-wheel angle and front-wheels angle.

I. Introduction

Lane departure is a factor in a large proportion of accidents involving fatal or serious injuries, and is usually induced by the driver's inattention, fatigue, impairment and distraction or improper control inputs in an emergency situation. Jermakian [100] estimated the potential of lane-departure warning (LDW) and asserts that lane departure appears relevant in 179,000 crashes per year and is related to the greatest number of fatal crashes; up to 7,500 fatal crashes per year in the United States.

Since 2001, Nissan motors in Japan have been offering a lane-keeping support system [25], with audible feedback that sounds if the vehicle begins crossing the lane markings/limits. In 2002 and 2003, Toyota and Honda launched their lane- keeping assist systems that apply steering-wheel torque to help drivers to keep the vehicle in the lane. Nowadays (2012), most high-end automobile manufacturers (Mercedes, Volvo, BMW, Nissan-Infiniti, Honda, etc.) offer similar assist systems in their top-class models. Most LDW systems utilize a camera to track road markings and estimate the vehicle position relative to the road. The feedback to the driver varies from audible, visual, and/or vibro-tactile signals, to haptic steering-wheel feedback. Nissan (Infiniti) was the first to offer lane-departure prevention (LDP), an extension of LDW [103]. In addition to the warning system (automatically enabled when the vehicle is started), LDP brakes slightly to help prevent unintended departure from the travelling lane. Due to the active intervention of LDP, Infiniti decided to require drivers to enable the system at will. Infiniti predicts that if LDP were fitted to all vehicles, some 12% of all road fatalities—around 5,000 deaths—could be prevented annually [70].

A study on a lateral drift-warning system by the U.S. Dept. of Transportation [45] showed that drivers improved their lane keeping, spent 63% less time outside the lane, and increased their use of turn signals. Drivers readily accepted this system, viewing it as an easy and comfortable way to increase safety. Interestingly, drivers rated this system as useful but less satisfying compared to adaptive cruise control (ACC). Braitman *et al*., [103] using telephone interviews to owners of Infiniti

vehicles equipped with LDW and LDP, investigated drivers' use and acceptance of these systems. The majority of the interviewees reported that they "disliked nothing" about the LDW system. They drifted from the lane less often. As for the LDP system, 50% reported that they "disliked nothing" about it; 68% reported that they drifted less and 22% were unaware that they were using LDP technology.

LDP systems have gained attention in academic research. Studies on vibro-tactile feedback for collision mitigation [97] and learning a lane-keeping task have given promising results [152]. Griffiths and Gillespie [131] have explored the benefits of augmented force-feedback to share control between the driver and automated steering to support lane keeping. Mulder *et al*. [119] proposed a haptic guidance system, where the driver and support system share steering control, showing that continuous haptic support is an efficient way to support drivers during curve negotiation. This assertion concurs with the continuous haptic steering-support system for obstacle avoidance designed by Della Penna *et al*. [122]. Their proposed system reduced the number of crashes, control effort, and activity in critical situations. A literature review by De Winter and Dodou [90] argued that the effects of haptic-shared control during routine tasks are adequately established, but more research into human factors needs to be done during safety-critical manoeuvres.

Although some studies tend to favour human-cantered automation, where the driver always has control and authority of the vehicle, solely receiving feedback guidance on the steering-wheel [119][122], the literature is still debating the required level of automation for a given task. Human-cantered automation may not always be the best solution [158][159] because of human limitations in speed and decision-making [22]. An example of driver-assist technology deviating from the principle of human-cantered automation (in the sense that it can act autonomously in emergencies and completely override the driver; i.e., a high level of automation) is a collision-mitigation system that can apply the brakes if the driver does not act in time. If such a high level of automation was not entirely effective in all circumstances, it would worsen the potential for collision when operated by an ineffectual driver (due to misunderstanding its functions) [159]. Research related to ACC [20][126] agrees with the former argument: although ACC is acknowledged to reduce mental workload, it has also been blamed for provoking false reliance on the system [126]. According to Seppelt et al. [20], reliance on ACC disengaged drivers from their primary task (driving), and increased their response time to vehicles braking ahead.

Summarizing, a high level of automation can lead to false reliance and/or miscomprehension of the functionality, that could reduce its potential benefits under certain conditions [159]. This suggests that careful design and rigorous testing is essential for emergency situations (additional to normal driving); see, for instance, the study by Itoh et al. [115] presenting a pedestrian collision-avoidance system in emergency situations.

Although numerous studies have shown the potential of lane-keeping and LDP systems [70][45][97][119][122], including drive-by-wire approaches [98], there are few studies related to their effects during driver-in-the-loop emergency manoeuvres.

The aim of this study is to investigate different levels of automation in an emergency scenario in conjunction with a road-departure prevention system. The systems are tested with 30 test drivers in a driving simulator. This road-departure prevention (RDP) system utilizes look-ahead information to derive the future lateral position of the vehicle with respect to the road. The RDP system intervenes by applying haptic (advisory) feedback torque or correcting the angle of the front-wheels (drive-by-wire) when road-departure is likely to occur. An RDP controller developed by Alirezaei et al. [112][111] determines the correcting steering input using the driver's steering input and the vehicle's driving speed (similar to [131][119][163]).

Four steering setups were evaluated in an emergency obstacle avoidance scenario; a setup without support was tested first followed by three support setups tested in randomized order:

i. **No support**: normal driving.
ii. Haptic-feedback (**HF**): if a road-departure is likely to occur, the RDP gives advisory steering torque such that human and machine carry out the emergency manoeuvre cooperatively.
iii. Drive-by-wire (**DBW)**: if a road-departure is likely to occur, the RDP imposes a front-wheels angle to keep the vehicle on the road, effectively overriding the driver.
iv. Combined (**DBW & HF**): if a road-departure is likely to occur, the RDP both imposes the front-wheels angle and gives advisory steering torque.

This study is the first to address the DBW concept for RDP in an emergency situation building on initial results presented in [42]. The current Chapter constitutes an aggregation of new results and in-depth analysis of the work in [42]. Section II deals with the test apparatus, the RDP controller operating principle including an example, the steering support setups, the driving task and test group, and the statistical analysis. The results are analysed in Section III and a discussion in Section IV concludes the Chapter.

II. Methods

A. Test apparatus

Driver-in-the-loop testing of the RDP controller was done in the X-Car driving simulator [32]. The simulator is based on a dSPACE real-time computer and runs a vehicle-dynamics model from the dSPACE Automotive Simulation Model package. The vehicle is an open Matlab®/ Simulink® model with 24 degrees of freedom. It incorporates semi-empirical tire models, suspension dynamics, and steering system model, etc. The vehicle-dynamics model is executed at 1 kHz (1 ms fixed time step). Communication with the environment (through interface boards) and the steering force-feedback controller are executed at 5 kHz. Steering-force-feedback is delivered through a brushless 3-phase motor, evaluated for its high fidelity in conjunction with its controllers [32]. Finally, three TFT monitors composed a viewing angle of 135°.

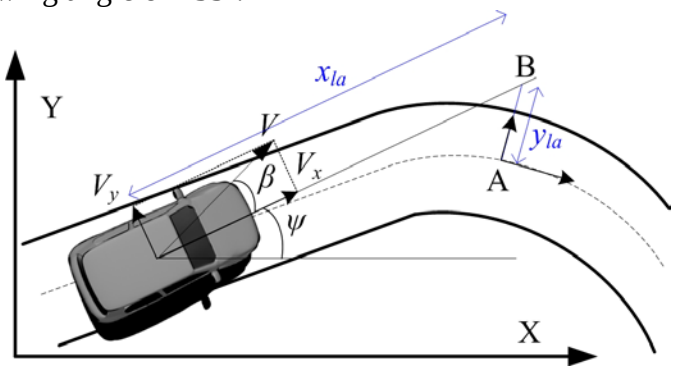

Fig. 4.1. Road-departure prevention concept. Whether the car turns or the on-coming road becomes curvy, the road prevention scheme is the same. The normal to the road line from point A intersects at point B with the line parallel to the vehicle's longitudinal velocity vector V_x, x_{la} meters ahead. The distance between points A and B gives y_{la}, which represents the lateral offset.

B. Road-departure prevention controller

Each driver tested a no-support setup and three RDP setups of the vehicle. The three RDP setups were designed according to principles described as follows.

The vehicle, with front-wheel drive, 1200 kg of mass and 2500 kg·m^2 of yaw inertia is assumed to utilize a camera for measuring the lateral offset between the vehicle and the road (Fig. 4.1).

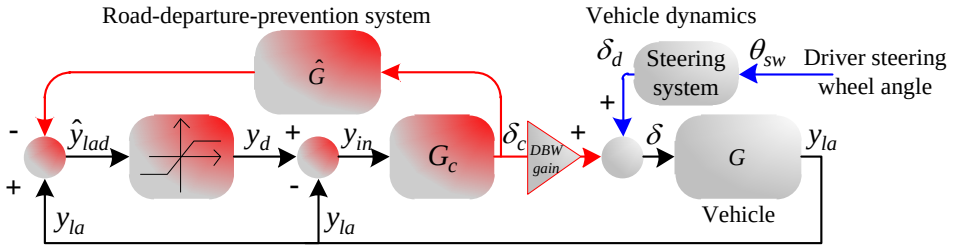

Fig. 4.2. Interaction scheme for road-departure prevention vehicle. Block G represents the vehicle dynamics from the front-wheel steering angle δ to y_{la}; $\hat{G}$ is the estimate of G. $\hat{G}$ was used to accommodate modelling errors and parameter uncertainty of G. As can be seen in the block diagram, y_{la} is computed as in (4.1) where δ_c is the G_c controller's correcting angle and δ_d the front-wheel steering angle deriving from the driver's steering-wheel angle θ_{sw}. The estimated desired lateral offset $\hat{y}_{lad}$ is given in (4.2). The desired lateral offset y_d, saturated by the road limits, is given by (4.3) where y_L denotes the lateral limit (road width). The input y_{in} to the G_c controller is given by (4.4)

The RDP system [112] is shown as a block diagram in Fig. 4.2. Assume that $\delta_c = 0$ and that y_{la} is within the road limits; then $y_d = y_{la}$, and therefore $y_{in} = 0$. In this case, the controller has no effect on the vehicle and $\delta_c = 0$. If the driver's steering input δ_d points the vehicle outside the road limits, the result is that $y_d \neq y_{la}$ induces the controller G_c to become active ($\delta_c \neq 0$). The Simulink® model from dSPACE, described briefly at the start of the Methods section, can calculate the future position of the vehicle and corresponding lateral offset with respect to the road. The RDP system (Fig. 4.2) was therefore fed with the y_{la} signal deriving from the vehicle-dynamics model. The look-ahead time was set to 0.7 s, determining the length x_{la} = 9.72 m at 50 Km/h (Fig. 4.1). This time was appointed with pilot tests to offer driving comfort and RDP efficiency. For more details on the design of the G_c controller, see the work by Alirezaei *et al.* [112][111].

$$y_{la} = G \cdot \delta \xrightarrow{\text{when } DBW\ gain=1} y_{la} = G \cdot (\delta_c + \delta_d) \tag{4.1}$$

$$\hat{y}_{lad} = y_{la} - \hat{G} \cdot \delta_c \tag{4.2}$$

$$y_d = \begin{cases} -y_L & if\ (\hat{y}_{lad} < -y_L) \\ \hat{y}_{lad} & if\ (|\hat{y}_{lad}| \leq y_L) \\ y_L & if\ (\hat{y}_{lad} > y_L) \end{cases} \tag{4.3}$$

$$y_{in} = y_d - y_{la} \tag{4.4}$$

C. Four steering setups

Four steering setups were used to evaluate the RDP during an emergency manoeuvre and to explore the differences between advisory (HF) and authoritarian support (DBW, DBW & HF):

i. **No support**: the RDP system is inactive and a mechanical connection is assumed between the steering wheel and the front wheels. Steering force-feedback offered in this setup feels realistic as it derives from non-linear tire simulation.

i. Haptic feedback (**HF**): the RDP system is active; a fixed mechanical connection is assumed between the steering wheel and front wheels. This setup applies an advisory haptic-feedback torque, assisting the driver to avoid road departure. The driver may disregard the feedback by resisting the applied force. Haptic torque is the product of the correcting angle δ_c provided by the RDP and a haptic stiffness term. The steering force-feedback offered in this setup feels realistic during normal driving ($\delta_c = 0$) as it derives from non-linear tires simulation.

ii. Drive by wire (**DBW**): the RDP is active; this setup allows decoupling of the steering wheel from the wheels thus giving an extra degree of freedom to assist the driver. It imposes a corrective steering angle δ_c on the driver's input δ_d (Fig. 4.2) resulting in a front-wheel steering angle δ (*DBW gain* = 1) that prevents road departure (even if the driver commands a deliberate road departure). When the driver steers back in the direction that will keep the vehicle within the road limits, then δ_c again becomes 0 and steering angle δ is again equal to the driver's input. Effectively this means the RDP system compensates for all driver-steering actions leading to road departure, without the driver obtaining any haptic feedback on the correction. The steering force-feedback offered in this setup is artificial during normal driving (δ_c = 0) and derives mainly from speed-related stiffness force (see next subsection for explanation).

iii. Combined **(DBW & HF)**: this setup operates identically to the DBW setup in terms of compensating driver's steering input that will induce road departure, and offers an advisory haptic-feedback torque guiding the driver to steering angles that will prevent road departure. A driver may override the feedback and can still adjust the steering-wheel angle θ_{sw} (Fig. 4.2). The G_c controller will still impose a corrective angle δ_c if θ_{sw} points the vehicle outside the road limits. The steering force-feedback offered in this setup feels realistic during normal driving (δ_c = 0), since it derives from non-linear tire simulation.

Table 4.1. Parameters and variables of the RDP steering setups.

Name	***Description***	***Name***	***Description***
$VTires_{ff}$	Force-feedback component from the 'virtual' front tires	G_{cff}	Advisory steering-torque component
$Speed_{ff}$	Speed-related force-feedback component	*DBW gain*	RDP binary gain, 0 disabled, 1 enabled
J	Steering-system moment of inertia (kg·m^2)	T_{driver}	Driver's torque (Nm)
θ_{sw}	Steering-wheel angle (rad)	T_{assist}	Power-assist torque (Nm)
K_s	Speed stiffness (Nm/rad)	K_c	RDP stiffness (Nm/rad)
G_{F2T}	Front wheels' lateral 'virtual tire' forces to steering-torque gain	l_f, t_r	Vehicle: distance of front axle from centre-of-gravity (m), track width (m)
$\hat{s}_{fj}$	Front left/right (*j: l, r*) 'virtual tires' *y* lateral slip	s_{fjx}	Front left/right (*j: l, r*) tires *x* longitudinal slip
$\hat{V}_{fjx}, \hat{V}_{fjy}$	Front left/right (*j: l, r*) 'virtual tires' *x, y* velocity	V_{fjx}, V_{fjy}	Car's *x, y* velocity, above the front left/right (*j: l, r*) wheels' steering axes
B,C,D	'Virtual tires' Pacejka coefficients.	F_{fjz}	Front left/right (*j: l, r*) tires normal load

D. Force-feedback generation for the four steering setups

Eq. (4.5) illustrates the various force-feedback components for the steering setups. Its components (explained below) are activated according to the RDP setup in use.

$$J\ddot{\theta}_{sw} = T_{driver} - VTires_{ff} - Speed_{ff} + G_{cff} + T_{assist}(T_{driver}) \tag{4.5}$$

$$VTires_{ff} = (\hat{f}_{fly} + \hat{f}_{fry}) \cdot G_{F2T} \tag{4.6}$$

$$Speed_{ff} = K_s \cdot V_X \cdot \theta_{sw} \tag{4.7}$$

$$G_{cff} = K_c \cdot \delta_c \cdot steering\_ratio \tag{4.8}$$

$$\hat{s}_{fjy} = (1 + s_{fjx}) \cdot \frac{\hat{V}_{fjy}}{\hat{V}_{fjx}}, \quad j: l, r \tag{4.9}$$

$$V_{flx} = V_x - (t_r / 2) \cdot \dot{\psi}, \quad V_{frx} = V_x + (t_r / 2) \cdot \dot{\psi} \tag{4.10}$$

$$V_{fjy} = V_y + l_f \cdot \dot{\psi}, \quad j: l, r \tag{4.11}$$

$$\hat{V}_{fjx} = V_{fjx} \cdot \cos(\delta_d) + V_{fjy} \cdot \sin(\delta_d), \quad j: l, r \tag{4.12}$$

$$\hat{V}_{fjy} = -V_{fjx} \cdot \sin(\delta_d) + V_{fjy} \cdot \cos(\delta_d), \quad j: l, r \tag{4.13}$$

$$\hat{s}_{fj} = \sqrt{\hat{s}_{fjy}^2 + s_{fjx}^2}, \quad j: l, r \tag{4.14}$$

$$\hat{\mu}_j = D \cdot \sin(C \cdot \text{atan}(\text{B} \cdot \hat{s}_{fj})), \quad j: l, r \tag{4.15}$$

$$\hat{f}_{jly} = \hat{\mu}_j \cdot F_{fjz}, \quad j: l, r \tag{4.16}$$

Table 4.1 summarizes the parameters and variables within (4.5)–(4.16).

VTires$_{ff}$ (4.6) represents the force-feedback to the steering wheel resulting from 'virtual' front left/right tire lateral forces as a function of the driver's front-wheel steering angle δ_d. 'Virtual tires' are used only for determining the steering force-feedback; the actual tire forces in the vehicle simulation derive from the dSPACE tire model as a function of δ. The use of circumflex (^) in (4.6)-(4.16) denotes variables belonging to the virtual tires. The virtual tire forces are calculated as a function of the virtual tire slip using Pacejka's Magic Formula [59]. Tire slip refers to the non-dimensional relative velocity of the tire with respect to the road. The virtual tire-friction coefficient $\hat{\mu}_j$ (4.15) is a function of the combined (longitudinal and lateral [89] (pp. 284).) slip $\hat{s}_{fj}$ (4.14) of the virtual tires (j: denotes left, right) and virtual tire-properties coefficients (D, C and B). The $\hat{s}_{fj}$ derives from [89] (pp. 284). -(4.13). When *DBW gain* = 1 and $\delta_c \neq 0$ (Fig. 4.2) the result is a change to the vehicle's states (V_x, V_y, $\dot{\psi}$) which will develop lateral slip $\hat{s}_{fj}$, creating advisory feedback torque in the direction that the RDP controller is steering. The virtual tire velocities (4.12), (4.13) are the same as in the dSPACE tire model, when δ_c = 0 (Fig. 4.2). The longitudinal slip s_{fjx} used in (4.9) and (4.14), and the normal forces F_{fjz} (4.16) originate from the dSPACE vehicle-dynamics model. The final virtual lateral forces are calculated as in (4.16).

Speed$_{ff}$ (4.7) represents a steering force-feedback term, which is a product of speed-related stiffness term K_s, the longitudinal velocity V_x and steering-wheel angle θ_{sw} (a relatively often-used approach to calculate steering force-feedback in driving simulators). K_s was selected to offer similar force-feedback magnitude levels at the speed of 50 km/h with the *VTires$_{ff}$*. The motivation for employing *Speed$_{ff}$* in addition to *VTires$_{ff}$* was to enable a DBW setup without the advisory feedback torque by decoupling steering force-feedback from the RDP intervention to the front-wheel steering angle.

The ***G$_{cff}$*** (4.8), is an advisory steering-torque component, product of the correcting angle δ_c (resulting from G_c), the *steering_ratio* and a stiffness term K_c determining the perceived force of haptic guidance. The advisory feedback torque has the direction that the G_c wants to steer the vehicle.

In an emergency manoeuvre, the correcting angle δ_c (4.8) can increase quickly, inducing a high-magnitude impulse torque on the steering wheel. Therefore, the advisory feedback torque was designed to be limited (stiffness term K_c (4.8) was set at 0.5 Nm/rad) to promote driver safety.

T$_{assist}$ (4.5) constitutes power-assist force designed as a driver torque-dependent lookup table found in modern vehicles [165]. It is active in all four RDP setups. Eq. (4.5) dictates the steering-wheel velocity $\dot{\theta}_{sw}$ constituting the command sent to the velocity-controlled force-feedback motor [32]. Steering force-feedback components per RDP setup are activated as follows:

1. **No support**: *VTires$_{ff}$* on, *Speed$_{ff}$* off, G_{cff} off, *DBW gain* = 0.
2. **HF**: *VTires$_{ff}$* on, *Speed$_{ff}$* off, G_{cff} on, *DBW gain* = 0.
3. **DBW**: *VTires$_{ff}$* off, *Speed$_{ff}$* on, G_{cff} off, *DBW gain* = 1.
4. **DBW & HF**: *VTires$_{ff}$* on, *Speed$_{ff}$* off, G_{cff} off, *DBW gain* = 1.

E. Road departure prevention operation: example

Fig. 4.3 illustrates the principles of operation of the drive-by-wire setups (DBW and DBW & HF). Initially the G_c controller is inactive and the front-wheel steering angle δ equals to δ_d (deriving from the steering-wheel angle θ_{sw}; Fig. 4.2). After X = 97 the driver steers the vehicle left to avoid an obstacle between X = 110 m and X = 130 m (the area is marked with vertical lines; the plot derives from driving task under test, which will be explained in the next section). This action induces the future lateral offset y_{la} to exceed the future desired lateral offset y_d (having an upper threshold of 2 m) at X = 105 m. From this point on, $y_{in} \neq 0$ (4.4), which induces the controller G_c to generate the correcting angle δ_c to prevent the predicted road departure. The resulting front-wheel angle δ, will keep the vehicle within the road limits. The controller's correcting angle δ_c will fade away if no further intervention is required, and δ will again become equal with δ_d.

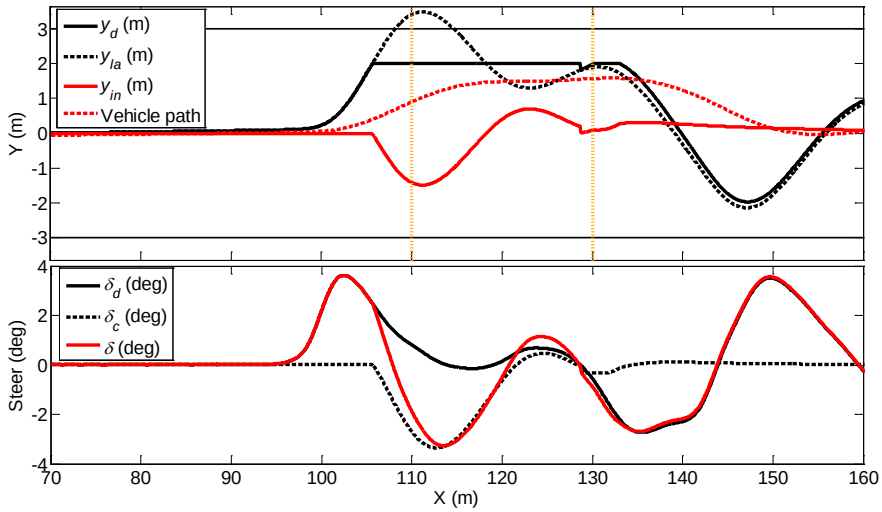

Fig. 4.3. Example of a DBW setup run. The top subplot shows the vehicle's path, the input y_{in} to the G_c controller as well as the future lateral y_{la} and future desired lateral y_d offset correspondingly. The bottom subplot displays the front-wheel angle δ, controller's correcting angle δ_c and driver's front-wheel steering angle δ_d deriving from the steering-wheel angle θ_{sw} (Fig. 4.2). Vertical lines (X = 110 m and X = 130 m) mark the area containing the obstacle.

F. Test procedure and driving task

To induce the risk of road departure during an evasive manoeuvre, the test drivers were asked to avoid a pylon-confined area (obstacle) and keep the vehicle within the road limits Y = [-3:3] m. The driving task is pictured in Fig. 4.4.

G. Participants and experiment setup

Of the 30 test drivers, two were female and all but one had a driver's license. The mean age was 29.7 years (*SD* = 5.0), their average driven number of kms per year was 10,095 (*SD* = 10,980), and the average driving license possession was 9.0 years (*SD* = 6.2). All drivers graded their own driving competence, resulting in a mean score of 6.93 (*SD* = 1.08) on a scale from 1 to 10, with 1 = incompetent driver and 10 = expert driver.

All drivers drove all four setups, with no support always driven first and the other three setups driven in random order. The operating principle of each setup was explained before testing began. The participants were divided in two groups. The first 20 drivers practiced no support for 10 runs and the other setups for 8 runs. Their performance was recorded on three additional runs. The remaining 10 drivers practiced no support for 8 runs and the other setups for 6 runs. Their performance was recorded on 7 additional runs as during the experiment we decided that more runs would enhance data reliability.

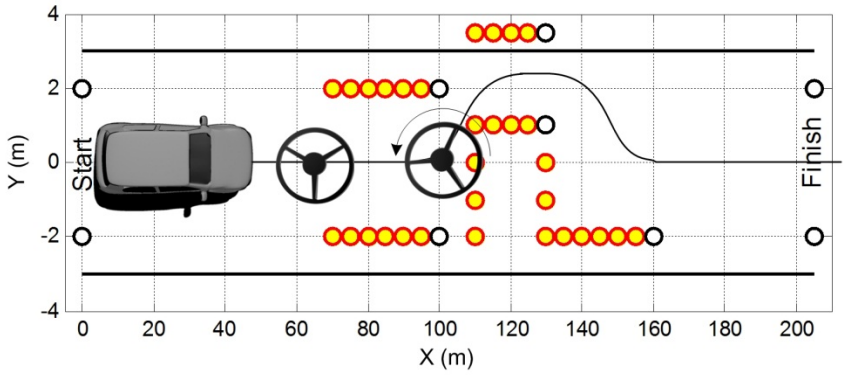

Fig. 4.4. Driving task. The vehicle started with 0 km/h and automatically accelerated up to a fixed speed of 50 km/h (reached around X = 30 m). The drivers were instructed to drive straight down the middle of the road (width = 6 m; Y = [-3:3] m) and to steer at the end of the pylon-confined passage (X = [70:100] m). They had to pass through a 2.5 m-wide pylon passage from X = [110:130] m, avoid leaving the road and hitting the pylons, then return to the middle of the road and drive up to the finish line, 205 m away from the start (Fig. 4.4). If the RDP was enabled, it helped drivers stay on the road, but did not help to avoid the pylons.

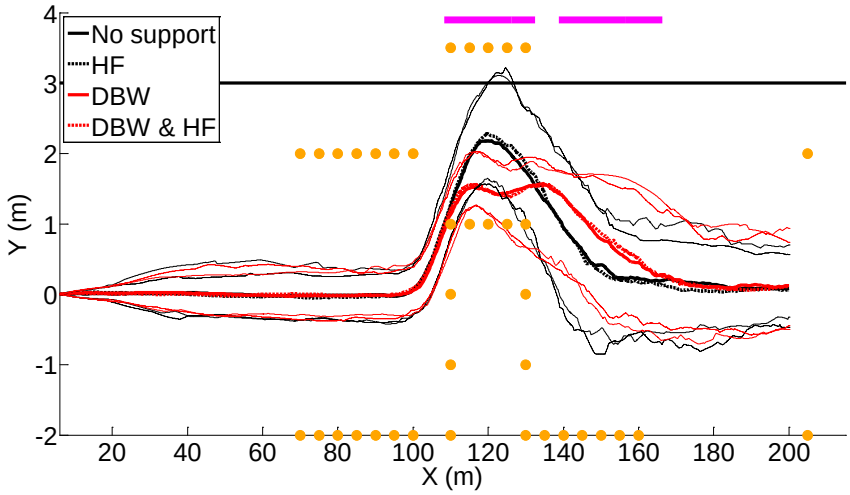

Fig. 4.5. Vehicle path: medians (thick), and 5th and 95th (thin) percentiles for the four setups (positive = to the left). The horizontal line at Y = 3 m represents the road boundary. Bars are visible on top when HF vs. DBW & HF (magenta) and DBW vs. DBW & HF (red) are statistically significant.

After completing each driving-setup session, the participant stepped out of the simulator to fill in the NASA Task Load Index (TLX). This questionnaire measures workload on six dimensions (mental demand, physical demand, temporal demand, performance, effort, and frustration level), and has been used in shared control car driving experiments before (Hart and Staveland [154], De Winter *et al*. [91]).

H. Statistical analysis

The 'percentiles' (medians, and 5th and 95th percentiles) and 'averages' were used for statistical analysis of the collected data. Percentiles, were calculated on all runs of all 30 drivers aggregated and averages were calculated first per individual and then over all 30 participants. Statistical significance of the results was assessed with paired *t*-tests, performed at the $p < 1\%$ significance level. The data were rank transformed [170] prior to submitting to the *t*-test, for higher robustness (cope with possible outliers) and to keep the ordinal scale.

III. Results

A. Objective evaluation

Fig. 4.5 shows the vehicle's lateral position relative to the lane centre for all four setups (medians, 5th and 95th percentiles). During initiation of the evasive manoeuvres, the trajectories coincide. Around X > 110 m, the RDP predicts an on-coming road departure and intervenes according to the considered setup. HF (see HF vs. no support and DBW & HF vs. DBW) had no noteworthy effect, whereas DBW made a large impact (see DBW vs. no support, and DBW & HF vs. HF). Participants on drive by wire drove more to the right between X = 110 and 130 m, and seemed to counter steer around X = 125 m. Participants on DBW were slower to return to lane centre (see X > 140 m).

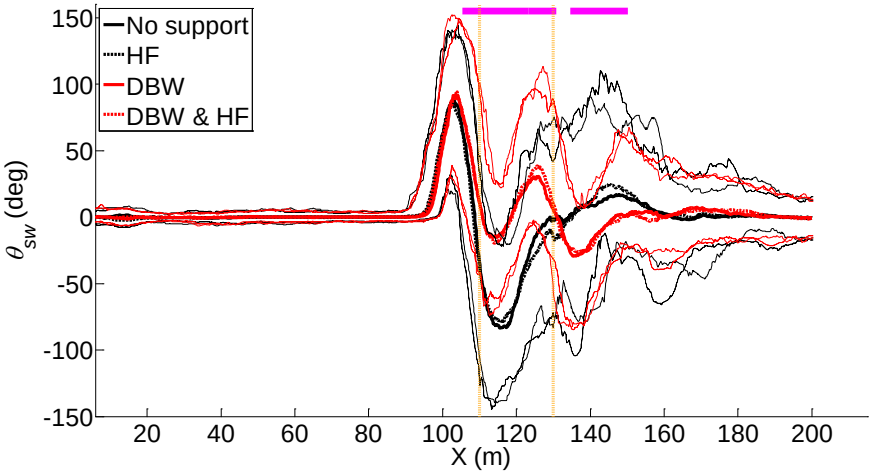

Fig. 4.6. Steering-wheel angle θ_{sw}: medians (thick lines), and 5th and 95th (thin lines) percentiles of the for the four setups (positive = to the left). The vertical lines (X = 110 m and X = 130 m) mark the first and last pylon that had to be avoided. Bars are visible on top when HF vs. DBW & HF (magenta) and DBW vs. DBW & HF (red) are statistically significant.

Fig. 4.6 shows medians, and 5th and 95th percentiles of the steering-wheel angle θ_{sw} for the four setups. The results confirm that HF had no noteworthy influence, whereas the DBW and DBW & HF setups had a big influence. We assumed that greater stiffness value K_c in (4.8), determining the magnitude of guiding torque, would exhibit different results.

Table 4.2. Run percentages with road departures and pylon hits (first calculated per participant and then averaged over all 30 participants). A run was considered a road departure when the Y coordinate of vehicle centre-of-gravity (CG) exceeded 2.22 m (Y > 2.22 m; the track width of the vehicle was set to 1.56 m and the road boundary was 3 m). A run was considered a 'pylon hit' when the CG cross-sectioned a pylon array.

	Road departure runs (%)	**Pylon hit runs (%)**
No support	52.9	29.5
HF	57.5	20.3
DBW	0.95	43.3
DBW & HF	0.48	44.4

When a mechanical connection is assumed in the steering system (no support and HF setups), the participants adopted a classical double pulse to avoid the obstacle. With the DBW and DBW & HF setups, drivers steered less to the right, between 110 < X < 120, while appearing to make a second steering pulse to the left (around X = 125 m) to avoid hitting the pylons positioned at Y = 1 m. This was related to the fact that the RDP system would steer the front wheels to prevent road departure faster than the drivers, minimizing the need for right steering (starting around X = 100 m). Apparently most drivers did not perceive this and their high magnitude steering overshot the system, driving the

cars toward the pylons (at Y = 1 m) necessitating the observed on-coming counter steering input at around X = 125 m. The run percentages with road departures and pylon hits are given in Table 4.2.

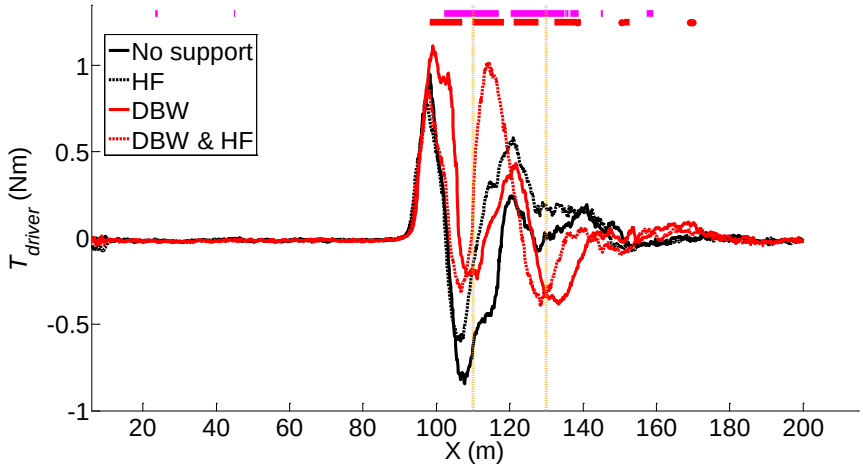

Fig. 4.7. Drivers' torque T_{driver}: medians for the four setups (positive = to the left). Vertical lines (X = 110 m and X = 130 m) mark the first and last pylon that had to be avoided. Bars are visible on top when HF vs. DBW & HF (magenta) and DBW vs. DBW & HF (red) are statistically significant.

Fig. 4.7 shows the medians of drivers' torque T_{driver} for all four setups. HF influenced the measured torques. The second steering pulse can be seen again for DBW (around 125 m for DBW only; and around 115 m for DBW combined with HF).

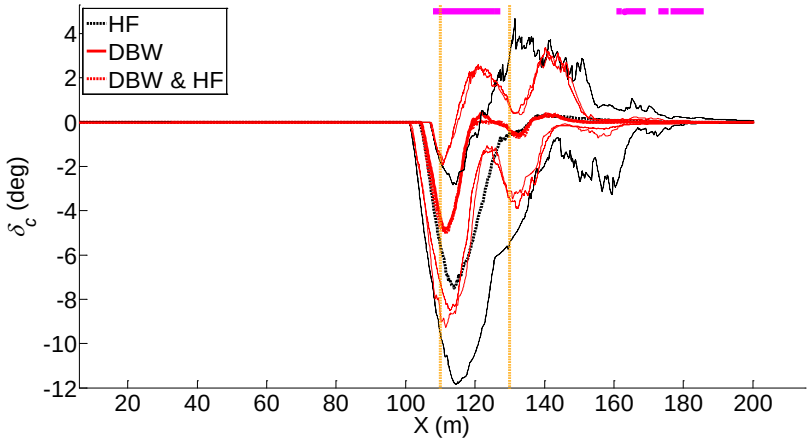

Fig. 4.8. Correcting angle δ_c: medians (thick lines), and 5th and 95th (thin lines) percentiles. Vertical lines (X = 110 m and X = 130 m) mark the first and last pylon that had to be avoided. Bars are visible on top when HF vs. DBW & HF (magenta) and DBW vs. DBW & HF (red) are statistically significant.

Fig. 4.8 displays the medians, and 5th and 95th percentiles of the correcting angle δ_c for the supported setups. The magnitude of the δ_c angle, as well as its variability from the median for the HF setup, is considerably higher compared to the drive-by-wire setups. The median path of the HF setup (Fig. 4.5) was closer or beyond the road limits, compared to the drive-by-wire setups, which in turn results in a greater input signal y_{in} (4.4) to the G_c controller; this is translated into a greater correcting angle. The same explanation holds for Fig. 4.9, which displays the medians and 5th and 95th percentiles of the future lateral offset y_{la} for the four setups.

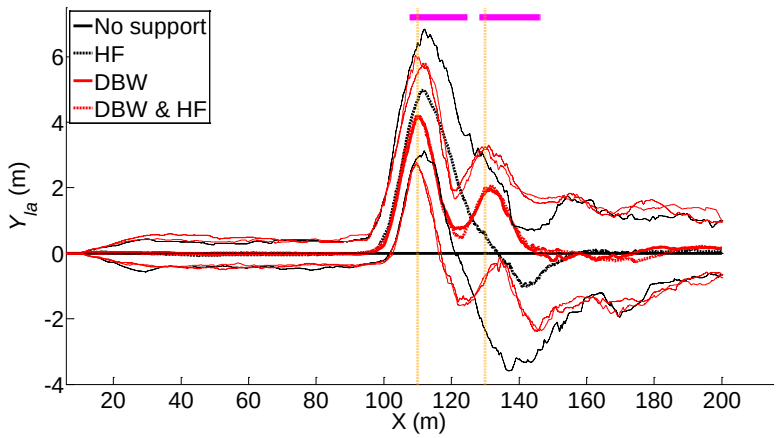

Fig. 4.9. Future lateral offset y_{la}: medians (thick lines), and 5th and 95th (thin lines) percentiles for the setups of all driven manoeuvres. The vertical lines (X = 110 m and X = 130 m) mark the first and last pylon that had to be avoided. Bars are visible on top when HF vs. DBW & HF (magenta) and DBW vs. DBW & HF (red) are statistically significant.

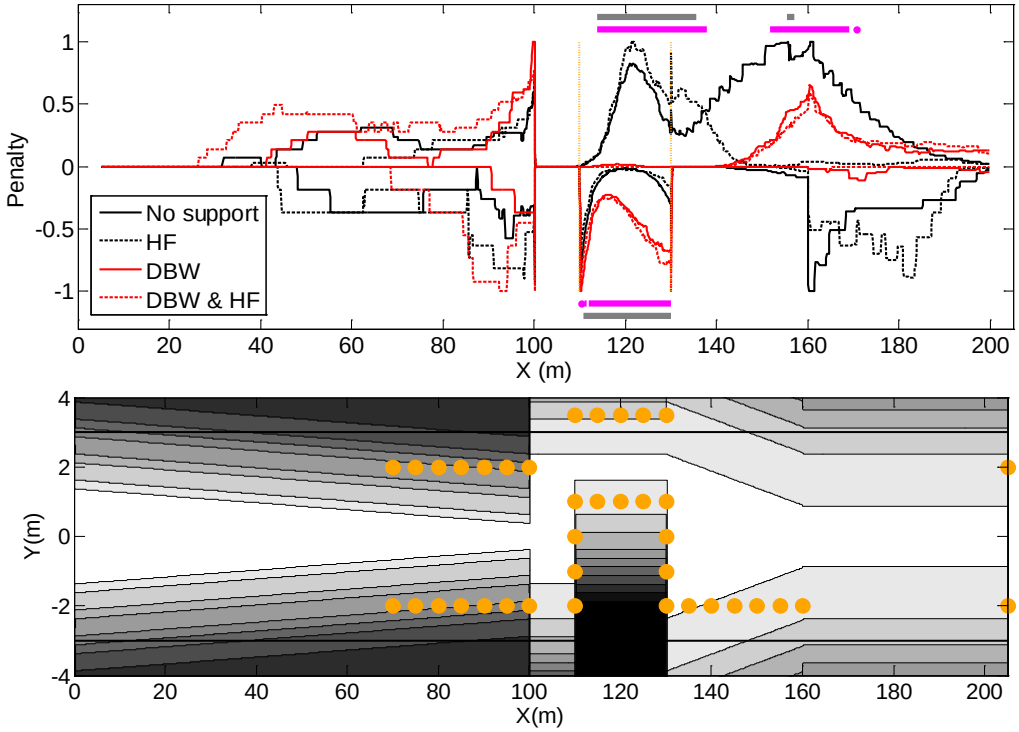

Fig. 4.10. Average penalty for the four setups for all driven manoeuvres (top). Penalty map as a function of X and Y coordinates; yellow dots represent the pylons (bottom). The darker the shade, the greater the absolute penalty value (increasing linearly per filled area; white area denotes zero penalty; map takes into account the 1.56 m track width of the vehicle). Positive values are shown above, and negative values below the white area on the map. The top subplot presents point-wise averages of positive points (vice versa for the negative). Averages were normalized (in the 0 – 1 scale) per task section: 0 – 100 m, 100 – 110 m, 110 – 130 m, 130 – 160 m, 160 – 205 m. The positive-negative scheme distinguishes the task deviation with respect to the white area in the map; e.g. in section 110 – 130 m, it shows that DBW and DBW & HF induced drivers to accumulate penalty from the pylon side (negative points), whilst in the no-support and HF setups, drivers accumulated penalty primarily by road departure (positive points). Bars are visible on top when HF vs. DBW & HF (magenta) and no support vs. DBW (grey) are statistically significant.

In the absence of an ideal driving trajectory, we employed penalty-based analysis to evaluate the impact of a setup on the driving task. An individual run accumulated penalty according to how much it

deviated from the given task. The penalty map in Fig. 4.10 (bottom) shows the penalty values (represented in shades of grey) as a function of the X and Y coordinates. The darker the shade, the greater the absolute penalty value (increasing linearly per shade area; white area denotes zero penalty). To distinguish between deviation events (road departure vs. pylon hit), the area to the (driver's) left of the ideal trajectory gets positive penalty values while the area to the (driver's) right gets negative values. The driving task was divided into five task sections: 0 – 100 m, 100 – 110 m, 110 – 130 m, 130 – 160 m, 160 – 205 m.

The top subplot of Fig. 4.10 shows the average penalty for the four setups for all driven manoeuvres determined through the penalty map (bottom). These averages were normalized (in the 0 – 1 scale) per task section. The important part of this figure lies in the task section X = 110 – 130 m. The no-support and HF setups mainly accumulated penalty through road departure (positive points), while the DBW and DBW & HF setups accumulated penalty primarily by hitting the pylons on the right (negative points). Both 110 – 130 m and 130 – 160 m task sections contain statistically significant results; HF vs. DBW & HF (magenta) and no support vs. DBW (grey). The remark made earlier for Fig. 4.5, that participants driving with drive by wire were slower to get back to lane centre for X > 140 m (thus accumulating penalty), can also be seen in Fig. 4.10. For X > 140 m, although the no-support and HF setups (mechanical connection assumed) have more penalties, this is because fewer runs deviated from the instructed task. This is also supported by the discrete steps of the penalty and not the homogenous lines for the drive-by-wire setups.

B. Subjective evaluation

Table 4.3 shows the results of the NASA TLX for measuring workload, revealing only small differences. The DBW and DBW & HF setups resulted in less temporal demand (p = .004) and less effort than no support did (p = .003). Perceived performance did not differ much between setups while objective performance indicated that the drive-by-wire setups reduced the number of road departures but increased the occurrence of crashes with the pylons at Y = 1 m for the DBW setups (DBW and DBW & HF).

Table 4.3. Means (standard deviations between parentheses) of the NASA Task Load Index on the top half of the table. The TLX ranges from 1 (very low/perfect) to 21 (very high/failure).

	Mental demand	**Physical demand**	**Temporal demand**	**Perfor mance**	**Effort**	**Frustration**
No support	12.0 (3.8)	8.5 (3.9)	11.9 (5.2)	10.9 (3.2)	12.7 (3.2)	8.4 (5.1)
HF	11.7 (3.6)	9.2 (3.4)	10.4 (4.6)	10.3 (4.1)	11.3 (3.0)	7.9 (4.3)
DBW	10.7 (4.2)	8.1 (3.4)	9.5 (4.6)	9.8 (4.7)	10.5 (3.7)	7.3 (4.5)
HF& DBW	11.7 (4.1)	8.8 (2.9)	10.8 (4.4)	9.3 (4.5)	11.9 (4.3)	8.0 (4.2)

IV. Discussion

We developed and tested a road-departure prevention system in an emergency scenario. Thirty participants were instructed to avoid a pylon-confined area (obstacle) while keeping the vehicle inside the road limits. The RDP system intervened when a road-departure was likely to occur by applying a low level of automation in the form of advisory haptic-feedback (HF) torque, and/or a high level of automation by correcting the front-wheels angle (DBW and DBW & HF).

HF had a profound influence on the measured steering torque, but no significant influence on steering-wheel angle or vehicle path. Apparently, in an emergency situation, drivers steer in an "open-

loop" fashion without much regard for additional feedback torques that are applied on the steering-wheel. That is, drivers used the best of their abilities to avoid an obstacle in an emergency, showing little inclination to give way to advisory steering-wheel torques. Note that the applied torques may have been too small to be able to override or guide the drivers' intentions and a higher haptic-stiffness (c.f. eq. (4.8)) could be needed to effectively prevent road-departure in this evasive maneuver. However, higher magnitude haptic-feedback torques in preliminary tests were perceived as authoritarian and were therefore discarded to promote driving comfort and safety.

The DBW setups helped drivers to keep a safe distance from the detected roadside (Fig. 4.5) and reduced mental workload. However, the DBW, which influenced the relationship between steering-wheel angle and front-wheels steering angle, resulted in drivers making an additional steering correction to avoid hitting the inner pylons. Drivers did not fully understand the functionality of the RDP system (although the operating principle of each setup was explained to the drivers before testing). Stimulus-response compatibility was lost with the DBW systems, that is, steering response stopped being unambiguously related to steering-wheel angle, an approach which may confuse the driver and disrupt his/her internal model of the vehicle.

This study is the first to address a high level of automation in the form of a drive-by-wire (DBW) concept for road-departure-prevention (RDP). This study provided clear results about the potentials and pitfalls of DBW and haptic-feedback, and the combination of both. We conclude that a drive-by-wire setup can prevent road-departure, reduce mental workload, and has the potential to promote safety. If drive-by-wire RDP controllers are adopted in real vehicles, they should be designed to avoid or compensate for the driver's counter-reactions. Careful design and rigorous testing should be the minimum precaution before drive-by-wire RDP controllers hit the road

V. Acknowledgment

The author is grateful to the test participants.

Chapter 5A. Race Car Instrumentation for Driving Behaviour Studies

"Have you ever noticed that anybody driving slower than you is an idiot, and anyone going faster than you is a maniac?"
George Carlin, 1956-2008 A.D.

Race Car Instrumentation for Driving Behaviour Studies

Abstract—Part A of Chapter 5 supplies a roadmap on how a researcher can effectively perform real vehicular experiments oriented to high speed driving research. It provides detailed guidelines for constructing versatile low-cost instrumentation suitable to be fitted on race cars. The custom built equipment, consisting of wheel speed sensors, steering angle-torque sensor, electronic boards etc. is thoroughly described. Furthermore, Part A depicts the required processing from raw measurements to user-friendly data suitable for driver behaviour studies. As an illustration, a case study on driving behaviour analysis is presented, during the execution of high speed circular manoeuvres. The recorded data showed markedly different driving behaviours between expert and novice drivers. The mechanical designs and the open-source based software are freely available on-line.

I. Introduction

Driver-car interaction studies were initiated in the 1960's [55]. The goal has always been the system's optimization for streamlining the driving experience. However, optimizing a vehicle with a real human in the loop is challenging due to the variation in the behaviour of different drivers. Consistency for the automotive refinement process is commonly sought by careful design of the test procedures [120][104], but is not always achieved [95]. Vehicular development can be aided with vehicle modelling and driver behaviour modelling at computer simulation level [150]. Early driver models were simple with error-compensating behaviour [55] but their complexity and potentials have considerably increased over time [16][23][145]. Models describing extreme steering behaviour incorporating variable preview times have already been proposed [24]. Experiments have shown how to measure the neuromuscular system (NMS) response to force-feedback [50]. NMS driver models have recently been proposed for objective assessment of the lateral stability induced by the car's steering system configuration [31]. The vast majority of the existing driver models have been developed by human-in-the-loop (HIL) testing in driving simulators. Although simulators can be fairly realistic [32][93], the development of a NMS driver model reacting to fully realistic vestibular stimuli would require real vehicle in-field HIL tests.

Vehicular instrumentation for testing and data processing dates back to the 1960's [80]. Nowadays, the wide introduction of Advanced Driver Assistance Systems (ADAS) like the Vehicle Stability Control (VSC) has propelled the off-the-factory vehicular sensory instrumentation to an intriguing level. Interfacing the fused data from the vehicle directly poses a severe challenge due to proprietary restrictions. The former leads automotive researchers to use externally attached test equipment which are mainly off-the-shelf commercial products [102][150], with a considerably high price tag. Low-cost open source solutions for scaled vehicle instrumentation exist [44] but limited information on full scale vehicle instrumentation is available in the literature.

This multidisciplinary study aims to provide information on how to instrument real race cars with a limited budget, and to enable data-acquisition required for studying driving behaviour. It condenses issues related to the building of electro-mechanical equipment, where all the developed solutions, mechanical-electronic designs and software are made freely available online in [33]. Raw measurement processing and data interpretation is presented and the Simple-Driver-Model (SDM) is introduced to

analyse driver behaviour. A case study in circular manoeuvring is presented comparing an expert and a novice driver. The novel SDM-based driving analysis is used to identify distinct driving behaviour characteristics of drivers with varying skill levels. By introducing the polar angle representation of kinematic data into deviations from the desired trajectory, control patterns unnoticeable in the time plots, are exposed.

The rest of this study is organized as follows: Section II discusses driver modelling and the necessary signals for driver model development. Section III focuses on the vehicle's instrumentation with Section IV dedicated to data logging. Section V discusses the required data-post-processing, whereas the yaw and lateral error calculation process for the preview driver model is described in section VI. High speed circular test drives are analysed and compared for a novice and an expert driver in Section VII. Finally, a Discussion Section numbers potential applications and concludes this study.

II. Driver modelling

A. Applications of driver models

A driver model is expected to deliver the longitudinal (throttle-brake) and/or lateral control (steering) inputs for performing a specified driving task. Driver models have a wide range of applications. They are commonly used for entertainment in game driving simulators. Game driver models, incorporate knowledge of the track's racing line [24] and the underlying internal vehicle dynamics, making them rather competitive opponents. Additionally, as mentioned in the introduction, they can effectively serve as experimental tool for developing human-centred ADAS, for: automotive steering systems [31], VSC and adaptive cruise control systems [77]. Motivated by the needs of automotive industry, driver models have also been used as low cost alternatives to track testing [146].

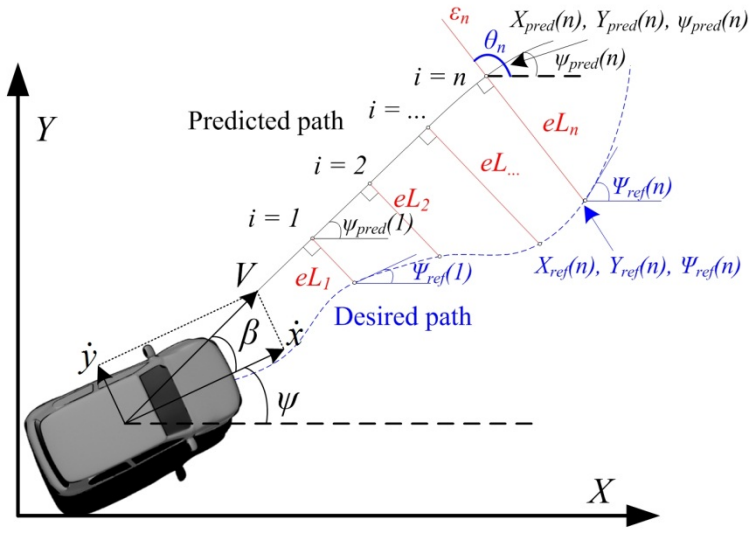

Fig. 5A 1. Schematic representation of a preview controller.

B. Driver models for lateral control

A common approach to modelling the lateral control of drivers is the preview model; it calculates the steering action based on the lateral [23] and/or the yaw [145] error between the desired path and a predicted path (eL_i and $e\psi_i = \psi_{pred}(i) - \Psi_{ref}(i)$ respectively in Fig. 5A 1). In Fig. 5A 1, ψ represents the vehicle's yaw angle with respect to the global coordinate system (X, Y) and β, the vehicle's slip angle defined as the angle between the vehicle's longitudinal axis and velocity vector V at the centre-of-gravity (CG). MacAdam [23] utilizes optimal control theory for estimating the desired steering angle

based on the weighted sum of the future lateral errors, incorporating also a visuomotor processing delay τ in error perception and correction. The "Predicted path" is estimated using a simplified internal vehicle dynamics model (as in references [16][24][31]).

Sharp's *et al*. [145] model uses a linear weighted sum of the future lateral errors and the current yaw error to derive the steering angle. The future vehicle's position in n time steps (predicted path) is estimated using the velocity V (Fig. 5A 1) and a preview time vector T_p, representing the driver's look-ahead distance [145] (i = 1, represents the current state of the vehicle). The predicted path in Sharp's implementation is estimated by assuming that V is constant (magnitude and orientation), that is, a straight line parallel to V originating from the vehicle's CG. MacAdam's original model has been greatly enhanced over time [16][24] for improved path tracking performance with increasing complexity. However, since the purpose of this document is to provide a framework on vehicular instrumentation for driver behaviour analysis, it is in favour of simplicity in modelling. A combination of MacAdam's [23] and Sharp's *et al*. [145] models with minor extensions will be used in the rest of the document. This model will serve as the foundation for the vehicle's instrumentation and the driver model-based case study between an expert and a novice driver, presented in Section VII.

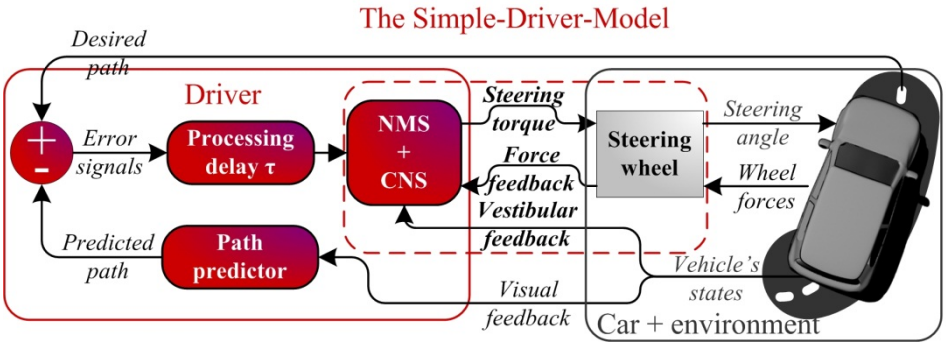

Fig. 5A 2. The Simple-Driver-Model structure.

C. The simple driver model

The Simple-Driver-Model (SDM) is depicted in Fig. 5A 2. It consists of the 'Driver' and the 'Car + Environment' blocks. The *Predicted_path* signal is generated from the vehicle's states from an internal vehicle dynamics model. The *Desired_path* represents the task the driver is performing (e.g. lane keeping). The *Path_error* defined in (5.1.1) is the weighted sum of the lateral eL_i and yaw $e\psi_i$ error signals, multiplied by the wL_i and $w\psi_i$ gains respectively. The *Path_error* pass through the brain processing delay τ to the driver's NMS and the Central-Nervous-System (CNS). This generates a *Steering_torque* which through the Steering wheel dynamics results to a *Steering_angle*.

$$Path\_error = \sum_{i=1}^{n} eL_i \cdot wL_i + \sum_{i=1}^{n} e\psi_i \cdot w\psi_i, \quad i = 1:n \tag{5.1.1}$$

The signals inside the dashed box in Fig. 5A 2 (in boldface letters) are the necessary ones for developing a driver model with NMS + CNS characteristics [31]. It has to be clarified that the SDM is not the end goal of this study. It intuitively depicts the fundamental information for the development of more advanced driver model structures [31]. The preview gains wL_i, $w\psi_i$ and the processing delay τ can be estimated through mathematical optimization from driver-in-the-loop test data [146][15]; the identification of the SDM parameters is not discussed further in this work. The accurate description of the end-goal NMS driver model can be found in [31].

The necessary vehicular instrumentation and processing to acquire the total signals for the SDM is described within the following Sections.

III. Vehicle instrumentation

A. Steering angle and torque measurement

The steering angle and steering torque signals are measured combining two separate assemblies: a) one mounted on the dashboard and b) one serving as an ‘extension hub’ mounted between the steering wheel hub and the steering wheel. The complete assembly is illustrated in Fig. 5A 3.

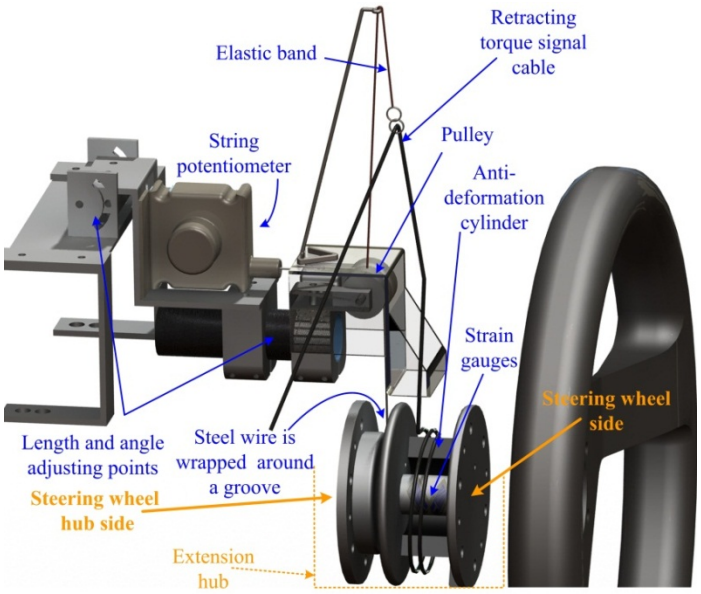

Fig. 5A 3. Steering wheel assembly for steering angle and torque measurement attached on the dashboard with clamps. The ‘extension hub’ is fitted with strain gauges and has a groove for the cable of the string potentiometer.

The dashboard assembly is attached with clamps on the dashboard. It holds a) a ‘string potentiometer’ [149] for measuring the steering angle and b) the ‘retracting torque signal cable’. Both the steel cable of the string potentiometer and the torque signal cable wire are being wrapped around the steering wheel ‘extension hub’ while it rotates. The torque and shear-strain at the hub is measured though a Wheatstone bridge formed with 2 Vishay two-element 90° rosette strain gauges, glued symmetrically around the shaft. The Wheatstone bridge offers temperature compensation and linearity between strain and voltage measurements [14]. Accessories from M-line line of Vishay have been used for the installation of the strain gauges (M-200, CSM1 degreaser, M-Prep Conditioner A and M-Prep Neutralizer 5A). Intuitive installation manuals are available online [164]. When the shaft is strained, the resistive changes of the bonded gauges unbalance the bridge resulting to a few mVs voltage deviation.

One hollow ‘anti-deformation cylinder’ (divided into 2 half-cylinders) has been precisely machined from polyoxymethylene (Derlin) thermoplastic (for its high stiffness and low friction properties) to fit around the strain-gauge instrumented ‘extension hub’ (torsion bar). The former protects the strain gauges and rejects deformations that are not caused by the steering torque. Axial induced forces on the steering wheel (e.g. the driver pushing the top) are supported by the half-cylinders and don’t cause any deformation on the torsion bar. One side of the cylinder is bolted to the ‘steering wheel side’ wall of the ‘extension hub’ while the other side slips freely at the opposing wall.

B. Wheels’ angular velocity

An experienced driver can control the wheel slip by throttle/brake in order to expand his control envelope. Therefore, individual wheel speed can be considered as an important driving cue. Four wheel

speed sensors are constructed to be externally fitted on the vehicle. The wheel speed sensors are illustrated in Fig. 5A 4. The ‘supporting plate’ is bolted on the ‘wheel nuts’ which are correspondingly bolted on the wheel studs supporting the wheels. The ‘supporting plate’ (perforated with the wheel’s stud pattern) transfers the rotational motion of the wheel through the ‘connecting shaft’. The shaft is based on two SKF 15 mm x 35 mm ‘ball bearings’ and is connected with a 05.2400.1122.0100 KÜBLER incremental optical encoder (100 pulses per rev.) through a 047102424 HUCO flexible coupling.

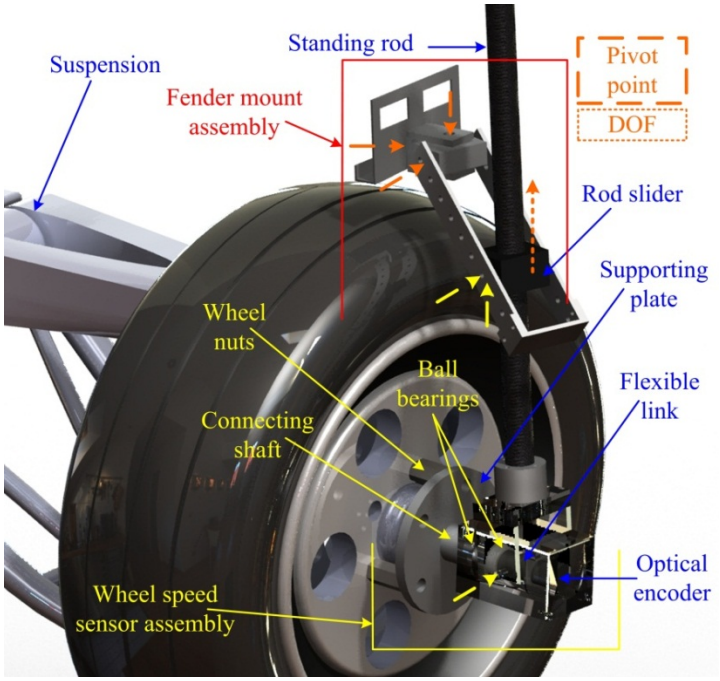

Fig. 5A 4. Externally fitted wheel speed sensor.

A ‘standing rod’ can slide frictionless within the ‘rod slider’ block while preventing the ‘wheel sensor speed assembly’ to rotate with the wheel rotation. The ‘fender mount assembly’ supports the ‘standing rod’ through the ‘rod slider’ and is designed with the suitable ‘pivot points’ so as to allow any ‘suspension’ movement without inducing any strain to the fender. The left and right ‘fender mount assembly’ are held attached on the fender with ratchet straps. All displayed parts of Fig. 5A 4 are machined out of aluminium, despite the ‘rod slider’ and the ‘standing rod’ which are from Derlin and carbon-fibre correspondingly.

C. Vehicle’s position and slip angle

The GPS standard signals, plus the true heading, the lateral velocity and the slip angle β (Fig. 5A 1) are measured with a commercial VBOX IISX data-logger from Racelogic [148]. The VBOX is using a twin antenna GPS engine offering 2 individual velocity vectors, estimated through the Doppler shift of the GPS carrier wave (accuracy of 0.27 m/s). Using the 2 velocity vectors, the VBOX can estimate the slip angle with less than 0.5° RMS error with 0.5 m antenna separation. The VBOX has ~3 m absolute position accuracy and stores the data in a SD memory card with 20 Hz frequency. It is also equipped with a CAN-bus interface 2.0A and 2.0B and has additionally, 2 digital and 2 analog outputs and a serial RS232 interface.

D. Vehicle's inertial states

A low cost Inertia Measurement Unit (IMU) with 5 degrees-of-freedom (DOF) IDG500/ADXL335 is placed near the estimated location of the vehicle's CG. This IMU combo board incorporates the IDG500 dual-axis gyroscope from Invensense and a small, low power, 3-axis ± 3 g ADXL335 accelerometer from Analog Devices. The IMU is positioned so that it can measure the vehicle's yaw and pitch rate, the angular rate around z-axis and y-axis correspondingly. Two additional breakout boards with the 2-axis ADXL322 ± 2 g accelerometer from Analog Devices are placed at the front and rear axles of the vehicle to measure the longitudinal and lateral acceleration. The practical breakout boards were employed from an OEM company [156] embedded in ergonomic break-out boards.

The ADXL335, ADXL322 and IDG500 have analog interfaces and incorporate low-pass filtering provisions for anti-aliasing through a simple capacitor. Although the performance of the accelerometers is exemplary, a higher specifications gyroscope (e.g. ADXRS300, [44]) would have provided higher accuracy measurements.

E. Brake and throttle position

Two brake pressure sensors manufactured by Bosch are placed in the foot pedal and handbrake actuated hydraulic brake circuits as illustrated in Fig. 5A 5. The race specs of the test vehicles' allowed for the sensors to be connected directly to the hydraulic lines leading to the front and rear brakes correspondingly. The driver's depression of the 'brake pedal' results in pressure build up in both 'front brake line' and 'rear brake line' measured by both the corresponding pressure sensors. This setup enables both, reading of the final pressure exerted at the callipers and also the brake bias between the front and rear brake system.

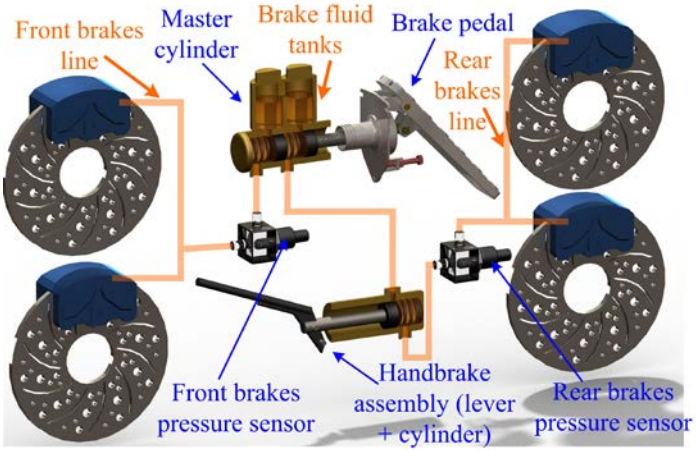

Fig. 5A 5. Brake pressure measurement setup. Two pressure sensors measure the brake pressure on individual front and rear hydraulic lines.

The 'handbrake assembly' is in series with the 'master cylinder' of the vehicle. A handbrake action results in brake pressure solely on the rear brake system. The brake sensors were purchased from an OEM company [149] and are specifically designed for measuring the high pressures in automotive braking systems. They have an analog interface and they are extremely robust and resistant to brake fluids, mineral oils, water and air and offer 250 bar of pressure range measurement with less than 5% error in the range of 35-250 bar.

The throttle position is measured through a simple potentiometer actuated from the Bowden cable going to the intake manifold.

F. Electronics

The sensory inputs are analog or digital TTL signals (wheel speed sensors), whereas the VBOX has its own data storage. An electronics board is constructed for powering the sensors and for conditioning signals before sampling. The power of the system is a 12V 2Ah lead acid battery. The battery voltage is initially regulated to 12 V with an LM7812 voltage regulator; its output is used to power an LM7805 and an LM731 to obtain the required levels for the sensors (5 and 3.3 V). To avoid aliasing, the outputs of all analog sensors are low-pass filtered; individual output of the brake sensors, throttle position and steering angle potentiometer is initially fed to a voltage buffer [32] and then fed to a 1^{st} order low pass passive RC filter (R = 20 kΩ, C = 2 uF) with 39 Hz bandwidth (to satisfy the Nyquist criterion; sampling rate is 100 Hz). The voltage-buffer is built with an LM741 op-amp and powered with an MEA1D1212SC Dc-Dc converter (-12 V and 12 V) from Murata Power Solutions. The "ideal" infinite and zero output resistances of the voltage buffer, prevents the RC filter to interfere with the operation of the above sensors.

Individual output of the accelerometers, is fed to a 2^{nd} order passive filter, two RC filters (R = 20 kΩ, C = 2 uF) in series (resulting to 25 Hz bandwidth). The outputs of the gyro are 1^{st} order low-pass filtered (no voltage-buffer is required for the inertial sensors). The accelerometers are expected to have power at high frequencies justifying the lower bandwidth and the 2^{nd} order filtering selection. The same circuitry as in [32] has been used for the amplification of the strain-gauges forming the torque sensor. All op-amps for the signal conditioning are LM741 and are all powered with the aforementioned Murata Dc-Dc converter (each Dc-Dc converter powered up to 4 op-amps, so as to lay within the nominal power specs).

The ExpressPCB, a free printed-circuit-board (PCB) software was used for designing the boards [72]. Through the software itself, the user can order the designed PCBs on-line for a fair price and with a fast turnaround time, a rather convenient feature for low-cost prototype applications.

The custom built-fitted sensor specifications are summarized in Table 5A 2 (Appendix).

IV. Data logging

The data logging is performed on a Toshiba NB200, a compact notebook with long battery-life. All the forthcoming peripherals related to data-logging are attached to it and in-house developed software, based exclusively on open-source software, handled the logging and synchronization process.

A. Computer peripherals related to data collection

A National Instruments (NI) USB-6211 USB M Series multifunction data-acquisition (DAQ) has been used for capturing the analog signals of the sensors. This USB bus-powered DAQ is connected to the notebook offering; 16 analog inputs and 2 outputs with ± 10 V range, 250 kS/s sampling rate for all combined channels together, 2 analog outputs, 4 digital inputs and 2 digital counter/timers. The USB-6211 is interfaced with the free NI-DAQmx C data acquisition driver [128]. The NI-DAQmx C is a versatile nicely documented C language application-interface (API) for controlling the NI DAQs. The choice of interfacing the NI DAQ with a C API, besides the lower cost offers flexibility and allows for software distribution.

A development board (AVR-P40-USB-8535) from Olimex Ltd. equipped with an 8-bit AVR ATMega32 microcontroller is used for interfacing with the optical encoders of the wheel speed sensors. The board was purchased from an OEM company [156] with embedded all the peripherals for operating the AVR (crystal, power supply filters etc.) and with an additional serial-to-USB interface through an FT232 converter from FTDI Ltd. The high-low transitions of the 4 optical encoders are measured by polling the 4 IO ports of the AVR. Although less computational expensive solutions from

polling exist [44], the small work-load of the AVR does not necessitate their use. The processed wheel speeds are sent in ASCII format from the serial port of the microcontroller to the FT232 chip and are received by the notebook on a USB port. The corresponding FT232 driver is installed in the notebook for emulating a USB port as a serial com port.

Two webcams, a Microsoft VX-3000 1.3Mp and a Logitech C500 1.3Mp, are used to capture visual data related to driving behaviour (e.g. one or two hands on the steering wheel, driver's distraction etc.).

Rides in race cars can cause the hard drive to stall. Therefore the captured data from the above peripherals are stored on high speed Transcend JetFlash® R110 8GB (TS8GJF110) USB flash memory drive. The R110 offers a write speed of 25 MB/s. A USB hub is used to accommodate the 5 in total USB connections to the notebook. The complete architecture of the system is illustrated in Fig. 5A 6.

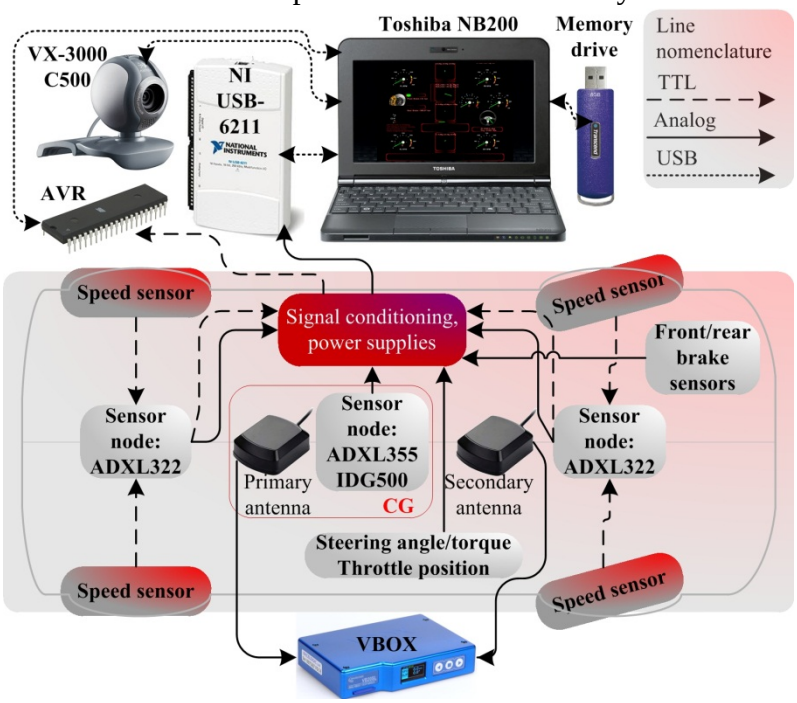

Fig. 5A 6. Race car sensory instrumentation architecture.

B. Software

Throughout the implementation free software development tools and libraries have been used for both the data logging software in the notebook [128][130] and the firmware on the AVR [171][18]. The code has been developed in C/C++. The automotive-data-logging (ADL) software in the notebook is responsible for communicating with the AVR and the NI-DAQ, capturing visual data from the webcams, synchronizing all the data together and storing them in the USB memory drive. The ADL utilizes the Open-Computer-Vision-Library (OpenCV) [130] for the image acquisition-processing from the 2 webcams and for the creation of the graphical-user-interface (GUI) (c.f. Fig. 5A 7). OpenCV is an open source computer vision library in C/C++, independent from the operating system and hardware, is optimized and is suitable for real time applications.

The GUI displays live info from all the captured sensory data (steering angle/torque, individual wheel speed, brake pressure etc.) using intuitive gauges (Fig. 5A 7) and the captured video stream from the 2 webcams. Through the GUI the user can manipulate the acquired data (adjusting offsets), assign log location and start/stop/resume the logging. The sensory data are stored in a tab delimited text file, where the captured images are stored in JPG format named as the corresponding log sample number (for image-data overlay).

The ADL is built to run on a standard Microsoft® Windows® XP operating system. All unnecessary modules of the operating system are disabled for the insusceptible operation of the ADL, developed to operate in a "real-time" approach. All the operations are performed in an infinite loop, whereas time-critical tasks are executed by interrupt-service-routines (ISRs). When an interrupt is triggered, the program immediately jumps to the corresponding ISR. The flow diagram of the ADL software is illustrated in Fig. 5A 8.

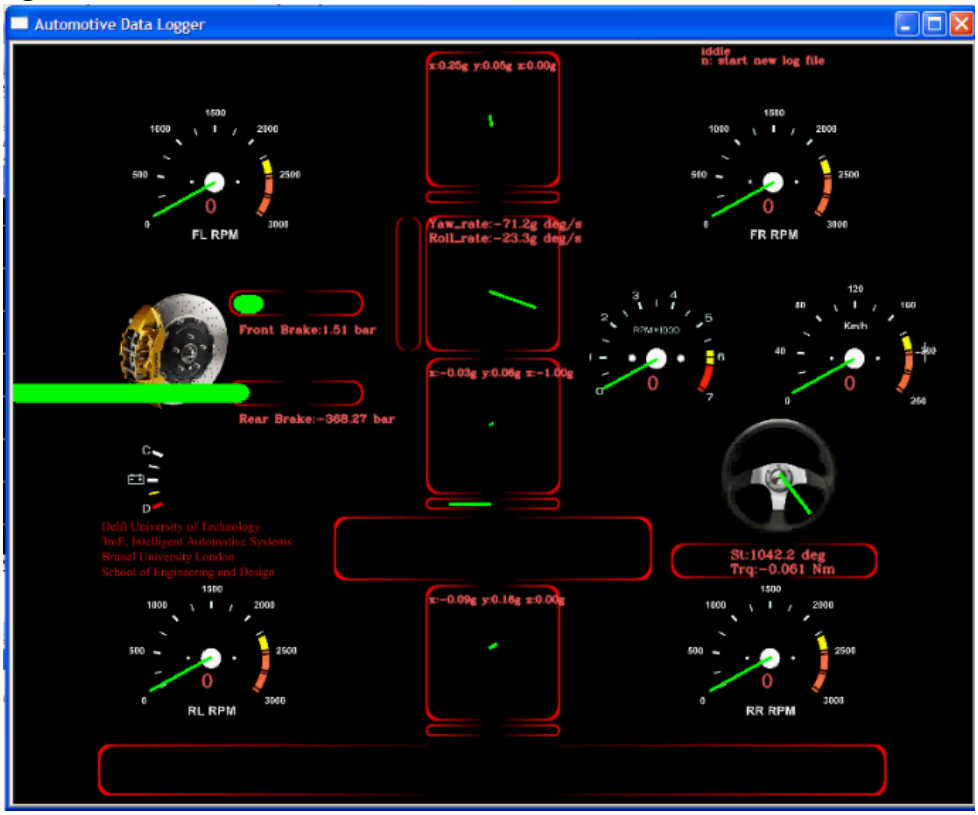

Fig. 5A 7. Automotive data logger (ADL) graphical user interface (GUI).

This NI-DAQ is initialized to perform analog-to-digital-conversion (ADC) with a sampling rate of 100 Hz (Fig. 5A 8). The time between two consecutive analog sensory data packets from the NI-DAQ buffer is always 10 ms (hardware controlled). The wheel speeds are updated at 20 Hz. The latest wheel speed values in the program, constitutes the *latest sensory data* (digital). Whenever an ADC is completed, an interrupt (NI-ISR) is issued from the NI-DAQ and the *latest sensory data* (analog + digital) (Fig. 5A 8) are appended to the log file. The interrupt-driven concept secures the task execution within prescribed time constraints and data synchronization, ensuring 100 Hz sampling rate.

C. Instrumentation development considerations

Developing instead of acquiring off-the-shelf instrumentation equipment is a trade-off between cost-developing time, flexibility (expandability and user-friendliness) and measurement quality.

The cost of the most economical off-the-shelf external wheel speed sensor surpassed the machining and angular encoder cost for four custom sensors. A commercial steering torque sensor would require brackets to be attached to the wheel hubs. A mounting construction would have also been necessary for the string potentiometer. Taking into consideration the aforementioned facts the decision to custom-develop the steering angle-torque assembly and the wheel speed sensors was sensible. The cost of an IMU from an automotive instrumentation firm [149] is more than ten times higher compared to one

from a retail sensor supplier [156]. In total the total cost for all the equipment of Section II, parts machining, sensors, electronic boards, netbook, NI-DAQ etc. excluding the VBOX was approximately 3500 £ (July 2009). In terms of flexibility, the electro-mechanical parts of the system can be connected to a commercial automotive data-logger. The same stands for the ADL software, which can be easily adapted to display and log the data from any commercial data logger with an accessible computer interface (USB or RS-232). Designing the mechanical components and PCBs, soldering the parts-sensors on the PCBs and housing them in cases, required approximately 40 workdays. Developing the data logging software for the ADL and the AVR required about 20 workdays. The quality of measurements is imposed by the sensory set used, the signal conditioning and the data logger itself. Selecting the correct components (as was performed) can ensure accurate measurements.

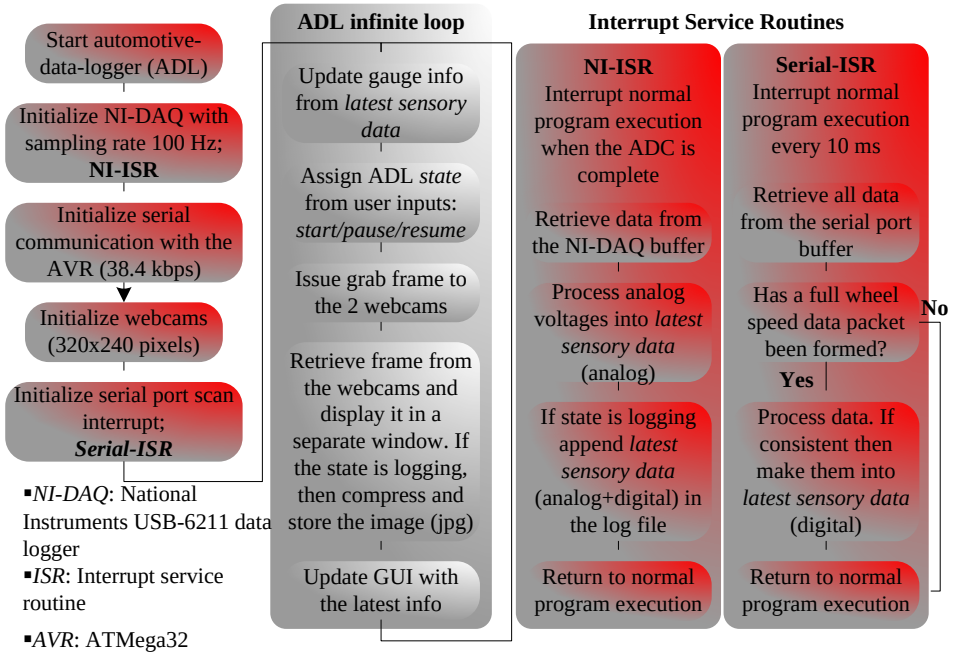

Fig. 5A 8. Automotive-data-logger (ADL) software flow diagram.

The complete instrumentation can be easily ported to different vehicles, in less than 1 workday, with the brake pressure sensors fit being the most vehicle intrusive and time consuming part of the process.

V. Data post-processing

The VBOX signals and the sensory data from the ADL originate from 2 different logging sources and have to be synchronized in time. The lateral acceleration (acc_y) from the VBOX and IMU at the vehicle's CG are used for the synchronization. Assume that the acc_y from the IMU is represented with a vector A as in (5.1.2) with the elements reversed ($A(1)$ contains the last sample and $A(\text{end})$ the first). The VBOX acc_y is represented with a vector B as in (5.1.3).

$$A \in R^M := IMU\_acc_y\_reverse(m/s^2) \tag{5.1.2}$$

$$B \in R^N := VBOX\_acc_y(m/s^2) \tag{5.1.3}$$

Initially the VBOX data is linearly interpolated to 100 Hz, so as both A and B contain 0.01 s time spaced data samples. The data synchronization is performed by applying the steps (5.1.4)-(5.1.13).

$$\Gamma(n)_{n=1:N+M+1} = \sum_{k} A(k) \cdot B(n+1-k)$$
$$k = max(1, n+1-N) : \min(n, M) \quad (5.1.4)$$

$$[max\_value, max\_position] = max(\Gamma) \quad (5.1.5)$$

$$offset = M - max\_position + 1 \quad (5.1.6)$$

if $offset > 0$

$$\gamma = \min(M + 1 - offset, N) \quad (5.1.7)$$

$$A\_index = offset : offset + \gamma - 1 \quad (5.1.8)$$

$$B\_index = 1 : \gamma \quad \text{endif} \quad (5.1.9)$$

if $offset \le 0$

$$neg\_offset = abs(offset) + 2 \quad (5.1.10)$$

$$\gamma = \min(M, N + 1 - neg\_offset) \quad (5.1.11)$$

$$A\_index = 1 : \gamma \quad (5.1.12)$$

$$B\_index = neg\_offset : neg\_offset + \gamma - 1 \quad \text{endif} \quad (5.1.13)$$

The vector $\Gamma \in R^{(N+M+1)\times 1}$ (5.1.4), is the discrete time convolution of the vectors *A* and *B;* it also is the cross-correlation of the VBOX and IMU acc_y signals. The notation used in (5.1.4)-(5.1.13) coheres with Matlab®. The function *max* (5.1.5) results to the maximum value, *max_value*, of vector Γ and its corresponding position, *max_position*. Indexes, *A_index* and *B_index* indicate where the two vectors *A* and *B* have optimal overlay: *A(A_index)* ≈ *B(B_index)*.

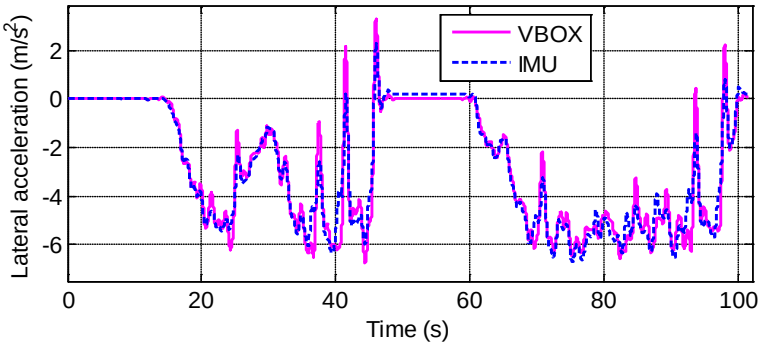

Fig. 5A 9. Offline data synchronization between the VBOX and IMU signals.

An instance of data synchronization is displayed in Fig. 5A 9. The displayed signals have been low-passed filtered with a zero phase 2nd order Butterworth filter at 1Hz. The disparities of the displayed signals are justified from the vehicle's body-roll during cornering and road bumps (affecting the IMU's measurements) and the VBOX's differentiation of the lateral velocity for estimating the lateral acceleration (inducing noise). The presented method can achieve unsupervised data overlay. Alternatively for synchronization a common signal or time stamp can be logged from both ADL and VBOX; e.g. output the slip angle from VBOX and capture it with the ADL.

To calculate the yaw and lateral errors with respect to the 'Desired path' (Fig. 5A 1) for the SDM (Fig. 5A 2), the GPS geodesic coordinates (latitude, longitude) should initially be translated into Cartesian coordinates (or Earth-Centred Earth-Fixed) for both the test track and the vehicle trajectory [88]. Racelogic [148] supplies the user with a simple transformation formula (5.1.14)-(5.1.15) converting latitude GPS_{lat} and longitude GPS_{long} (from minutes $\in R$) to planar coordinates X_{gps}, Y_{gps} (to meters $\in R$). The following can be applied for small altitude variation over the GPS data.

$$X_{gps} = -1853 \cdot GPS_{long} \cdot \cos(\frac{\pi}{180} \cdot (\frac{GPS_{lat}}{60})) \tag{5.1.14}$$

$$Y_{gps} = GPS_{lat} \cdot 1853 \tag{5.1.15}$$

The resulting X_{gps}, Y_{gps} from (5.1.14)-(5.1.15) have fairly large values (offset from [0, 0]). Therefore, a reference point [$X_{gps\_track\_ref}$, $Y_{gps\_track\_ref}$] from the GPS-logged track coordinates is used to remove this offset from the track X_{gps_track}, Y_{gps_track} and vehicle X_{gps_car}, Y_{gps_car} GPS-logged coordinates (5.1.16) -(5.1.17).

$$\begin{aligned} X_{track} &= X_{gps\_track} - X_{gps\_track\_ref} \\ Y_{track} &= Y_{gps\_track} - Y_{gps\_track\_ref} \end{aligned} \tag{5.1.16}$$

$$\begin{aligned} X_{car} &= X_{gps\_car} - X_{gps\_track\_ref} \\ Y_{car} &= Y_{gps\_car} - Y_{gps\_track\_ref} \end{aligned} \tag{5.1.17}$$

VI. Preview yaw and lateral error calculation

This Section describes an explicit implementation of the yaw and lateral error calculation with respect to a reference trajectory of [141][87]. To derive the yaw and lateral error for the preview driver model, the 'Predicted path' is estimated using a simplified internal vehicle dynamics model as in [31] using the state space model form of (5.1.18). Input to the system is the wheel angle δ (5.1.18), deriving from the ADL logged steering wheel angle θ_{sw_car} multiplied by the 1/*steering_ratio* [63]. The longitudinal velocity $\dot{x}_{car}$ originates from the VBOX and is assumed constant over the T time preview window (5.1.18). The parameter values used in (5.1.18) are summarized in Table 5A 1. The vehicle's local coordinates x, y, ψ are translated to the global X, Y, ψ with (5.1.19). For each logged sample t the predicted path for T time ahead is estimated through (5.1.19) by solving the system of (5.1.18) and by using the sampled X_{car}, Y_{car}, ψ_{car} and $\dot{y}_{car}$, $\dot{\psi}_{car}$ for initial conditions (the lateral velocity $\dot{y}_{car}$ is also measured with the VBOX). The subscript "$_{car}$" denotes the real sampled value logged from either the VBOX-GPS or the ADL.

$$\begin{aligned} &\frac{d}{dt}\begin{Bmatrix} \dot{y} \\ \dot{\psi} \end{Bmatrix} = \begin{bmatrix} -\frac{C_f + C_r}{m\dot{x}} & \frac{C_r l_r - C_f l_f}{m\dot{x}} - \dot{x}_{car} \\ \frac{C_r l_r - C_f l_f}{I_z \dot{x}} & -\frac{C_f l_f^2 + C_r l_r^2}{I_z \dot{x}} \end{bmatrix} \cdot \\ &\begin{bmatrix} \dot{y} \\ \dot{\psi} \end{bmatrix} + \begin{bmatrix} C_f / m \\ C_f l_f / I_z \end{bmatrix} \delta \\ &\delta = \theta_{sw\_car} \cdot (1 / steering\_ratio) \end{aligned} \tag{5.1.18}$$

$$\begin{aligned} X(t+T) &= \int_t^{t+T} \left(\dot{x}\cos\psi - \dot{y}\sin\psi \right) d\tau + X_{car}(t) \\ Y(t+T) &= \int_t^{t+T} \left(\dot{x}\sin\psi + \dot{y}\cos\psi \right) d\tau + Y_{car}(t) \\ \psi(t+T) &= \int_t^{t+T} \dot{\psi} d\tau + \psi_{car}(t) \end{aligned} \tag{5.1.19}$$

The differential equation (5.1.18) is solved with the Euler method with 0.01 s integration step. The previous process yields the predicted path vectors X_{pred}, Y_{pred} and ψ_{pred} (Fig. 5A 1). The lateral and yaw errors can now be calculated as in Fig. 5A 1.

The 'Desired path' is represented by three vectors $Track := [X_{track}\ Y_{track}\ \Psi_{track}]$ ($Track \in R^{L\times 3}$; length of e.g. X_{track} is L). GPS sampled coordinates on the actual 'Desired path' are linearly interpolated with 0.1 m interval to derive the X_{track}, Y_{track} (5.1.16)-(5.1.17). The 'Desired's path' yaw angle, Ψ_{track} is estimated as in (5.1.20)-(5.1.21) and its values are bounded in the $[0, \pi]$ range (5.1.22). The notation used follows Matlab®. Function *mod* (5.1.21) gives the modulus after division.

Table 5A 1. Vehicle dynamics model parameters.

Symbol	Description	Value	Unit
m	Mass of the vehicle	850	Kg
I_z	Moment of inertia around the Z axis at the CG	1400	kg·m^2
l_f, l_r	Distance of front/rear axle from the CG	1.5, 0.9	M
C_f, C_r	Cornering stiffness front/rear axle	8.9, 15	KN/rad
$\dot{x}$, $\dot{y}$	Longitudinal, lateral velocity	-, -	m/s
steering_ratio	Steering ratio; steering wheel angle to wheel angle ratio	16.7	-

$$\Psi_{track}(2:L) = \tan^{-1}\left(\frac{dY_{track}(1:L)}{dX_{track}(1:L)}\right),\ \Psi_{track}(1) = \Psi_{track}(2) \tag{5.1.20}$$

$$\Psi_{track}(1:L) = \mathrm{mod}(\Psi_{track} + 2\cdot\pi, \pi) \tag{5.1.21}$$

The slope *alpha* (5.1.23), and y-intercept *beta* (5.1.24) of the perpendicular line ε_n (Fig. 5A 1) at the n preview point (Fig. 5A 1) which intersects the 'Desired path' (curve formed by the X_{track}, Y_{track}) is estimated through (5.1.22)-(5.1.24).

$$\theta_n = \psi_{pred}(n) + \pi/2 \tag{5.1.22}$$

$$alpha = \tan(\theta_n)$$

$$\left\{\begin{array}{l} if\ \ abs(alpha) > 30 \\ aplha = sign(alpha)\cdot 20 \end{array}\right\} \tag{5.1.23}$$

$$beta = Y_{pred}(n) - alpha \cdot X_{pred}(n) \tag{5.1.24}$$

$$y_{\varepsilon_n} = aplha \cdot x_{\varepsilon_n} + beta \tag{5.1.25}$$

$$Y_{track\_estimated}(1:L) = aplha \cdot X_{track}(1:L) + beta \tag{5.1.26}$$

The equation of the line ε_n is given by (5.1.25) and applying the X_{track} vector on (5.1.25) yields the $Y_{track\_estimated}$ vector (5.1.26). The following step is to find the p smaller values of the Y_{track_error} (5.1.27) using (5.1.28); p represents the number of potential intersections of the line ε_n on the track, e.g. for a circular track is 2.

$$\begin{array}{l} X_{track\_temp}(1:L) = X_{pred}(n) \\ Y_{track\_error}(1:L) = |\, Y_{track} - Y_{track\_estimated}\,| + |\, X_{track} - X_{track\_temp}\,| \end{array} \tag{5.1.27}$$

for $k = 1:p$

$$[\min_{value}(k), \min_{index}(k)] = \min(Y_{track\_error})$$
$$Y_{track\_error}(\min_{index}(k)) = \infty \quad (5.1.28)$$

endfor

The distances between the predicted future point ($X_{pred}(n)$, $Y_{pred}(n)$) and the p closer track points found with (5.1.28) are estimated using (5.1.29). The minimum of the $min_{indexdist}$, is the index of the 1 track point out of the p, closer to the line ε_n (5.1.30).

for $k = 1:p$

$$dist(k) = | X_{track}(\min_{index}(k)) - X_{pred}(n) | + | Y_{track}(\min_{index}(k)) - Y_{pred}(n) | \quad (5.1.29)$$

endfor

$$[\min_{valuedist}, \min_{indexdist}] = \min(dist_{1:p}) \quad (5.1.30)$$

$$index = \min_{index}(\min_{indexdist}) \begin{cases} X_{ref}(n) = X_{track}(index) \\ Y_{ref}(n) = Y_{track}(index) \\ \Psi_{ref}(n) = \Psi_{track}(index) \end{cases} \quad (5.1.31)$$

Equation (5.1.31) yields the *index* of the track data vectors *Track* := [X_{track} Y_{track} Ψ_{track}] that the perpendicular line ε_n intersects the track ('Desired path'). The values of the track at the *index* point as referred as reference values $X_{ref}(n)$, $Y_{ref}(n)$, $\Psi_{ref}(n)$ (5.1.31). Because the track interval values are spaced with 0.1 m, as mentioned earlier, a finer search for reference values is being performed by linear interpolating the previous, *Track(index-1)* and the next index point, *Track(index+1)* from the estimated *index* (5.1.31) of the track. Interpolating the yaw angle is difficult; if the next and previous yaw angle from the index fall within an angle wrap case (e.g. $\Psi_{track}(index-1)=0$ and $\Psi_{track}(index+1)=\pi$), then the interpolation will yield the wrong value; in that case, the $\Psi_{track}(index)$ is used. Then the process of (5.1.27)-(5.1.31) is repeated but with the *Track* being the local track formed between the *Track(index-1)* and *Track(index+1)*. This process will yield the final reference values that will be used for estimating the lateral (5.1.32) [145] and the temporary yaw error (5.1.34). The predicted vehicle yaw angle should be bounded in the [0, 2·π] range (5.1.33) (λ: ($\psi_{pred}(n)+\lambda \cdot 2 \cdot \pi) \geq 0$).

$$eL_n = (Y_{pred}(n) - Y_{ref}(n)) \cdot \cos(\psi_{pred}(n)) - (X_{pred}(n) - X_{ref}(n)) \cdot \sin(\psi_{pred}(n)) \quad (5.1.32)$$

$$\psi_{pred}(n) = \mathrm{mod}(\psi_{pred}(n) + \lambda \cdot 2 \cdot \pi, 2 \cdot \pi) \quad (5.1.33)$$

$$e\psi_{n\_temp} = \psi_{pred}(n) - \Psi_{ref}(n) \quad (5.1.34)$$

$$
\begin{aligned}
&\text{if } e\psi_{n\_temp} \geq \pi/2 \\
&\quad e\psi_{n\_temp} = \psi_{pred}(n) - (\Psi_{ref}(n) + \pi) \\
&\quad \text{if } e\psi_{n\_temp} \geq \pi/2 \\
&\quad\quad e\psi_{n\_temp} = \psi_{pred}(n) - (\Psi_{ref}(n) + 2\cdot\pi) \\
&\quad \text{endif} \\
&\text{elseif } e\psi_{n\_temp} \leq -\pi/2 \\
&\quad e\psi_{n\_temp} = \psi_{pred}(n) - (\Psi_{ref}(n) - \pi) \\
&\quad \text{if } e\psi_{n\_temp} \leq -\pi/2 \\
&\quad\quad e\psi_{n\_temp} = \psi_{pred}(n) - (\Psi_{ref}(n) - 2\cdot\pi) \\
&\quad \text{endif} \\
&\text{endif}
\end{aligned}
\tag{5.1.35}
$$

$$
e\psi_n = e\psi_{n\_temp} \tag{5.1.36}
$$

The temporary yaw error will yield the final yaw error $e\psi_n$ (5.1.36) bounded in the $[-\pi/2, \pi/2]$ range using (5.1.35) so as to yield an error signal without any discontinuities. The maximum range of the yaw error can be extended to $[-\pi, \pi]$ range in case the 'Desired path' direction of driving is taken into account. However, this case will not be presented.

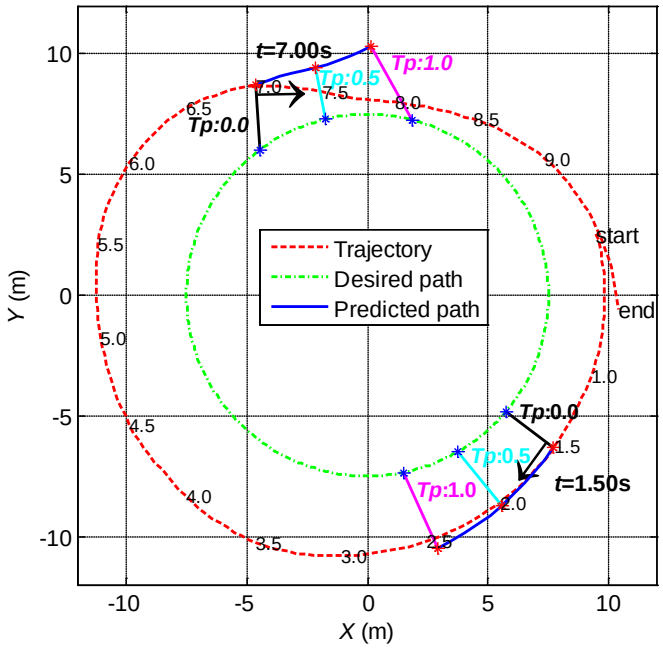

Fig. 5A 10. Yaw and lateral error determination on circular drive skid-pad. At time t = 1.5 and 7 s the resulting perpendicular lines from the predicted to the desired path are displayed, for preview look-ahead points Tp: 0, 0.5 and 1 s. The arrow shows the current yaw angle of the vehicle. The numbers on the trajectory (red dashed line) denote the experimental time in s.

VII. Circular manoeuvring case study

A. Simple driver model states and driver inputs correlation

In the current section, circular drive skid-pad tests (Fig. 5A 10) are presented for a novice and an expert in race driving. The data was logged and post-processed as described in the previous 2 sections. The test vehicle was a Rear-Wheel-Drive (RWD) with no power steering and the test track was on loose gravel on an uneven surface. A single circular run for the novice driver is analysed in Fig. 5A 10, Fig. 5A 11 and Fig. 5A 12.

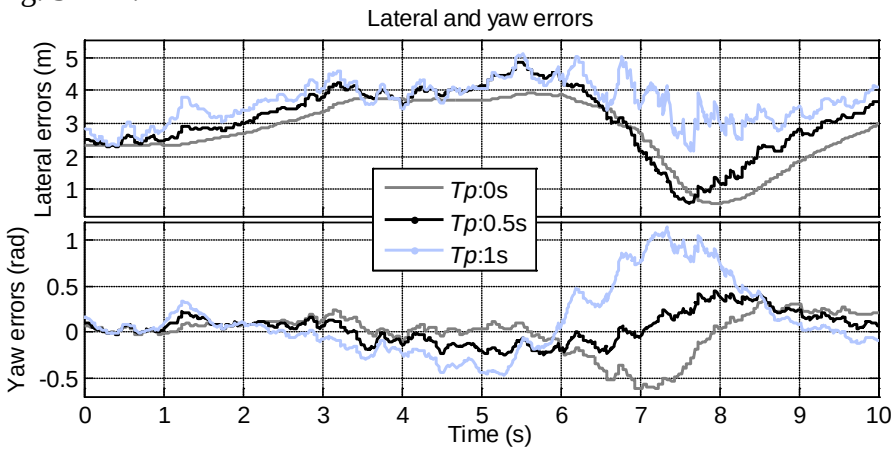

Fig. 5A 11. Yaw and lateral error on circular drive skid-pad for the trajectory of Fig. 5A 10.

In Fig. 5A 10 the vehicle's 'Trajectory' and the perpendicular lines from the 'Predicted path' on the 'Desired path' are plotted for preview look-ahead time points *Tp*: 0.0, 0.5 and 1.0 s, for the novice driver. The driver performs circular cornering manoeuvres, as fast as he can, outside a 7.5 m radius circle marked with tires. The lateral and yaw errors are shown in Fig. 5A 11 and the driver inputs and vehicle states are illustrated in Fig. 5A 12. The lateral error in Fig. 5A 11 represents the distance from the tire marked track and apparently the driver purposefully drives about 2 m outside the marked circle.

The driver before t = 5 s (see Fig. 5A 12) is performing near steady-state cornering; *dx/dt*, *dy/dt*, yaw rate, steering angle, lateral (Lat acc) and longitudinal acceleration (Long acc) are nearly constant. Just before t = 5 s an unintentional drift occurs as the vehicle starts to oversteer without the driver changing steering or throttle commands. This can be identified with the increasing slip angle (β in Fig. 5A 12) resulting from the excessive rear wheel spin (RL and RR in Fig. 5A 12).

Excessive wheel spin reduces tires' cornering forces and hence the stabilizing yaw moment of the rear wheels increasing the magnitude of the yaw rate (t = 5 to 6 s) and sideslip angle (t = 5 to 7.5 s). The driver can perceive the vehicle's oversteering behaviour through the excessive spin (tactile and audio feedback), the increasing (in magnitude) slip angle and yaw rate (vestibular feedback) and the drop in required steering torque (haptic feedback) at approximately t = 5 s. He starts to react at approximately t = 5.2 s by reducing his steering input. The lateral error and yaw error signals (Fig. 5A 1) (visual feedback) are not affected considerably at t = 5.2 s, despite the fact that the driver has already started to react.

After t = 5.2 s the driver starts steering the front wheels towards the opposite direction with respect to the corner (counter-steering) and closes the throttle for 0.2 s at t = 6.1 s. Counter-steering lasts from approximately t = 6.1 s to t = 7.9 s and results to the change of sign of the yaw rate (angular rate around the vehicle's CG) from approximately t = 7.1 to t = 7.9 s. An interesting time point is where the yaw rate and the slip angle curves intersect at approximately t = 7.3 s. At approximately the same time the driver starts steering again towards the correct direction with respect to the corner. Apparently, the

driver's reaction is ahead of his visual feedback (lateral and yaw error): if he would have relied solely on the relatively slow response of his visual inputs (even if that would occur without a processing delay) he would have lost control.

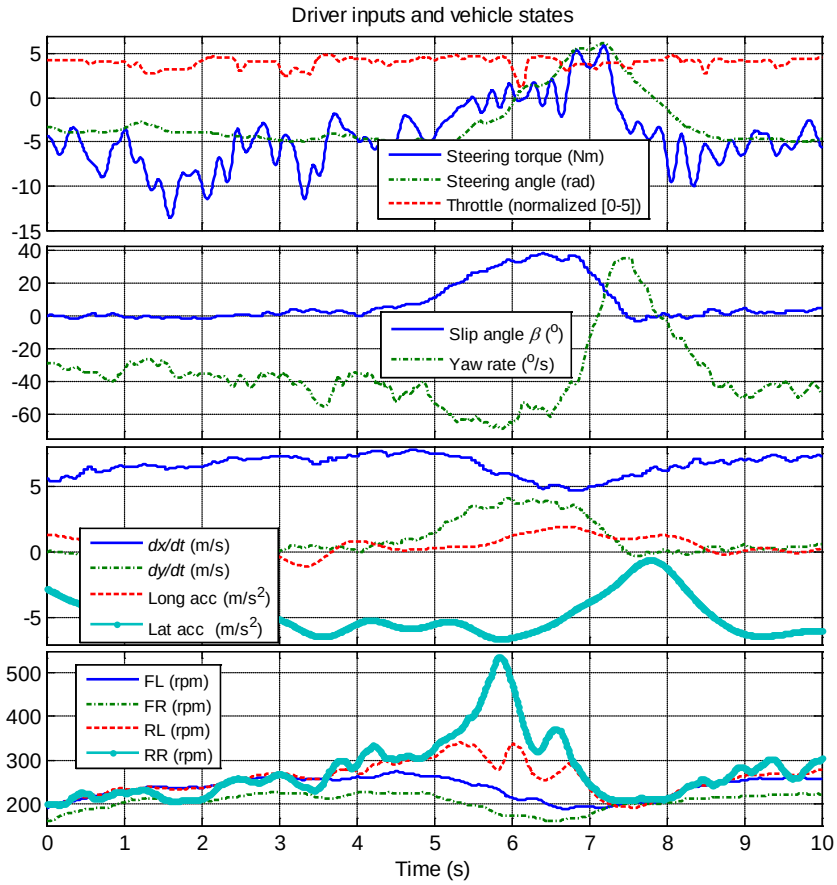

Fig. 5A 12. Driver inputs and vehicle states for the circular drive of Fig. 5A 10. Nomenclature; *dx/dt*: longitudinal velocity, *dy/dt*: lateral velocity, Long Acc: longitudinal acceleration, Lat Acc: lateral acceleration, FL, FR, RR, RR: front/rear left/right wheel speed in revolutions per minute (rpm).

B. Expert vs. novice driver

In order to demonstrate how the described vehicle instrumentation can contribute to understanding driver behaviour, a second example is presented. An expert world-rally-car (WRC) class and the same novice driver from the previous sub-section drove on the same 7.5 m radius circular test-track. They performed three separate attempts of closely driving around a set of tires that marked a circle 7.5 meters in radius, as fast as they could. The measurements yielded a large amount of data, allowing in-depth analysis of driving behaviour. This study presents only a brief analysis, showing how the measurements can be used to investigate to what extent driving strategies and performance are influenced by practice and experience.

Longitudinal and lateral control was mainly achieved through the throttle and steering wheel inputs; the foot brake and hand brake were rarely used. Fig. 5A 13 shows the realized trajectories of the expert driver (top panels) and the novice driver (bottom panels); for the first set of circular drives (left panels) and the last (right panels).

The experienced driver could apparently learn quickly how to perform repeatable trajectories, unlike the novice driver. The lateral error eL_1 (0 s preview point) as described in Sections II and VI, is shown

in Fig. 5A 14, plotted against the polar angle. The trajectories were made clockwise with 0^o defined at "3-o-clock" in the figures, i.e. when X is positive and Y is zero. This prototypal representation can evince control patterns and repeatable actions, which are indiscreet in the time plots.

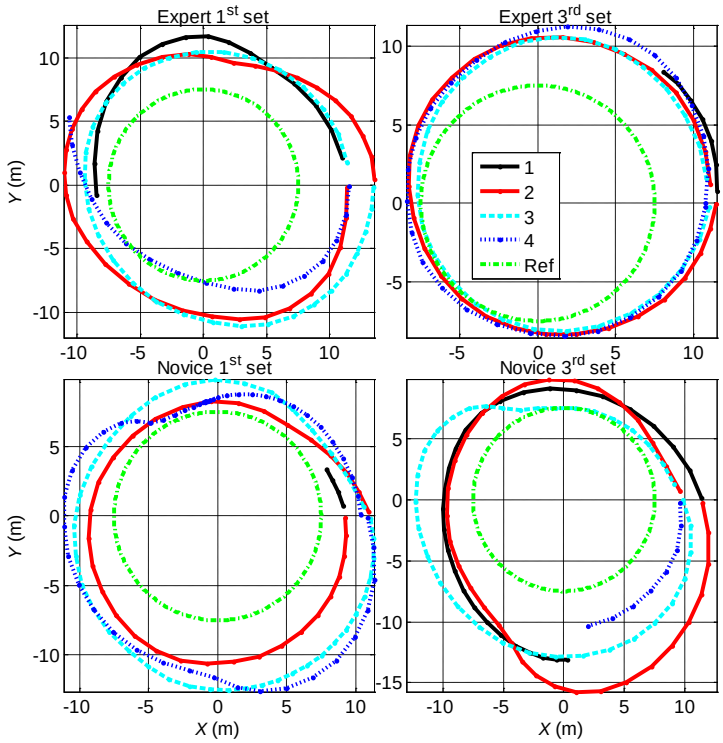

Fig. 5A 13. Expert vs. novice driver trajectories for circular drive. The sets of trajectories are split into four full circles representing rounds 1-4, each plotted with a different line. 'Ref', denotes the tire marked 'Desired path'. Line notation is common for all subfigures.

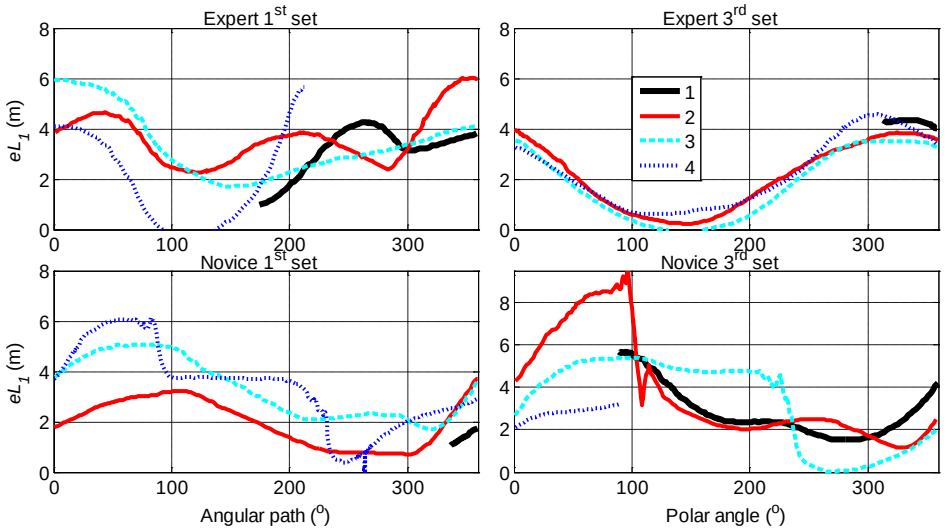

Fig. 5A 14. Lateral error eL_1 for the expert and novice driver plotted against polar angle (0-360°). Line notation is common for all subfigures.

The consistently high performance of the expert driver was realized by relatively small correcting inputs (steering wheel angle, throttle). The top panels of Fig. 5A 15 show how the steering actions become more synchronized over time for the experienced driver, but not for the novice driver. Other

measured signals (e.g. slip angle, wheel speeds) showed very similar trends: experienced drivers are able to quickly learn how to generate the correct inputs to the vehicle, to yield repeatable vehicle behaviour and consistently perform well. A more in-depth analysis of the observed driver behaviour will be presented in part B of Chapter 5 and Chapter 7.

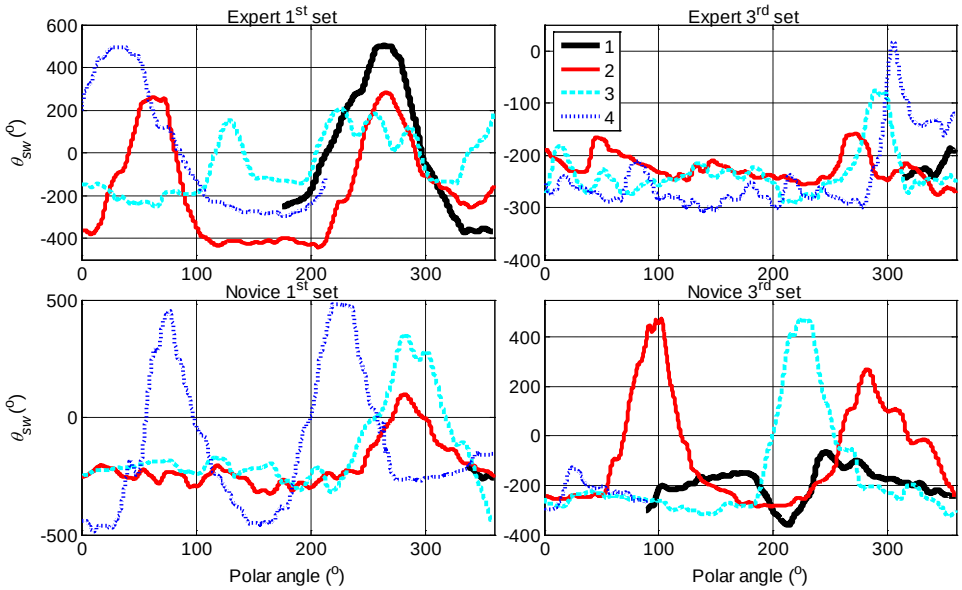

Fig. 5A 15. Steering angle inputs for the expert and novice driver plotted against polar angle (0-360^o). Line notation is common for all subfigures.

VIII. Discussion

Part A of Chapter 5 supplies a roadmap on how a researcher can effectively perform experiments with real vehicles and obtain the required measurements for studying dynamic driving behaviour. It provides detailed guidelines for constructing a versatile low-cost experimental apparatus suitable to be fitted on race cars, oriented to high-speed driving modelling research. Part A discusses in-field testing with instrumented vehicles to develop and validate driver models. The presented Simple-Driver-Model serves as an indicator on where driver modelling research is currently heading and depicts the required processing from raw measurements to user-friendly data suitable for research. Driver models developed from in field data can be used as an unbiased performance metric for vehicle dynamics simulation testing and offer understanding on driving control effort. Incorporating driving behaviour while driving at the limit [68][63][65] can improve the realism of a driver model.

An application of the raw data post-processing methods is given for circular test drives. A discussion is being made on novice and expert drivers' stimuli in the high speed vehicle control task.

The improvement of the position accuracy of the system is essential for extending this work for optimizing driver model parameters [146][15]. A GPS receiver can measure velocity with accuracy of 5 cm/s using the Doppler shift of the GPS carrier wave [54]; the former, combined with inertial measurements and a reference starting point can greatly improve the position accuracy. An alternate solution would be a low cost differential-GPS solution with reference-station [118].

The custom built equipment, from the mechanical parts to the open-source based software are thoroughly described and are freely available online [33] for general public use. The aforementioned along with the progressive driver model based analysis, using the described yaw and lateral error calculation method, and the polar angle representation of kinematic data constitute the terminus of this

work. Results and methods described in this study have been applied in Chapter 3, Chapter 5 part B and C, Chapter 6 and Chapter 7.

A photo of a vehicle fitted with the presented instrumentation is illustrated in Fig. 5A 16.

Fig. 5A 16. An instrumented 4WD Subaru Impreza GT during testing.

IX. Appendix

Table 5A 2. Custom built and fitted sensor specifications.

Sensor description	Source	Range	Accuracy
Steering angle: semi-custom	Measured	≥ ± 700 ^{o}	< 0.5 ^{o}
Steering torque: custom	Measured	≥ ± 100 Nm	< 0.1 Nm
Wheel speed sensors: custom	Designed	5 revs/50 m/s	3.6 ^{o}/rev
Brake pressure sensors: Bosch	Specs	0-250 bar	≤ 5%
Gyroscope: IDG500	Specs	± 500 ^{o}/s	± 0.4 ^{o}/s
3-axis accelerometer: ADXL355	Specs	± 3 g	1.3 mg (50 Hz)
2-axis accelerometer: ADXL322	Specs	± 2 g	3.1 mg (50 Hz)
Throttle position: custom	Measured	0-10 KΩhm	≤ 5%
GPS absolute position; VBox	Specs	-	± 3 m
GPS velocity; VBox	Specs	0-1609 km/h	0.27 m/s

X. Acknowledgment

The research was supported by the Automotive Development Center of SKF as part of the project Mobility Intelligence using Loadbased Lateral Stability (MILLS). E. Velenis was supported by a Marie Curie International Reintegration Grant within the 7th European Community Framework Programme, and a Brunel University BRIEF award. D. Abbink was supported through a VENI grant from NWO.

The author is grateful to Ross Bowman, Peter and Bill Gwynne from Bill Gwynne Rally School in Brackley UK, Keith Withers and Guy Fitch from School of Engineering and Design, Brunel University and Malcolm Ferris from MFG Engineering, Uxbridge UK.

Chapter 5 B. Driver Control Actions in High Speed Circular Driving

“Two things control men's nature, instinct and experience”
Blaise Pascal, 1623-1662 A.D.

Driver Control Actions in High Speed Circular Driving

Abstract—In this pilot study we investigate driver control actions during high speed cornering with a rear wheel drive vehicle. Six drivers were instructed to perform the fastest manoeuvres possible around a marked circle, while trying to retain control of the vehicle and constant turning radius. The data reveal that stabilization of the vehicle is achieved with a combination of steering and throttle regulation. The results show that the drivers used steering control to compensate for disturbances in yaw rate and sideslip angle. Vehicle accustomed drivers had the most consistent performance resulting in reduced variance of task metrics and control inputs.

I. Introduction

Driving control analysis studies were initiated as early as in the 1930's [96]. It was soon realized that the driving task can be divided into a leading and a compensation action and that drivers primarily apply steering in an anticipatory feedforward manner to an estimated future path; in addition, drivers employ a closed-loop adaptive-control strategy to compensate for deviations of the vehicle from the demanded trajectory [56]. The dominant approach in the design of human-like driver controllers is to decouple the anticipatory and compensatory actions [83]; however, the full understanding of human driving in terms of compensation to steering disturbances [31] remains an open issue. The majority of driver-car interaction studies dealing with the driver's compensatory behaviour are performed in a simulation environment [15] since real in-field extreme driving tests can be difficult to interpret [95]. Expert rally driving techniques and their corresponding mathematical analysis, which involves operation of the vehicle outside the stable operation envelope has recently started to receive attention [67]. The former invited the introduction of vehicle stabilization controllers employing solely driver inputs [68].

Challenged by the human's compensatory behaviour while driving beyond the vehicle's stable envelope, we commenced a pilot study to investigate the relationship between driver's sensory inputs and compensatory control-actions. The sensory inputs can be visual, kinesthetic (steering torque) or vestibular (lateral acceleration, yaw rate and slip angle) feedback. Six drivers with varying driving skill level were instructed to execute high-speed circular manoeuvres on a loose surface (dirt), aiming at maintaining approximately a constant sideslip angle and distance from the centre of the tire-marked circular path (with 7.5 m radius). By analysing the driver control actions and the vehicle response, we studied the cross-correlation of the sensory inputs and the corresponding control actions (steering, throttle).

II. Methods

The tests took place at the facilities of the Bill Gwynne Rally School in Brackley, UK, using a rally-race prepared rear-wheel-drive (RWD) 1980 Ford Escort Mk1 with a 1.6 lt engine producing approximately 110 bhp (c.f. Fig. 5B 1). A VBOXIISL data-logger from Racelogic was used to measure the vehicle's absolute position, true heading, velocity and sideslip angle β. A low cost Inertia Measurement Unit (IMU) with 5 degrees-of-freedom IDG500/ADXL335 was placed near the estimated location of the vehicle's centre-of-gravity (CG) to measure 3-axis body accelerations and 2-axis body angular rates. Externally fitted optical encoders (speed sensors) were used to measure the rotational speed of individual wheels. The steering angle/torque signals were measured using an 'extension hub'

mounted between the steering wheel hub and the steering wheel. Strain gauges on the 'extension hub' enabled steering torque reading and a string potentiometer wrapped around the 'extension hub' measured the steering wheel angle. Throttle position was measured through a potentiometer. The vehicle was fitted with two brake pressure sensors allowing us to distinguish between application of foot brake and handbrake. A National Instruments USB-6211 USB M Series data-acquisition was used to capture the analog signals and an 8-bit AVR ATMega32 microcontroller was used for interfacing the optical encoders of the wheel speed sensors. The data logging was performed at 100Hz on a Toshiba NB200 notebook. In-house developed software, based exclusively on open-source solutions, handled the logging and synchronization process. The vehicle instrumentation is shown in Fig. 5B 1. For more details on the custom built equipment and the corresponding processing, the reader can refer to [34].

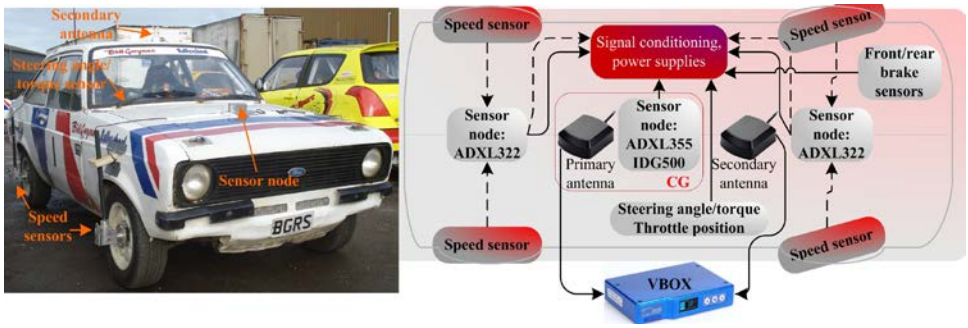

Fig. 5B 1. Vehicle instrumentation for data recording.

Three drivers (D1, D2, D3) with extensive racing experience (expert drivers) and three with no racing experience (D4, D5, D6) (normal drivers) were employed for testing. Each driver was asked to perform three sessions of at least two clockwise circular runs. High speed cornering at high sideslip angles involves operation of the vehicle in an unstable regime [63] and hence is a challenging control task. The drivers were instructed to use only throttle and steering to regulate the vehicle, so as to make a simplified one-to-one relationship (c.f. Table 5B 2) between driver inputs and vehicle's response in the absence of tire force data.

Mean and standard deviation of several task related metrics were calculated for each test. The mean values describe the steady-state condition achieved. The standard deviations describe deviating vehicle kinematics emerging from physical disturbances, such as variations of tire grip which are compensated by the human controller. As described below, we relate the measured control actions to the kinematic deviations. The vehicle states are the velocity V, the sideslip angle β and the yaw rate $\dot{\psi}$ (Fig. 5B 2; left); Table 5B 1 summarizes the vehicle variables.

Throughout part B of Chapter 5 we assume that the vehicle operates near a steady-state cornering condition. Under this assumption, the vehicle sketches a circular trajectory with radius R tangent to the velocity vector V (Fig. 5B 2; left). The radius R of the circle can be calculated using (5.2.1). Counter-clockwise rotation corresponds to a positive yaw rate (Fig. 5B 2; right) and therefore positive R. Referring to Fig. 5B 2 we define D as the distance of the car's CG ($[X, Y]$) to the centre C_M of the marked path; thus D is always greater than or equal to 0.

$$R = V / \dot{\psi} \tag{5.2.1}$$

$$RVisual = R - sign(R) \cdot D \tag{5.2.2}$$

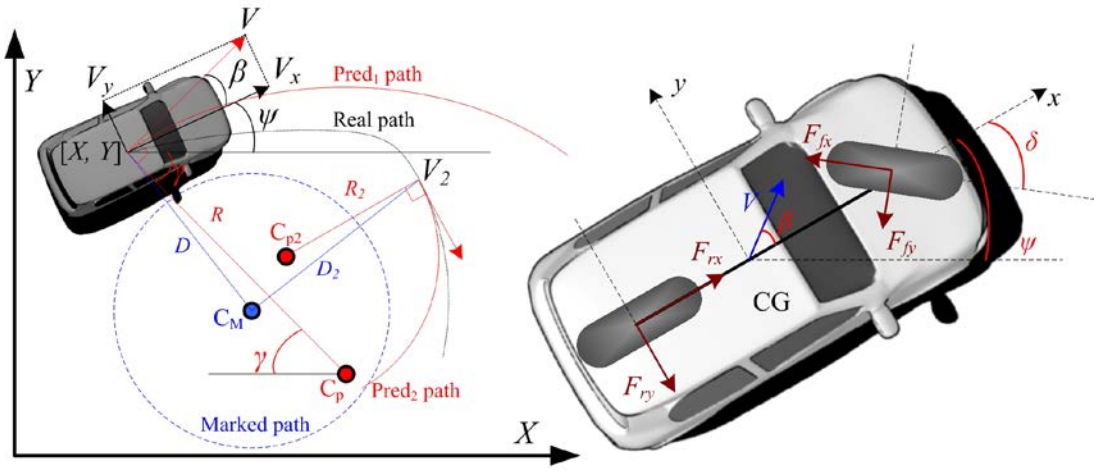

Fig. 5B 2. Vehicle's predicted path (left) and cornering model with forces (right); $R < 0$.

Table 5B 1. Vehicle variables nomenclature.

V, δ	Velocity, steering angle
F_{fy}, F_{ry}	Lateral forces: front, rear axle
F_{fx}, F_{rx}	Tractive forces: front, rear axle
X, Y	Global frame coordinates: X, Y
x, y, ψ	Vehicle frame coordinates: x, y, yaw angle
θ_{sw}, θ_{th}	Steering wheel angle, throttle angle
acc_y, β, $\dot{\psi}$	Lateral acceleration, sideslip angle, yaw rate

We define the relationship between the driver's sensory inputs and control actions as "acting" so as to achieve a task or "counteracting" so as to compensate an unexpected disturbance. As sensory inputs we consider the 1st order derivatives of *RVisual* (5.2.2), yaw rate, lateral acceleration acc_y and sideslip angle β. As control actions we consider the 1st order derivatives of the steering θ_{sw} and θ_{th} throttle angle. The differentiated signals are low pass filtered at 2.5 Hz with a zero-phase 3rd order Butterworth filter. The relationships between sensory inputs and control actions are defined in Table 5B 2.

An example is shown in Fig. 5B 3, showing instances from the relationship 3 of Table 5B 2. Δt (c.f. Fig. 5B 3) is the lead-lag time difference where the sensory input and the control signal have their maximum overlay (coherence); always with the sensory input being the reference. When a relationship is "acting," the control should lead the sensory input ($\Delta t < 0$). In a "counteracting" relationship the sensory input should lead the control ($\Delta t \geq 0$); otherwise the sample is discarded. The relationships are denominated in Table 5B 2 as "acting" or "counteracting" according to which cross-correlation combination (positive + or negative - control) between the sensory input and control action gives the greatest coherence value (coherence := maximum value of the cross-correlation sequence).

When $\Delta t \geq 0$, we shall call it lag time. The samples in Fig. 5B 3 shown as discarded did not support the lead-lag time criteria of the relationship. The displayed control signal is shifted by the Δt time with the respect to the sensory input signal, at the time where both signals have their maximum coherence. The cross-correlation of the sensory input and the control action is being calculated at the switching points where the sensory input crosses zero (derivative zero ➔ change of direction in the signal) for T_{ahead} time ahead in the future. The sensory input signal within T_{ahead} range should have a maximum value above the 85% of the values of the whole length of the signal; otherwise we assume that the

sensory input cannot excite adequately a compensatory response from the driver and the sample is discarded.

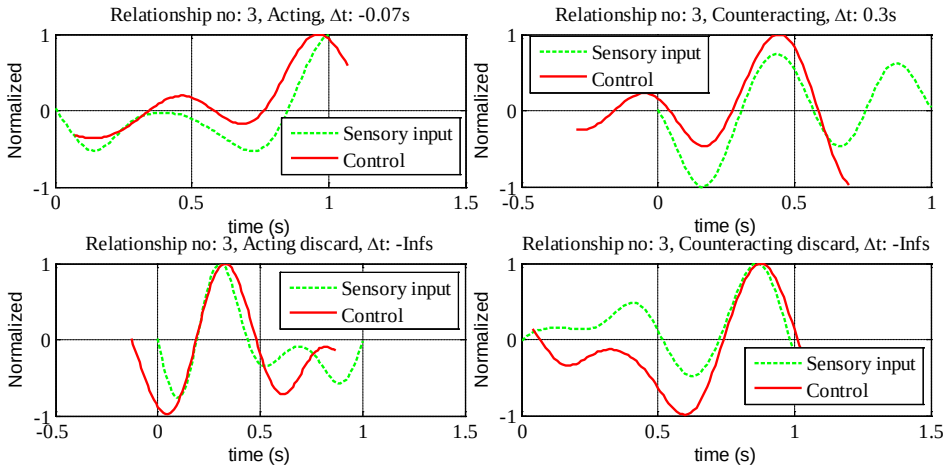

Fig. 5B 3. Acting-counteracting relationship 3; 1st time derivatives of yaw rate (sensory input) and steering wheel angle (control). The signals are normalized (to lie within [-1, 1]) in their T_{ahead} range before being cross-correlated.

Consider, for example, the visual feedback *RVisual* sensory input defined in (5.2.2). Assuming a clockwise turn, the radius *R* will be negative according to (5.2.1). Now if *RVisua l*< 0 (*-R* > *D* ➔ |*R*| > *D*) we expect that if the driver does not correct for his/her future path, (s)he will drive away from the Marked path (c.f. Fig. 5B 2 left; case *V*). S(he) should therefore control towards reducing the magnitude of the radius *R*. The driver may reduce the magnitude of R by increasing the applied steering command towards the direction of the corner [161], which corresponds to relationship 1 in Table 5B 2.

Table 5B 2. Relationships between driver's sensory inputs and control actions.

	Control actions					
Sensory inputs	**Steering**: $\dot{\theta}_{sw}$			**Throttle angle**: $\dot{\theta}_{th}$ ($R \geq 0$ case; inverse + and - for R < 0)		
	(+)		(-)	(+)		(-)
dRVisual/dt (+)	counteracting	**1**	acting	counteracting	**2**	acting
$\ddot{\psi}$ (+)	acting	**3**	counteracting	acting	**4**	counteracting
$dacc_y/dt$ (+)	acting	**5**	counteracting	acting	**6**	counteracting
$\dot{\beta}$ (+)	counteracting	**7**	acting	counteracting	**8**	acting

The inverse will happen if |*R*| < *D*. The driver should then increase the turning radius (c.f. Fig. 5B 2 left; case V_2); otherwise (s)he will cross the marked path (or might perform a trajectory which does not even encircle the Marked path). The relationships 4, 8 between the application of throttle and the induced oversteer (increase in magnitude of yaw rate and sideslip angle) can be explained if we recall the tire force mechanism under combined acceleration and cornering as discussed in [63]. Essentially, the application of throttle and resulting increase in tire slip ratio results in a decrease of the stabilizing yaw moment of the rear tires, which is experienced as an increase of the vehicle yaw rate and sideslip angle. We observe that the $\dot{\theta}_{th}$ control relationships in Table 5B 2 depend on the sign of the radius, which is due to the fact that the θ_{th} is an unsigned variable (in contrast to the θ_{sw}), normalized in the 0-1 range, representing off-throttle and full-throttle correspondingly. Therefore, its impact on the vehicle response differs according to the vehicles' states.

Table 5B 3. Mean μ and standard deviation σ for vehicle's signals, control actions and lag times of the relationships of Table 5B 2. NaN means no sample passed the selection process.

	Driver	D1				D2				D3			
	Run	1st		3rd		1st		3rd		1st		3rd	
		μ	σ	μ	σ	μ	σ	μ	σ	μ	σ	μ	σ
	$V_{(m/s)}$	6,93	0,82	6,67	0,88	7,51	0,66	6,69	0,78	6,45	1,89	7,07	0,74
	$d\psi/dt(^o)$	-33,04	21,70	-38,44	7,34	-32,90	16,09	-39,98	11,21	27,88	9,23	-37,18	21,81
	$\beta(^o)$	14,84	15,72	2,36	3,53	12,14	11,24	4,39	6,05	-1,75	2,50	12,10	14,39
	$acc_y(g)$	-0,46	0,13	-0,54	0,13	-0,55	0,16	-0,51	0,13	0,39	0,19	-0,49	0,15
	$RVisual$	-1,64	28,54	-0,38	2,15	-5,62	23,74	1,09	15,37	0,37	3,53	-2,58	16,17
	$\theta_{sw}(^o)$	-56,44	256,01	-231,80	52,70	-90,82	153,78	-215,71	81,87	271,86	121,03	-68,05	209,78
	$\theta_{th}(norm)$	0,75	0,22	0,82	0,13	0,77	0,25	0,71	0,14	0,61	0,18	0,81	0,14
Relationships. Lag time (s)	**1**	0,18	0,08	0,37	0,10	0,26	0,25	0,21	0,21	0,40	0,27	0,29	0,19
	2	0,70	0,09	0,32	0,21	0,67	0,15	0,28	0,36	0,15	0,26	0,28	0,21
	3	0,32	0,12	0,38	0,13	0,44	0,15	0,34	0,15	0,36	0,11	0,22	0,09
	4	0,29	0,19	0,24	0,17	0,32	0,21	0,14	0,15	0,27	0,27	0,22	0,22
	5	0,27	0,15	0,29	0,21	0,27	0,21	0,23	0,16	0,19	0,13	0,26	0,13
	6	0,43	0,23	0,28	0,22	0,37	0,24	0,45	0,28	0,49	0,24	0,27	0,21
	7	0,18	0,05	0,28	0,16	0,10	0,08	0,29	0,09	0,24	0,19	0,12	0,04
	8	0,20	0,18	0,26	0,19	NaN	NaN	0,29	0,24	0,37	0,22	0,12	0,17
	Driver	D4				D5				D6			
	Run	1st		3rd		1st		3rd		1st		3rd	
		μ	σ	μ	σ	μ	σ	μ	σ	μ	σ	μ	σ
	$V_{(m/s)}$	7,15	0,71	6,82	0,98	6,70	0,94	6,79	0,85	6,30	0,76	6,20	0,56
	$d\psi/dt(^o)$	-36,70	17,44	-33,68	24,49	-37,66	17,28	-40,42	12,00	-34,11	19,52	-35,29	11,98
	$\beta(^o)$	9,17	10,17	10,26	14,41	6,67	7,40	9,39	8,50	5,58	9,14	0,75	2,34
	$acc_y(g)$	-0,51	0,13	-0,45	0,18	-0,51	0,19	-0,50	0,13	-0,44	0,16	-0,43	0,15
	$RVisual$	-2,82	19,52	-0,07	29,06	0,72	18,22	-0,66	19,06	-0,16	12,88	-1,97	8,91
	$\theta_{sw}(^o)$	-168,32	192,14	-117,90	214,48	-207,32	143,82	-150,33	142,22	-207,38	165,30	-237,20	84,03
	$\theta_{th}(norm)$	0,77	0,15	0,69	0,18	0,78	0,15	0,77	0,17	0,70	0,24	0,66	0,14
Relationships. Lag time (s)	**1**	0,34	0,17	0,38	0,23	0,32	0,25	0,32	0,22	0,33	0,29	0,42	0,00
	2	0,47	0,15	0,19	0,17	0,07	0,03	0,17	0,12	0,34	0,31	0,13	0,08
	3	0,43	0,17	0,35	0,07	0,38	0,10	0,33	0,12	NaN	NaN	0,33	0,08
	4	0,40	0,29	0,34	0,09	0,29	0,23	0,28	0,21	0,11	0,00	0,24	0,14
	5	0,27	0,20	0,41	0,10	0,28	0,20	0,33	0,22	0,73	0,00	0,40	0,11
	6	0,31	0,25	0,31	0,20	0,30	0,13	0,49	0,20	0,17	0,20	0,41	0,26
	7	0,35	0,03	0,10	0,11	0,22	0,11	0,20	0,14	0,12	0,06	0,30	0,09
	8	0,44	0,04	0,01	0,00	0,19	0,23	0,37	0,25	0,40	0,02	0,24	0,18

III. Results

Table 5B 3 shows mean and standard variation (σ) of several task related metrics (velocity, slip angle etc.) for the circular test drives. It additionally shows results of the coherence analysis by presenting the calculated lag time for all the relationships of Table 5B 2 (using only instances determined to be counteracting; $\Delta t \geq 0$ in Fig. 5B 3) for all six drivers for their 1st and 3rd test run using T_{ahead} = 1 s. The drivers D1, D2, and D3 have race driving experience with the driver D1 having the greatest race distinction. Drivers D4, D5 and D6 have no race record. Drivers D1, D2 and D5 were accustomed with the test vehicle. All drivers besides driver D3 achieved their maximum mean speed in their 1st run, which was reduced in their 2nd run and increased again in the final 3rd run. The mean velocity V ranged from 6.2 to 7.5 m/s and the magnitude of the mean lateral acceleration that all drivers achieved was approximately 0.5 g, with approximately 0.15 g σ. Driver's D3 and D6, lost completely the control of the vehicle during their 1st run and had to start accelerating again from standstill. D3 continued the 1st run counter-clockwise after losing control. Only the second, successful parts of these tests have been analysed. The performance of D1, D2 (the drivers which achieved best circular trajectories) increased with the number of runs. This can be seen by the small (compared to the rest of the test group) σ on the vehicle's states (velocity, yaw rate and slip angle) and steering angle. A small σ on the steering shows small corrections on the steering wheel to retain control of the vehicle; a

characteristic found in expert drivers. A high σ on the throttle angle means that the driver is controlling the vehicle using the rear wheel slip; characteristic again of an expert driver (the throttle response is direct for the race-specifications test vehicle used). Driver D6 was the least trained driver; still though, though conservative driving (small V) he managed a reduced variance of the task metrics in his 3rd run. Drivers D1, D2 and D5 have the steadiest behaviour in terms of their achieved trajectories and relationship results, the most consistent of the test group. Lack of experience with the test vehicle induced the distinguished race driver D3 to perform worse than expected. In order for a relationship of Table 5B 2 to give a reasonable lag time we should anticipate a σ which is at least half that of the corresponding mean; also the mean should remain within similar levels over the same test driver for all the 3 test runs. The relationships 3 and 7, describing the driver's steering reaction on a yaw rate and slip angle changes correspondingly are the most consistent. Relationship 3 has approximately $\Delta t = 0.35$ s lag time with σ of 0.12. Relationship 7 has a smaller lag time, but at the same time, a smaller σ. Relationship 5, describing the driver's steering angle reaction on lateral acceleration change, although it gives reasonable results has great variability. Relationship 1 describing the control reactions to visual sensory inputs has small coherence. This result was anticipated since the drivers during testing seem to minimally rely on their visual feedback to compensate for disturbances in the vehicle's response [34].

IV. Discussion

In this pilot-study we discussed the human's compensatory behaviour and driving outside the vehicle's stable envelope where considerable control effort is required to retain stability. Six different test drivers executed high-speed circular manoeuvres on a loose surface, instructed to maintain constant sideslip angle and distance from the centre of the tire-marked circular path. By employing a method which relates the driver's sensory inputs with control actions we can get a notion of their coupled relationship and their lead-lag time difference. From the results, we can see that a driver will likely counteract through steering to an exciting enough change (sensory input signal should contain a maximum value, above the 85% of the values of the whole length of the signal) of the yaw rate and the slip angle, with a time delay of approximately 0.4 and 0.2 s correspondingly. Drivers accustomed with the test vehicle exhibit smaller standard deviation (σ) in their steering inputs and the realized vehicle's states and higher σ in the throttle control. They also display more consistent lag times for the relationships of Table 5B 2 with small variation in the mean (per run) and low standard deviation in total. The metrics could therefore be used to asses driving skills. The employed method is sensitive because of the complex nature of the driver-car system and despite the fact that the selection process rejects multiple outliers, the results can be still debatable. This pilot study does not allow drawing definite conclusions about the relationships. The application of classical system-identification techniques [32], which would perturb the vehicle's response by applying a known disturbance would give more rigorous conclusions. Still, the suggested method can potentially give fruitful results by expanding the test group. Definitely though, being a race driver assures high performance, but being accustomed with the test vehicle seems also to be of great importance.

V. Acknowledgment

The research was supported by the Automotive Development Center of SKF as part of the project Mobility Intelligence using Loadbased Lateral Stability (MILLS). E. Velenis was supported by a Marie Curie International Reintegration Grant within the 7th European Community Framework Programme.

Chapter 5 C. Stabilization of Steady-State Drifting for a RWD vehicle

“Βουλεύου μεν βραδέως, εκτελεί δε ταχέως τα δόξαντα.”
Ισοκράτης, 436-338 π.Χ.

“Think slow, but act fast.”
Isocrates, 436-338 B.C.

Stabilization of Steady-State Drifting for a RWD Vehicle

Abstract—In part C of Chapter 5 we present data of driver control commands and vehicle response during the execution of cornering manoeuvres at high sideslip angles (drifting) by an expert driver using a RWD vehicle. The data reveal that stabilization of the vehicle with respect to such cornering equilibria requires a combination of steering and throttle regulation. A four wheel vehicle model with nonlinear tire characteristics is introduced and the steady-state drifting conditions are solved numerically to derive the corresponding control inputs. A sliding mode control is proposed to stabilize the vehicle model with respect to steady-state drifting, using steering angle and drive torque inputs. The performance of the controller is validated in a high fidelity simulation environment.

I. Introduction

Recently, numerous studies on the dynamic behaviour and control of vehicles considering their full handling capacity along with the operation of the tires in their nonlinear region have appeared in the literature. It is envisioned that a new generation of active safety systems will employ expert driving skills, instead of restricting the vehicle's response within the predictable linear region of operation of the tires, to actively manoeuvre vehicles away from accidents. A mathematical analysis of expert driving techniques was initiated in [66][67][69]. The driving techniques investigated in the above references using numerical optimization were those used by rally drivers, and clearly involve operation of the vehicle outside the stable operation envelope enforced by current active safety/stability systems.

The analysis in [66][67][69] provided a significant understanding of the dominant effects during execution of expert driving techniques, but the openloop nature of the numerical optimization approach is not implementable in the presence of uncertainties. Several studies have appeared in the literature recently, contributing to a closed loop formulation of vehicle cornering at high sideslip angles. Derivation of steady-state cornering equilibria with the tires operating in their nonlinear region, a stability analysis using phase-plane techniques and the design of a robust stabilizing steering controller, neglecting the longitudinal forces (tractive or braking) at the tires, appeared in [62]. High sideslip angle (drifting) steady-state cornering conditions were derived in [109] using the lateral dynamics of a four wheel rear-wheel-drive (RWD) vehicle model and a combined traction/cornering tire friction model. The stability of steady-state drifting using a rich four wheel RWD vehicle model, incorporating longitudinal and lateral dynamics, load transfer effects and a combined motion tire friction model, was discussed in [82]. Derivation of drifting equilibria using vehicle models of lower order, and hence more appropriate for control design, were discussed in [61] and [139].

In addition to the steering controller in [62], stabilization of drifting equilibria appeared in [65] and [26]. In [65] a sliding mode control, using independent front and rear wheel drive/brake torque inputs, and assuming a fixed steering angle at its steady-state value, was designed to stabilize a single-track vehicle model with respect to drifting equilibria. In [26] a steering controller based on the lateral dynamics of a single-track model was implemented on an autonomous vehicle platform to perform steady-state drifting, while a separate speed controller was used to regulate the speed to the desired steady-state value.

In this work we present a controller to stabilize a RWD vehicle with respect to drifting equilibria, based on a rich vehicle dynamics model, and using coupled lateral (steering) and longitudinal (drive

torque) control inputs. We first present the results of a data collection experiment during the execution of steady-state drifting by an expert driver and discuss the driver steering, brake and throttle commands during the stabilization of the vehicle. We introduce a four wheel vehicle model, incorporating nonlinear tire friction characteristics, longitudinal and lateral load transfer effects and coupling of the rear wheels drive torques through modelling of a differential system. Using the four wheel model we calculate numerically the steady-state tire friction forces and the associated drive torque and steering angle control inputs corresponding to drifting equilibria. A linear controller is designed to stabilize the vehicle with respect to drifting equilibria using front wheel steering angle and rear wheel slip ratios (or equivalently rear wheel rotation rates). A sliding mode control scheme is then employed providing the drive torque input necessary to regulate the rear wheel speeds to the values dictated by the above linear controller. Finally, the control scheme is implemented in a high fidelity simulation environment.

II. Methods

A. Data analysis

In this section we present data of driver control inputs and corresponding vehicle response collected during the execution of a drifting manoeuvre by an experienced rally race driver. The data collection took place at the facilities of the Bill Gwynne Rally School in Brackley, UK, using a rally-race prepared 1980 1.6lt, 110bhp engine Ford Escort with a RWD transmission and a limited slip differential (c.f. Fig. 5B 1). The vehicle vector velocity and sideslip angle were measured using a VBox twin GPS antenna sensor at 20Hz. An inertial measurement unit was placed on the centreline of the vehicle close to the estimated location of the vehicle's centre-of-gravity (CG) to measure 3-axis body accelerations and 3-axis body rotation rates. Externally fitted optical encoders were used to measure the rotational speed of each individual wheel. A string potentiometer was used to measure the steering angle at the steering wheel, and a rotational potentiometer was fitted on the throttle pedal to measure the pedal position. The vehicle was fitted with two brake pressure sensors at the front and rear pairs of wheels. The data was collected using a purpose-built data logger at 100Hz. The driver executed drifting manoeuvres on a loose surface (dirt on tarmac), aiming at maintaining approximately constant speed and sideslip angle along a path of approximately constant radius.

In Fig. 5C 1 we present data for the vehicle states, namely, vehicle speed V, sideslip angle β, yaw rate $\dot{\psi}$ and individual wheel speeds ω_{ij}, $i = F$ (Front), R (Rear), $j = L$ (Left), R (Right), during stabilization of the vehicle at a steady-state clockwise trajectory of radius approximately 13m. The vehicle sideslip and yaw rate are positive along the counter-clockwise direction. In the same figure we also present the corresponding driver inputs, namely, the steering angle of the front wheels, with positive values corresponding to turning the steering wheel to the left, as well as the normalized throttle pedal position, and normalized front and rear axle brake pressures. Part of the vehicle trajectory is shown in Fig. 5C 2.

Throughout the 13m radius trajectory the driver applied no brake command, except from a small value during a brief interval around $t = 20$ sec. The vehicle started from standstill and accelerated while cornering to the right. Between $5 \leq t \leq 10$sec the vehicle developed a high sideslip angle of approximately 30 deg. At the beginning of this interval we notice application of full throttle, which resulted in the rear wheels to rotate at a considerably higher rate than the front ones. Hence the slip ratio at the rear wheels was increased and the rear cornering forces decreased (in accordance to the combined traction/ braking and cornering operation of a tire [59]).

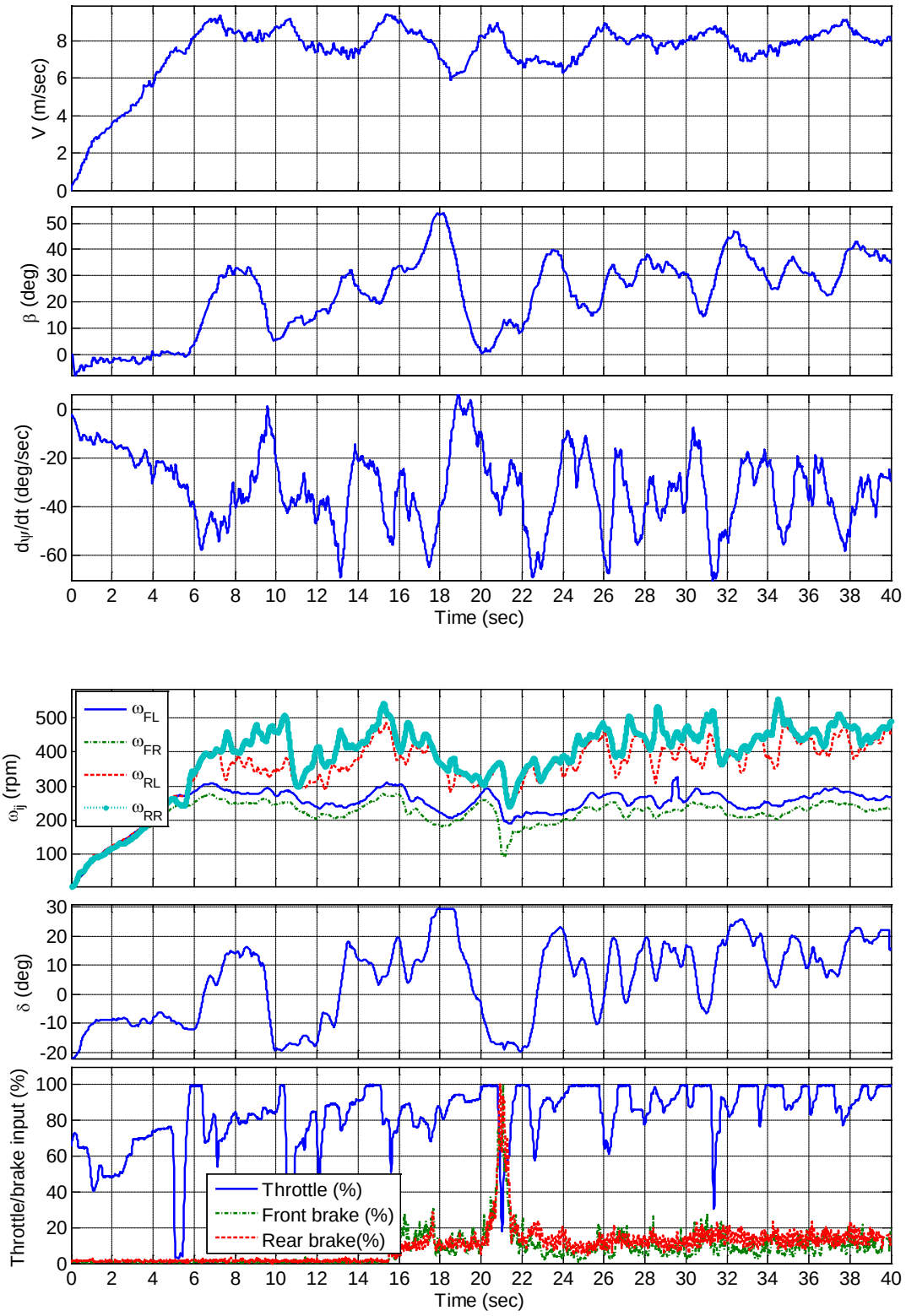

Fig. 5C 1. Vehicle states and driver's inputs.

The vehicle sideslip and yaw rate increased and the driver regulated the vehicle yaw moment by steering the front wheels towards the opposite direction with respect to the corner (counter-steered),

while applying a high value of throttle input. Similarly, we notice peaks of sideslip angle at approximately t = 13 sec and t = 17.5 sec under high throttle commands and counter-steer. During 25 ≤ t ≤ 40 sec we notice that the vehicle speed was stabilized close to 8.1m/sec and the yaw rate close to 36 deg/sec. The sideslip angle is stabilized at approximately 32 deg. We notice that the driver applied throttle close to the maximum and consistently counter-steered. Despite the corrections in the control inputs by the driver and the fluctuations of the vehicle states in this interval, we consider that the vehicle achieved a steady-state cornering condition, characterized by a high sideslip angle, which is referred to as steady-state drifting or powerslide [82].

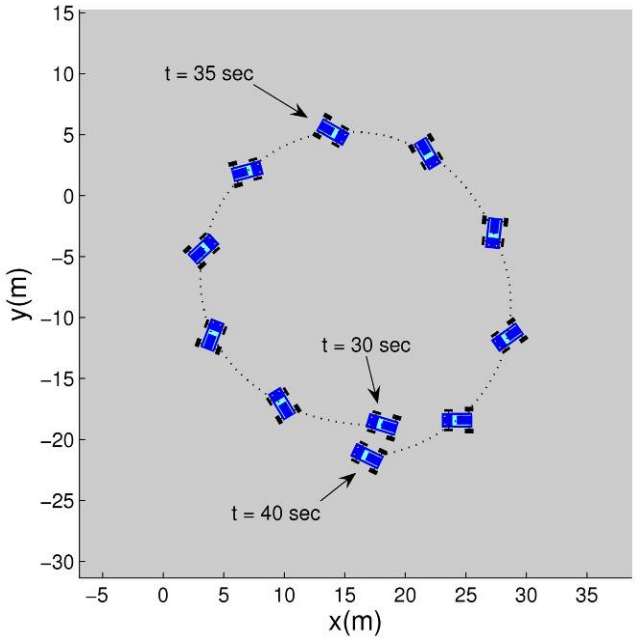

Fig. 5C 2. Vehicle's trajectory.

The equations of motion of a four-wheel vehicle, with front wheel steering, travelling on a horizontal plane (c.f. Fig. 5C 3) are given through equations (5.3.1) to (5.3.4). In the those equations m is the vehicle's mass, I_z is the moment of inertia of the vehicle about the vertical axis, V is the vehicle velocity at the CG, β is the sideslip angle at the CG and ψ is the yaw angle.

$$m\dot{V} = (f_{FLx} + f_{FRx})\cos(\delta-\beta) - (f_{FLy} + f_{FRy})\sin(\delta-\beta) + (f_{RLx} + f_{RRx})\cos\beta + (f_{RLy} + f_{RRy})\sin\beta \tag{5.3.1}$$

$$\dot{\beta} = \frac{1}{mV}\left[(f_{FLx} + f_{FRx})\sin(\delta-\beta) + (f_{FLy} + f_{FRy})\cos(\delta-\beta) - \left(f_{RLx} + f_{RRx}\right)\sin\beta + \left(f_{RLy} + f_{RRy}\right)\cos\beta\right] - \dot{\psi} \tag{5.3.2}$$

$$I_z\ddot{\psi} = \ell_F\left[(f_{FLy} + f_{FRy})\cos\delta + (f_{FLx} + f_{FRx})\sin\delta\right] + w_L\left(f_{FLy}\sin\delta - f_{FLx}\cos\delta - f_{RLx}\right) + w_R\left(f_{FRx}\cos\delta - f_{FRy}\sin\delta + f_{RRx}\right) - \ell_R\left(f_{RLy} + f_{RRy}\right) \tag{5.3.3}$$

$$I_w\dot{\omega}_{ij} = T_{ij} - f_{ijx}r \ \ (i = F, R, j = L, R). \tag{5.3.4}$$

The moment of inertia of each wheel about its axis of rotation is I_w, the radius of each wheel is r, and the rotation rate of each wheel is ω_{ij} ($i = F, R, j = L, R$). The steering angle of the front wheels (assuming equal angle for left and right front wheels) is denoted by δ, and the drive/brake torque applied on each wheel is T_{ij}. We have neglected the rolling resistances and self-aligning moments at the tires. The longitudinal and lateral friction forces at each wheel are denoted by f_{ijk} ($i = F,R, j = L,R$ and $k = x, y$). The distances ℓ_F, ℓ_R, w_L and w_R determine the location of the CG with respect to the centre of each wheel, as in Fig. 5C 3.

The tire forces f_{ijk} in the above vehicle model are calculated as functions of tire slip and wheel normal load using Pacejka's Magic Formula [59]. Tire slip refers to the non-dimensional relative velocity of the tire with respect to the road. The slip ratio and lateral slip [11] are defined as in equation (5.3.5), where V_{ijk} ($i = F, R, j = L, R, k =x, y$) are the tire frame components of the vehicle velocity vector at the centres of the four wheels. Neglecting vertical motion and pitch and roll rotations of the sprung mass of the vehicle, we calculate the normal load at each of the four wheels considering the static load distribution and longitudinal/lateral normal load transfer under longitudinal/lateral acceleration. For instance, acceleration a_x along the longitudinal body axis results in load transfer from front to rear wheels as in equation (5.3.6), where h is the distance of the vehicle's CG from the road level. Similarly, acceleration a_y along the lateral body axis results in load transfer from front-left to front-right and rear-left to rear-right wheels.

$$s_{ijx} = \frac{V_{ijx} - \omega_{ij} r_{ij}}{\omega_{ij} r_{ij}}, \qquad s_{ijy} = \frac{V_{ijy}}{\omega_{ij} r_{ij}} \tag{5.3.5}$$

$$\Delta f^{x} = \frac{mha_x}{\ell_F + \ell_R} \tag{5.3.6}$$

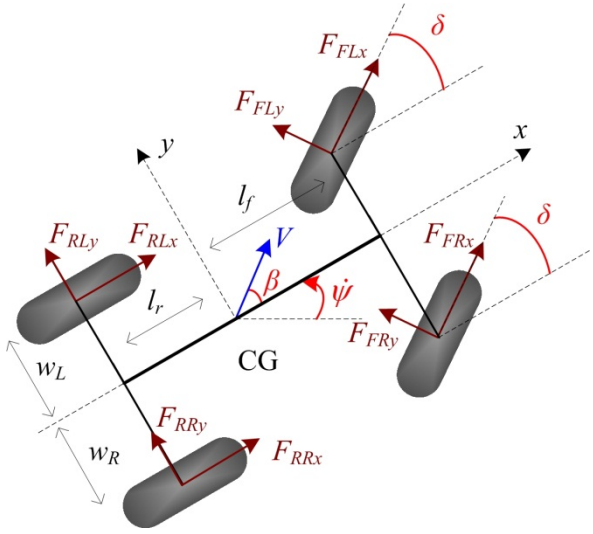

Fig. 5C 3. The vehicle dynamics model.

Finally, we introduce the model of a limited slip differential (LSD) system, which provides coupling of the drive torques of the driven rear-left and rear-right wheels, and allows us to consider a single drive torque input, corresponding to the driver's throttle command. Considering a RWD vehicle and assuming no braking command we have front wheel torques $T_{Fj} = 0$, ($j = L, R$). The output drive torque T_R from the gearbox will then be distributed between the rear-left and rear-right wheels, providing T_{RL} and T_{RR} of equation (5.3.4). In this work we use the torque transfer characteristics of a LSD differential model of the CarSim vehicle simulation software [29]. In particular, the torque transfer as a function of

the wheel speed differential is provided in CarSim in the form of a look-up table (c.f. Fig. 5C 4). The data of the look-up table were used to identify the following explicit expression of the differential torque transfer as a function of the wheel speed differential (c.f. equation (5.3.7)).

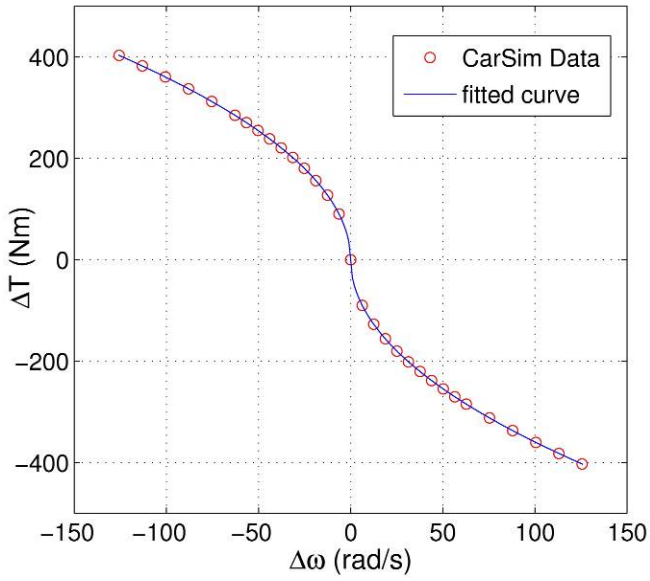

Fig. 5C 4. LSD torque transfer characteristic.

$$\Delta T(\Delta\omega) = -\text{sign}(\Delta\omega) C_d \sqrt{|\Delta\omega|} \tag{5.3.7}$$

$$T_{RR} = \frac{T_R - \Delta T(\Delta\omega)}{2},\ T_{RL} = \frac{T_R + \Delta T(\Delta\omega)}{2} \tag{5.3.8}$$

$$I_w \frac{d\Delta\omega}{dt} = \Delta T(\Delta\omega) - (f_{RLx} - f_{RRx}) r \tag{5.3.9}$$

In equation (5.3.7), $\Delta T = T_{RL} - T_{RR}$, $\Delta\omega = \omega_{RL} - \omega_{RR}$, and C_d is a positive constant. We may now consider a single torque input $T_R = T_{RL} + T_{RR}$ corresponding to the gearbox torque output, providing rear-left and rear-right wheel torques as in equations (5.3.8), where $\Delta T(\Delta\omega)$ derives from equation (5.3.7). Finally, using equations (5.3.4), (5.3.7) we derive the dynamics of the rear wheels speed differential as given in equation (5.3.9).

III. Steady state cornering

Steady-state cornering is characterized by a trajectory of constant radius $R = R^{SS}$, negotiated at a constant speed $V = V^{SS}$, constant yaw rate $\dot{\psi} = \dot{\psi}^{ss} = V^{ss} / R^{ss}$ constant sideslip angle $\beta = \beta^{SS}$, and constant wheel rotation rates $\omega_{ij} = \omega_{ij}^{SS}$. In steady-state cornering the control inputs, namely the steering angle $\delta = \delta^{SS}$ and rear axle torque $T_R = T_R^{SS}$ also remain constant.

Enforcing a steady-state cornering condition:

$$\dot{V} = 0, \quad \dot{\beta} = 0, \quad \ddot{\psi} = 0, \quad \dot{\omega}_{ij} = 0 \tag{5.3.10}$$

$$s_{Fjx}^{SS} = 0,\ f_{Fjx}^{SS} = 0,\ T_{Fj}^{SS} = 0,\ j = L,\ R \tag{5.3.11}$$

Now considering a RWD transmission and no braking command, that is enforcing free rolling of the front wheels we derive to equation (5.3.11). Providing fixed values for the steady-state pair (R^{ss}, β^{ss}), we are able to solve numerically equations (5.3.1)-(5.3.8) for the rest of the steady-state state variables

V^{SS}, ω_{ij}^{SS}, steady-state slip quantities and tire forces s_{ijk}^{SS}, f_{ijk}^{SS}, normal loads at the wheels f_{ijz}^{SS} and steady-state control inputs δ^{SS} and T_R^{SS} ($i = F, R, j = L, R, k = x, y$).

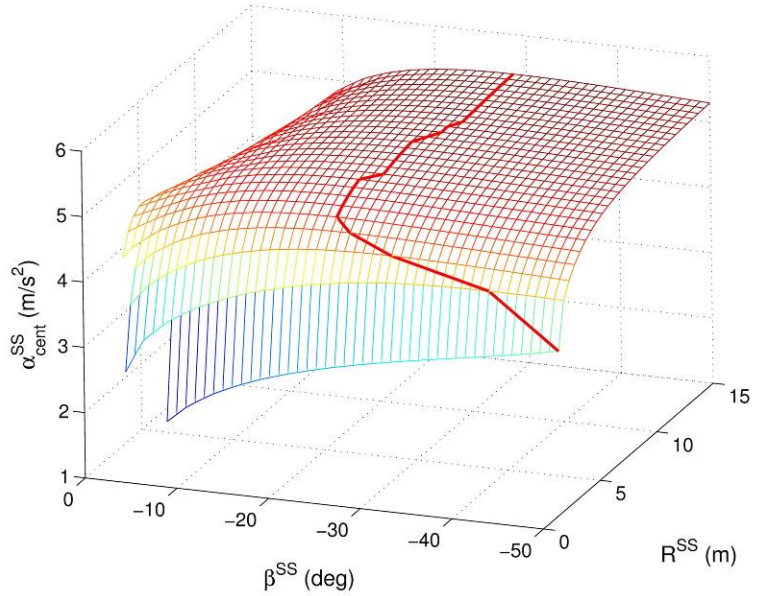

Fig. 5C 5. Steady-state cornering equilibria for a range of R^{ss} and β^{ss}.

Table 5C 1. Vehicle and tire friction model parameters.

m (kg)	850	l_f (m)	1.25
I_z (kgm^2)	1400	l_r (m)	1.25
I_w (kgm^2)	0.6	r (m)	0.311
w_L, w_R (m)	0.74	B	4
Cd (Nm/(rad/s)$^{1/2}$)	35.949	C	1.3
h (m)	0.5	D	0.62

In Fig. 5C 5 we present cornering equilibria for a range of path radius R^{ss} and sideslip angle β^{ss}, considering the vehicle and tire model parameters of Table 5C 1. In particular, we have plotted the steady-state value of the centripetal acceleration $a_{cent}^{SS} = (V^{SS})^2 / R^{SS}$. The solid line in Fig. 5C 5 passes through the maximum a_{cent}^{SS} for fixed R^{SS}. We notice the existence of steady-state conditions at extremely low path radii, which may expand the mobility characteristics of the vehicle, and that along paths of low radii the vehicle achieves the highest speed equilibria at higher sideslip angles.

IV. Stabilization of steady-state cornering

In the following we propose a control scheme to stabilize a RWD vehicle with respect to drifting equilibria, using control inputs directly correlated to the driver's commands. The proposed architecture consists of a linear controller providing stabilizing front wheel steering angle (corresponding to the driver's steering command), and rear wheel slip ratio inputs. In addition, a sliding mode controller calculates the rear differential drive torque necessary for the rear-left and rear-right wheels to achieve the slip ratios dictated by the previous linear controller.

Neglecting the dynamics of rotation of each individual wheel (equation (5.3.4)) we express the equations of motion of the full-car model (equations (5.3.1)-(5.3.3)), including the rear wheel speed

differential equation (equations (5.3.9)), as a system driven by the control inputs δ and one of the rear-left or rear-right wheel slip ratios, for instance s_{RRx}:

$$\dot{\tilde{x}} = f(\tilde{x}, u) \tag{5.3.12}$$

where $\tilde{x} = [V \ \beta \ \dot{\psi} \ \Delta\omega]^T$ and $\tilde{u} = [s_{RRx} \ \delta]^T$. We notice that, given the state variables *V*, and $\dot{\psi}$, the control input s_{RRx} can be used to calculate the rear-right wheel speed ω_{RR} from the definition (5.3.5). Then, using the state variable $\Delta\omega$, we calculate the rear-left wheel speed ω_{RL}, and rear-left wheel slip ratio s_{RLx} from (5.3.5). Hence, we may calculate longitudinal and lateral friction forces at both rear wheels, using the tire model of [59]. We also enforce free rolling of the front wheels (5.3.11).

Equations (5.3.12) are linearized about the equilibrium $\tilde{x}^{SS} = [V^{SS} \ \beta^{SS} \ \dot{\psi}^{SS} \ \Delta\omega^{SS}]^T$ and $\tilde{u}^{SS} = [s_{RRx}^{SS} \ \delta^{SS}]^T$ and a linear quadratic regulator is designed

$$\tilde{u} - \tilde{u}^{SS} = -\mathcal{K}(\tilde{x} - \tilde{x}^{SS}) \tag{5.3.13}$$

to stabilize the system (5.3.12) with respect to the equilibrium $\tilde{x}^{SS}$, using steering angle and rear-right wheel slip ratio inputs.

Next, we design a sliding mode controller using the rear drive torque T_R to regulate the slip ratios of the rear wheels to the values generated by the control law (5.3.13). We define the variable $\tilde{z}_{RR}$ as the difference between the actual wheel angular rate ω_{RR} and a reference wheel angular rate corresponding to a reference value of longitudinal slip $\hat{s}_{RRx}(V, \beta, \dot{\psi}, \Delta\omega)$:

$$\tilde{z}_{RR} = \omega_{RR} - \phi_{RR}(V, \beta, \dot{\psi}, \Delta\omega) \tag{5.3.14}$$

where $\phi_{RR}(V, \beta, \dot{\psi}, \Delta\omega)$ is the value of wheel rotation rate corresponding to the longitudinal slip $\hat{s}_{RRx}$ generated by (5.3.13):

$$\phi_{RR}(V, \beta, \dot{\psi}, \Delta\omega) = \frac{V_{RRx}}{(1 + \hat{s}_{RRx}(V, \beta, \dot{\psi}, \Delta\omega))r}$$

The sliding mode controller generates the following rear-right wheel torque

$$T_{RR} = T_{RR}^{\text{eq}} + I_w \hat{v}_{RR} \tag{5.3.15}$$

where

$$T_{RR}^{\text{eq}} = f_{RRx} r + I_w \left(\frac{\partial \phi_{RR}}{\partial V} f_1 + \frac{\partial \phi_{RR}}{\partial \beta} f_2 + \frac{\partial \phi_{RR}}{\partial \dot{\psi}} f_3 + \frac{\partial \phi_{RR}}{\partial \Delta\omega} f_4\right) \tag{5.3.16}$$

The component T_{RR}^{eq} is referred to as the *equivalent control*. Taking $T_{RR} = T_{RR}^{\text{eq}}$ results in $\dot{\tilde{z}}_{RR} = 0$ and ensures that the vehicle's states will remain in the *sliding manifold* $\tilde{z}_{RR} = 0$.

Equations (5.3.4), (5.3.14), (5.3.15) and (5.3.16) yield

$$\dot{\tilde{z}}_{RR} = \hat{v}_{RR} \tag{5.3.17}$$

Finally, we take

$$\hat{v}_{RR} = -\lambda_{RR} \text{sat}(\tilde{z}_{RR}), \ \lambda_{RR} > 0 \tag{5.3.18}$$

It can be readily shown that the control (5.3.18) stabilizes (5.3.17) [75]. In fact, all trajectories starting off the *sliding manifold* $\tilde{z}_{RR} = 0$ will reach it in finite time under the control input (5.3.15). We

notice that given T_{RR} from (5.3.15) we can calculate the corresponding rear differential drive torque T_R and rear-left wheel torque T_{RL} from equation (5.3.8).

V. Simulation results

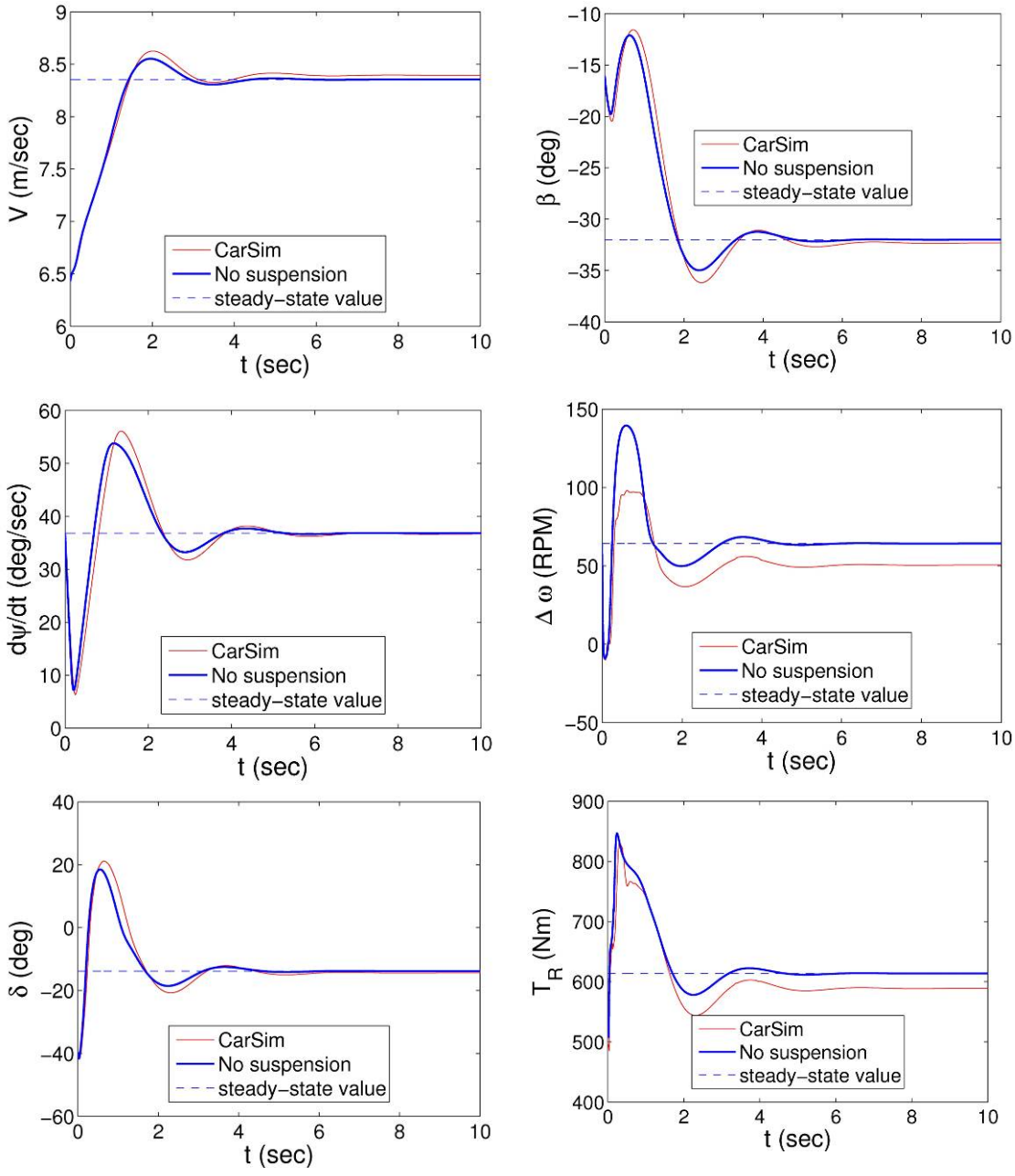

Fig. 5C 6. Vehicle states and control inputs during stabilization with respect to the cornering equilibrium of Table 5C 2.

In the following we present the implementation of the control scheme of the previous section in simulation. The parameters of the vehicle and tire friction model used in the numerical calculations are summarized in Table 5C 1, and we consider stabilization with respect to the calculated steady-state condition of Table 5C 2.

The initial velocity is perturbed by 30% and the initial sideslip angle by 50% from their steady-state values. The vehicle states and control inputs are shown in Fig. 5C 6. The states and inputs corresponding to the simulation of the full-car model (5.3.1)-(5.3.3), (5.3.4) with static normal load transfer (5.3.6), are denoted as "no suspension." The controller (5.3.13), (5.3.15) successfully stabilizes the vehicle with respect to the corresponding cornering equilibrium in finite time.

Table 5C 2. Steady state drifting conditions.

Variable	Data	Calculated
V^{SS}(m/s)	8.1	8.35
$\lvert\beta^{SS}\rvert$(kgm^2)	31.4	32
$\lvert\dot{\psi}^{SS}\rvert$ (deg/s)	36	36.8
$\lvert\Delta\omega^{SS}\rvert$ (RPM)	42.7	64.2
$\lvert\delta^{SS}\rvert$ (deg)	12.5	13.8

To further validate the control architecture, we implement the sliding mode controller using CarSim to simulate the response of a high-fidelity vehicle model including suspension dynamics. For consistency we incorporate the same tire friction model as with the "no suspension" model. We observe that the responses of the two different models are very close, and that the suspension dynamics essentially have no effect on the performance of the controller. We recall that the steady-state equilibria were derived after neglecting the suspension dynamics. Fig. 5C 7 shows the trajectory of the vehicle during stabilization, generated by the animation tool of CarSim.

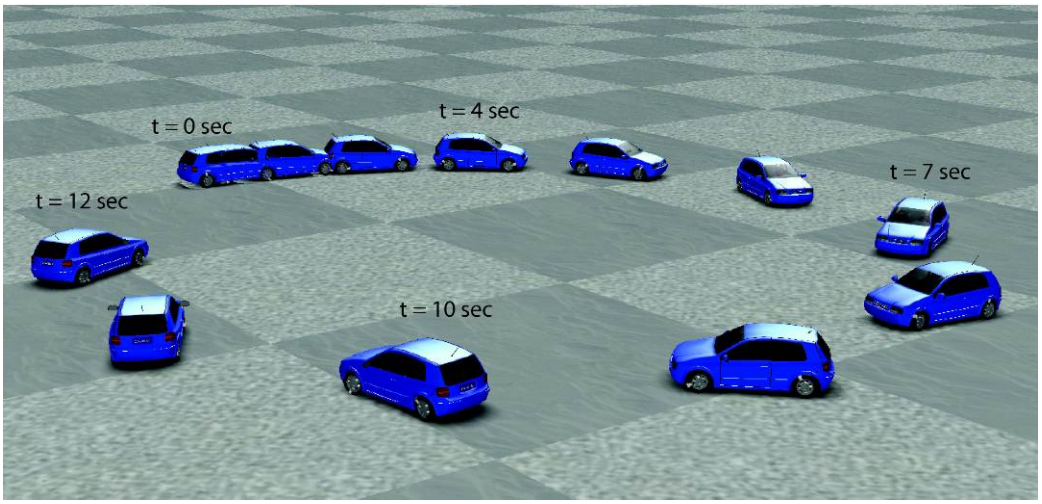

Fig. 5C 7. Vehicle's trajectory during stabilization.

VI. Conceptual driving steering support drifting interface

The proposed controller could motivate driver steering support drifting interface in the by-wire sense. The concept is illustrated in Fig. 5C 8. The 'desired steady-state derivation' block determines a steady-state pair of R^{SS}, β^{SS} using the car's states and the steering wheel and throttle position determined by the driver. The 'non-linear solver' block, solves numerically equations (5.3.1) to (5.3.9), to derive the rest of the steady state variables $\dot{\psi}_{SS}$, V^{SS}, ω_{ij}^{SS} steady-state slip quantities and tire forces s_{ijk}^{SS} normal loads at the wheels f_{ijz}^{SS} and steady-state control inputs δ^{SS}, T_R^{SS}. The 'solution selection' block then selects (out of the pool of steady-state solutions) the steady-states that are "closer"

(determined with a suitable cost function) to the current vehicle state and feeds them to the drifting stabilisation controller; the controller will in turn stabilise the vehicle by commanding a reference front wheels' angle δ_{ref} to the driver-by-wire steering system and the drive torque T_R to the limited slip differential.

The aforementioned concept for driver steering support drifting interface has to facilitate two issues. The first one is to derive the steady-state pair of R^{SS}, β^{SS} from the driver inputs and the current vehicle states. This could be implemented for instance with multidimensional look-up tables (created offline by the driver) or by simple functions relating vehicle speed, throttle position and steering wheel angle to the steady-state pair; presumably an extra input from the driver could be also fed into the system; e.g. the position of a knob at the steering related to the desired body-slip angle. The second one is the actual selection of the steady-state solution deriving from the non-linear solver. In the previous paragraph, we suggested as a potential approach for solving this issue, the selection of the steady-states which are "closer" to the current vehicle state. The second issue is also related to the time required to stabilize the vehicle near the steady-state. The controller can converge to a physically achievable steady-state in finite time; which might be not fast enough in a real application. Thus, the steady state solution selection could be weighted by the time required to stabilise the vehicle to a desired steady state from the current steady-state. Both aforementioned issues can prove difficult to overcome. However, we do envision vehicles with similar support systems in the near future utilizing the emerging technologies in sensors (e.g. the SKF load sensing wheel hubs [21][155], body-slip angle measurement etc.), actuators (e.g. driver-by-wire, torque vectoring techniques though sophisticated differentials or individual electric wheel drive motors etc.) and plenty in-vehicle computing-control power.

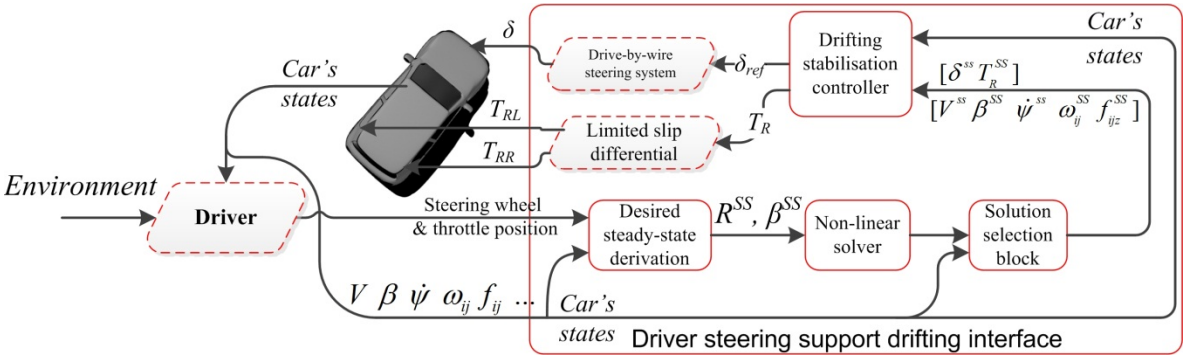

Fig. 5C 8. Driver steering support drifting interface.

VII. Discussion

In this work we studied the stabilization of RWD vehicles with respect to cornering equilibria characterized by aggressive sideslip angles. We discussed the results of a data collection experiment during execution of steady-state drifting by an expert driver and concluded that RWD vehicle drifting stabilization requires a combination of throttle and steering regulation. A full-car vehicle model with nonlinear tire characteristics was introduced to numerically calculate the steady-state cornering states and inputs. Incorporating realistic drive-train modelling we were able to derive control input variables with direct correlation to the driver's steering and throttle commands, namely, the steady-state front wheel steering angle and rear differential drive torque. A sliding mode control scheme was then proposed to stabilize the vehicle with respect to drifting cornering equilibria. The controller used combined steering angle and drive torque inputs, in accordance to our experimental observations, and was successfully validated via implementation in a high fidelity simulation environment. Finally, we

conceptually described how the proposed controller could motivate a driver steering support drifting interface in the by-wire sense.

Chapter 6. Driver Model with Visual and Neuromuscular Feedback for Objective Assessment of Automotive Steering Systems

"It is not by muscle, speed, or physical dexterity that great things are achieved, but by reflection, force of character, and judgment."
Marcus Tullius Cicero, 106-43 B.C.

Driver Model with Visual and Neuromuscular Feedback for Objective Assessment of Automotive Steering Systems

Abstract—Objective evaluation of vehicular steering systems can be enhanced through detailed driver models. In this Chapter a model is presented that consists of a preview controller part that responds to visual information and a neuromuscular component that reacts to steering force-feedback. The goal of this Chapter is to show that the developed model is sensitive towards steering wheel systems with different dynamics, and can predict both goal-directed steering wheel movements, as well as neuromuscular feedback. To provide evidence, different parameterizations of a steering system were simulated and tested in conjunction with the developed driver model. It was concluded that the developed model could predict the expected response for different steering setups.

I. Introduction

In the design process of new vehicle systems, performance evaluation is important but difficult. Although certain vehicular evaluation methods like the “moose test” are often used for handling rating, they are sometimes characterized unsuitable for objective assessment of the vehicle’s performance because the driver is involved in the control loop [95]. Objectivity can be ensured by examining solely the vehicle’s behaviour, but the total performance is always realized in conjunction with the driver. In other words, the driver will always have an important role in the vehicle behaviour, not only during manual control but also during supervisory control of an automatic system (e.g. if dissatisfied he can switch off the ESP [117]).

The design of steering systems has gained renewed interest with the electrically power assisted steering (EPAS) trend. With EPAS, the “steering feel” (which can be regarded as the relation between the applied steering wheel torque and the resulting steering wheel angle) can be easily manipulated and optimized. Traditional design methods rely on real field tests, a time-consuming subjective process with limited adjustment range. An alternative would be to use high-fidelity moving base driving simulators [32] in the prototyping process, since they offer a high flexibility in steering system modelling. Still, a human-in-the-loop (HIL) test will be subjective, and entail issues like inter and intra-subject variability.

Substituting test drivers by a validated driver model would enable the definition of an objective performance metric. If both the vehicle and the driver are replaced by a computer model the optimal steering system can be sought through traditional optimization methods.

Traditionally, driving is seen as a visually dominant task [96][123] and most driver models are limited to describing responses to visual feedback (e.g. preview driver models [145]). However, drivers also rely on neuromuscular (NMS) and vestibular feedback [145], especially in more extreme manoeuvres. Only recently, kinesthetic features on driver modelling have been proposed [145][49][11], that recognize that a driver responds to steering wheel forces not only cognitively, but also instantaneously (through limb inertia and visco-elasticity from co-contracted muscles) as well reflexively (with fast responses from proprioceptive sensors in the muscles).

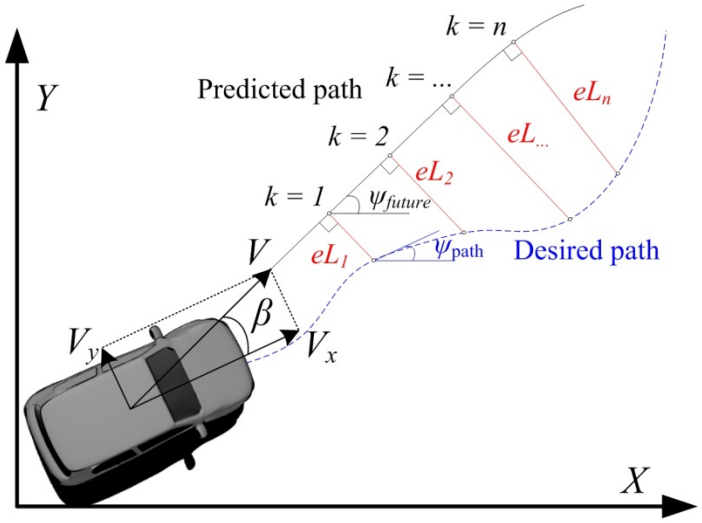

Fig. 6.1. Illustration of the path-following part of the FFDM. The driver's desired steering angle is determined by independent gains on the lateral errors *eLn* and yaw angle error $\psi_{future} - \psi_{path}$.

The goal of this Chapter is to introduce a Force-Feedback Driver Model (FFDM) based on previous NMS models developed at TU Delft [51][10][168] to evaluate the driver-car interaction with various steering systems settings, under different test scenarios that involve response to forces. This required combining the existing NMS models with a preview driver model leading to a coherent structure proposed earlier by Pick and Cole [11]. The resulting FFDM was coupled to a vehicle and steering system dynamics model.

Section II describes the preview controller where Section III details a general model of the steering system. Section IV introduces the total driver model with NMS dynamics which translates desired steering inputs to muscle torques using feedforward and feedback control. In Section V two test scenarios (lane-keeping with a force perturbation and lane change) are used to demonstrate that the model can predict driver's control actions (steering torques and angles) for different power steering gains, steering ratios and settings of the NMS stiffness. Finally in Section VI the results and future work will be discussed, and Section VII concludes the Chapter.

II. Preview controller and vehicle dynamics model

Early driver models were simple with error compensation behaviour (e.g. McRuer *et al*. [56]). A preview path tracking functionality was soon incorporated into them [116] where the steering action was decided upon the lateral error between the desired path and the predicted vehicle position a certain distance ahead of the vehicle. MacAdam [23], proposed a preview model based on optimal control theory for the calculation of the desired steering angle. It estimates its future path through an internal bicycle Vehicle Dynamics Model (VDM). It uses a weighted sum of the previewed lateral errors for each preview point and does not account for the yaw angle error. Sharp's *et al* model [145]uses a weighted sum of the future lateral and the current yaw error.

In this Chapter a multi-point preview driver model similar to Sharp *et al*. [145] has been implemented (c.f. Fig. 6.1). The steering angle command is determined from the yaw angle error, $e\psi_k = \psi_{future} - \psi_{path}$ ($k = 1$) and the lateral errors eL_k ($k = 1,.., n$) between the "Predicted path" and the "Desired path." The lateral errors eL_k are determined from the length of the perpendicular line of the n equally time-spaced points (up to the $T_{preview}$ time ahead) as in Fig. 6.1. Both yaw and lateral error vectors are multiplied with an individual gain vector $W\psi$ and WL, to derive the error signals $E\psi = e\psi \cdot W\psi / |W\psi|$ and $E_L = eL \cdot WL / |WL|$ for the controller.

The predicted path *X, Y* is estimated through a bicycle model which is also the vehicle model used in the simulations (Fig. 6.2). The lateral tire forces are estimated as the product of the tire slip angle and the lumped left and right tire cornering stiffness as in (6.1) [142] (pp. 15-49). The slip angle is defined as the angle between the longitudinal axis of the wheel and its velocity vector (α_f, α_r in Fig. 6.2). The slip angles are calculated as in (6.2) [142]. The vehicle dynamics model parameters are summarized in Table 6.1.

$$F_{fy} = \alpha_f C_f,\ F_{ry} = \alpha_r C_r \tag{6.1}$$

$$\alpha_f = \delta - \tan^{-1}\left(\frac{\dot{y} + l_f\dot{\psi}}{\dot{x}}\right),\ \alpha_r = -\tan^{-1}\left(\frac{\dot{y} - l_f\dot{\psi}}{\dot{x}}\right) \tag{6.2}$$

Applying Newton's second along the lateral axis y and the vertical axis around the centre-of-gravity (CG) results in the following equations:

$$I\ddot{\psi} = l_f F_{fy} - l_r F_{ry} \tag{6.3}$$

$$m\left(\ddot{y} + \dot{\psi}\dot{x}\right) = F_{fy} + F_{ry} \tag{6.4}$$

Substituting from equations (6.1) and (6.2)to (6.3) and (6.4) and assuming small angles (e.g. *atan (α) ≈ α*) the space model form of (6.5) can be obtained [142].

$$\frac{d}{dt}\begin{Bmatrix}\dot{y}\\ \dot{\psi}\end{Bmatrix} = \begin{bmatrix} -\frac{C_f + C_r}{m\dot{x}} & \frac{C_r l_r - C_f l_f}{m\dot{x}} - \dot{x} \\ \frac{C_r l_r - C_f l_f}{I_z\dot{x}} & -\frac{C_f l_f^2 + C_r l_r^2}{I_z\dot{x}} \end{bmatrix} \cdot \begin{bmatrix}\dot{y}\\ \dot{\psi}\end{bmatrix} + \begin{bmatrix} C_f / m \\ C_f l_f / I_z \end{bmatrix}\delta \tag{6.5}$$

The vehicle's longitudinal velocity $\dot{x}$ in (6.5) is considered to be a constant parameter of the system. The vehicle's local coordinates *x, y* are translated to the global *X, Y* with (6.6):

$$\begin{aligned} X(t+T) &= \int_t^{t+T}\left(\dot{x}\cos\psi - \dot{y}\sin\psi\right)d\tau + X(t) \\ Y(t+T) &= \int_t^{t+T}\left(\dot{x}\sin\psi + \dot{y}\cos\psi\right)d\tau + Y(t) \end{aligned} \tag{6.6}$$

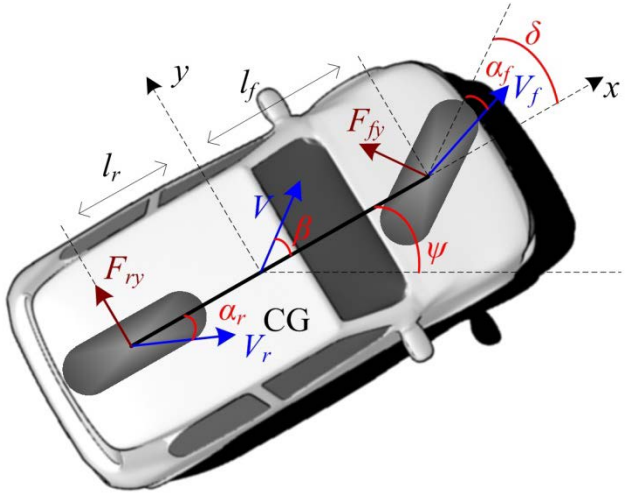

Fig. 6.2. The bicycle model for estimating the Predicted path.

The predicted path for T time ahead over time t is estimated through (6.6) by solving the system of (6.5). The VDM of (6.5) has been also used for the rest of this work for estimating the vehicle's planar dynamics.

Table 6.1. Vehicle dynamics model parameters.

Symbol	Description	Value	Unit
M	Mass of the vehicle	1200	kg
I_z	Moment of inertia around the Z axis at the CG	2100	kg·m^2
l_f, l_r	Distance of front/rear axle from the CG	1.5 1.4	m
C_f, C_r	Cornering stiffness front/rear axle	42, 45	KN/rad
$\dot{x}$, $\dot{y}$	Longitudinal, lateral velocity	19.4, -	m/sec

Table 6.2. Preview controller parameters.

Symbol	Description	Value	Unit
$T_{preview}$	Preview look-ahead time	1	sec
$WL, W\psi$	Lateral, yaw gain vectors	(4,1.7,1.5,1.3,1,1,1,1,1,1), (3)	
G_L,G_ψ	Lateral, yaw error gains	0.25, 2	-
τ_{vd}	Visual transport delay	0.16 [11]	sec
St_{ratio}	Steering ratio ($1/(Rs \cdot R_x W_\delta)$)	13.33	(Explained in Section III)

The complete preview controller is illustrated in Fig. 6.3. The "Path predictor" predicts the future position X_{future}, Y_{future} for $T_{preview}$ time ahead, using the *Vehicle states* and the output of the "Global vehicle position," global coordinates X, Y, ψ. The "Desired path selector" block uses the predicted path information and determines the "Desired path" (as in Fig. 6.1). Its output is a local map of the desired path within a 30 m radius from the CG. The "Error calculator" estimates the yaw E_ψ and lateral E_L error signals which are multiplied by the G_ψ and G_L gains. The calculation E_ψ and E_L is described in detail in [34]. Their summations results to a desired steering angle $\delta_{desired}$ which passes through the steering ratio St_{ratio}. Its output is subjected to a visual transport delay τ_{vd} to derive the desired steering wheel angle signal $\theta sw_{desired}$.

The $\theta sw_{desired}$ fed through the steering system, results to the angle δ (Fig. 6.2). The values used are summarized in Table 6.2.

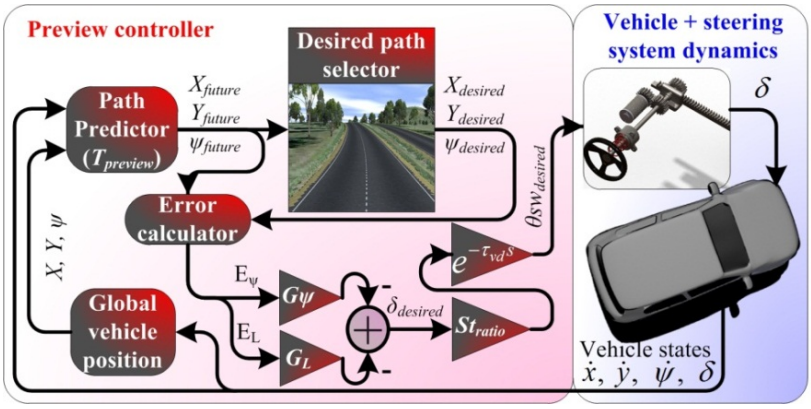

Fig. 6.3. Multipoint point path preview controller + vehicle and steering system dynamics model without the NMS part.

III. Steering system modelling

Fig. 6.4 illustrates the steering system model which was coupled to the preview controller and the VDM. It is a realistic representation of an EPAS system found in modern vehicles, consisting of a steering column, a torque sensing element, an assist motor, and a rack-pinion assembly. The system equations are described in (6.7)-(6.11). The parameters and nominal values of the system are summarized in Table 6.3.

$$J_s\ddot{\theta}sw = T_d - T \tag{6.7}$$

$$T_s = k_s(\theta sw - \frac{x_r}{R_s}) + b_s(\dot{\theta}sw - \frac{\dot{x}_r}{R_s}) \tag{6.8}$$

$$T_{assist} = G_a(\theta sw - \frac{x_r}{R_s}) \tag{6.9}$$

$$m_r\ddot{x} = \frac{(T_s + T_{assist})}{R_s} - b_r\dot{x}_r - F_r \tag{6.10}$$

$$\delta = x_r \cdot R_x W_\delta,\ F_r = F_{fy} \cdot W_f R_f \tag{6.11}$$

The forces acting on the steering system are the driver's torque and the forces from the front wheels. The power assist T_{assist} is a function of the strain at the steering column (6.9). The resulting rack displacement x_r from the T_d application is translated through the R_xW_δ to the wheels' angle δ (6.11). The R_xW_δ factor represents the suspension kinematics. The lateral wheel forces F_{fy} are translated to rack forces F_r through the W_fR_f (6.11) factor which represents the suspension kinematics the mechanical trail and the pneumatic trail of the tires.

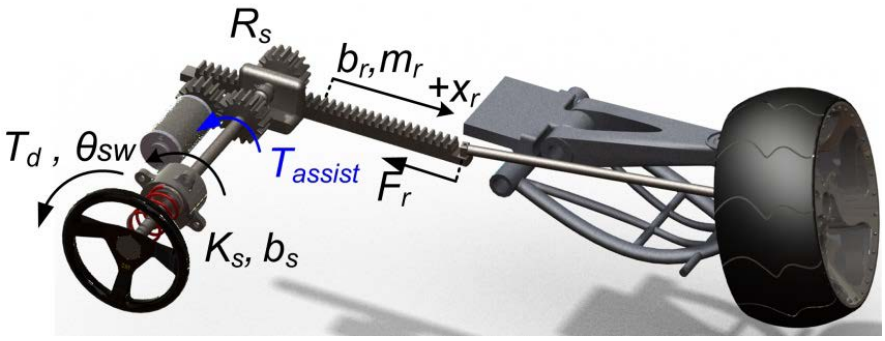

Fig. 6.4. Steering system dynamic model.

Table 6.3. Steering system variables and parameters.

Variables		Parameters	
Name	Description (value)	Name	Description (value)
T_d	Driver's torque (Nm)	G_a	Power assist gain (5)
T_{assist}	Assist torque (Nm)	R_s	Pinion gear radius (0.015 m/rad [134])
F_r	Rack force from tie rod (N)	b_s	Steering column damping (0.07 Nm/rad/sec [134])
θsw	Steering wheel angle (rad)	J_s	Steering wheel + column moment of Inertia (0.16 kg·m^2 [134])
x_r	Rack displacement (m)	b_r	Rack damping (0.2 N/m/s [134])
		m_r	Rack + suspension + wheels mass (50 kg [134])
		W_fR_f	Wheel force to rack force gain (0.1)
		R_xW_δ	Rack displacement to wheel angle (5 rad/m)
		k_s	Steering column stiffness (170 Nm/rad [134])

IV. The neuromuscular driver model

In the modelling approach followed in this Chapter, the desired steering angle $\theta sw_{desired}$ from the preview controller is a set-point for the NMS model. The NMS system will realize this angle exactly, if a) the commanded motion does not exceed the NMS bandwidth, b) there are no force perturbations, c) there is no execution noise, and d) if the driver has a perfect internal model of his own limb, steering system and VDM dynamics. On top of such goal-directed movements, the driver can adjust his impedance through co-contraction and reflexive impedance [106] in order to respond to the dynamics of the steering system or resist possible force perturbations. Experiments and NMS modelling showed that it is even possible to use muscle activity and reflexes to actively give way to forces, which is useful in case of haptic guidance [51].

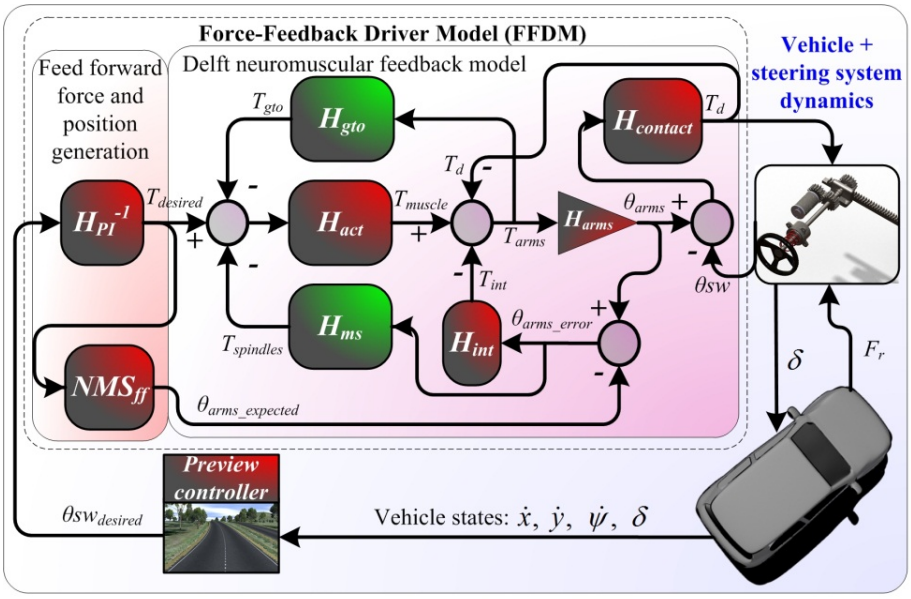

Fig. 6.5. The total Force-Feedback Driver Model, with focus on the neuromuscular model structure. The preview controller is shown in Fig. 6.3.

The use of a NMS model for steering has been thoroughly investigated in the Driver Vehicle-Dynamics Group at Cambridge [11][12]. Their research has used model simulations and optimizations to find reasonable parameter values that describe co-contraction and muscle spindle feedback. A slightly different model structure, of which the parameter values can be identified during human-in-the loop experiments has been developed at TUDelft [10][168]. Identification methods have been extended to separate visual and NMS feedback in car-following [51]. In this Chapter the existing NMS model structure, was extended to a driver model for steering (Fig. 6.5). An important adaptation needed to extend the NMS feedback models to goal-directed movements is the addition of an internal model [11][106]. This internal model describes the combined physical interaction dynamics (e.g. inertia, damping, stiffness) resulting from the driver's arms and the steering wheel. The driver needs such a model "H_{PI}^{-1}" (c.f. Fig. 6.5) to determine the required steering torque to reach the $\theta sw_{desired}$.

The output of the internal model "H_{PI}^{-1}" is a supraspinal signal that represents the muscle torque $T_{desired}$ required to reach a desired position θsw (Fig. 6.6) as in (6.17). The $T_{desired}$ is the input to the "Delft NMS feedback model" block (described in detail in Ref. [10]) shown in Fig. 6.5. All important motion control mechanisms are described here shortly as well.

The supraspinal input is combined with possible input from reflexive pathways to form a combined activation input for the lumped muscle activation dynamics of the arms "H_{act}," modelled as a second-

order low-pass filter (6.12). Reflexive pathways provide the driver with muscle stretch and stretch velocity feedback from the muscle spindles "H_{ms}" (6.13) as well as muscle force-feedback from Golgi Tendon Organs "H_{gto}." Both reflexive pathways are characterized by a spinal time delay τ_{spin} limiting its effective bandwidth. Instantaneous visco-elastic properties from already (co)-contracted arm muscles are contained in "H_{int}" (6.14), which can increase the overall limb stiffness and damping at the expense of metabolic energy. Increased co-contraction levels can reduce errors due to torque perturbation as well as due to imperfections in the "H_{PI}^{-1}" and are commonly encountered when learning new movements [57]. The resulting torque T_{arms} accelerates the inertia of the arms "H_{arms}" (6.15) leading to the arms position θ_{arms}. The θ_{arms} through the contact dynamics "$H_{contact}$" (6.16) results in the steering wheel angle θsw. The resultant steering wheel position θsw will be identical to the position of the hands on the wheel, in case the driver grasps the steering wheel in an infinitely stiff grip. In reality this is not the case, and experiments have shown that some finite grip visco-elasticity "$H_{contact}$" is always present [168].

$$H_{act}(s) = \frac{\omega_n^2}{s^2 + 2\zeta\omega_n + \omega_n^2} \tag{6.12}$$

$$H_{ms}(s) = \frac{T_{spindle}(s)}{\theta_{arms\_error}(s)} = (k_{spin} + b_{spin}s) \cdot e^{-s\tau_{spin}} \tag{6.13}$$

The NMS feedback parameters used in this Chapter are summarized in Table 6.4 and were obtained from initial parameter identification on a single subject holding a steering wheel in response to torque perturbations, using techniques tested for lower limb motion control [168]. The low values were measured during relaxed conditions, and the high values when asking the subject to resist force perturbations. Note that for ease of modelling and explanations, we assumed GTO activity to be zero. The "H_{PI}^{-1}" internal model is expressed by (6.17). It contains identical parameters as the NMS and steering system, in other words a perfect internal model. It also provides a moving reference point to the muscle spindle feedback and intrinsic feedback, so that they do not counteract intended movements. To this purpose, the output of the "H_{PI}^{-1}" block is fed to the block "NMS_{ff}" (ff; feed-forward). The "NMS_{ff}" represents the driver's knowledge, on where his arms will reach if he develops the $T_{desired}$ torque. It is the transfer function from the $T_{desired}$ to the θ_{arms} with disabled spindles and intrinsic dynamics, yielding the arms expected angle $\theta_{arms\_expected}$ when the $T_{desired}$ torque is being applied (6.18).

$$H_{\text{int}}(s) = \frac{T_{\text{intrinsic}}(s)}{\theta_{arms\_error}(s)} = k_{\text{int}} + b_{\text{int}}s \tag{6.14}$$

$$H_{arms}(s) = \frac{1}{I_{arms}s^2} \tag{6.15}$$

$$H_{contact}(s) = \frac{T_d(s)}{\theta_{arms}(s) - \theta sw(s)} = k_{hands} + b_{hands}s \tag{6.16}$$

$$H_{PI}^{-1}(s) = \frac{T_{desired}(s)}{\theta sw(s)} \ (with\ H_{ms}, H_{\text{int}}, H_{gto} = 0) \tag{6.17}$$

$$NMS_{FF}(s) = \frac{\theta_{\text{arms\_expected}}(s)}{T_{desired}(s)} (with\ H_{ms}, H_{\text{int}}, H_{gto} = 0) \tag{6.18}$$

The analytic expressions of the aforementioned transfer functions (6.17), (6.18) can be obtained with the signal-flow graph method of Mason [143] through Fig. 6.6.

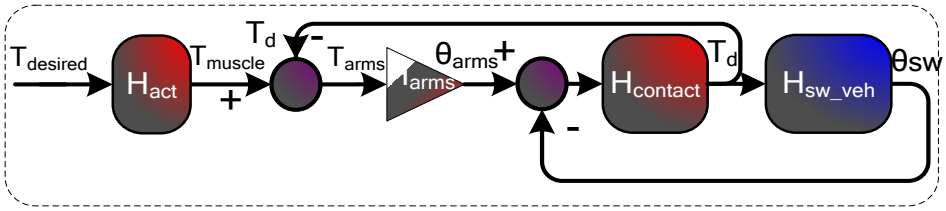

Fig. 6.6. Block diagram for obtaining the "NMS_{ff}" and "H_{PI}^{-1}" transfer functions. The "H_{sw_veh}" in the transfer function from the T_d to θsw.

Table 6.4. Neuromuscular feedback parameters.

Block	Value		Block	Value	
Activation dynamics "H_{act}"	ω_n	2.17·2·π rad/s	Spindles "H_{spin}"	k_{spin}	0- 4 Nm/rad
	ζ	0.74		b_{spin}	0.3- 1.65 Nm/rad/s
				τ_{spin}	20 ms
"H_{gto}"	0		Arm inertia "H_{arms}"	I_{arms}	0.16 kg·m^2
Intrinsic dynamics "H_{int}"	k_{int}	5- 52.5 Nm/rad	Contact dynamics "$H_{contact}$"	k_{hands}	600 Nm/rad
	$b_{int,}$	0.7- 0.85 Nm/rad/s		b_{hands}	13 Nm/rad/s

V. Simulation results

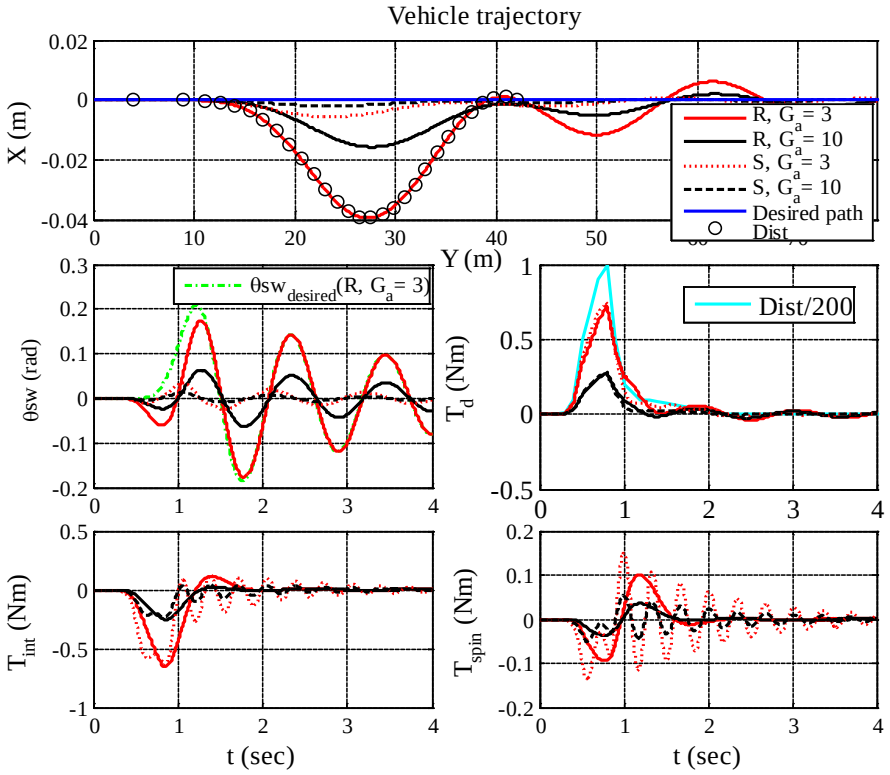

Fig. 6.7. Lane keeping simulation with 70 km/h with a force disturbance applied to the steering rack; Relaxed (R) and a Stiff (S) driver with power assist gain G_a = 3, 10 and R_s = 0.015. The top subplot shows the vehicle's trajectory where the rest shows internal components of the FFDM; steering wheel angle θsw, driver's torque T_d, intrinsic torque T_{int} and spindle torque T_{spin}. Visual transport delay τ_{vd} = 0.16 sec. The notation in the legend is common for all subplots. The $\theta sw_{desired}$ has been additionally plotted (green dashed-dotted line) for the of 'R, G_a = 3' case.

To gain confidence that the developed model can address differences in steering wheel systems or NMS settings, two different simulation scenarios are tested. The first one is a simulation of lane

keeping where a force disturbance is introduced to the front wheels, inducing the steering rack to move. In this simulation it can be expected that lateral deviations will be smaller when the driver's NMS dynamics are stiff or the power assist gain is high. The second scenario simulates a lane change manoeuvre, with the goal to show that the same trajectories can be realized with different power assist gains or steering wheel ratios, although they will entail different steering wheel torques and positions.

Fig. 6.7 illustrates the lane keeping simulation with a visual delay τ_{vd} = 0.16 sec. Four different parameterizations are shown: Relaxed 'R' and Stiff 'S' driver (corresponding to the minimum and maximum values of Table 6.4) for two power assist gains G_a = 3, 10. On the top subplot one can see the trajectory of the vehicle. The circles on the trajectory for (R, G_a = *3*) denote the application time window of the disturbance, which is illustrated normalized in the T_d subplot (200N peak). For readability the 'circles' have been plotted only for one parameterization.

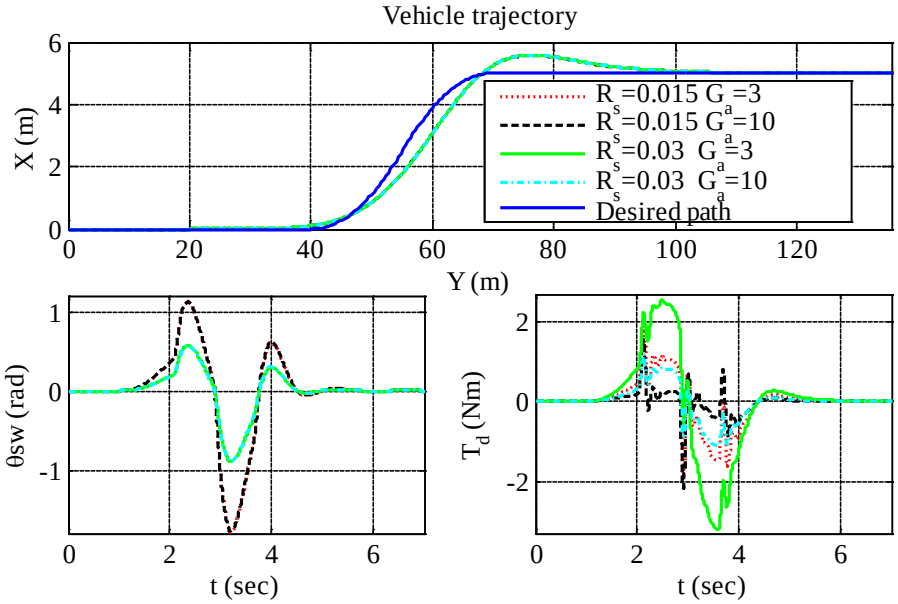

Fig. 6.8. Lane change manoeuvre at 70km/h simulated for power assist gains G_a = 3, 10 and pinion gear radii R_s = 0.015, 0.03. Visual transport delay τ_{vd} = 0 sec. The driver's NMS is considered to be stiff. The notation in the legend is common for all subplots.

As expected, the simulation results in Fig. 6.7 show that the torque perturbation will have the largest influence on the travelled trajectory in case of relaxed NMS settings and a low power assist gain G_a (red solid line). The perturbation will be rejected best in case of a large G_a combined with stiff NMS settings (black dashed line). The driver will need to deliver the largest torques in case of a low power assist gain (red lines). Note that during lane keeping, feedback not only occurs due to fast NMS feedback, but also due to slow visual feedback (G_L and G_ψ gains for the preview controller have been set to 0.12 and 1.2 respectively).

Fig. 6.8 illustrates the lane change simulation with τ_{vd} = 0 sec. The desired trajectory was derived with the methodology described in detail in [34]. Four different steering system combinations are tested: pinion gear radius R_s = 0.015, 0.03 and power assist gain G_a = 3, 10. The results are compared in terms of the trajectory, desired steering angle θsw and driver torque T_d. In this undisturbed case the realized vehicle trajectories are identical (within computational limits) for all four steering system settings (remember the "H_{PI}^{-1}" is considered to be perfect). However the steering system setup does influence the T_d and θsw signals. As expected the θsw with R_s = 0.03 is half compared to that of R_s = 0.015 and the T_d is the largest for the G_a = 3 and R_s = 0.03 and the lowest for G_a = 10 and R_s = 0.015.

The G_L and G_Ψ are given in Table 6.2 and about 40% higher compared to that of the lane keeping manoeuvre.

VI. Discussion

One of the issues concerning the model is the visual feedback during lane keeping and lane change. There is still controversy over how visual feedback is used by drivers [74]. For example, experiments conducted with high speed driving [34][63] show that a driver decides the steering actions in a feedforward manner with minimum corrections from his visual inputs. Especially expert drivers generate better feedforward steering inputs over high speed manoeuvres, relying less on their visual feedback, compared to non-expert drivers who tend to overcorrect their steering actions. In this simulation, it was chosen to use a visual feedback controller for both lane keeping and lane changing, with different gains and time delays in order to yield stable controllers.

The lane keeping task was simulated with a visual feedback delay. However, a linear controller with visual delay would not describe a real driver who anticipates to steer on a tight curve (e.g. that of Fig. 6.8); where a visual delay in the scale of 100 msec would make the driver-car system unstable. Without proposing a better model structure, it was chosen to adopt the approach often used in literature: to model a lane changing behaviour as visual feedback control with zero time delay. Relatively small feedback gains were needed to retain stability, and even though the time-delay is zero, still the desired path in Fig. 6.8 is not reached without some overshoot.

Fig. 6.7 shows that, when the disturbance is introduced during lane keeping, co-contraction (modelled by intrinsic dynamics) will counteract it instantaneously, followed by the muscle spindles, which start their contribution with delay τ_{spin} from the time that an unexpected difference in steering wheel displacement is sensed by the nervous system. Only when the steering angle displacement affects the trajectory of the vehicle, will the preview controller start to correct with τ_{vd} delay, which causes the oscillatory behaviour of Fig. 6.7. To further illustrate the difference between visual feedback and NMS feedback during the perturbed lane keeping, the output of the preview controller $\theta sw_{desired}$ has been plotted (only for '*R*, G_a = 3') together with the realized steering wheel position θsw. The perturbation influences θsw instantaneously, due to the properties of the steering system and the response of the NMS system, whereas the $\theta sw_{desired}$ only is affected after τ_{vd} sec. Besides the lower G_L and G_Ψ gains (compared to the lane change) the model cannot compensate for the decaying oscillatory behaviour introduced by the visual delay. This is not realistic, and a better model must be found for describing lane changes and other types of (partly) open-loop control.

A serious limitation of the lane change modelling is that the 0 sec visual delay and the higher G_L and G_Ψ gains cause the preview controller to react instantaneously on the visual changes. In other words, the controller output $\theta sw_{desired}$ is equal to θsw (Fig. 6.5), since "H_{PI}^{-1}" is assumed perfect and no unexpected disturbances occur. This essentially means that such a model structure provides visual feedback reaction without a time delay, within the same scale of reaction speed with the NMS system.

Experiments for system identification of the NMS part of the model (according to [168]) have already been performed (2012) using the Opel Astra presented in Chapter 7. The results will investigate the extent to which open-loop feedforward control and closed-loop feedback control contribute to steering (which is still a matter of debate [74]); culminating in an elaborate total model identification and validation of the FFDM. The final goal is the coupling of a validated FFDM to a high fidelity vehicle dynamics model to guide steering system optimization according to the driver's requirements, the vehicle's setup and the driving conditions. The validated model will be able to predict drivers control actions in response to naturally occurring torques from a designed steering system, as well as additional guiding torques from haptic guidance systems [49].

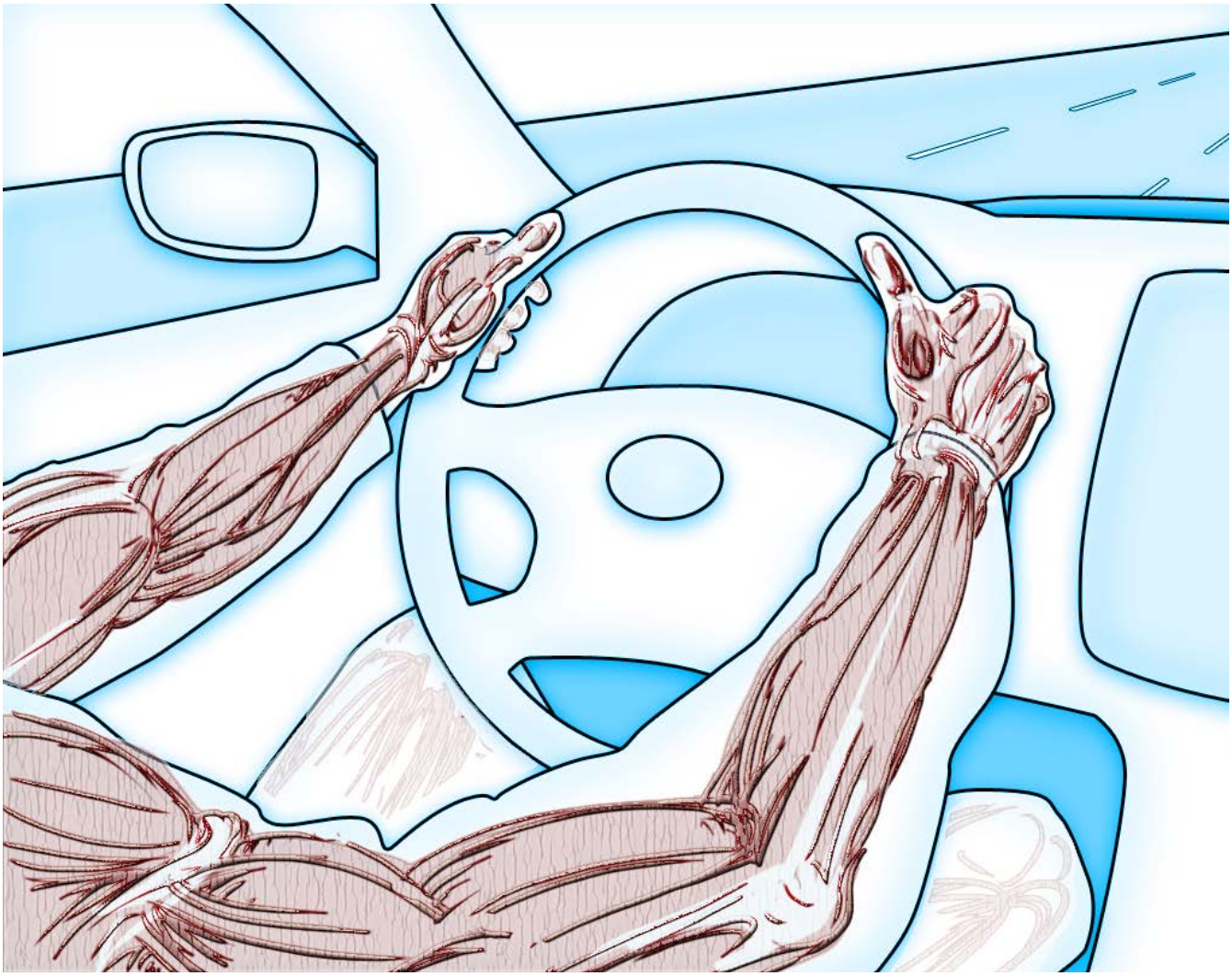

Fig. 6.9. Neuromuscular driver representation. Designed by Antonis Katzourakis and presented in AVEC10 [31].

VII. Conclusion

The objective evaluation of the impact of certain vehicular components on the driving task, with the driver in the loop, required the development of a suitable driver model. Therefore a Force-Feedback Driver Model (FFDM) was developed, consisting upon a preview controller and a neuromuscular (NMS) model both described in detail. Two different simulation scenarios with multiple steering system setups illustrate that the model captures how steering system settings and NMS settings affect driving performance

It is too early to draw broader conclusions because the validation process of the FFDM is still on-going. However, within the content of this Chapter, it has been shown that the FFDM has the potential to become a useful tool in vehicular steering system evaluation.

VIII. Acknowledgements

The research was supported by the Automotive Development Center of SKF as part of the project Mobility Intelligence using Loadbased Lateral Stability (MILLS). David Abbink was supported through the VENI grant from NWO.

Chapter 7A. Haptic Steering Support for Driving Near the Vehicle's Handling Limits; Skid-Pad Case

“I couldn't find the sports car of my dreams, so I built it myself.”
Ferdinand Porsche, 1875-1951 A.D.

Haptic Steering Support for Driving Near the Vehicle's Handling Limits; Skid-pad Case

Abstract—Current vehicle dynamic control systems from simple yaw control to high-end active steering support systems are designed to primarily actuate on the vehicle itself, rather than stimulate the driver to adapt his/her inputs for better vehicle control. The driver though dictates the vehicle's motion, and centralizing him/her in the control loop is hypothesized to promote safety and driving pleasure. Exploring the above statement, the goal of this study is to develop and evaluate a haptic steering support when driving near the vehicle's handling limits (Haptic Support Near the Limits; HSNL). The support aims to promote the driver's perception of the vehicle's behaviour and handling capacity (the vehicle's internal model) by providing haptic (torque) cues on the steering wheel. The HSNL has been evaluated in (a) driver-in-the-loop simulation and in (b) real track testing with a vehicle (Opel Astra G/B) equipped with a variable steering feedback torque system. In the simulator study (a) 25 drivers attempted to achieve maximum velocity, on a dry skid-pad while trying to retain control of the simulated vehicle parameterized as the Astra. In (b) 17 drivers attempted to achieve maximum velocity, around a wet skid-pad while trying to retain control of the Astra. Both the driving simulator and the real vehicle tests led to the conclusion that haptic support assisted the test subjects to drive closer to the designated path while achieving effectively the same speed. In the presence of haptic support, the drivers operated the tires in smaller slip angles and hence avoided saturation of the front wheels' lateral forces and excessive understeer. Finally, the support reduced their mental and physical demand.

I. Introduction

Modern cars are equipped with advanced driving assist systems such as the electronic stability control (ESC), active front steering (AFS) and lane departure warning/prevention (LDW/P) systems. Several studies since 1998 have showed the ESC's effectiveness [71], depicting that the global installation of ESC could reduce skidding accidents by even 80% [127]. Similarly, active steering systems have been credited to improve the handling characteristics of the car and increase the driving comfort [166][167]. Considering now systems designed to operate in less dynamic driving conditions, LDW/P systems have also proven to promote safety [70][45] even in emergency situations [41]. Likewise, steering support in low acceleration curve negotiation, has exposed that haptic support is an efficient way to improve the driver-car interaction [131][119][122], improving curve negotiation performance and decreasing driving effort.

Support systems for moderate driving conditions, often share control with the driver in the "haptic shared control" sense [48], operating under the principle that the driver should be aware of the system's activity by force information on the control interface (e.g. the steering wheel in a LDW/P system). Systems that provide force information to the driver in a wider dynamic range near the vehicle's handling limits, where for instance the ESC and AFS would intervene, appear not to have been academically studied prior to this study (to the best of the author's knowledge).

This Chapter elaborates on the concept of a haptic steering support when driving near the vehicle's handling limits (Haptic Support Near the Limits; HSNL). Handling limits denotes operation near the lateral acceleration limits imposed by the tire-road adhesion. The goal of the system is to promote the driver's perception of the vehicle's behaviour and handling capacity (the vehicle's internal model) by providing haptic cues on the steering wheel. The haptic controller was initially tested in a driving simulator and was later adapted-improved to be tested in a 1.8L Opel Astra (Fig. 7A 1) equipped with a variable steering feedback torque system. Results showed, that an informative haptic force to the steering wheel promoted driving closer to the designated path while achieving effectively the same speed. The support also induced driving with smaller in magnitude tire slip angles and decreased driving effort (mental and physical demand).

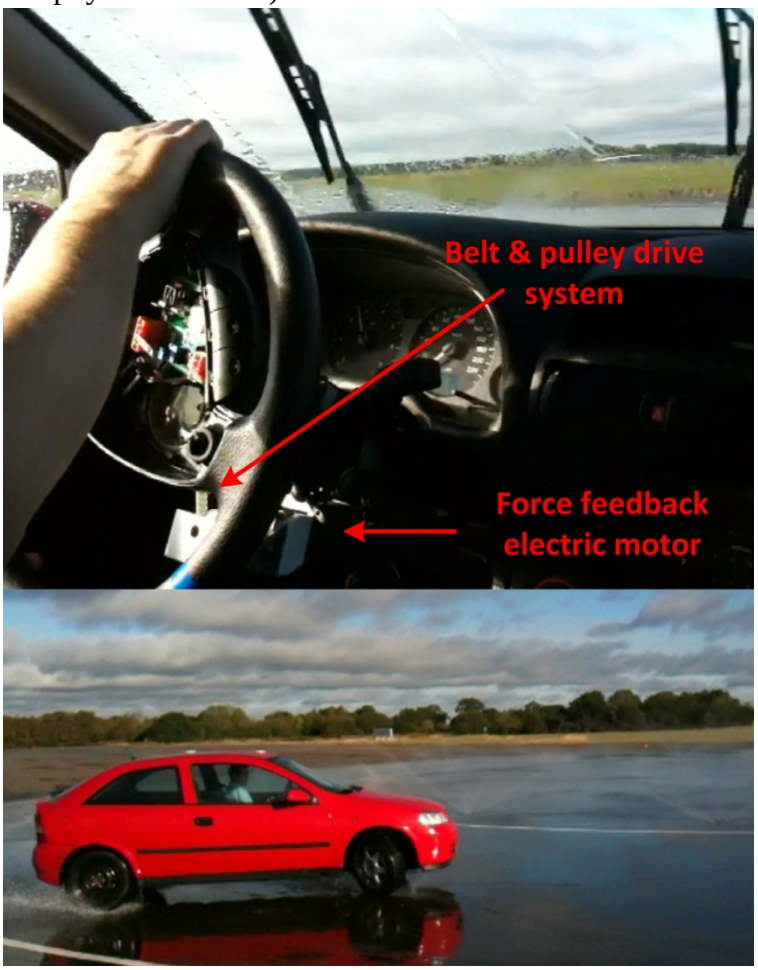

Fig. 7A 1. Force-feedback Opel Astra in wet skid-pad testing.

This study is organized as follows: the rationale of HSNL is first introduced in section II, followed by a brief description of the support controller. In continuation, the human in the loop simulation tests and real track driving tests including the corresponding methods and results, are presented into sections III and IV correspondingly. The simulation and the real test results are then compared in the discussion section V which concludes this study.

II. Haptic steering support rationale

A. The vehicle's inherent steering feedback

The rationale behind the HSNL, derives from the vehicle's property to reduce the steering "stiffness" (the steering feedback torque as a function of the steering wheel angle) before the vehicle reaches its handling limits and starts to understeer. Understeering occurs when the front axle slip angle becomes greater in magnitude than the slip at the rear axle [161] (pp. 203). The HSNL, exaggerates the reduction of steering "stiffness" and makes it profound to the driver, so he/she avoids excessive steering angle inputs which will result in increased tire slip and consequently lateral force loss.

The reduction effect of the self-aligning moment at the steering wheel has been credited as valuable feedback to the driver [142] (pp. 408); but had not been experimentally proven since present (2012). This effect is normally concealed under certain vehicle's properties, such as the non-linear speed-dependent power steering assist [40][165][134], the coulomb friction and damping in the steering rack [134], the suspension compliance [89] (pp. 284) etc. Even in case of a "rich in feedback" steering system, this information would be hardly noticeable by less experienced the drivers, because it is subtle and would require high concentration on the haptic information arriving from the steering wheel. This effect becomes profound when the front wheels stop developing more lateral forces with increasing slip angle (referred as terminal understeer).

The tire peak lateral force depends mainly on the tire-road friction coefficient μ and the normal force. The friction coefficient though, has minor influence on the lateral forces at small slip angles [110](Ch. II, pp. 22); the C_F tire's cornering stiffness (slope of lateral force vs. slip angle at zero slip angle) is therefore not or hardly influenced by the condition of the road being wet or dry (c.f. [79], pp. 6 and [30], pp. 329). This is illustrated in Fig. 7A 2 (top). The magenta dashed line, displays the front axle's cornering stiffness of both front tires lumped together, with different friction coefficients μ values (1, 0.7, 0.5, 0.2).

The tires though do offer a mechanism to inform in advance the driver that the tires' handling limits are being approached. This mechanism is the reduction of the pneumatic trail L_{pt} [89]. The pneumatic trail is the distance L_{pt} of the point of action of the resultant tire force from the geometric centre of the contact patch. The L_{pt} length starts to reduce at smaller slip angle values than the value where the tire lateral peak force occurs [89] (pp. 95). The lateral force F_y multiplied with the pneumatic trail L_{pt} (decreasing with increasing slip angle), constitutes the resultant self-aligning moment M_z (c.f. Fig. 7A 2) at the front axle (left and right wheels lumped together). Fig. 7A 2 has been created using the pneumatic trail definition of Hsu and Gerdes [173] and the non-linear Bakker-Pacejka (1987) [59] tire model by adjusting the tire's B and D parameters for individual μ using constant values (B_{con}, C_{con}, D_{con}). The product BCD multiplied with the normal force depicts the slope of the lateral force at zero slip angle (thus the cornering stiffness) in Fig. 7A 2. For creating individual curve in Fig. 7A 2 for the displayed μ values, D is multiplied with μ ($D = D_{con} \cdot \mu$) and B divided with μ ($B = B_{con} / \mu$) so that the product BCD remains the same for all μ values. The steering rack forces in the bottom subplot of Fig. 7A 2, derive from the M_z and F_y through the mechanical trail L_{trail} (due to the caster angle) and the steering arm lever length L_{arm} (on the suspension knuckle). The values used can be found in [40] ('X-car' case).

Fig. 7A 2 shows that the rack force is dominated by term a (due to F_y) rather than term b (due to M_z) and hence provides limited cues regarding road friction and lateral grip limits. Concepts that inject the steering feedback torque with artificial components date back to the 1970 [53]. In [53] the steering feedback torque was augmented with an additional component induced by a pendulum's movement due to the lateral acceleration experienced by the vehicle. A haptic support system has been patented by

TRW Automotive [85] generating a haptic steering torque based upon the vehicle's a) lateral acceleration and the b) the yaw rate error (difference between the real vehicle's yaw rate and the desired yaw rate deriving from the driver's inputs). When a) the vehicle's "lateral acceleration builds up," the controller will increase the "effective road reaction feedback" sensed by the driver. When b) the "yaw rate error builds up," corresponding to understeer or oversteer of the vehicle, the haptic torque controller will reduce the "road reaction feedback" sensed by the driver. The inventors depict that "there is a general perception that these effects improve the handling of a vehicle, and therefore they can be quite important in certain market segments."

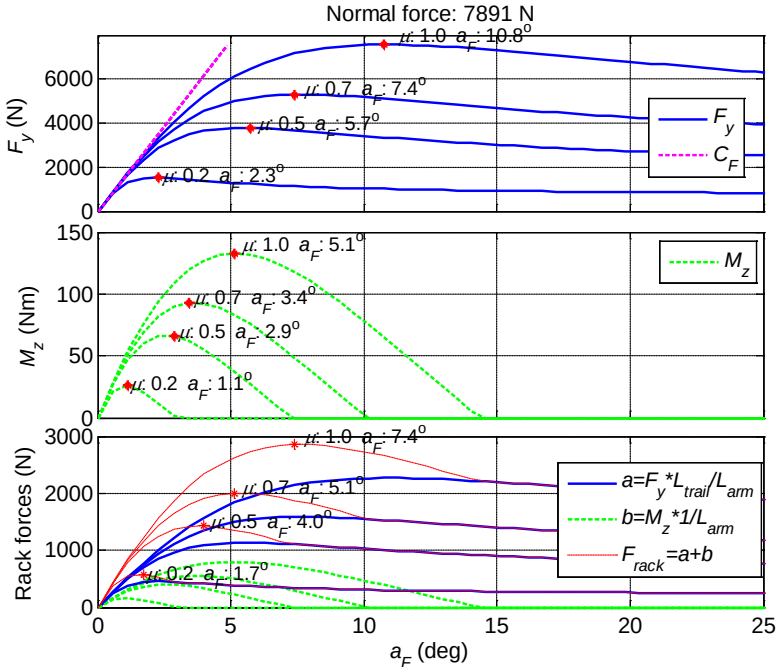

Fig. 7A 2. Front axle forces and torques, assuming zero longitudinal slip. Front axle lateral force F_y (top), self-aligning torque M_z of the front wheels lumped together due to the pneumatic trail (middle) and steering rack forces due to F_y and M_z through the suspension (bottom); all as a function of the front axle slip angle a_F.

B. Haptic support controller

Fig. 7A 3 portrays the haptic support (HS) concept, which was implemented and tested in simulation and the real vehicle. The 'Alert detection' block, using the vehicle current states and properties, signals an 'alert' when an undesired effect is imminent, e.g. excessive front wheels' slip which can lead understeer. The *resulting torque* in Fig. 7A 3 divided by the inertia of the steering wheel J_{sw}, will impose the acceleration $\ddot{\theta}_{sw}$, the velocity $\dot{\theta}_{sw}$ and finally the angle θ_{sw} of the steering wheel. The θ_{sw} will dictate the front wheel's steering angle δ. δ will determine the vehicle states which will create the rack force F_{rack} which will be fed into the steering system and determines the *steering feedback torque*. The T_{HS} has always the same sign as the T_{driver} (and a smaller value; *HS factor* always < 1). The controller assumes knowledge of the friction coefficient μ (the detailed operation of the controller cannot be explained; patent pending; Chapter 1IV).

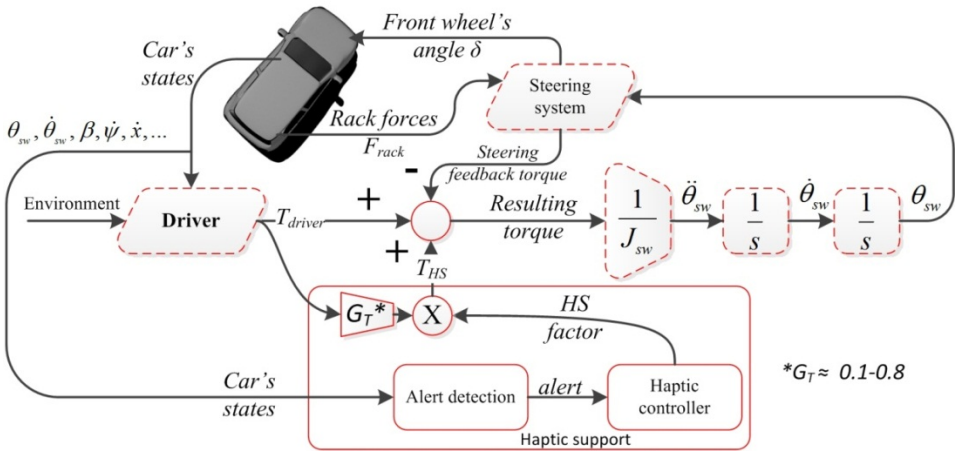

Fig. 7A 3. Block diagram of the HSNL concept. The 'alert' signal induces the 'haptic controller' to produce the *HS factor* (HS: haptic support), a signal between 0 and 1. This signal is multiplied with the 'driver's torque' T_{driver} (conditioned with the gain G_T) to derive the haptic support torque component the T_{HS}. When *HS factor* increases, it exaggerates the reduction of the aligning moment at the steering wheel.

Fig. 7A 4 illustrates the principle of operation of the controller in open loop dry (μ = 0.9; top subplots) and slippery (μ = 0.28; bottom subplots) simulation with longitudinal speeds of 48 and 22 Km/h correspondingly. The steering wheel angle starts from 0^o and increases by 17^o/s up to 310^o for μ = 0.9 and up to 270^o for μ = 0.28. In the left subplots, the blue solid line represents the 'normal' feedback torque, where the green dashed line shows the steering feedback torque with the HSNL enabled as function of the steering angle (steering "stiffness"); the right subplots show the vehicle's yaw rate and desired yaw rate (c.f. equation (7.1.1) [142], subsection VI.A) as a function of steering angle. With haptic-support (HS) the steering torque (left subplots) starts to drop before the vehicle starts to severely understeer (right subplots) resulting to a "lighter" steering. The displayed simulation results of Fig. 7A 4, were generated using a purpose built Matlab/Simulink FWD vehicle dynamics model, with 7 degrees-of-freedom (DOF), incorporating a 4 DOF steering system as in [40], load transfer (function of accelerations) and non-linear Bakker-Pacejka (1987) tire model [59] with the pneumatic trail definition of Hsu and Gerdes [173].

C. Haptic support alternatives

One would argue that restricting the driver from achieving an unsafe steering input might also be an efficient way for support. This could be achieved by increasing the steering "stiffness" if the vehicle is severely understeering or oversteering (in both cases further increase of the steering should be avoided). This support would fall into the "haptic shared control" domain [48], where haptic torques guide the driver towards a certain steering angle [119][122].

The author argues that the haptic guidance approach would offer an unrealistic steering feedback, as explained in the rationale subsection A. The unrealistic feedback could contradict with the driver's internal vehicle model; a driver would expect that with the increasing feedback torque the vehicle can develop higher cornering forces. Also, a strong guiding torque (trying to impose a "certain" steering wheel angle), would approach automation similar to ESC and AFS, where the system actuates directly on the vehicle. Since the "certain" steering wheel angle could be imposed by the AFS itself, the HSNL would be unnecessary in the first place. The above two arguments, in conjunction with the rationale subsection A, depict the author's choice for evaluating the suggested HSNL.

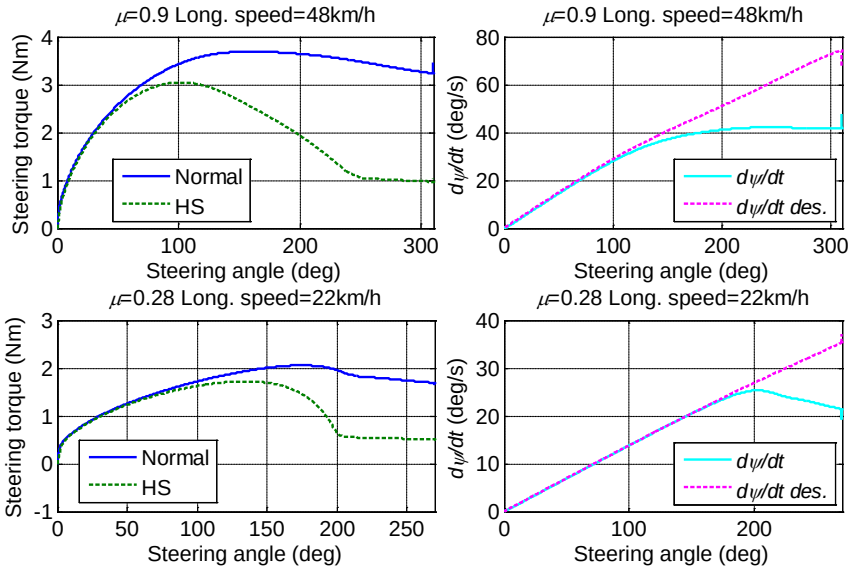

Fig. 7A 4. Principle of operation of the haptic controller for 2 simulated conditions: μ = 0.9 with 48Km/h longitudinal speed (top panel) and μ = 0.28 with 22Km/h longitudinal speed (bottom panel). Steering torque vs. steering angle (steering "stiffness") (left) and yaw rate and desired yaw rate vs. steering angle (right).

III. Driving simulator tests

A. Methods

i)The simulator

The tests for the haptic steering support have been performed in the X-Car simulator [32]. The simulator is based on a dSPACE real-time computer and runs a commercial 24 DOF vehicle dynamics model (VDM) employing Pacejka's non-linear tire model. The VDM is developed on a Matlab/Simulink block, from the dSPACE Automotive Simulation Model package. The simulation fidelity (vehicle's dynamical response and steering force-feedback) of the X-Car was assessed using the steering torque gradient and steering sensitivity metrics, from empirical results [40].

ii)Test procedure

The test was designed to be a "within-subject" experiment for reduction in error variance associated with individual differences [137]. The test subjects were instructed to drive a FWD car (parameterized as a nominally understeering Opel Astra G/B) around a circular track (skid-pad) of 20 m radius. The radius was set to achieve a theoretical maximum velocity of 50.4 Km/h (14.0 m/s) (imposed by the tire-road adhesion limit) with the friction coefficient set to μ = 1.

The drivers were instructed to follow the white line in the middle of the road (centring the vehicle on top) while attempting to achieve maximum velocity without losing lateral control. In order to get the subjects accustomed with the simulator, they drove around the track for 5 minutes. Afterwards, they drove 7 practice runs and 9 recorded runs of 25 seconds each, with and without support, summing up to a total of 14 practice and 18 recorded runs. They always drove counter-clockwise starting with the vehicle centred on the middle line marking the 20 m radius skid-pad.

The test group consisted of 25 male drivers with a mean age 25.2 (σ = 11.7) years. The drivers possessed their driving licence on average for 6.9 (σ = 10.8) years, they had an average of 0.1 (σ = 0.3) crashes and graded themselves with mean 7.4 (σ = 0.8), in a scale from 1-10, with 1 being incompetent to 10 being an expert driver. To compensate a potential learning effect, 18 drivers first drove without

support and the remaining 7 first drove with support. After the 9 recorded runs, the drivers were asked to fill in the NASA Task Load Index (TLX) form [154].

iii)Data processing and analysis

To isolate a close to steady state cornering condition and compensate for the extreme cases of control loss, which would statistically harm the analysis, the first 5 seconds were excluded from individual test, as well as, all instances where the speed was lower than 35 Km/h and/or the lateral error was greater than 4 m. On average this resulted in 18.54 and 18.50 seconds of data per run for the no-support and the support case correspondingly (statistically insignificant difference as assessed with a paired *t*-test; $p < 5\%$). The root-mean-square (RMS) values of individual metric was used in the analysis. The RMS values from all 9 runs per driver were averaged together to derive a data vector with 25 observations. Statistical significance of the results was assessed with paired *t*-tests, performed at the $p < 5\%$ significance level. The data were rank transformed [170] before performing the *t*-test, for higher robustness (to cope with possible outliers) and to keep the ordinal scale.

Objective performance was evaluated with the metrics described in the appendix subsection VI.A. The results are illustrated using boxplots of the RMS values of the metrics. On each box within a boxplot (e.g. Fig. 7A 5), the median is the central mark, the 25^{th} and 75^{th} percentiles are illustrated with the edges of the box and the whiskers extend to the most extreme data points not considered outliers. Points are drawn individually as outliers if they are larger than $p75 + 1.5\cdot(p75 - p25)$ or smaller than $p25 - 1.5\cdot(p75 - p25)$, where p25 and p75 are the 25^{th} and 75^{th} percentiles, respectively. The Y label of individual boxplot, depicts the corresponding metric. The 'normal' and 'HS' label in the X-axis of individual boxplot corresponds to the no-support and the HSNL tests correspondingly. The *p* value of the *t*-test is shown between the 'normal' and 'HS' boxes; *p* values in red indicate that the difference between the 'normal' and the 'HS' mean values was statistically significant with greater than 95% confidence. The mean RMS values of the metrics are displayed above the central mark on individual box.

Objective performance was also evaluated using the probability distribution and its corresponding cumulative sum of the absolute yaw rate difference, the absolute lateral error at the vehicle's CG with the respect to the 20 m middle line and the absolute front axle slip angle. The probability distributions have been created by aggregating all corresponding values from all 25 drivers and their 9 runs into one vector.

B. Results

i)Objective results

In general terms all drivers managed to perform the task both with and without support. Drivers did not report any discomfort or physical fatigue while driving. However, on average they reported that controlling the vehicle required high level of concentration and that the task was not trivial. Several runs involved a complete loss of control. This is reflected in the average amount of data per run which did not differ significantly between the no-support and support condition as discussed in the previous subsection A.iii).

Fig. 7A 5 to Fig. 7A 7 are related to the vehicle's control performance, whilst Fig. 7A 8 and Fig. 7A 9 are related to the driver's control effort.

ii)Vehicle's control performance

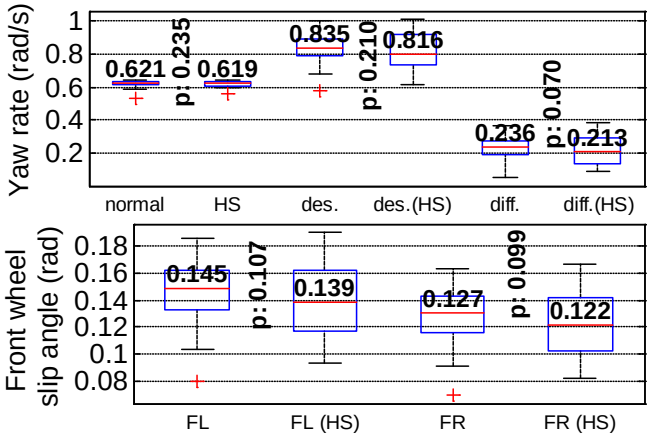

Fig. 7A 5. Boxplots related to yaw rate (top) and front left (FL) and front right (FR) wheel slip angles (bottom). The top boxplot displays the yaw rate (normal and HS), the yaw rate desired (des. and des. (HS)) and yaw rate difference (diff. and diff.(HS)) for both the 'normal' and the 'HS' cases.

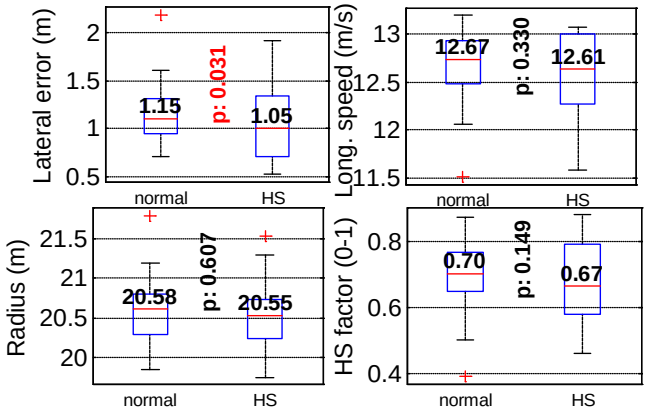

Fig. 7A 6. Boxplots of 1) the lateral error (top left) at the vehicle's CG with the respect to the 20 m middle line; 2) the longitudinal speed (top right); 3) the cornering radius (bottom left) and 4) the *HS factor* (c.f. Fig. 7A 3) (bottom right) for both the 'normal' and 'HS' cases.

The top boxplot of Fig. 7A 5 shows the RMS yaw rate, desired yaw rate and yaw rate difference as defined in equation (7.1.1) (c.f. subsection VI.A). The RMS yaw rate for 'normal' was not significantly different compared to 'HS'; the desired yaw rate for the 'HS' was lower (2.3% difference) compared to 'normal'. Although the drivers achieved almost similar yaw rate in both test cases, they understeered less with 'HS' (p = 0.07). The bottom boxplot of Fig. 7A 5 displays the RMS slip angle of the front left and right wheels. The 'HS' case yielded smaller slip angles for both wheels. The drivers in the 'HS' case, achieved a similar yaw rate as in the 'normal' case (Fig. 7A 5, bottom boxplot), but they used a smaller slip angle spectrum. They therefore achieved similar performance while "pushing" their tires less.

The top left boxplot of Fig. 7A 6 displays the RMS lateral error with respect to the centre line. The 'HS' case exhibited a statistically significant smaller lateral error which can be interpreted as better vehicle lateral control performance compared to the 'normal' case. The top right boxplot of Fig. 7A 6 shows no significant difference for the longitudinal speed for the 'normal' and the 'HS' case. The cornering radius was not statistically significant different between the 'normal' and 'HS' case (bottom left boxplot of Fig. 7A 6). The *HS factor* signal (c.f. Fig. 7A 3) which defines an imminent alert was

lower in the 'HS'. It is noted that the *HS factor* in the 'normal' case did not alter the steering feedback torque. It is only being displayed for comparison purposes.

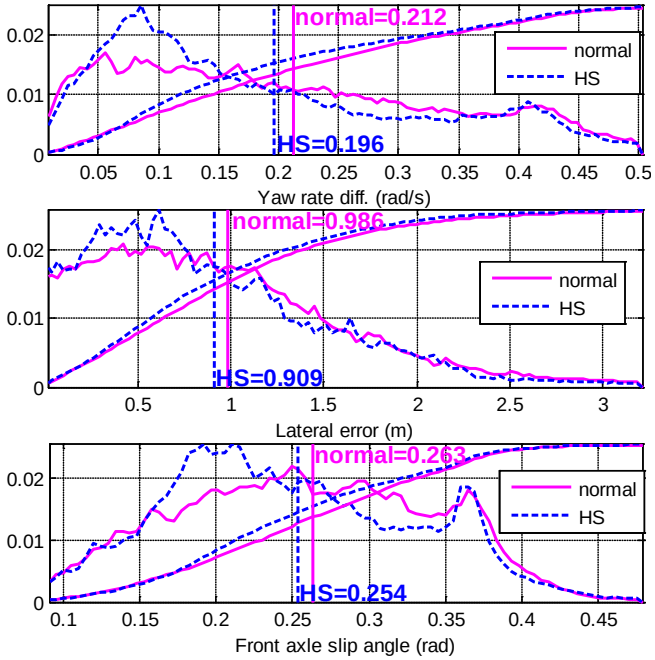

Fig. 7A 7. Probability distribution and its corresponding cumulative sum of the absolute yaw rate difference (top), the absolute lateral error at the vehicle's CG with the respect to the 20 m middle line (middle) and the absolute front axle slip angle (bottom) for both the 'normal' and the 'HS' cases. The vertical lines and the corresponding text show the mean absolute value of the corresponding metric. For illustration purposes, the cumulative sum plots have been multiplied with the maximum probability of the either the 'normal' or the 'HS' case (the highest of two). The probability distributions have been created by aggregating all corresponding values from all 25 drivers and their 9 runs into a vector.

Fig. 7A 7 shows the probability distribution and its corresponding cumulative sum of the absolute yaw rate difference (top), the absolute lateral error at the vehicle's CG with the respect to the 20 m middle line (middle) and the absolute front axle slip angle (bottom) for both the 'normal' and the 'HS' cases. The cumulative sum normally ranges from 0 to 1; however, for illustration purposes both 'normal' and 'HS' curves have been multiplied with the maximum probability value of the either the 'normal' or the 'HS' case (the highest of two). For all the three displayed metrics in Fig. 7A 7, the 'HS' cumulative sum curve has a higher value compared to 'normal' around the mean (designated with the vertical lines). Hence with 'HS', the drivers were more probable to experience: less understeer (smaller yaw rate difference), smaller lateral error and smaller front axle slip values. In general, the HSNL helped the drivers to avoid the corresponding extreme values.

iii)Driver's control effort

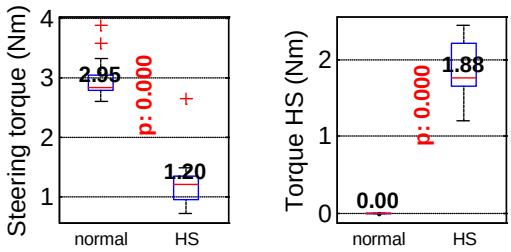

Fig. 7A 8. Boxplots of steering torque (left) and the T_{HS} (c.f. Fig. 7A 3) (right) for both the 'normal' and 'HS' cases.

The left boxplot of Fig. 7A 8 shows the RMS steering torque for the 'normal' and the 'HS' case. The 'HS' yields as expected lower RMS steering torque due the haptic controller which decreases the steering feedback torque at the steering wheel when an alert is imminent (almost continuously for the tested scenario). The right box plot displays the RMS of the Torque HS which is the T_{HS} signal (c.f. Fig. 7A 3).

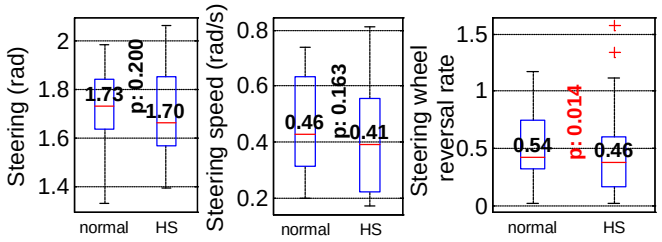

Fig. 7A 9. Boxplots of steering wheel angle (left), the steering wheel speed (middle) and the steering wheel reversal rate (middle) for both the 'normal' and 'HS' cases.

The left and middle boxplot of Fig. 7A 9 shows the RMS steering angle and speed correspondingly. Both were marginally higher for the 'normal case'. Similarly the steering wheel reversal rate was smaller for the 'HS' case (c.f. Fig. 7A 9; right). The drivers in the 'normal' case had to put higher effort to retain control of the vehicle and were therefore trying to explore the "correct" steering angle by constantly steering around it. The simulated surface was uniform; no disturbances were introduced towards the vehicle. So in the 'HS' case, as soon as the driver found the "correct" steering angle, it was easy to keep the vehicle into that state. The reduced steering feedback torque in the 'HS' case contributed effectively in that (Fig. 7A 8; left); a driver could steer faster and therefore could retain control of the vehicle around the "correct" steering angle easier.

Table 7A 1. TLX results of the simulation test.

Metric	Normal mean (σ)	HS mean (σ)	Significance *p*
Mental demand	10.4 (4.1)	9.2 (4.2)	0.10
Physical demand	10.8 (4.3)	7.7 (4.3)	0.00
Temporal demand	9.2 (3.9)	9.3 (3.5)	0.45
Performance	9.6 (3.7)	8.3 (4.4)	0.13
Effort	11.1 (4.4)	10.2 (3.8)	0.23
Frustration	9.0 (4.6)	7.5 (4.1)	0.02

iv)Subjective

The NASA TLX subjective results from the 25 drivers are displayed in Table 7A 1. The paired *t*-test has been applied to the data of the NASA TLX test (they have not been ranked transformed). The table displays the mean, standard deviation (σ) and the *p*-value from the *t*-test. It can be seen that, the physical demand, as well as the frustration level, is statistically significant reduced for the 'HS' case. Note that the 'performance' index in the TLX is reversed. A lower performance value, means higher performance self-rating.

IV. Real car testing

A. Methods

i) The vehicle

The tests for the haptic steering support have been performed in a 1.8L Opel Astra (Fig. 7A 1), which can provide variable steering feedback torque. The car has been purpose built by the author. The variable feedback torque is achieved through a Maxon, brushed 36V DC motor with 200W power

controlled through a Maxon 500W motor controller (c.f. Fig. 7A 1, top). The motor's torque is delivered on the steering column though a belt-pulley drive system for reduced backlash.

The inertial states of the vehicle are measured with two breakout boards from Sparkfun; the IMU Analog Combo Board Razor – 6 DOF Ultra-Thin IMU, break-out-board and the Gyro Breakout Board - MLX90609 - 300^o/s.

The computing power is a real time computer dSPACE Microautobox, executing in real time Matlab/Simulink blocks. The dSPACE is interfaced through an Intel: D510MO 1.66GHz Dual Core Atom Mini-ITX Motherboard, which also logs the test data. A Racelogic VBOX20SL with a twin antenna GPS engine has been used for slip angle measurement, which in conjunction with a Racelogic, DGPS base station for GPS correction, offers 40 cm absolute position accuracy. The steering torque was measured using Omega Strain gauges. All the analog signals were conditioned (amplified, filter, level converted) with custom designed electronics. ExpressPCB, has been used for the PCB manufacturing. A guide on how to efficiently instrument a vehicle can be found in [34].

i)Test procedure

The tests took place at Prodrive's proving ground in Warwickshire, UK. The test subjects were instructed to drive the Opel Astra in a slippery (low friction polymer surface sprinkled with water) skid-pad and were instructed to stay as close as possible to the inner circle while attempting to achieve maximum velocity without losing lateral control (c.f. Fig. 7A 10, bottom). The inner circle radius (marked with a visible white stripe in the coloured surface; Fig. 7A 1) was of radius R = 12.5 m and the estimated friction coefficient $\mu \approx 0.28$ impose a theoretical maximum velocity of 22.32 Km/h (6.2 m/s). The drivers were instructed to drive the direction (clockwise or counter-clockwise) which was more comfortable to them. The haptic controller was adapted-improved compared to the simulation test, so as to offer a natural steering feedback when driving far from a dangerous zone and offered a quite profound haptic feedback when approaching the vehicle's handling limits.

In order to get the subjects accustomed with the vehicle, they drove around the test facilities for 5 minutes. The drivers drove 5 practice runs and 7 recorded runs of 35 seconds each, with and without support, summing up to a total of 10 practice and 14 recorded runs. After the 7 recorded runs, the drivers filled in the NASA Task Load Index (TLX) form [154].

The test group consisted of 15 male and 2 female drivers with a mean age 33.1 ($\sigma = 6.6$). The drivers possessed their driving licence on average for 14.1 ($\sigma = 7.5$) years, they had an average 0.1 ($\sigma = 0.3$) crashes and graded themselves from 1-10 (1 being incompetent to 10 being an expert driver) with 6.3 ($\sigma = 0.9$). To compensate a potential learning effect, 8 drivers first drove without support and the remaining 9 first drove with support.

ii)Data processing and analysis

The first 5 seconds were excluded from each test to isolate a close to steady state cornering condition. All instances where the speed was lower than 14.4 Km/h and the radius was greater than 20 m were also excluded from the test. On average this resulted in 28.93 and 29.12 seconds of data per run for the no-support and the support case correspondingly (statistically insignificant difference as assessed with a paired *t*-test). The RMS values of individual metric were used. The RMS values from all 7 runs per driver were averaged together to derive a data vector with 17 observations. Statistical significance of the results was assessed with paired *t*-tests, performed at the $p < 5\%$ significance level. The data were rank transformed [170] before performing the *t*-test, for higher robustness (to cope with possible outliers) and to keep the ordinal scale.

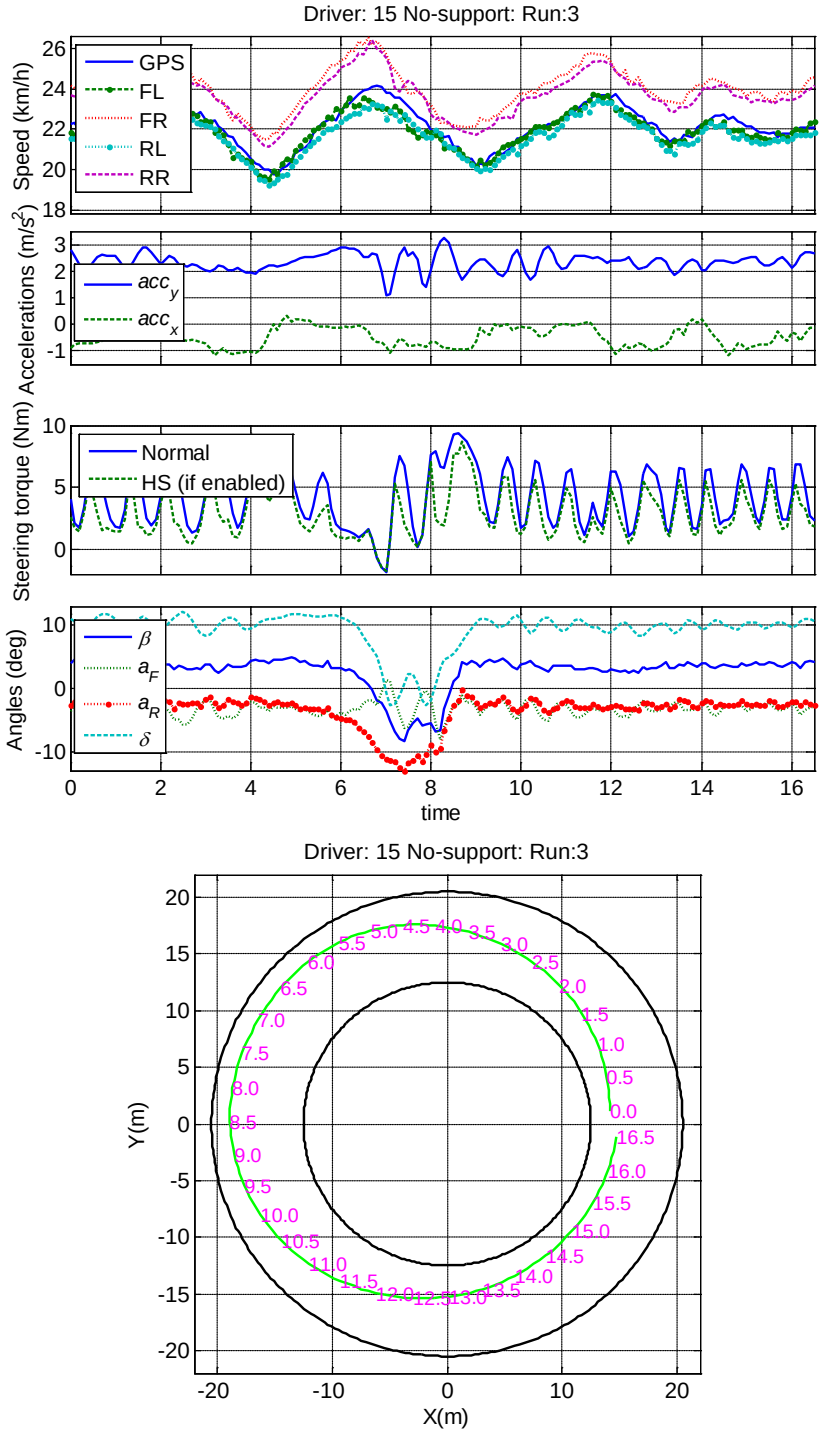

Fig. 7A 10. Example from the real vehicle testing; vehicle states data (top panel) and vehicle trajectory (bottom panel). On the top panel, the 1st subplot shows the vehicle's speed from the VBOX (GPS speed), and individual wheel speed from the ABS tapped sensors; front left FL and right FR and rear RL left and right RR wheel speeds. The 2nd subplot shows the longitudinal acc_x and lateral accelerations acc_y. The 3rd subplot shows the steering torque without support '*normal*' and what the torque would be with '*HS*'. The 4th subplot shows the vehicle's bodyslip angle β, the front a_F and rear a_R axle slip angle and the average steering angle δ at the front wheels. The reader can observe the extreme drifting and correction between 6 and 10 s.

Objective performance in the real car testing was evaluated using the majority of the metrics used for the simulation tests (appendix subsection VI.A) plus some additional metrics described in the appendix subsection VI.B. The results are illustrated using boxplots of the RMS values of the metrics. The statistical methods (boxplots with RMS and paired *t*-test) used in the objective analysis of the simulation tests, described in III.A.iii), have also been used for the real vehicle tests. Objective performance, was also assessed using the probability distribution and its corresponding cumulative sum of the absolute yaw rate difference, the cornering radius and the absolute front axle slip angle. The probability distributions have been created by aggregating all corresponding values from all 17 drivers and their 7 runs into a vector.

B. Results

i) Objective results

Similar to the simulation tests, the drivers managed to perform the task both with and without support. Some of the drivers reported to be feeling dizzy after several runs. However, no driver reported any major discomfort or physical fatigue that would necessitate pausing or quitting the test. Similar to the simulation tests, they on average reported that controlling the vehicle required high level of concentration and that the task was not trivial. Several runs involved loss of control of the vehicle due to terminal understeer. However, this is reflected in the average amount of data per test case as discussed in the previous subsection A.ii).

i)Vehicle's control performance

Fig. 7A 11 to Fig. 7A 15 are related to the vehicle's control performance, whilst Fig. 7A 16 and Fig. 7A 17 are related to the driver's control effort. The top boxplot of Fig. 7A 11 shows the RMS values of the yaw rate, the desired yaw rate and the yaw rate difference as defined in equation (7.1.1) (c.f. appendix section VI.A). None of the values is statistically significant different between the 'normal' and the 'HS'. The bottom boxplot of Fig. 7A 11 shows the front wheel slip angle for the front outer (Out) and inner (In) wheels.

The left boxplot of Fig. 7A 12 shows the longitudinal speed. The cornering radius was statistically significant smaller in the 'HS' case (c.f. Fig. 7A 12, middle) translated as better task following. The *HS factor* signal (c.f. Fig. 7A 3) which defines an imminent alert was statistically significant lower in the 'HS' case compared to the 'normal' case (c.f. Fig. 7A 12; right). The *HS factor* in the 'normal' case did not alter the steering wheel feedback force. It is being displayed only for comparison purposes.

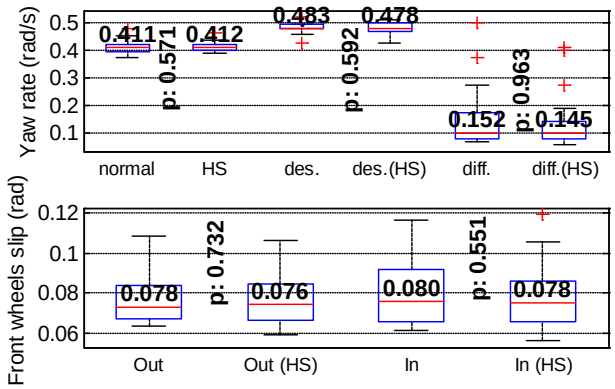

Fig. 7A 11. Boxplots of yaw rate, yaw rate desired and yaw rate difference (top) and front outer (Out) and inner (In) wheels' slip angle (bottom) for both 'normal' and 'HS' cases.

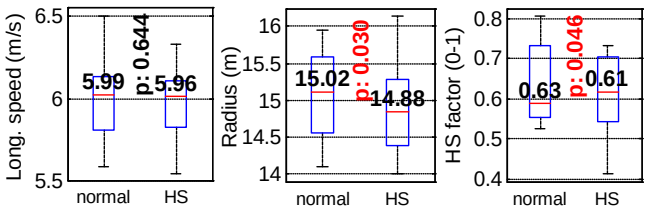

Fig. 7A 12. Boxplots of 1) the longitudinal speed (left); 3) the cornering radius (middle) and 3) the *HS factor* (c.f. Fig. 7A 3) (right) for both the 'normal' and 'HS' cases.

The top boxplot of Fig. 7A 13 shows the RMS for the front and rear inner and outer (with respect to the corner) wheel speed during 'normal' and with 'HS' driving. The bottom left boxplot of Fig. 7A 13 shows the lateral speed for both test conditions. The RMS longitudinal and lateral acceleration are shown in Fig. 7A 13, bottom right.

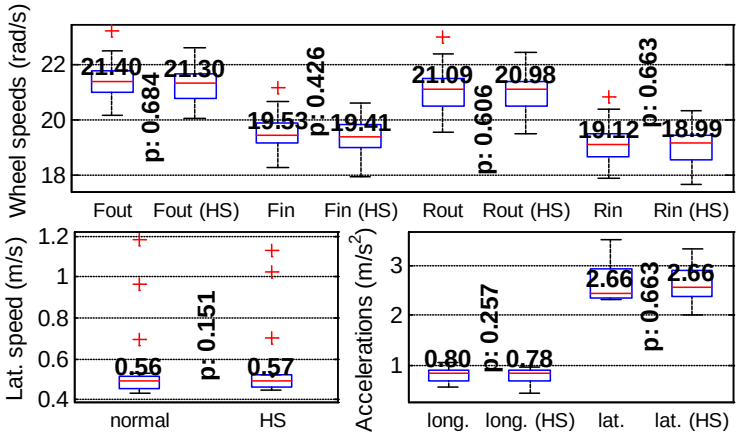

Fig. 7A 13. Top boxplots with front (F) and rear (R) outer (out) and inner (in) wheel speed (outer and inner with respect to the corner). Vehicle's lateral velocity (bottom left) and lateral acceleration (bottom right). The results for both 'normal' and 'HS' cases are displayed.

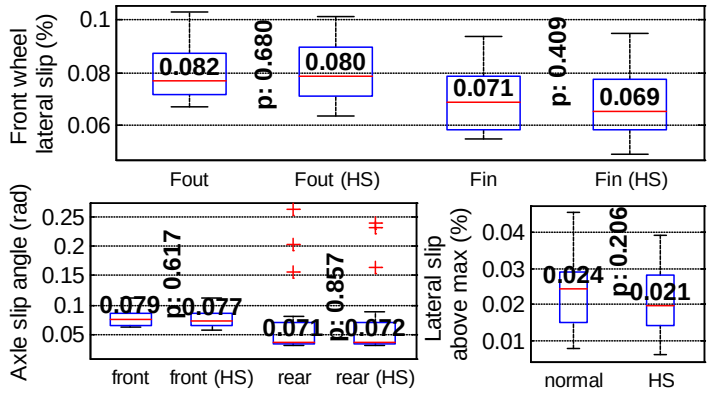

Fig. 7A 14. Boxplots: 1) front (F) and rear (R) outer (out) and inner (in) (outer and inner with respect to the corner) wheels' lateral slip percentage taking into account the longitudinal slip (top), 2) front and rear axle slip angle (bottom left) and 3) front axle percentage offset above the theoretical maximum lateral forces that the axle can generate (bottom right). The results for both 'normal' and 'HS' cases are displayed.

The top boxplot of Fig. 7A 14 shows the front wheel's lateral slip percentages (taking into account the longitudinal slip [59]) for inner and outer wheel (with respect to the corner). The bottom left boxplot of Fig. 7A 14 shows front and rear axle slip angle for the 'HS' and 'normal' case while the

bottom right boxplot of Fig. 7A 14 portrays the percentage of test time that drivers spend, where the front axle lateral slip was above the value providing maximum tire force (%). With 'HS', the drivers spend less time beyond the maximum lateral force that the axle (left and right tire lumped together) can generate.

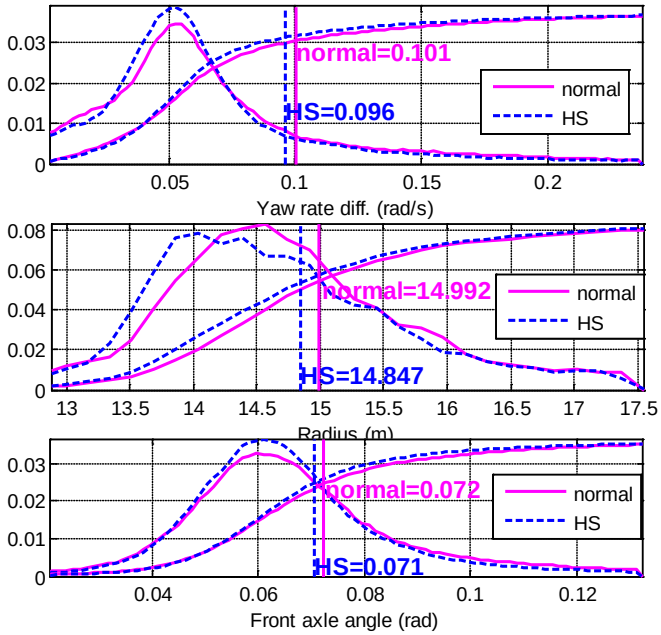

Fig. 7A 15. Probability distribution and its corresponding cumulative sum of the absolute yaw rate difference (top), the cornering radius (middle) and the absolute front axle slip angle (bottom) for both the 'normal' and the 'HS' cases. The vertical lines and the corresponding text show the mean absolute value of the corresponding metric. For illustration purposes, the cumulative sum plots have been multiplied with the maximum probability value of the either the 'normal' or the 'HS' case (the highest of two). The probability distributions have been created by aggregating all corresponding values from all 17 drivers and their 7 runs into a vector.

Fig. 7A 15 shows the probability distribution and its corresponding cumulative sum of the absolute yaw rate difference (top), the cornering radius (middle) and the absolute front axle slip angle (bottom) for both the 'normal' and the 'HS' cases. For all the three displayed metrics, the 'HS' cumulative sum curve has a higher value compared to 'normal' around the mean (designated with the vertical lines). Similarly to the human-in-the-loop simulation tests of section III, in the presence of 'HS', the drivers were more probable to experience: less understeer (smaller yaw rate difference), smaller cornering radius and smaller front axle slip values. In general, the HSNL helped the drivers to avoid the corresponding extremes values.

ii)Driver's control effort

The left boxplot of Fig. 7A 16 shows the RMS steering torque for the 'normal' and the 'HS' case. The 'HS' case yields as expected lower RMS steering torque due the principle of the HSNL to decrease the steering feedback torque when an alert is imminent (continuously for the scenario tested). It can be noticed, that the differences between the 'normal' and the 'HS' in the real test is not as great as in the simulation tests (c.f. Fig. 7A 8), due to the adaptation made into the controller for more natural feedback in the safe driving zone and delayed activation (compared to the simulation) shifted closer to the handling limits. The right box plot displays the RMS of the HSNL torque (c.f. Fig. 7A 3; T_{HS}).

The boxplots of Fig. 7A 17 shows the RMS steering angle and speed correspondingly and steering wheel reversal rate. None exhibited any significant statistical difference. This was not the case for the simulation tests, where the 'HS' case exhibited statistically significant smaller RMS steering wheel

reversal rate. In the real car tests though, the wet skid-pad surface was not as uniform as the simulated one and there was constantly a small variation on the friction coefficient; thus minor steering corrections were almost always necessary.

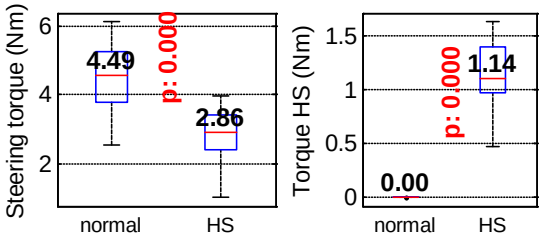

Fig. 7A 16. Boxplots of steering torque (left) and the T_{HS} (c.f. Fig. 7A 3) (right) for both the 'normal' and 'HS' cases.

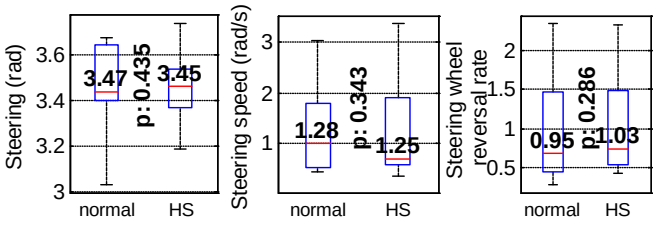

Fig. 7A 17. Boxplots of steering wheel angle (left), the steering wheel speed (middle) and the steering wheel reversal rate (middle) for both the 'normal' and 'HS' cases.

iii)Subjective

The NASA TLX subjective results from the 17 drivers are displayed in Table 7A 2. The paired *t*-test has been applied to the data of the NASA TLX test (they have not been ranked transformed). The table displays the mean, standard deviation (σ) and the *p*-value from the *t*-test. It can be seen that, the mental demand and the physical demand were statistically significant reduced for the 'HS' case, in accordance with the simulation results. The effort level was also perceived as lower. The rest of the indices also favour the 'HS'.

Table 7A 2. TLX results of the real car testing.

Metric	Normal mean (σ)	HS mean (σ)	Significance *p*
Mental demand	11.4 (4.3)	9.1 (4.4)	0.02
Physical demand	9.2 (4.7)	6.3 (3.4)	0.01
Temporal demand	7.8 (4.7)	5.9 (3.0)	0.05
Performance	8.9 (4.4)	7.4 (2.4)	0.20
Effort	11.5 (4.5)	9.3 (3.9)	0.00
Frustration	8.2 (5.5)	6.3 (4.1)	0.07

V. Discussion and conclusions

A. Driving simulator testing

Objective and subjective results in the simulation tests did favour the HSNL. The support was informing the driver when he/she was approaching an imminent undesired vehicle state. It influenced positively the drivers inducing them to adopt a relatively safer driving style which in turn helped to better control the vehicle close to the handling limits. The support, helped drivers 1) to deviate less from their desired yaw rate (less understeer), 2) exert smaller steering forces to perform the same manoeuvre (less physical effort) and less corrections (smaller steering wheel reversal rate), 3) deviate less from their desired trajectory (smaller lateral error). At the same time, the drivers maintained

smaller (in magnitude) slip angles at the front wheels; thus with support they kept their wheels in a safer operating zone (c.f. Fig. 7A 2).

On the subjective side, the drivers perceived the system as less physically demanding while inducing less frustration (c.f. Table 7A 1). A common remark made from all drivers was that with support "it was easier to find the limit."

B. Real car testing

Objective and subjective results in the real car testing did also favour the HSNL, as in the simulation tests. Drivers achieved similar longitudinal and lateral speed for both test conditions, while at the same time, the cornering radius was significantly smaller with the support.

Similarly as in the simulation tests, the drivers were more probable to experience smaller front axle slip angle and yaw rate difference in the presence of support (c.f. Fig. 7A 15). The *HS factor* signal which defines an imminent alert (c.f. Fig. 7A 3) was statistically significant reduced with HSNL (c.f. Fig. 7A 12).

As discussed earlier, because of the non-ideal uniformity on the slippery skid-pad, the drivers had to continuously explore the region around the "correct" steering wheel angle. The support helped drivers to sense that region easier and due to the smaller steering feedback torque (the steering torque with support was significantly lower) it was also easier to steer around this region. At the same time, the haptic controller was adapted-improved compared to the simulation test as discussed in the section IV.A.i) so as to offer a natural steering feedback when driving far from a dangerous zone and offered a quite profound stiffness drop when approaching the vehicle's handling limits.

As far as the subjective results, the HSNL reduced mental and physical demand and required smaller effort level (c.f. Table 7B 1). A general remark by the test drivers was that they could "easily feel the understeer coming." Interestingly, some drivers reported that they felt that the vehicle handled better with support, although the vehicle was not altered and the operating principle was explained to them.

This paragraph contains subjective remarks from the author of this study deriving from the real car testing. Interestingly, drivers with low driving skills tend to rate themselves as "above average" drivers. Although those un-skilled drivers tend to be more cautious so that they do not exceed the handling limits, when they lose control they are incapable of regaining it back. Skilled drivers though, will try to approach closer to the vehicle's handling limit with higher chances of inducing severe understeer or oversteer. However, they can regain control of the vehicle if it is still responding to their inputs. In a sense, skilled drivers lose control more often compared to un-skilled.

C. Simulation vs. real car testing

Real car tests are irreplaceable for developing systems related to dynamic driving [34][39], but can be difficult to interpret [95] and they certainly are a financial burden. On the other side, driving simulators enable to present virtual environments and scenarios in a controlled manner, assess driving performance accurately, and evaluate hazardous situations without actual risk [40]. Although simulators incorporate high level of detail [40][32] it is not possible to incorporate all the aspects and uncertainties that affect driving performance. Developing concepts in simulation and fine-tuning/validating those in the real car should provide a rule-of-thumb for innovative system production related to human-machine-interface.

In the current experiment, the simulation and real car tests had differences. The simulation tests preceded the real car tests and were primarily used to obtain an initial understanding about the objective and of the subjective impact of the HSNL in the driving task. Those results helped to better set-up the test procedure (which in real car testing had to be error free for safety and high data fidelity) and fine tune-adapt the controller for real vehicle usage.

The differences with respect to the task can be summarized as follows. The friction coefficient μ in the simulation test was 1 and in the real test was estimated at 0.28. On the one hand, the friction coefficient of 1 is closer to normal driving conditions compared to 0.28. On the other hand, testing in a real car with a friction in a surface with a friction coefficient of 1 would necessitate a costly all-round tire change per test driver. The tasks did also differ in the skid-pads' setup. In simulation, the driver's had to drive the vehicle on top of a 20 m radius white marked circle. In the real tests, they had to drive around a 12.5 m radius, without crossing the line.

In simulation, the only driving cue besides the visual feedback, was the steering wheel force-feedback; something which can potentially amplify the positive effects of the HSNL. In the real tests, the drivers besides the visual and haptic force-feedback, they were receiving vestibular feedback (lateral acceleration, yaw acceleration, side slip angle change etc.), tactile feedback from the seat etc. which in the vehicle handling limits, are irreplaceable driving cues [39]. At the same time, the drivers were receiving acoustic feedback from the wet polymer surface; when the vehicle started to severely understeer, the tire scrub on the surface was quite intense; the drivers could "hear" the imminent undesired phenomenon approaching. This diminished the positive impact of the HSNL compared to no-support, because drivers were receiving this acoustic cue which would not be present in a real life situation.

The steering excursions and corrections with and without support in the simulation and real experiments test exhibited differences. In simulation it was relatively "easy" to stay close to the "correct" steering angle without unnecessary steering excursions, due to the simulated uniform surface. Therefore as soon as the driver found the "correct" steering angle, it was "easy" to keep the vehicle close to steady state; hence the smaller steering wheel reversal rate (c.f. Fig. 7A 9). The haptic controller in simulation was providing a profound region to keep the steering wheel angle, but it was intervening early, offering an unnatural steering feedback.

In the real car testing, the environment was naturally rich in disturbances, such as the friction variations on the slippery skid-pad, and hence the drivers had to continuously explore the region around the "correct" steering wheel angle. The support helped drivers to sense that region easier and due to the steering feedback torque it was also easier to steer around this region. As discussed earlier because, the haptic controller was adapted-improved for the real car test, to offer a more natural steering feedback when driving in the "safe" zone; the controller in conjunction with the surface variation friction stimulated driving closer to the actual handling limit (compared to the simulation controller). Mental and physical demand decreases according to driver's perception (c.f. Table 7A 2).

D. Haptic support works!

Despite the differences, both the driving simulator and the real vehicle test showed that HSNL had significant beneficial effects on drivers' lateral control performance. In the presence of HSNL, the drivers operated the tires in smaller slip angles and hence avoided saturation the front wheels' lateral forces and excessive understeer. The high in-between-drivers and in-between-runs variance restricted the statistical significance only in certain metrics. However, the author of this study argues that a higher number of test-drivers would have exhibited statistically significant differences in most of the assessed metrics, favouring the HSNL.

The HSNL principle has also been evaluated in high speed test track driving where the same haptic controller was applied in a sharp curvy route at the adverse handling track of Prodrive Automotive in UK. The HSNL proved again to be beneficial and was generally "welcomed" by the drivers. The high speed track testing results will be juxtaposed with the current's study results in Chapter 7 part B [37] to derive a complete scientific study about HSNL on a wide dynamic range.

Upon this innovative work, it can be concluded that haptic support at the vehicle's handling limits (HNSL) can improve the driver-car interaction and promote safety. The proposed system can be characterized diverse, in terms that it can improve the vehicle's perceived sportiness and at the same time promote safety. The author would encourage the adoption of such systems into modern vehicles enabled at will with the press of a "sport" button. A small video from track testing is available online [157].

VI. Appendix

A. Simulation metrics

Objective performance in simulation was evaluated calculating root-mean-square (RMS) values of the following signals:

Lateral error with respect to the centre line.

Longitudinal speed.

Angular rate around the vehicle's z-axis:

Yaw rate $\dot{\psi}$.

Desired yaw rate $\dot{\psi}_{des}$(7.1.1). The desired yaw rate is calculated using the vehicle's longitudinal speed $\dot{x}$, the front wheels steering angle δ, the vehicle's wheelbase L and the understeer coefficient K_u [142] deriving from the vehicle properties: mass, tires' cornering stiffness and weight distribution.

Yaw rate difference $\dot{\psi}_{diff}$ (7.1.1).

$$\dot{\psi}_{des.} = \frac{\dot{x}}{L + \dot{x}^2 \cdot K_u} \cdot \delta, \quad \dot{\psi}_{diff.} = \dot{\psi}_{des} - \dot{\psi} \tag{7.1.1}$$

Front left and right wheel slip angle

The imminent alert signal *HS factor* (c.f. Fig. 7A 3).

The cornering radius.

Steering torque.

The haptic support torque T_{HS} (c.f. Fig. 7A 3).

Steering angle.

Steering wheel angular speed.

The steering wheel reversal rate. The reversal rate is derived using the steering wheel speed. A reversal (gives a value of 1) is assumed when within one speed sign reversal (positive to negative or vice-versa), the maximum absolute speed of both positive and negative signal, is greater than 20^o/sec. A reversal rate of 1, would designate 1 reversal per sec.

B. Real car testing metrics

Objective performance in the real tests was evaluated using the majority of the metrics used in the simulation (above), plus some additional metrics depicted below:

Front outer and inner (with respect to the corner) wheel slip angle.

Front/rear – outer/inner (with respect to the corner) wheel speed (Fout, Fin, Rout, Rin).

Longitudinal $\dot{x}$ and lateral velocity $\dot{y}$.

Longitudinal acc_x and lateral acceleration acc_y.

Front a_F and rear a_R axle slip angle.

The percentage of test time that drivers spent, where the front axle lateral slip was above the slip value where maximum forces can be generated. This was calculated taking also into account the longitudinal slip [59].

Front outer and inner (with respect to the corner) lateral slip as defined in [59]. This was calculated taking also into consideration the longitudinal slip.

VII. Acknowledgment

The author is grateful to Jeroen Beerens, Joost de Haan, Richard Nefs, Timothy Schuit for performing the simulator tests. The research was supported by the Automotive Development Center of SKF, in the Netherlands and Prodrive Automotive in UK. E. Velenis was supported by an EPSRC First Grant Award (award number EP/I037792/1). Special thanks to Oliver Jones, Dave Rollet, Mat Taylor, Chris Roberts, Ben Garrat, Scott Parton, Adrian Hall. The parts for modifying the steering system were manufactured at TUDelft through Johannes Dukker and Jan van Frankenhuyzen. We would also like to thank Circuit Park Zandvoort, for granting usage of their test facilities.

Chapter 7 B. Haptic Steering Support for Driving Near the Vehicle's Handling Limits; Test-Track Case

“Τάχιστον νους, δια παντός γαρ τρέχει.”
Θαλής ο Μιλήσιος,643-548 π.Χ.

“The mind is the fastest of-all, overtaking everything.”
Thales of Miletus,643-548 B.C.

Haptic Steering Support for Driving Near the Vehicle's Handling Limits; Test-track Case

Abstract—Current vehicle dynamic control systems from simple yaw control to high-end active steering support systems are designed to primarily actuate on the vehicle itself, rather than stimulate the driver to adapt his/her inputs for better vehicle control. The driver though dictates the vehicle's motion, and centralizing him/her in the control loop is hypothesized to promote safety and driving pleasure. Exploring the above statement, the goal of this study is to develop and evaluate a haptic steering support when driving near the vehicle's handling limits (Haptic Support Near the Limits; HSNL). The support aims to promote the driver's perception of the vehicle's behaviour and handling capacity (the vehicle's internal model) by providing haptic cues on the steering wheel. The HSNL has been evaluated in a test-track where 17 test subjects drove around a narrow-twisting tarmac circuit, a vehicle (Opel Astra G/B) equipped with a steering system able to provide variable steering feedback torque. The drivers were instructed to achieve maximum velocity through corners, while receiving haptic steering feedback cues related to the vehicle's cornering potentials. The test-track tests led to the conclusion that haptic support reduced drivers' mental and physical demand without affecting their driving performance.

I. Introduction

Vehicle dynamics and control technology related to cornering performance started to become a main stream of research in the mid-1980s [172]. This control technology has evolved through various phases from chassis control with mechanical four wheel steering, to the advanced driving assist systems such as the electronic stability control (ESC), active front steering (AFS) and lane departure warning/prevention (LDW/P) systems. Several studies since 1998 have showed the ESC's effectiveness [86][71], depicting that the global installation of ESC could reduce skidding accidents by even 80% [127]. Similarly, active steering systems have been credited to improve the handling characteristics of the car and increase the driving comfort [166][167].

The global adoption of new sensor technologies (GPS, cameras, radar, etc.) has enabled driver support systems beyond the concepts applied to chassis control. Systems for example, designed to mitigate collisions and apply the brake if they detect an imminent collision [101]. Considering now systems designed to operate in less dynamic driving scenarios, LDW/P systems have also proven to promote safety [70][45] even in emergency situations [41]. The utilization of cameras to detect the lane markings has enabled steering control to maintain the vehicle's intended path [153]. The aforementioned systems discussed in this paragraph, do not aim to improve the vehicle's physical dynamical performance, but do effectively reduce driving effort. Diminishing the driver's load is one of the primal goal of the current and future vehicles for automotive manufacturers [172].

Steering support in low acceleration curve negotiation, has exposed that haptic support is an efficient way to improve the driver-car interaction [131][119][122] and reduce the driving load. Support systems for moderate driving, often share control with the driver in the "haptic shared control" sense [48], operating under the principle that the driver should be aware of the system's activity by force information on the control interface (e.g. the steering wheel in a LDW/P system). Systems that share control with the driver in a wider dynamic range when driving near the vehicle's handling limits, where for instance the ESC and AFS would intervene, have only recently been studied [35] and

displayed significant positive effects on the vehicle's lateral control performance and reduction of the driving effort (mental & physical demand).

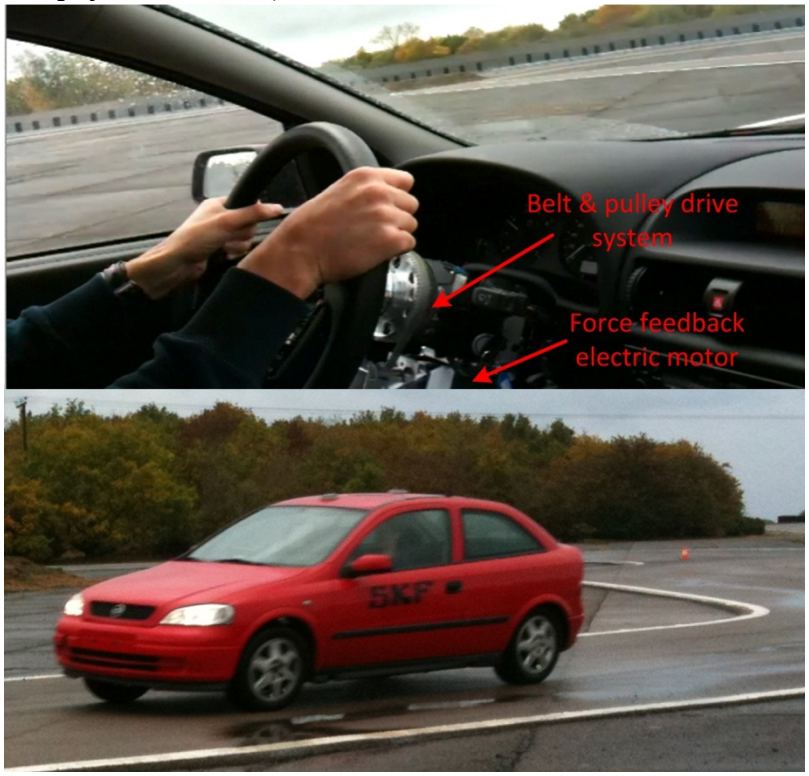

Fig. 7B 1. Force-feedback Opel Astra during test-track driving.

The current study elaborates on the concept of a haptic steering support in near the vehicle's handling limits (Haptic Support Near the Limits; HSNL) in a test-track. The goal of the system is to promote the driver's understanding of the vehicle's cornering potentials by providing haptic cues on the steering wheel. The haptic controller was initially tested in a driving simulator and was later adapted-improved to be tested in a 1.8L Opel Astra (Fig. 7B 1), which can provide variable steering feedback torque. The work presented here, constitutes the integration of research on the influence of haptic steering support when driving near the vehicle's handling limits initially presented in Chapter 7 part A [35][36]. The work in Chapter 7 part A consisted of driver-in-the loop simulation and real car tests. In the simulation part, 25 drivers attempted, to achieve maximum velocity, on a dry 20 m radius skid-pad while trying to retain control of the simulated FWD vehicle parameterized as Opel Astra G/B. In the real car tests, 17 drivers attempted to achieve maximum velocity, around a 12.5 m radius slippery skid-pad while trying to retain control of an Opel Astra G/B. Results from both the simulation and the real car testing showed that in the presence of HSNL, the drivers operated the tires in smaller slip angles and hence avoided saturation the front wheels' lateral forces and excessive understeer, while experiencing reduced mental and physical demand.

The principle to assess the HSNL into two fundamentally different conditions derives from prior driver behaviour research. Studies related to driving that had set off in the 1930's [96] manifest that drivers primarily steer in an anticipatory feed-forward manner to an estimated future path while they use an adaptive-control strategy to compensate for deviations of the vehicle from the demanded trajectory [56]. Such studies have deduced driver models [15] for the assessment of vehicular systems [27][31] so as to facilitate the difficult interpretation of real in-field tests [95]. Objective assessment of active safety systems could benefit from driver models designed to operate at the vehicle's handling

limits [99][24]. Correspondingly, studying rally-race car driving techniques [68][34] and incorporating them into a driver model [145] can enable racecar driver-type controllers [64]. A racecar driver will control the vehicle (speed and steering) using a feedforward (predict the speed and steering) and feedback (compensation for perception mismatch or disturbances) strategy [105]. A controller incorporating the aforementioned features, would be a priceless tool at the disposal of development engineers.

Continuing upon the aforementioned statements, the drivers in the skid-pad testing in Chapter 7 part A were expected to mainly employ feedback control to compensate for disturbances (e.g. friction coefficient changes) or driver's perception mismatch [56][105]. On the contrary in the test-track driving, drivers were expected to mainly employ feedforward steering control, due to the repetitive test-track driving test, where drivers would try to memorize and re-apply the same control inputs. Therefore, the two experiments were aiming to stimulate the two different parts of the human controller facilitating the analysis.

This study has been organized as follows. The rationale of HSNL is summarized in section II followed by a brief description of the haptic controller. In continuation, the methods section III, describes the vehicle, the test procedure and the data processing. The results are correspondingly being presented in section IV. Section V summarizes the results obtained in the skid-pad tests presented in Chapter 7 part A [35][36] and discusses the high speed test-track driving results presented in the current study. The results are juxtaposed so as to derive a concrete argument about the influence of HSNL in real-life driving.

II. Haptic steering support rationale

A. The vehicle's inherent steering feedback

The rationale behind the HSNL, derives from the vehicle's property to reduce the steering "stiffness" (the steering feedback torque as a function of the steering wheel angle) before the vehicle reaches its handling limits and starts to understeer. Understeering occurs when the magnitude of the front axle slip angle greater than the rear axle [161] (pp. 203). The HSNL, exaggerates the reduction of steering "stiffness" and makes it profound to the driver, so he/she avoids excessive steering angle inputs, which will result in increased tire slip and consequently lateral force loss. For more details about the rationale of the HSNL, the reader is referred to subsection A, in part A of this Chapter.

B. Haptic support controller

Fig. 7A 3 (Chapter 7, part A) portrays the haptic support (HS) concept, which was implemented and tested in simulation and the real vehicle. The 'Alert detection' block, using the vehicle current states and properties, signals an 'alert' when an undesired effect is imminent, e.g. excessive front wheels' slip which will create understeer. The *resulting torque*, divided with the inertia of the steering wheel J_{sw}, will impose the acceleration $\ddot{\theta}_{sw}$, the velocity $\dot{\theta}_{sw}$ and finally the angle θ_{sw} of the steering wheel. For more details about the controller the reader is referred to subsection B in part A of this Chapter.

III. Methods

A. The vehicle

The tests for the haptic steering support have been performed in a 1.8L Opel Astra (Fig. 7B 1), which can provide variable steering feedback torque. The car has been purpose built by the author of this study. The variable feedback torque is achieved through a Maxon, brushed 36V DC motor with 200W power controlled through a Maxon 500W motor controller (c.f. Fig. 7B 1, top). The motor's torque is delivered on the steering column though a belt-pulley drive system for reduced backlash.

The inertial states of the vehicle are measured with two breakout boards from Sparkfun; the IMU Analog Combo Board Razor – 6 DOF Ultra-Thin IMU, break-out-board and the Gyro Breakout Board - MLX90609 - 300^{o}/s.

The computing power is a real time computer dSPACE Microautobox, executing in real time Matlab/Simulink blocks. The dSPACE is interfaced through an Intel: D510MO 1.66GHz Dual Core Atom Mini-ITX Motherboard, which also logs the test data. A Racelogic VBOX20SL with a twin antenna GPS engine has been used for slip angle measurement, which in conjunction with a Racelogic, DGPS base station for GPS correction, offers 40 cm absolute position accuracy. The steering torque was measured using Omega Strain gauges. All the analog signals were conditioned (amplified, filter, level converted) with custom designed electronics. ExpressPCB, has been used for the PCB manufacturing. A guide on how to efficiently instrument a vehicle for driver behaviour studies can be found in [34].

B. Test procedure

The tests took place at Prodrive's proving ground in Warwickshire, UK. The route was established in the narrow-twisting "adverse" tarmac circuit (c.f. Fig. 7B 2; bottom). In order to become accustomed with the vehicle, the subjects drove the wet skid-pad test presented in Chapter 7 Part A [35][36], lasting approximately 30 minutes. When the wet skid-pad experiment was completed, the test subjects drove counter-clockwise the designated route with and without HSNL. The operating principle of the HSNL was explained to the drivers prior to testing; the drivers were instructed to achieve maximum velocity through the corners while keeping the vehicle under control. They drove multiple (on average above 3; according to skill levels) practice 'flying runs'. A 'flying run' is defined as: start from standstill behind the start line, perform a full lap and cross the start line and then stop behind the start line (2 laps in total). The recording time was 70 seconds, with the data logging automatically starting when the vehicle's longitudinal speed surpassed 1 km/h. The 'start line' as well as the 'split lap' line are shown in Fig. 7B 2 (bottom). Not all drivers managed to complete the full flying run within the 70 seconds tests time. Therefore, the 'split lap' line was selected in post processing, as a point that all drivers crossed twice within their 'flying run'. Thus all runs contained a full lap starting run from the 'split lap' line, which will be referred as split lap.

To enable the data processing for the split run, the time logged data (time-data), were translated into travel-distance data (c.f. Fig. 7B 2; top); 0 m of travel-distance is on top of the 'split lap' line and 425.2 m of travel-distance is a full split lap back to the 'split lap' line. This will be more elaborately explained in the next subsection C. After the practice 'flying runs', the test subjects drove 3 recorded 'flying runs' of the track, with and without support. After the 3 recorded 'flying runs', the drivers filled in the NASA Task Load Index (TLX) form [154].

The test group consisted of 15 male and 2 female drivers with a mean age 33.1 (σ = 6.6). The drivers possessed their driving licence on average for 14.1 (σ = 7.5) years, they had an average 0.1 (σ = 0.3) road accidents while driving and graded themselves from 1-10 (1 being incompetent to 10 being an expert driver) with 6.3 (σ = 0.9). To compensate a potential learning effect, 8 drivers drove initially without support and 9 drove initially with support.

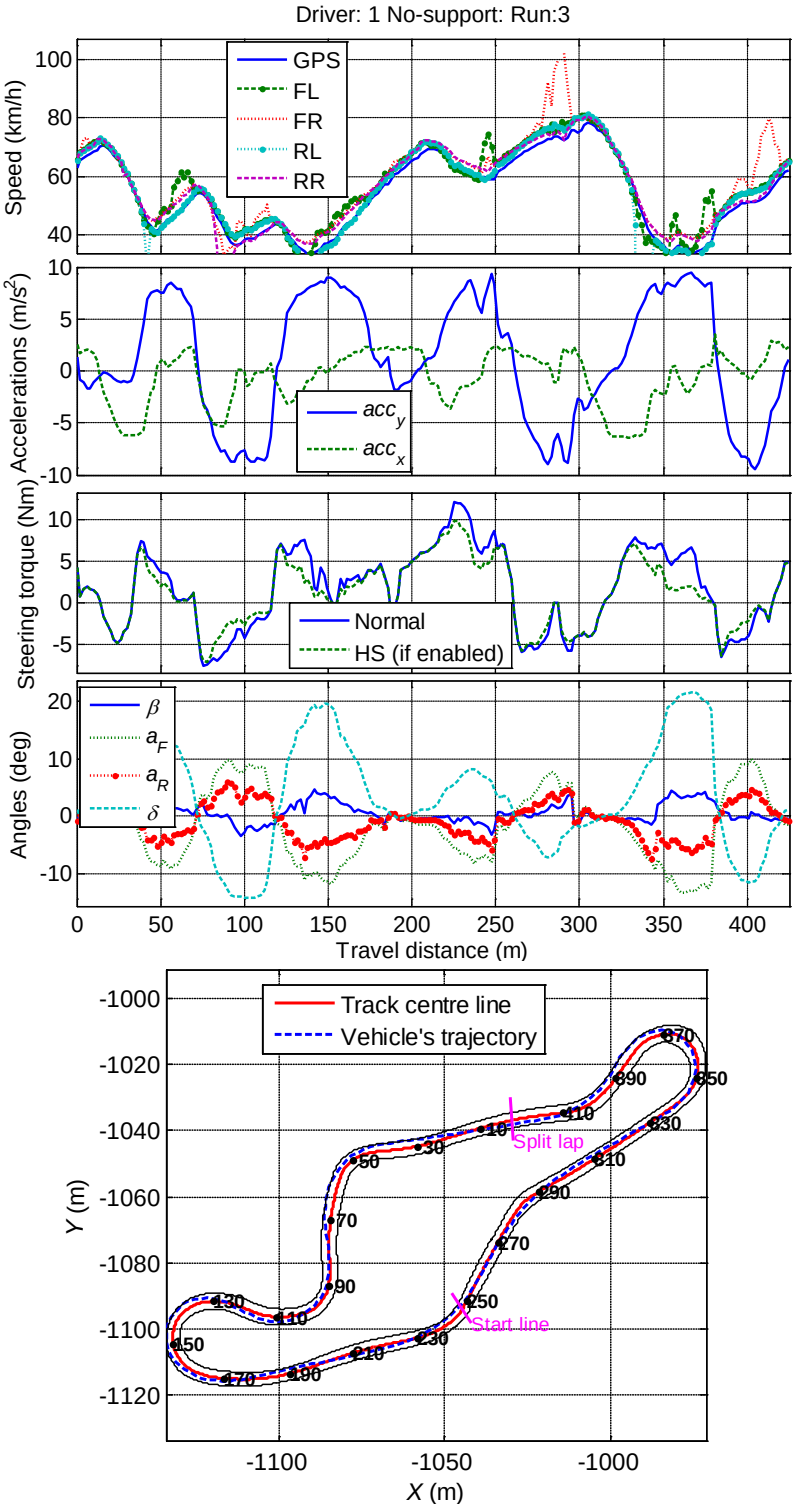

Fig. 7B 2. Example from the real testing; vehicle states data as a function of travel-distance (top panel) and vehicle's trajectory (bottom panel). On the top panel, the 1st subplot shows the vehicle's speed from the VBOX (GPS speed), and individual wheel speed from the ABS tapped sensors; front left FL and right FR and rear left RL and right RR wheel speeds. The 2nd subplot shows the longitudinal acc_x and lateral accelerations acc_y. The 3rd subplot shows the steering torque without support '*normal*' and what the torque would be with '*HS*'. The 4th subplot shows the vehicle's bodyslip angle β, the front a_F and rear a_R axle slip angle and the average steering angle δ at the front wheels.

All the tests were performed on dry track and with tire tread depth, within the legal limits for the U.K. When the tires which were experiencing the greatest load (front right; FWD driven car with the test-track setup straining mainly the right side tires) started to wear intensively, they were swapped with the other side (from right to left). When both front tires had worn out, they were swapped with the rear. When all four tires had worn out, they were all replaced. In total, 4 "almost" new and 5 new tires were used for the experiment. The tires used, were always standard summer tires. They were not always from the same brand. All drivers completed their test, having the same tires all around the vehicle.

C. Data processing and analysis

As shortly discussed in the previous subsection B, the time-data were translated into travel-distance data. To compensate for different trajectories within the road limits followed by different drivers, distance is measured along the test track's centre-line (c.f. Fig. 7B 2; inside thick solid red line). The centre-line was derived from logged data of the inner and outer limits of the road (c.f. Fig. 7B 2; outside thin solid black lines). The discretization step of the distance along the track's centre-line was set at 0.2 m. For individual point of the 'track's centre line', the time-entry with the nearest coordinates (shortest Euclidean distance) from the time-data was selected; this results the time-data to be translated into a vector which has equal length as the 'track centre line'. For example, point 21 is 4 m ahead of point 1 (in terms of travel-distance). The data on the top panel of Fig. 7B 2, as well as the vehicle trajectory (bottom panel) have been created is this way.

The travel-distance translated data, from all 3 split laps of each of the 17 drivers were averaged. Thus, 17 mean values were used to derive the statistical data for individual travel-distance point. The data were then analysed with respect to 'travel-distance' (c.f. section IV.A) and 'individual corner' (c.f. section IV.B).

In the travel-distance analysis (c.f. section IV.A), the 17 values per travel-distance point were used to derive the 10^{th}, 50^{th} and 90^{th} percentiles of the data. Statistical significance of the mean of the 17 values was assessed with paired *t*-tests, performed at the $p < 0.1\%$ significance level. The data were rank transformed [170] before performing the *t*-test, for higher robustness (cope with possible outliers) and to keep the ordinal scale. A green horizontal line is visible on top, if the difference of the means between the 'normal' and the 'HS' is statistically significant. The test-track plot on the right side of individual figure, depicts where the corresponding distance points are located on the track. Objective performance was evaluated with the metrics described in the appendix subsection VI.A. The split lap time is not used as a metric, since the task instructions suggested that the drivers should achieve maximum velocity though the corners and no to perform minimum lap time.

In the individual corners analysis IV.B, the track was divided into corner segments using the mean (mean of the 17 drivers of the 3 average runs for the 'HS' case) lateral acceleration signal acc_y (c.f. Fig. 7B 4; bottom).

Starting from travel-distance of 0 m, a corner segment was devised, when the magnitude of the lateral acceleration was greater than 6 m/s^2 and extended up to the travel-distance point (end of segment) that the standard deviation of the lateral acceleration, between the start of the segment and the end of the segment was lower than 0.6 m/s^2. This resulted into 12 individual corner segments. Using the lateral acceleration as a metric to devise the corner segments, enables the severity rating of individual corner segment, while it also defines travel-distance segments that the vehicle's states can be characterized as "relatively" steady; thus they can be averaged and compared. Objective performance was evaluated with the metrics described in the appendix subsection VI.B.

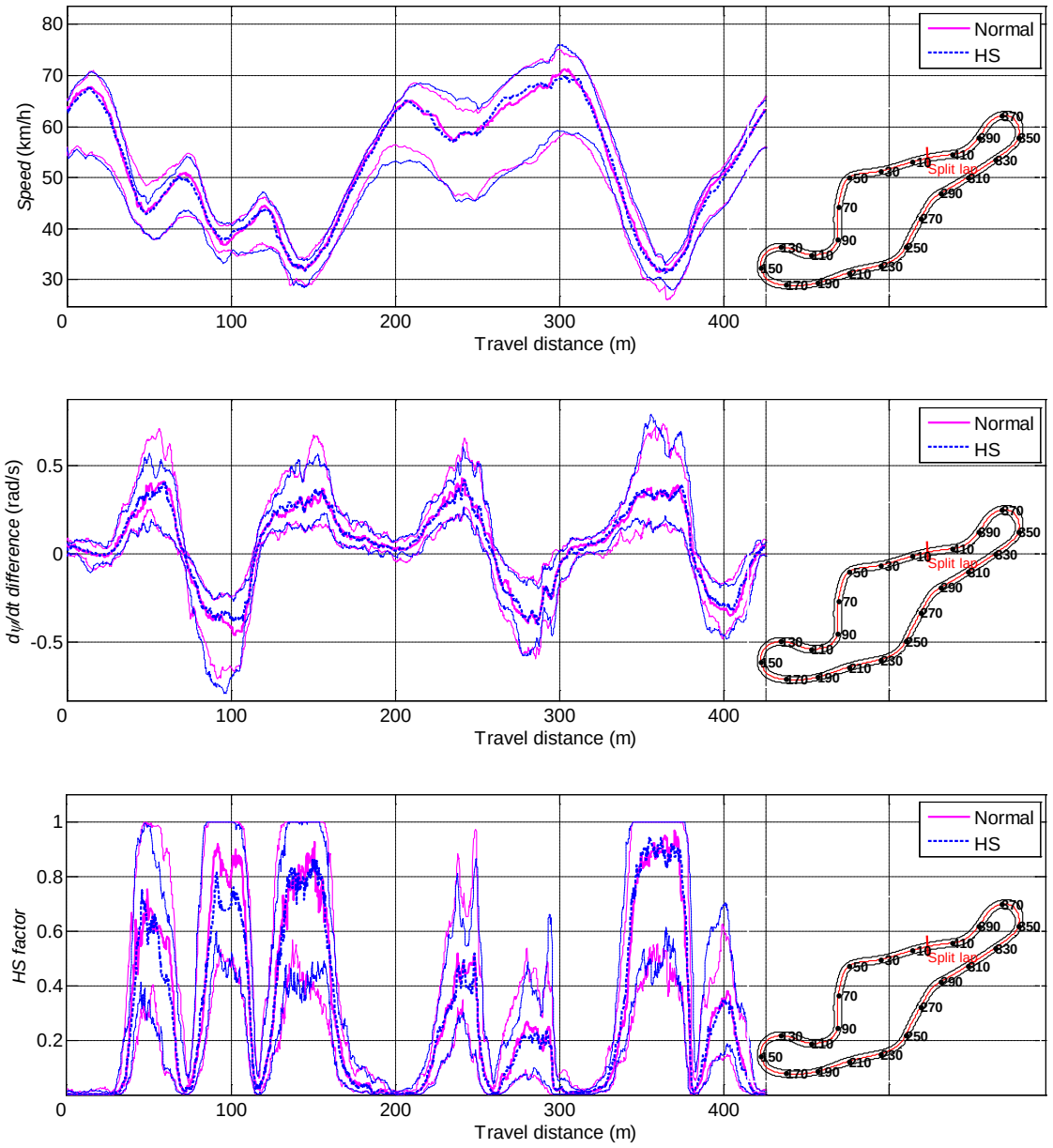

Fig. 7B 3. Resulting vehicle's speed (top), yaw rate difference $\dot{\psi}_{diff.}$ (middle) and imminent alert signal, *HS factor* (bottom). 10th (thin lines), 50th (thick lines) and 90th (thin lines) percentiles of both the 'normal' (solid line) and the 'HS' (dashed line) case of the 3 averaged runs of the 17 drivers.

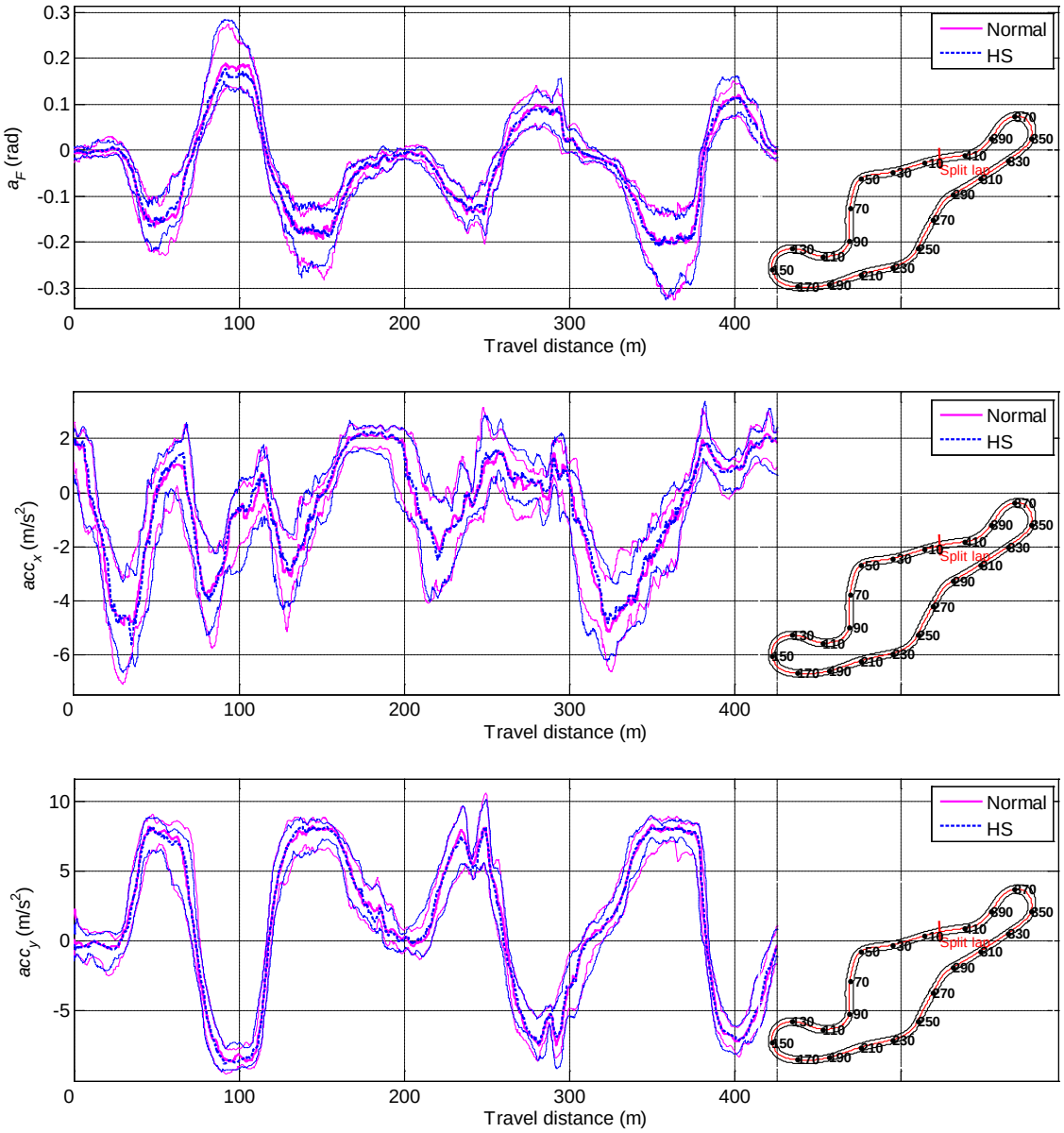

Fig. 7B 4. Front axle slip angle a_F (top), longitudinal acc_x (middle) and lateral acc_y acceleration (bottom). 10th (thin lines), 50th (thick lines) and 90th (thin lines) percentiles of both the 'normal' (solid line) and the 'HS' (dashed line) case of the 3 averaged runs of the 17 drivers.

IV. Results

The drivers managed to perform the task both with and without support. No driver reported any major discomfort or physical fatigue that would necessitate pausing or quitting the test.

A. Objective results; travel-distance analysis

The plots in Fig. 7B 3 and Fig. 7B 4 are related the vehicle's control performance, whilst the plots in Fig. 7B 5 are related with the driver's control effort.

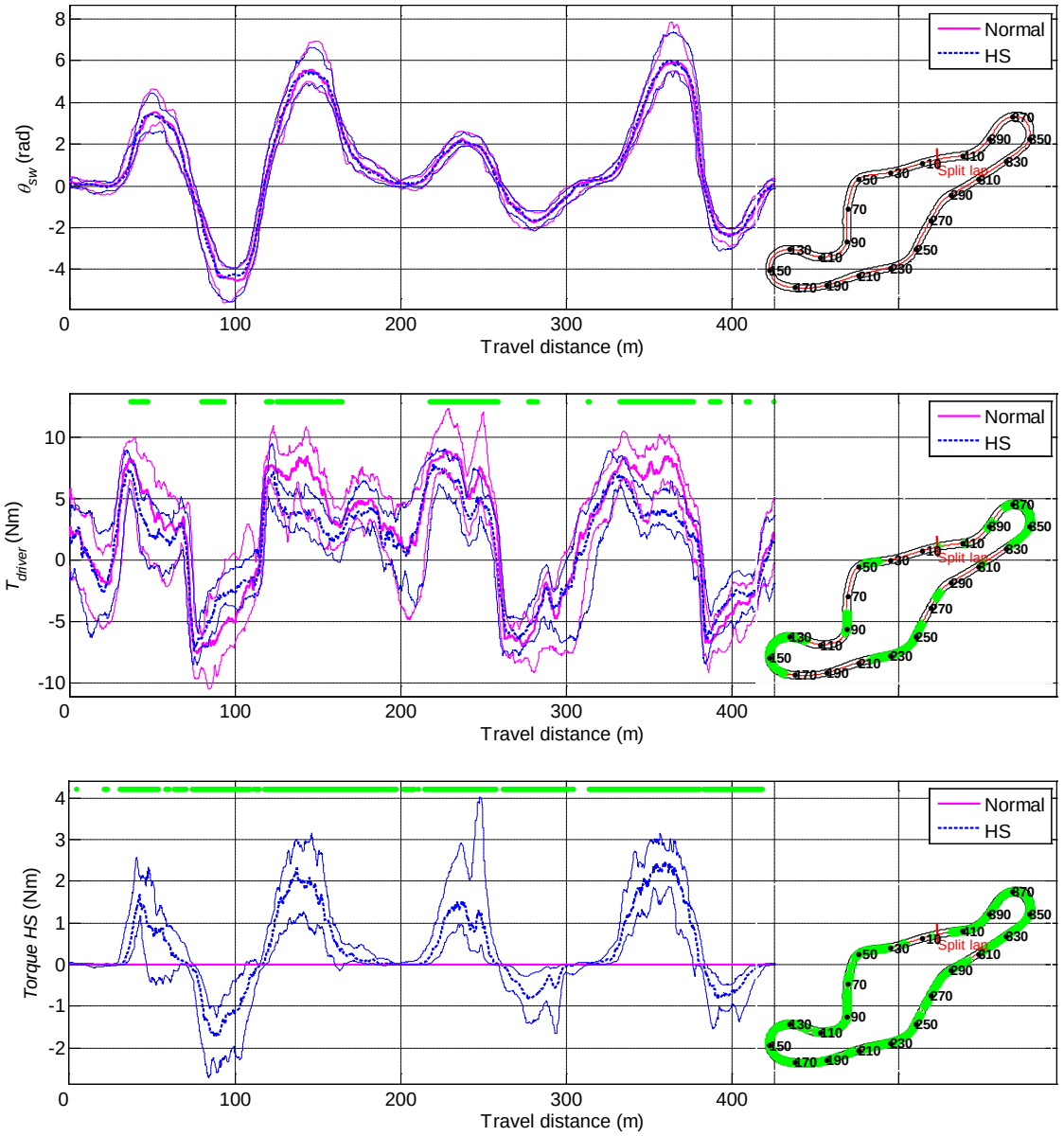

Fig. 7B 5. Steering angle θ_{sw} (top), steering torque T_{driver} (middle) Haptic support torque T_{HF} (bottom). 10th (thin lines), 50th (thick lines) and 90th (thin lines) percentiles of both the 'normal' (solid line) and the 'HS' (dashed line) case of the 3 averaged runs of the 17 drivers. A green horizontal line is visible on top, when the difference of the means between the 'normal' and the 'HS' is statistically significant ($p < 0.1\%$).

i)Vehicle's control performance

The resulting vehicle's speed in Fig. 7B 3 (top) between the 'normal' and the 'HS' case is approximately the same for the whole travel-distance. The varying driving skill level, induces this high variance which only drops in tight corners (for instance from 130 to 170 m and 330 to 390 m). The yaw rate difference in Fig. 7B 3 (middle) appears to be greater in magnitude for the 'normal' case compared to the 'HS' for certain travel-distance; the drivers are closer to their desired yaw rate, as defined in equation (defined in section VI.A in appendix). The *HS factor* signal (c.f. Fig. 7A 3) which defines an imminent alert is often lower in the 'HS' case compared to the 'normal' case (c.f. Fig. 7B 3; bottom), especially in the corners requiring moderate (below 4 rad) steering wheel angle (c.f. Fig. 7B 5; top).

The *HS factor* in the 'normal' case does not alter the steering feedback torque. It is displayed only for comparison purposes.

The front axle slip angle a_F displayed in Fig. 7B 4 (top), appears smaller in magnitude for the 'HS' case compared to the 'normal'. However, the variance of the data per distance point makes it difficult to derive a definite conclusion about the corresponding means. The HSNL appears not to be influencing the longitudinal and lateral acceleration of the vehicle in Fig. 7B 4 (middle and bottom). The variance, especially for the longitudinal acceleration is high; the lateral acceleration appears to have less variance. This agrees with the observation made earlier for the resulting vehicle's speed, where the variance was dropping in cornering (c.f. Fig. 7B 3; top).

ii)Driver's control effort

The top subplot of Fig. 7B 5 illustrates the steering wheel angle. The steering wheel variance tends to increase in tight corners; for instance around the 140 to 160 m and the 350 to 370 m corners. The steering torque T_{driver} shown in Fig. 7B 5 (middle) for the 'HS' case is significantly lower in magnitude compared to the 'normal' case in the majority of the travel-distance. Fig. 7B 5 (bottom) displays the HSNL torque T_{HF} (c.f. Fig. 7A 3) during driving; it is approximately equal to the difference between the T_{driver} for the 'normal' case and the 'HS' case.

Although Fig. 7B 3 to Fig. 7B 5 show a great amount of information regarding the vehicle's states, they cannot provide a concrete answer on the influence of the HSNL due to the few observation per distance point and the great in-between drivers and runs variance. The following subsection, individual corner analysis (described in the previous section III.C) will further elaborate on the influence of the support.

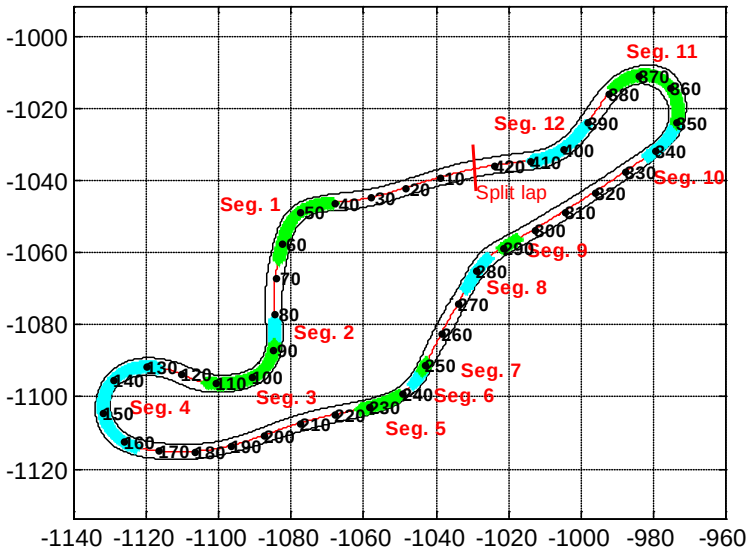

Fig. 7B 6. The 12 corner segments (Seg. 1 to Seg. 12) used for the individual corner analysis overlaid on the test-track, displayed with alternating colours. The corner segments have been devised from the mean lateral acceleration signal of all the 17 drivers (c.f. Fig. 7B 4; bottom) as described in section III.C. The resulting travel-distance per segment is shown in the 'Corner segment (distance (m))' column in Table 7B 2.

B. Objective results; individual corner analysis

The test-track was divided into various distance length corner segments, devised from the mean lateral acceleration of all 17 drivers as described in section III.C. The resulting corner segments from the process are displayed in the column 'Corner segment (distance (m))' in Table 7B 2. The analysis will not focus on individual corner, rather than the whole picture of the results from all the corners

combined. The metrics from the beginning of the table are associated with vehicle's control performance up to the T_{driver} and T_{HF} row where from there and onwards the metrics are related to the driver's control effort.

Table 7B 2 shows an analogous influence between the metrics related to the driver's control performance: front axle slip angle a_F (and its variants; front left a_{fl} and right a_{fr} wheel slip angle and lateral slip percentage s_{flY} and s_{frY}) yaw rate difference $\dot{\psi}_{diff.}$ and imminent alert signal, *HS factor*; they either are all higher or lower in magnitude (per corner segment). The results in Table 7B 2 conform to the results from with the travel-distance analysis from subsection A and shows no discernible difference between 'normal' and 'HS'.

Regarding the driver's control effort metrics, the steering torque T_{driver} is considerably reduced and drivers appear to be performing fewer steering corrections using smaller steering speed $\dot{\theta}_{sw}$. In fact the reduction in the mean steering speed for the 12 corners segments with 'HS' compared to 'normal' is statistically significant as assessed with a paired *t*-test having $p = 0.014$ (the validity of this value can be debatable due to the way the mean values derived).

Table 7B 1. TLX results of the real car testing.

Metric	Normal: mean (σ)	HS: mean (σ)	Significance: *p*
Mental demand	12.6 (4.3)	11.1 (5.1)	0.01
Physical demand	13.1 (4.0)	10.2 (4.1)	0
Temporal demand	8.9 (5.9)	8.1 (5.3)	0.1
Performance	7.6 (3.2)	7.2 (3.0)	0.48
Effort	13.4 (4.7)	10.9 (4.4)	0.00
Frustration	8.5 (4.9)	6.9 (4.3)	0.07

C. Subjective results

The NASA TLX subjective results from the 17 drivers are displayed in Table 7B 1. The paired *t*-test has been applied to the data of the NASA TLX test (they have not been ranked transformed). The table displays the mean, standard deviation (σ) and the *p*-value. It can be noticed that, the reduction in the mental demand and the physical demand in the 'HS' case was statistically significant. The effort level was also perceived as lower. The rest of the indices also favour the 'HS'.

V. Discussion and conclusions

A. Previous results from the skid-pad testing

As mentioned in the introduction section, the influence of haptic steering wheel support during skid-pad driving in simulation and in real track testing, was initially presented in [35]. The relevant findings from [35] will be summarized in this subsection, so that they can be compared with the new results from the high speed test-track driving.

In the simulation tests of [35], the task was to achieve maximum velocity, around a dry skid-pad while trying to retain control of the simulated FWD vehicle parameterized as Opel Astra G/B. Objective and subjective results in the simulation tests did favour the HSNL. It positively influenced the drivers to adopt a relatively safer driving style which in turn helped to better control the vehicle close to the handling limits. The support, helped drivers 1) to deviate less from their desired yaw rate (less understeer), 2) exert smaller steering forces to perform the same manoeuvre (less physical effort) and fewer corrections (smaller steering wheel reversal rate), 3) deviate less from their desired trajectory (smaller lateral error). On the subjective side, the drivers had smaller frustration level and perceived the system as less physically demanding.

Table 7B 2. Mean absolute values of all 3 runs of the 17 drivers, within the specified corner segments ('Corner segment (distance (m))' column), during 'normal' and 'HS'. The corner segments are displayed in Fig. 7B 5. The '$|acc_y|$' column has been coloured formatted, so that the lowest values appear in a light background (green) and highest in dark (red). The cell of individual metric which has the greatest value between 'normal' and 'HS' has been coloured (red).

Corner segment (distance (m)):		a_{fl} (rad)		a_{fr} (rad)	
	$\|acc_y\|$	normal	HS	normal	HS
1 40.5 to 65.2	7.17	0.148	0.142	0.141	0.135
2 81.7 to 88.2	7.16	0.140	0.146	0.148	0.154
3 88.3 to 112.8	8.13	0.167	0.163	0.178	0.174
4 126.9 to 164.2	7.50	0.171	0.169	0.162	0.160
5 227.5 to 239.1	6.90	0.117	0.114	0.113	0.110
6 243.7 to 248.3	7.06	0.130	0.124	0.126	0.120
7 248.3 to 251.2	7.50	0.115	0.114	0.112	0.111
8 274.4 to 285.2	6.57	0.090	0.086	0.093	0.088
9 289.7 to 294.7	6.55	0.082	0.083	0.084	0.085
10 337.5 to 349.7	7.15	0.149	0.159	0.142	0.151
11 349.7 to 378.5	7.75	0.199	0.202	0.187	0.190
12 390.9 to 409.4	6.66	0.098	0.101	0.102	0.105

Corner segment (distance (m)):		$\dot{\psi}$		$\dot{\psi}_{diff.}$	
	$\|acc_y\|$	normal	HS	normal	HS
1 40.5 to 65.2	7.17	0.567	0.568	0.352	0.318
2 81.7 to 88.2	7.16	0.531	0.539	0.347	0.361
3 88.3 to 112.8	8.13	0.674	0.668	0.386	0.375
4 126.9 to 164.2	7.50	0.758	0.764	0.305	0.296
5 227.5 to 239.1	6.90	0.411	0.416	0.332	0.311
6 243.7 to 248.3	7.06	0.415	0.409	0.325	0.319
7 248.3 to 251.2	7.50	0.337	0.349	0.281	0.288
8 274.4 to 285.2	6.57	0.342	0.336	0.342	0.334
9 289.7 to 294.7	6.55	0.273	0.287	0.221	0.218
10 337.5 to 349.7	7.15	0.566	0.579	0.268	0.288
11 349.7 to 378.5	7.75	0.819	0.821	0.359	0.374
12 390.9 to 409.4	6.66	0.426	0.433	0.284	0.293

Corner segment (distance (m)):		acc_x (m/s^2)		acc_y (m/s^2)	
	$\|acc_y\|$	normal	HS	normal	HS
1 40.5 to 65.2	7.17	1.37	1.52	7.27	7.17
2 81.7 to 88.2	7.16	3.50	3.53	7.06	7.16
3 88.3 to 112.8	8.13	1.34	1.34	8.18	8.13
4 126.9 to 164.2	7.50	1.50	1.45	7.46	7.50
5 227.5 to 239.1	6.90	1.19	1.15	6.85	6.90
6 243.7 to 248.3	7.06	1.26	1.12	7.23	7.06
7 248.3 to 251.2	7.50	1.53	1.50	7.44	7.50
8 274.4 to 285.2	6.57	0.58	0.70	6.66	6.57
9 289.7 to 294.7	6.55	1.31	1.18	6.33	6.55
10 337.5 to 349.7	7.15	3.11	3.20	6.95	7.15
11 349.7 to 378.5	7.75	1.30	1.21	7.68	7.75
12 390.9 to 409.4	6.66	1.00	0.98	6.60	6.66

Corner segment (distance (m)):		*HS factor (0-1)*		*Speed (Km/h)*	
	$\|acc_y\|$	normal	HS	normal	HS
1 40.5 to 65.2	7.17	0.570	0.532	45.17	44.61
2 81.7 to 88.2	7.16	0.532	0.550	42.77	42.70
3 88.3 to 112.8	8.13	0.714	0.673	38.78	38.94
4 126.9 to 164.2	7.50	0.668	0.669	35.14	35.01
5 227.5 to 239.1	6.90	0.382	0.354	57.10	57.15
6 243.7 to 248.3	7.06	0.468	0.424	56.75	56.75
7 248.3 to 251.2	7.50	0.395	0.383	56.70	56.69
8 274.4 to 285.2	6.57	0.249	0.226	64.02	65.14
9 289.7 to 294.7	6.55	0.229	0.224	65.89	67.05
10 337.5 to 349.7	7.15	0.561	0.608	41.56	41.68
11 349.7 to 378.5	7.75	0.776	0.786	32.97	33.20
12 390.9 to 409.4	6.66	0.291	0.311	49.65	49.53

Corner segment (distance (m)):	$\|acc_y\|$	s_{flY} (%) normal	s_{flY} (%) HS	s_{frY} (%) normal	s_{frY} (%) HS
1 40.5 to 65.2	7.17	0.127	0.125	0.143	0.137
2 81.7 to 88.2	7.16	0.147	0.152	0.149	0.154
3 88.3 to 112.8	8.13	0.173	0.169	0.142	0.139
4 126.9 to 164.2	7.50	0.142	0.141	0.170	0.168
5 227.5 to 239.1	6.90	0.112	0.109	0.114	0.110
6 243.7 to 248.3	7.06	0.113	0.111	0.125	0.120
7 248.3 to 251.2	7.50	0.104	0.104	0.109	0.109
8 274.4 to 285.2	6.57	0.089	0.085	0.083	0.080
9 289.7 to 294.7	6.55	0.080	0.081	0.073	0.075
10 337.5 to 349.7	7.15	0.154	0.165	0.148	0.157
11 349.7 to 378.5	7.75	0.160	0.161	0.199	0.201
12 390.9 to 409.4	6.66	0.097	0.101	0.083	0.085

Corner segment (distance (m)):	$\|acc_y\|$	a_F (rad) normal	a_F (rad) HS	a_R (rad) normal	a_R (rad) HS
1 40.5 to 65.2	7.17	0.145	0.139	0.072	0.073
2 81.7 to 88.2	7.16	0.144	0.150	0.068	0.070
3 88.3 to 112.8	8.13	0.172	0.169	0.080	0.079
4 126.9 to 164.2	7.50	0.167	0.165	0.085	0.084
5 227.5 to 239.1	6.90	0.115	0.112	0.061	0.061
6 243.7 to 248.3	7.06	0.128	0.122	0.075	0.070
7 248.3 to 251.2	7.50	0.113	0.113	0.069	0.067
8 274.4 to 285.2	6.57	0.091	0.087	0.043	0.040
9 289.7 to 294.7	6.55	0.083	0.084	0.053	0.054
10 337.5 to 349.7	7.15	0.146	0.155	0.086	0.089
11 349.7 to 378.5	7.75	0.194	0.197	0.093	0.092
12 390.9 to 409.4	6.66	0.100	0.103	0.047	0.048

Corner segment (distance (m)):	$\|acc_y\|$	T_{driver} normal	T_{driver} HS	T_{HF} normal	T_{HF} HS
1 40.5 to 65.2	7.17	4.29	2.71	0.00	0.95
2 81.7 to 88.2	7.16	6.75	4.59	0.00	1.64
3 88.3 to 112.8	8.13	4.04	2.41	0.00	1.17
4 126.9 to 164.2	7.50	5.94	3.32	0.00	1.53
5 227.5 to 239.1	6.90	8.35	6.11	0.00	1.52
6 243.7 to 248.3	7.06	6.88	4.94	0.00	1.43
7 248.3 to 251.2	7.50	7.14	4.48	0.00	1.39
8 274.4 to 285.2	6.57	5.70	4.77	0.00	0.75
9 289.7 to 294.7	6.55	4.22	3.73	0.00	0.57
10 337.5 to 349.7	7.15	6.99	4.46	0.00	1.75
11 349.7 to 378.5	7.75	6.39	3.44	0.00	1.92
12 390.9 to 409.4	6.66	4.47	3.42	0.00	0.69

Corner segment (distance (m)):	$\|acc_y\|$	θ_{sw} normal	θ_{sw} HS	$\dot{\theta}_{sw}$ normal	$\dot{\theta}_{sw}$ HS
1 40.5 to 65.2	7.17	3.12	3.04	1.69	1.65
2 81.7 to 88.2	7.16	3.18	3.26	2.88	2.83
3 88.3 to 112.8	8.13	4.18	4.10	1.45	1.47
4 126.9 to 164.2	7.50	4.69	4.70	1.77	1.75
5 227.5 to 239.1	6.90	2.00	1.96	1.27	1.19
6 243.7 to 248.3	7.06	1.99	1.96	1.31	1.02
7 248.3 to 251.2	7.50	1.66	1.71	2.06	1.63
8 274.4 to 285.2	6.57	1.63	1.57	0.93	0.79
9 289.7 to 294.7	6.55	1.12	1.14	1.52	1.32
10 337.5 to 349.7	7.15	3.11	3.25	2.55	2.38
11 349.7 to 378.5	7.75	5.48	5.52	1.76	1.63
12 390.9 to 409.4	6.66	2.20	2.26	1.11	1.19

In the real car tests, the task was to achieve maximum velocity, around a slippery skid-pad while trying to retain control of the same Opel Astra G/B, also used in the tests presented in the current Chapter. Objective and subjective results did also favour the HSNL. Drivers achieved similar

longitudinal and the lateral speeds for both test conditions, while at the same time, the cornering radius was statistically significant smaller with the support. Similarly as in the simulation tests, the drivers were probable to experience smaller front axle slip angle and yaw rate difference with the support. The *HS factor* signal which defines an imminent alert was statistically significant reduced with HSNL. Regarding the subjective results, drivers perceived that the test required smaller effort level and had significantly reduced physical and mental demand.

B. High speed test-track testing

The results displayed from Fig. 7B 3 to Fig. 7B 5 for the travel-distance analysis in IV.A illustrate information regarding the vehicle's states and drivers' control inputs. They provide limited information on the influence of the HSNL. This was due to the few observation per distance point and the great in-between drivers and runs variance. To overcome the aforementioned limitation, the test-track was divided into various discrete corners as described in section III.C. The proposed analysis revealed no major influence of the HSNL on the metrics related with the vehicle's control performance. As far as the driving effort metrics, the steering torque T_{driver} was considerably reduced (c.f. Fig. 7B 5; middle). At the same time, the drivers' appeared to be performing less steering corrections; the steering speed was lower in almost all corners.

The drivers subjectively complimented the support. They reported less mental and physical demand as well as smaller effort level. Test drivers reported in general that they could "easily feel the understeer coming." It is worth to mention that certain drivers reported that they thought that the vehicle handled better with support, although the vehicle was not altered and the operating principle was explained to them. The aforementioned statement corresponds with the observation from [6], where they test subjects believed that their vehicle was equipped with ESC while it was not.

C. Haptic support works!

The skid-pad tests of [35] as well as the high speed test-track driving presented here showed that HSNL was beneficial, influencing positively the drivers' vehicle control performance while reducing drivers' control effort. The evaluation of the HSNL was divided in those two adjunct tests so as to enable an assessment which will offer statistical significant answers, the skid-pad test, and an analysis which will provide a close to real life driving appraisal, the test-track driving.

Driving near the vehicle's handling limits in the skid-pad tests, "close" to steady state, gave the drivers the opportunity to continuously interact with the support in their endeavour to keep the vehicle under control. This controlled experiment allowed for data collection which were continuously revolving around an average state enabling to derive statistical significance conclusions. In the high speed test-track driving, the vehicle was continuously in transient state; although the vehicle was "pushed" to its handling limits (the lateral acceleration was often approaching 1 g, c.f. Fig. 7B 4; bottom), it was far from a steady state condition, even within the individual corners. A subjective remark that can be made from the author of this study, is that skilled drivers, will try to approach closer to the vehicle's handling limit with higher chances of inducing severe understeer or oversteer. However, they can regain control of the vehicle if it is still responding to their inputs. In a sense, skilled drivers lose control more often compared to un-skilled. This observation harmonises with the results from [6] investigating the effect of ESC on driver behaviour, suggesting that if the driver "feels that he/she has control over the situation, and a positive attitude and acceptance from others, he/she is more likely to drive in a risky way."

The diverse driving group, which consisted, from unskilful drivers, to car enthusiasts, to test drivers and amateur race drivers resulted to varying travelling paths and control inputs, in-between drivers and also in-between drivers' runs; the test drivers (3 out of the group of 17 drivers) were the most

consistent group achieving the most repeatable runs. Also, as it was discussed in the introduction section, drivers primarily steer in an anticipatory feed-forward manner to an estimated future path while they use an adaptive compensatory strategy to correct for deviations of the vehicle from the demanded trajectory [56]. Drivers in the test-track driving, would apply their control inputs in a feedforward manner while in the skid-pad testing, drivers were expected to employ feedback control to compensate for disturbances (perception mismatch, friction coefficient changes etc.) [56][105]. Due to the fact that HSNL provides only information and not a strong guidance to the driver (as for example [131][119][122]), it mainly affects the driver's compensatory control part; thus the support was not expected to yield measureable impact on the test-track driving.

Recalling that one of the primal goal of automotive manufacturers [172] is reducing the driving load, then it can be concluded that HSNL at the vehicle's handling limits can improve the driver-car interaction and potentially promote safety; the support effectively helped drivers to deviate less from their desired trajectory (skid-pad test) and reduced their mental and physical demand (overall; skid-pad and test-track test). The proposed system can be characterized diverse, in terms that it can improve the vehicle's perceived sportiness and at the same time promote safety. Of course there is the controversy that such a system might spark riskier driving (c.f. ESC in [6]) but the author subjectively suggests that benefits and drivers satisfaction would overwhelm the risks. This assertion should be further investigated though. The author would encourage the adoption of such systems into modern vehicles enabled at will with the press of a "sport" button. A small video from track testing is available online [157].

VI. Appendix

A. Travel-distance analysis metrics

Objective performance for the travel-distance analysis was evaluated with the following metrics:

Vehicle's resulting speed.

Yaw rate difference $\dot{\psi}_{diff}$ (7.2.1).

Yaw rate $\dot{\psi}$.

Desired yaw rate $\dot{\psi}_{des}$ (7.2.1). The desired yaw rate is calculated using the vehicle's longitudinal speed $\dot{x}$, the front wheels steering angle δ, the vehicle's wheelbase L and the understeer coefficient K_u [161] deriving from the vehicle properties: mass, tires' cornering stiffness and weight distribution.

$$\dot{\psi}_{des.} = \frac{\dot{x}}{L + \dot{x}^2 \cdot K_u} \cdot \delta, \quad \dot{\psi}_{diff.} = \dot{\psi}_{des} - \dot{\psi} \tag{7.2.1}$$

The imminent alert signal *HS factor* (c.f. Fig. 7A 3).

Steering torque, T_{driver}.

The haptic support torque T_{HF} (c.f. Fig. 7A 3).

Steering angle, θ_{sw}.

Front axle slip angle a_F.

Longitudinal acc_x and lateral acceleration acc_y.

B. Individual corner analysis metrics

Objective performance for the individual corner analysis was evaluated using the majority of the metrics used in travel-distance analysis (above), plus the additional metrics depicted below:

Steering wheel angular speed, $\dot{\theta}_{sw}$.

Longitudinal acc_x and lateral acceleration acc_y.

Front a_F and rear a_R axle slip angle.

Front left a_{fl} and a_{fr} right wheel slip angle.

Front left s_{flY} and right s_{frY} lateral slip as defined in [59]. This was calculated taking also into consideration the longitudinal slip.

VII. Acknowledgment

The research was supported by the Automotive Development Center of SKF, in the Netherlands and Prodrive Automotive in UK. E. Velenis was supported by an EPSRC First Grant Award (award number EP/I037792/1). Special thanks to Oliver Jones, Dave Rollet, Mat Taylor, Chris Roberts, Ben Garrat, Scott Parton, Adrian Hall. The parts for modifying the steering system were manufactured at TUDelft through Johannes Dukker and Jan van Frankenhuyzen. We would also like to thank Circuit Park Zandvoort, for granting usage of their test facilities.

Chapter 8. Conclusions

“Εφ’ εκάστου έργου, σκόπει τα καθηγούμενα και τα ακόλουθα αυτού και ούτως έρχου επ’ αυτού.”
Επίκτητος, 50-120 μ.Χ.

“For every attainment, you should consider what drove you towards it and its oncoming effects.”
Epictetus, 50-120 A.D.

Driver Steering Support Interfaces Near the Vehicle's Handling Limits; Conclusions

Abstract—The current conclusions Chapter, reflects the original goal on the accomplished work and distils the results from Chapters 2 – 7. It provides recommendations deriving from the acquired results and concludes this thesis by citing the author's vision on automotive systems.

I. Synopsis

The goal of this thesis is to propose steering support systems that reduce the driving load and can promote safety. The philosophy is to increase driver's responsibility and support him/her in the sense of information rather than automation. The research focuses on cornering near the vehicle's handling limits (operating near the lateral acceleration limits imposed by the tire-road adhesion), aiming to promote the driver's perception of the vehicle's behaviour and handling capacity (the vehicle's internal model) by providing haptic cues on the steering wheel. We assumed the availability of emerging sensor technologies, such as load sensing bearings, body-slip angle sensors, on-board cameras that can detect lane markings and the vehicle's position with respect to the road etc.

Reflecting our goal on the actual accomplished work we may conclude that we successfully introduced driver steering support systems that can reduce driving load (c.f. Chapter 4 and Chapter 7) and potentially promote safety; the steering interfaces for road-departure-prevention (RDP), presented in Chapter 4 [41] and the haptic steering support near the vehicle's handling limits (Haptic Support Near the Limits; HSNL), presented in Chapter 7. Concerning the RDP, we concluded that a drive-by-wire setup can prevent road departure, reduce mental workload, and has the potential to promote safety. As-far-as the HSNL of Chapter 7, during the compensatory skid-pad test [36], the support helped the drivers to operate the tires in smaller slip angles and hence avoid saturation of the front wheels' lateral forces and excessive understeer. The support, overall reduced drivers' control effort and physical demand for all testing conditions [37].

Realizing the aforementioned support system proved challenging. It necessitated a concrete knowledge of vehicle dynamics and control, equipment preparation (driving simulators and test vehicles) for performing the experiments, a solid understanding of driver-steering interaction near the vehicle's handling limits, support controller setup and fine-tuning and finally driver testing followed by in-depth data analysis to evaluate the potentials of the support.

Deciphering the human-controller in Chapters 4, 5 and 7 concluded that humans are overwhelmingly diverse in their control inputs when it comes to driving. They exhibit high variance (even in-between themselves) and may realize the same task (achieving comparable vehicle states) by employing a different strategy each time. Adaptation towards a specific task is highly related with the skill levels. Expert drivers, compared to non-experts, will adapt faster and achieve repeatable inputs for a giving stimulus (visual or vestibular) exhibiting smaller variance for a specific control-task, as shown in Chapter 5 Part A and B and discussed in Chapter 7. There are cases that drivers do completely fail to adapt to a given support system; when for instance drive with the RDP system (c.f. Chapter 4). The adaptation incompetence may be related to the fact that drivers did not fully understand the functionality of the RDP system (although the operating principle of each setup was explained to the drivers before testing). Stimulus-response compatibility was lost with the drive-by-wire systems, that

is, steering response stopped being unambiguously related to steering-wheel angle, an approach which may confuse the driver and disrupt his/her internal model of the vehicle

As mentioned in Chapter 7, drivers with low driving skills tend to rate themselves as “above average” drivers. Although un-skilled drivers tend to be more cautious so that they do not exceed the handling limits, when they lose control they are incapable of regaining it back. Skilled drivers though, will try to approach closer to the vehicle’s handling limit with higher chances of exceeding it. Thus, a support system exhibits different impact on expert, average and unskilled drivers (c.f. Chapter 4 and 7). An information-feedback support system, for instance the HSNL of Chapter 7 may benefit more skilled drivers, while the authoritarian drive-by-wire RDP support of Chapter 4 may benefit more unskilled drivers. However, a support system should work effectively under all circumstances; if not beneficial, it should at least not be a hindrance (e.g. [73]).

Research always starts with a hypothesis which might prove wrong, with the method-results not necessarily the anticipated ones; thus not all initial goals were accomplished. For instance, we conceptually wanted to stimulate the average driver to control the vehicle near its handling limits, as an expert driver would, solely by haptic cues. Promoting a normal driver to achieve the same control inputs as an expert-driver would, takes more than information on the steering wheel (c.f. Chapter 5) or even steering guidance [73]. Additionally, designing a neuromuscular driver model which can effectively be used for developing steering systems, necessitates real drivers’ properties, i.e. the arm’s admittance and driver’s steering behaviour (experiments for acquiring those properties have already been performed using the Opel Astra and they will be merged with Chapter 6 and be published as future work). With realistic parameters the model could prove useful when designing systems such as the RDP and the HSNL.

II. Milestones on experimental tools, driver behaviour study and steering support interface development

This section condenses Chapters 2 – 7 into 3 distinct scientific groups, in accordance with the 3 milestone goal groups presented in the introductory Chapter 1.

A. Develop the means-tools for performing the research

The work time distribution of the current research was biased towards the equipment preparation and data analysis-results reporting. The experimental setup for the steering force-feedback of the driving simulator, the race-car data acquisition apparatus and finally the steering force-feedback Opel Astra, necessitated a great amount of developing time as-well-as extensive manufacturing-financial support (c.f. acknowledgements of Chapters 2, 5 and 7). Despite the harsh manipulation during testing, nothing of the developed equipment broke or behaved out of the original specifications. The development of the equipment brought along engineering design acquaintance, automotive mechatronics hands-on knowledge and project management experience; characteristics that every automotive development engineer should have.

The goal to develop a high fidelity force-feedback (FF) steering device, aimed to enable human-in-the-loop automotive simulations was achieved in Chapter 2 [32]. The developed system was able to simulate a wide range of virtual dynamics, allowing realistic FF from a large variety of steering systems comparable to those of a real vehicle. The system was later used the in work presented in Chapters 3, 4 and 7. Our aim a) to assess the steering metrics of real cars during lane change manoeuvres and b) to investigate how key parameters of the vehicle determine these steering metrics was addressed in Chapter 3 [40]. The corresponding results enabled to assess the realism and easily parameterize the driving simulator used in Chapters 4 and 7.

Our target to mathematically determine the control inputs of an expert driver for a stabilization task, and propagate those control inputs to the average driver, so as he/she becomes expert appears in part C of Chapter 5 [63][64]. There, we studied the stabilization of RWD vehicles with respect to extreme body-slip angle cornering equilibria. This work is considered to be the basis for developing driver steering support systems. We collected experimental data (using the setup presented in part A during the execution of steady-state drifting of a RWD vehicle. The sliding mode control scheme proposed to stabilize the vehicle with respect to drifting cornering equilibria, used combined steering angle and drive torque inputs, in accordance to our experimental observations. However, after completing this work we could not directly motivate a support system that would be effective with a driver-in-the-loop; the support system would have to inform the driver about the position of the throttle, the brake and the steering angle simultaneously, while it would necessitate the reference cornering radius, body-slip angle and velocity; it would be more suitable for autonomous high-speed driving utilizing knowledge of the infrastructure (road maps). The above controller though, could motivate support in the by-wire sense; that is, the driver gives through his/her by-wire steering and throttle inputs a reference cornering radius, bodyslip angle and vehicle velocity and the controller will stabilise the vehicle with respect to those desired inputs.

Our goal to have in our disposal a tool for objective evaluation of steering systems, using a Force-Feedback Driver Model (FFDM) with neuromuscular (NMS) characteristics, is addressed in Chapter 6 [31]. The FFDM that consists upon a preview controller and a NMS model was shown to have the potential to become a useful tool in vehicular steering system evaluation; as long it would be validated with real driving data. The preview controller aimed to mimic human steering inputs for cornering, while its force-interaction characteristics targeted to represent the human's NMS properties. Using lane-change tests from six drivers (Chapter 5, part A), we tried to parameterize the preview part of the driver model. We employed optimization tools to solve the preview gains. The optimization process was able to converge to a solution; however no reasonable preview gains were derived, rather than over-fitted gains on the specific driving paths. Therefore this idea was temporarily set-aside and results not reported; however from the tests that appear in Chapter 7 part B and additional tests for measuring the drivers' arm admittance (that do not appear in this thesis) we shall pursue the FFDM's development.

B. Driver behaviour study

Our goal to study unsupported and supported driving has been addressed in Chapters 4, 5 and 7. The work of Chapter 5 and the corresponding tests, preceded in time the work of Chapters 4 and 7. The knowledge from Chapter 5 was later used for accomplishing the work of Chapter 4 and 7 (will be referred in the next subsection). Part A of Chapter 5 [34] supplied a roadmap on how a researcher can effectively perform experiments with real vehicles and obtain the required measurements for studying dynamic driving behaviour. It provided detailed guidelines for constructing a versatile low-cost experimental apparatus suitable to be fitted on race cars, oriented to high-speed driving modelling research. Part A introduced in-field testing with instrumented vehicles to develop and validate driver models. Part B of Chapter 5 [39], discussed the human's compensatory behaviour and driving outside the vehicle's stable envelope where considerable control effort is required to retain stability. Six different test drivers executed high-speed circular manoeuvres on a loose surface, instructed to maintain constant sideslip angle and distance from the centre of the tire-marked circular path. Drivers accustomed with the test vehicle exhibited smaller standard deviation (σ) in their steering inputs and the realized vehicle's states and higher σ in the throttle control. We can conclude that drivers are fairly diverse in their control inputs exhibiting high variance and may achieve the same vehicle states by

applying different inputs each time. Being an enthusiastic driver accustomed with the test-vehicle may well mean superior control performance compared to a recognized race-driver.

C. Driver steering interfaces

Our aim to develop and test a road-departure-prevention (RDP) system in an emergency scenario is presented in Chapter 4 [41]. For the RDP development we used the force-feedback steering system of Chapter 2. The RDP system intervened when a road departure was likely to occur by applying a low level of automation in the form of an advisory haptic-feedback (HF) torque, and/or a high level of automation by correcting the front-wheel angle (DBW and DBW & HF). HF had a profound influence on the measured steering torque, but no significant influence on steering-wheel angle or vehicle path. Apparently, in an emergency situation, drivers steer in an "open-loop" fashion without much regard for additional feedback torques that are applied on the steering wheel. The DBW setups helped drivers to keep a safe distance from the detected roadside and reduced mental workload. However, the DBW, resulted in drivers making additional corrections to avoid hitting the inner pylons. The study provided clear results about the potentials and pitfalls of DBW and haptic-feedback, and the combination of both. We concluded that a drive-by-wire setup can prevent road departure, reduce mental workload, and has the potential to promote safety.

The milestone of this thesis, the influence of haptic steering wheel support when driving near the vehicle's handling limit (Haptic Support Near the Limits; HSNL) appears in Chapter 7 [35][36][37][38]. The HSNL, exaggerates the reduction of the steering "stiffness" and makes it profound to the driver, so that he/she avoids excessive steering angle inputs which will result in increased tire slip and consequently lateral force loss. Chapter 7 is divided into two parts (A,B). Part A of Chapter 7 [35][36], studies the HSNL when driving near the vehicle's handling limits in driver-in-the-loop simulation and real track testing with a vehicle (Opel Astra G/B) equipped with a variable steering feedback torque system. In the simulator study 25 drivers attempted to achieve maximum velocity, on a dry skid-pad while trying to retain control of the simulated vehicle parameterized as the Astra. In the real tests, 17 drivers attempted to achieve maximum velocity, around a wet skid-pad while trying to retain control of the Astra. Both the driving simulator and the real vehicle test showed that haptic support had significant beneficial effects on drivers' lateral control performance with drivers operating the tires in smaller slip angles and hence avoiding saturation of the front wheels' lateral forces and excessive understeer. Part B of Chapter 7 [37][38], studies the HSNL during high speed cornering in a test-track. 17 test subjects drove around a narrow-twisting tarmac circuit, the Opel Astra. The drivers were instructed to achieve maximum velocity through corners, while receiving haptic steering cues related to the vehicle's cornering potentials. Due to the fact that haptic support provides only information and not a strong guidance to the driver (as for example [131][119][122]), it did not influence significantly the feed-forward steering task. One of the primal goals of automotive manufacturers [172] is to reduce the control effort and mental load; thus it can be concluded that the HSNL improves the driver-car interaction.

III. Recommendations

The diverse behaviour of drivers, discussed in Chapters 4, 5 and 7, revealed that support systems related to the driver-car interface should be evaluated in real life (test-rack and public roads tests) in addition to human-in-the-loop driving simulation. Although simulators can incorporate high level of detail it is not possible to evaluate all the aspects and uncertainties that affect driving performance. Developing concepts in simulation and fine-tuning/validating those in the real car should provide a rule-of-thumb for innovative system production related to human-machine-interaction.

According to prior research [56][105], drivers primarily appear to steer in an anticipatory feed-forward manner to an estimated future path while they use an adaptive compensatory strategy to correct for deviations of the vehicle from the demanded trajectory. Paralleling this statement to Chapter 7, driving on a skid-pad near the vehicle's handling limits, gives the drivers the opportunity to continuously interact with the support in their endeavour to keep the vehicle under control to compensate for disturbances (perception mismatch, friction coefficient changes etc.) [35][36]. Driving in a test-track near the vehicle's handling limits, induces drivers to feedforward apply their control inputs so as to maximize their performance [37][38]. Results acquired for the driver's feedforward control do not necessarily apply for compensatory control, as suggested from the results of Chapter 7, part A and B. Steering support systems, should therefore be evaluated for both driver's feedforward and compensatory control mechanisms.

The driver has boundaries and a system which improves the driver-car interface is not necessarily sufficient to induce better vehicle control. Even the best driver, if he is not paying attention can lose control in a relative moderate scenario (c.f. Chapter 4, 5 and 7). It is suggested that the driving task is either fully automated (automated in the sense of an autonomous vehicle.) or the driver is in full authority. Intermediate solutions might not be good enough; for example the drive-by-wire interfaces for RDP (c.f. Chapter 4) where the controller can override the driver's inputs that will lead to road departure but will not compensate for other faulty inputs (i.e. driving towards an obstacle).

Driver's fatigue, impairment or distraction can lead to lane departure which appears relevant in 179,000 crashes per year and related up to 7,500 fatal crashes per year in the United States [100]. Getting the driver out of the control-loop spoils the fun and may promote drowsiness and in correspondence unsafe driving. Driver steering support systems should keep the driver "awake" and concentrated on the driving task. We encourage systems that motivate and reward the driver with a lively steering feedback (wide frequency feedback torque spectrum). We may assume that driving dynamically provokes the driver to be more concentrated on the task; potentially more prone to accidents but unlikely to be distracted.

IV. Vision

Observing the evolution of the vehicle dynamics technology [172], we can assume that active safety systems still have potentials to promote chassis control; especially if we take into consideration the available torque-vectoring technologies (electric motors controlling individual wheel or torque-split differentials) which can effectively expand the control envelope of current vehicles. However, the chassis control will always be governed by the laws of physics and the driver; thus a driver's input may still provoke a crash that a support system cannot compensate for. Given the current available technologies (and especially the emerging ones), vehicles should not be allowed to crash at all. Therefore, if we want to make the roads safer, we should take advantage of the current infrastructure, such as road-geometry (curvature, velocity speed profiles etc.), in-vehicle cameras and other sensors (which can detect traffic signals, pedestrians, on-coming vehicles, lane-markings etc.), wireless communication for co-operative vehicle driving, and should further promote its development and its utilization in automotive safety.

Future driver support systems, should utilize the knowledge of the infrastructure and incorporate it within the feedback itself. For instance, the support systems should advise drivers to adapt the speed according to the oncoming curve and the road-friction coefficient, potentially estimated through the emerging technology of load-sensing wheel hubs [155][21]. This advice may be delivered to the driver visually or with haptic gas pedal cues [51]. Road-departure-prevention (RDP) (c.f. Chapter 4) technology may be combined with haptic support near the vehicle's handling limits (HSNL) (c.f.

Chapter 7). For instance, a combined controller may increase the steering-stiffness if the driver is trying to surpass the optimal steering angle (the HF case in Chapter 4 and the exactly opposite philosophy to that of Chapter 7). The effectiveness of the above scheme could be further investigated.

We should recall that the steering interface is not only about safety but also about feel and driver satisfaction. The introduction of electrically power assisted steering (EPAS) has brought to the scene a new "headache" to automotive developers. The undisputed benefits of EPAS systems, in terms of fuel economy, weight-space saving and reduced manufacturing-service cost, compared to traditional hydraulic power assisted steering (HPAS) systems have promoted EPAS into a modern vehicle commodity. However, car manufactures with pedigree for pronounced feedback fidelity at their steering systems, have been heavily criticized for losing their "feel" during their transition from HPAS to EPAS. One of greatest sports car series of all time, the Porsche 911, renowned for its steering feel, has adapted EPAS in its latest version the 991 but not without criticism: "*The steering is indeed more filtered, with most of the hyper-organic jiggles and tugging tossed out...*" [78]. Similarly, the BMW 5 series one of the best sports saloon series, has also adopted EPAS in its latest version F10. The reviews are not charming: "*Although weighty, the setup feels artificial and provides zero feedback… The electric power steering is something all 5-series buyers have to live with*." [28]. BMW though offers the high-end models of the 5 series range, e.g. the BMW M5, with HPAS [81] avoiding the "*risky dalliance with a known buzz-kill*" [78] of the EPAS. The comment "*Steering feel, even at 10 mph, is alive and well in the M5… BMW, I don't care about the 0.001 mpg saved by switching to electric power assist: clearly, this is the right solution. Bring back hydraulic steering on all 5- and 7-series*." [81] distils the situation between EPAS and HPAS.

Although the EPAS inherent properties allows for flexible software control, it appears to be an undermining factor in the design philosophy and/or lack of understanding on the driver desired feedback. The latter is reflected in the corresponding EPAS control methods which will determine the feedback forces perceived by the driver. We therefore envision the "brand-by-wire" concept which will assess the current EPAS design philosophy, advocate the necessary hardware for reinstating the feedback components of HPAS and will manifest the control guidelines for achieving a steering "feel" tailored to individual car brand-model irrelevant of the underlying hardware components.

Concluding, road safety will come through revolution in the automotive infrastructure rather than evolution on current safety systems. However, cars are more than a mean for commuting to work and steering-feel is and should always remain a high priority in every automotive manufacturer's list.

References

“Της παιδείας (φασίν) την μεν ρίζαν πικράν τους δε καρπούς γλυκείς.”
Ισοκράτης, 436-338 π.Χ.

“Education’s (people say) roots are bitter, but the fruits are sweet.”
Isocrates, 436-338 B.C.

References

[1] A. Baviskar, J.R. Wagner, D.M. Dawson, D. Braganza, P. Setlur, "An adjustable steer-by-wire haptic-interface tracking controller for ground vehicles," *IEEE Trans. On Vehicular Tech.*, vol. 58, no. 2, pp. 546-554, Feb. 2009.

[2] A. Kemeny, "Simulation and perception," *Proc. of the Driving Simul. Conf*., Paris, France, pp. 21–28, Jul. 1999.

[3] A. Kemeny, F. Panerai, "Evaluating perception in driving simulation experiments," *Trends in Cognitive Sciences*, vol. 7, no. 1, pp. 31–37, 2003.

[4] A. Kempski, R. Smolenski, "Decomposition of EMI Noise into common and differential modes in PWM inverter drive system," *J. of Electrical Power Quality and Utilization*, vol. 12, no.1, pp. 53-58, 2006.

[5] A. Liu, S. Chang, "Force feedback in a stationary driving simulator," *Proc. of the Human Factors Ergon. Soc. Annu. Meeting*, Vancouver, BC, Canada, Oct. 1995, pp. 1671–1675.

[6] A. Vadebya, M. Wiklundb, S. Forwarda, "Car drivers' perceptions of electronic stability control (ESC) systems," *Accident Analysis and Prevention*, vol. 43 pp. 706-713, 2011.

[7] A. Zaremba, R.I. Davis, "Dynamic analysis and stability of a power assist steering system," *Proc. of the ACC*, Seattle, Washington, June 1995, pp. 4253-425.

[8] A.C. Newberry, M.J. Griffin, M. Dowson, "Driver perception of steering feel," *Proc. of the Institution of Mechanical Engineers Part D, Journal of Automobile Engineering*, vol. 221, no. 4, pp. 405-415, 2010.

[9] A.C. Schouten, E. de Vlugt, J.J.B. van Hilten, F.C.T. vd Helm, "Design of a torque-controlled manipulator to analyse the admittance of the wrist joint," *J. of Neuroscience Methods*, vol. 154, no. 1, pp. 134–141, 2006.

[10] A.C. Schouten, W. Mugge, F.C.T. vd Helm, "NMClab a model to assess the contributions of muscle visco-elasticity and afferent feedback to joint dynamics," *Journal of biomechanics*, vol. 41, 2008, pp. 1659-67.

[11] A.J. Pick, D.J. Cole, "A mathematical model of driver steering control, including neuromuscular dynamics," *J. of Dynamic Sys. Measurements and Control*, vol. 130, no. 3, 2008.

[12] A.J. Pick, J. Cole, "Dynamic properties of a driver's arms holding a steering wheel," *J. Automobile Engineering*, vol. 221, no. 12, pp. 1475-1486, 2007.

[13] A.K. Zschocke, A. Albers, "Links between subjective and objective evaluations regarding the steering characteristics of automobiles," *International Journal of Automotive Technology*, vol. 9, no. 4, pp. 473-481, 2008.

[14] A.L. Window, *Strain Gauge Technology*, Springer, 1992, pp. 151-154.

[15] A.M.C. Odhams, D.J. Cole, "Identification of a driver's preview steering control behaviour using data from a driving simulator and a randomly curved road path," *Proc. of the 10th International Symposium on Advanced Vehicle Control*, *AVEC2010*, 2010, pp. 605-609.

[16] A.Y. Ungoren, H. Peng, "An adaptive lateral preview driver model," *Vehicle System Dynamics*, vol. 43, no. 4, pp. 245-259, April 2005.

[17] ABB, "Direct Torque Control-the world's most advanced AC drive technology, Technical guide no. 1. Available: http://www.abb-drives.com/StdDrives/RestrictedPages/Marketing/Documentation/files/PRoducts/DTCTechGuide1.pdf

[18] *AVR Studio: Integrated Development Environment*, ATMEL Corporation, 10/2007. Available: http://www.atmel.com/dyn/products/tools_card.asp?tool_id=2725

[19] B. Carter, "A single-supply op-amp circuit collection," Application report, SLOA058, Texas Instruments, Nov. 2000. Available: http://focus.ti.com/lit/an/sloa058/sloa058.pdf

[20] B. Seppelt, M. Lees, J. Lee, "Driver distraction and reliance: adaptive cruise control in the context of sensor reliability and algorithm limits," *Proc. of the 3rd International Driving Symposium on Human Factors in Driver Assessment, Training and Vehicle Design*, pp. 255-261, 2005.

[21] Bernie Van Leuuwen, Joost Zuurbier, "Vehicle State Estimation based on Load Sensing, Project Smart Cars, 2004-2006 (SKF-TNO)," presentation on *Vehicle Dynamics Expo 2007*. Available: http://www.vehicledynamics-expo.com/07vdx_conf/day_2/zuurbier.pdf

[22] C. Grover, I. Knight, F. Okoro, I. Simmons, G. Couper, P. Massie, B. Smith, "Automated Emergency Brake Systems: Technical requirements, costs and benefits," published project report for the European Commission, TRL ltd, Contract ENTR/05/17.01, April 2008, Available: http://ec.europa.eu/enterprise/sectors/automotive/files/projects/report_aebs_en.pdf Accessed, Apr. 2012.

[23] C. MacAdam, "Application of an Optimal Preview Control for Simulation of Closed-Loop Automobile Driving," *IEEE Trans. on Systems, Man and Cybernetics*, vol. 11, no. 6, pp. 393-399, June 1981.

[24] C. MacAdam, Development of a Driver Model for Near/At-Limit Vehicle Handling, Technical Report for GM Corp., The University of Michigan, Transportation Research Institute, Dec. 2001. Available: http://deepblue.lib.umich.edu/handle/2027.42/1485

[25] C. Schweinsberg, "Infiniti Lane Departure Prevention to Debut on New M." Available: http://wardsauto.com/ar/infiniti_lane_prevention/ Accessed, Apr. 2012.
[26] C. Voser, R. Hindiyeh, J.C. Gerdes, "Analysis and control of high sideslip maneuvers," *in 21st International Symposium on Dynamics of Vehicles on Roads and Tracks*, Aug. 17-21 2009.
[27] C.I. Chatzikomis, K.N. Spentzas, "A path-following driver model with longitudinal and lateral control of vehicle's motion," *Forsch Ingenieurwes*, vol. 73, pp. 257-266, 2009.
[28] Car and Driver magazine, "2011 BMW 528i," 2011. Available: http://www.caranddriver.com/reviews/bmw-5-series-review-2011-bmw-528i-test
[29] CarSim User Manual. Mechanical Simulation Corp., Ann Arbor, MI, 2009.
[30] D. Crolla, *Automotive Engineering: Powertrain, Chassis System and Vehicle Body*, Butterworth-Heinemann, 1st ed., Aug. 2009.
[31] D. Katzourakis, C. Droogendijk, D. Abbink, R. Happee, E. Holweg, "Force-Feedback Driver Model for Objective Assessment of Automotive Steering Systems," *Proc. of the 10th International Symposium on Advanced Vehicle Control, AVEC10*, pp. 381-386, 2010. Available: https://docs.google.com/open?id=0B6SAzlTF5b48ZDQwMmMxODAtODI1My00YWRlLTk5NmUtM2U5ZjdlMWFiYzg1
[32] D. Katzourakis, D. Abbink, R. Happee, E. Holweg, "Steering Force Feedback for Human Machine Interface Automotive Experiments," *IEEE Trans. on Instrumentation and Measurement; Special Issue on Haptic Enabled Virtual Environments*, vol. 60, no. 1, pp. 32-43, Jan. 201.
[33] D. Katzourakis, E. Velenis, "Rally Car Instrumentation for Dynamics Driving Behaviour Studies." Available: http://students.ceid.upatras.gr/~katzourd/rally
[34] D. Katzourakis, E. Velenis, D. Abbink, R. Happee, Edward Holweg, "Race Car Instrumentation for Driving Behaviour Studies," *IEEE Trans. on Instrumentation and Measurement*, vol. 61, no.2 pp. 462 – 474, 2012.
[35] D. Katzourakis, E. Velenis, E. Holweg, R. Happee, "Haptic Steering Support when Driving at the Tires' Cornering Limits," accepted for presentation on the *11th International Symposium on Advanced Vehicle Control*, AVEC12, Korea, 2012
[36] D. Katzourakis, E. Velenis, E. Holweg, R. Happee, "Haptic Steering Support for Driving Near the Vehicle's Handling Limits; Skid-pad case," submitted for review, 2012.
[37] D. Katzourakis, E. Velenis, E. Holweg, R. Happee, "Haptic Steering Support for Driving Near the Vehicle's Handling Limits; Test-track case," submitted for review, 2012.
[38] D. Katzourakis, E. Velenis, E. Holweg, R. Happee, "Haptic Steering Support in High Speed Cornering," *to be presented on the 1st International Conference on Human Factors in Transportation*, San Francisco, U.S., Jul. 2012.
[39] D. Katzourakis, E. Velenis, R. Happee, "Driver Control Actions in High Speed Circular Driving," *Proc. of the 6th International Driving Symposium on Human Factors in Driver Assessment, Training and Vehicle Design*, California, pp. 598-605, June 2011.
[40] D. Katzourakis, J.C.F. de Winter, S. de Groot, R. Happee, "Driving simulator parameterization using double-lane change steering metrics as recorded on five modern cars," in press on *Simulation Modeling Practice and Theory*, vol. 26, pp. 96-112, 2012.
[41] D. Katzourakis, J.C.F. de Winter, M. Alirezaei, M. Corno, R. Happee, "Road Departure Prevention in an Emergency Obstacle Avoidance Situation," submitted for review, 2012.
[42] D. Katzourakis, M. Alirezaei, J.C.F. de Winter, M. Corno, R. Happee *et al*., "Shared Control for Road Departure Prevention," *Proc. of the IEEE Int. Conf. SMC*, Alaska, U.S.A., pp. 1037-1043, Oct. 2011.
[43] D. Katzourakis, M. Gerard, E. Holweg, R. Happee, "Design issues for haptic steering force feedback on an automotive simulator," *Proc. of the IEEE Int. Workshop on Haptic-Audio Visual Environments and Games*, 2009, pp. 1-6.
[44] D. Katzourakis, Y. Papaefstathiou, M. Lagoudakis, "An Open-Source Scaled Automobile Platform for Fault-Tolerant Electronic Stability Control," *IEEE Trans. on Instrumentation and Measurement*, vol. 59, no. 10, pp. 2303-2314, Sep. 2010.
[45] D. LeBlanc, J. Sayer, C. Winkler, R. Ervin, S. Bogard, et. Al., "Road Departure Crash Warning System Field Operational Test: Methodology and Results," vol. 1, Technical report, June 2006. Available: http://www.nhtsa.gov/DOT/NHTSA/NRD/Multimedia/PDFs/Crash%20Avoidance/2006/RDCW-Final-Report-Vol-1_JUNE.pdf. Accessed, Apr. 2012.
[46] D. Toffin, G. Reymond, A. Kemeny, J. Droulez, "Influence of steering wheel torque feedback in a dynamic driving simulator," *Proc. of the Driving Simul. Conf.*, Dearborn, MI, Oct. 2003.
[47] D. Toffin, G. Reymond, A. Kemeny, J. Droulez, "Role of steering wheel feedback on driver performance: driving simulator and modeling analysis," *Vehicle System Dynamics*, vol. 45, no.4, pp. 375-388, 2007.

[48] D.A. Abbink, M. Mulder, "Advances in Haptics," *InTech*, pp. 499-516, April 2010.
[49] D.A. Abbink, M. Mulder, "Exploring the dimensions of haptic feedback support in manual control," *J. of Computing and Information Science and Eng.*, vol. 9, no. 1, 2009.
[50] D.A. Abbink, M. Mulder, F C.T. van der Helm, M. Mulder, E.R. Boer, "Measuring Neuromuscular Control Dynamics during Car Following with Continuous Haptic Feedback," *IEEE Trans. on Systems, Man, and Cybernetics-Part B*, vol. 41, no. 5, pp. 1239-1249, 2011.
[51] D.A. Abbink, *Neuromuscular Analysis of Haptic Gas Pedal Feedback during Car Following*, Ph.D. Thesis, Faculty of Mechanical Engineering, Delft University of Technology, 2006.
[52] D.E. Smith, J.M. Starkey, "Effects of Model Complexity on the Performance of Automated Vehicle Steering Controllers: Model Development, Validation and Comparison," *Vehicle System Dynamics*, vol. 24, no. 2, pp. 163-181, 1995.
[53] D.L. Nordeen, General Motors, "Vehicle power steering gear with lateral acceleration feedback means," United states patent: 3552517, Patented: Jan. 1971.
[54] D.M. Bevly, J.C. Gerdes, C. Wilson, "The Use of GPS Based Velocity Measurements for Measurement of Sideslip and Wheel Slip," *Vehicle System Dynamics*, vol. 38 no. 2, Feb. 2003, pp. 127-147.
[55] D.T. McRuer, D.H. Weir, "Theory of manual vehicular control," *IEEE Trans. on Man-Machine Systems*, vol. 10, no. 4, pp. 257-291, Dec. 1969.
[56] D.T. McRuer, E. Krendel, "Mathematical Models of Human Pilot Behavior," AGARD AG 188, STI-P-146. 1974. Available: http://www.systemstech.com/
[57] D.W. Franklin, R. Osu, E. Burdet, M. Kawato, T.E. Milner, "Adaptation to stable and unstable dynamics achieved by combined impedance control and inverse dynamics model," *Journal of neurophysiology*, vol. 90, 2003, pp. 3270-82.
[58] dSPACE, Automotive Simulation Models, Available: http://www.dspace.com/en/pub/home/products/sw/automotive_simulation_models.cfm, Accessed, Apr. 2011.
[59] E. Bakker, L. Nyborg, H. Pacejka, "Tyre modelling for use in vehicle dynamics studies," SAE paper no. 870421, 1987.
[60] E. de Vlugt, A.C. Schouten, F.C.T. vd Helm, P. C. Teerhuis, G. G. Brouwn, "A force controlled planar haptic manipulator for posture control analysis of the human arm," *J. Neurosci. Methods*, vol. 129, no. 2, pp. 151–68, 2003.
[61] E. Frazzoli, "Discussion on "Optimality Properties and Driver Input Parameterization for Trail-Braking Cornering," *European Journal of Control*, vol. 14, no. 4, July-Aug. 2008.
[62] E. Ono, S. Hosoe, H. Tuan, S. Doi, "Bifurcation in vehicle dynamics and robust front wheel steering control," *IEEE Trans. on Control Systems Technology*, vol. 6, no. 3, pp. 412–420, May 1998.
[63] E. Velenis, D. Katzourakis, E. Frazzoli, P. Tsiotras, R. Happee, "Stabilization of Steady-State Drifting for a RWD Vehicle," *Proc. of the 10th Int. Symp. on Advanced Vehicle Control*, AVEC10, 820-825, 2010.
[64] E. Velenis, D. Katzourakis, E. Frazzoli, P. Tsiotras, R. Happee, "Steady-State Drifting Stabilization for RWD Vehicles," *Control Engineering Practice Journal*, vol. 19, no. 11, Nov. 2011, pp. 1363-1376, 2011.
[65] E. Velenis, E. Frazzoli, P. Tsiotras, "On steady-state cornering equilibria for wheeled vehicles with drift," *Proc. of the 48th IEEE Decision and Control Conference*, CDC/CCC 2009, Dec. 2009, pp. 3545-3550.
[66] E. Velenis, P. Tsiotras, "Minimum time vs maximum exit velocity path optimization during cornering," *in 2005 IEEE International Symposium on Industrial Electronics*, Dubrovnic, Croatia, June 2005, pp. 355–360.
[67] E. Velenis, P. Tsiotras, J. Lu, "Modeling aggressive maneuvers on loose surfaces: The cases of trail-braking and pendulum-turn," *Proc. of the 2007 European Control Conference*, Kos, Greece, July 2-5 2007.
[68] E. Velenis, P. Tsiotras, J. Lu, "Modeling aggressive maneuvers on loose surfaces: Data analysis and input parameterization," *IEEE Proc. of the 2007 Mediterranean Conference on Control and Automation*, Athens, Greece, 2007.
[69] E. Velenis, P. Tsiotras, J. Lu, "Optimality properties and driver input parameterization for trail-braking cornering," *European Journal of Control*, vol. 14, no. 4, pp. 308–320, July-Aug. 2008.
[70] EuroNCAP, Infiniti Departure Prevention System: Available: http://www.euroncap.com/rewards/infiniti_ldp.aspx Accessed, Apr. 2012.
[71] European New Car Assessment Programme (EuroNCAP) and European Commission, "Choose ESC," 2007.
[72] ExpressPCB. Available: http://www.expresspcb.com/
[73] G. van Gerwen, *Haptic Feedback on the Steering to Maximize Front axle Grip*, MSc thesis, 3mE, TUDelft, 18th of Apr. 2012.
[74] G. Wallis, A. Chatziastros, J. Tresilian, N. Tomasevic, "The role of visual and nonvisual feedback in a vehicle steering task," *Journal of experimental psychology. Human perception and performance*, vol. 33, 2007, pp. 1127-1144.
[75] H. Khalil, *Nonlinear Systems*, 2nd ed. Upper Saddle River, New Jersey: Prentice Hall,1996.

[76] H. Mohellebi, A. Kheddar, S. Espié, "Adaptive haptic feedback Steering wheel for driving simulators," *IEEE Trans. on Vehicular Technology*, vol. 58, no. 4, pp. 1654-1666, May 2009.
[77] H. Peng, "Evaluation of Driver Assistance Systems-A Human Centered Approach," Keynote speech, AVEC2002, Hiroshima, Japan, Sep. 2002. Available: http://www-personal.umich.edu/~hpeng/Publications.htm
[78] H. Rubinovich, Evo magazine UK, "Driven: all-new Porsche 911 Carrera S," Nov. 2011, Available: http://www.evo.co.uk/carreviews/evocarreviews/275107/driven_allnew_porsche_911_carrera_s.html
[79] H.B. Pacejka, *Tyre and vehicle dynamics*, SAE International, 2nd ed., 2006.
[80] H.P. Snider, "Vehicle Instrumentation for Crash Testing," *IEEE Trans. On Industrial Electronics and Control Instrumentation*, vol. 11, no. 1, Feb. 1964, pp. 44- 49.
[81] J. Cammisa, Automobile Magazine, "First Drive: 2012 BMW M5," Sep. 2011, Available: http://www.automobilemag.com/reviews/driven/1109_first_drive_2012_bmw_m5/viewall.html#ixzz1qLFV1VoT
[82] J. Edelmann, M. Plochl, "Handling characteristics and stability of the steady-state powerslide motion of an automobile," *Regular and Chaotic Dynamics*, vol. 14, no. 6, pp. 682–692,2009.
[83] J. Edelmann, M. Plöchl, W. Reinalter, W. Tieber, "A passenger car driver model for higher lateral accelerations," *Vehicle System Dynamics*, vol. 45, no.12, pp. 1117-1129, 2007.
[84] J. Lepka, P. Stekl, "3-Phase AC induction motor vector control using a 56F80x, 56F8100 or 56F8300 device design of motor control application," Application note, Freescale Semiconductor, 2005. Available: http://www.freescale.com/files/product/doc/AN1930.pdf
[85] J. Owen, P. Farrelly *et al*, "Haptic controller for road vehicles," European patent number: 7234564, Patented: Jun 26, 2007.
[86] J. Strandroth, M. Rizzi, M. Ola, A. Lie, C. Tingvall, "The effects of studded tires on fatal crashes with passenger cars and the benefits of electronic stability control (ESC) in Swedish winter driving," *Accident analysis and prevention*, vol. 45, pp. 50-60, 2012.
[87] J. Wang, J. Steiber, B. Surampudi, "Autonomous Ground Vehicle Control System for High-Speed and Safe Operation," *Proc. of the American Control Conference*, June 2008, pp. 218-223.
[88] J. Zhu, "Conversion of Earth-centered Earth-fixed coordinates to geodetic coordinates," *IEEE Trans. on Aerospace and Electronic Systems*, vol. 30, no. 3, July 1994, pp. 957-961.
[89] J.C. Dixon, Tires, *Suspension and Handling*, SAE, 2nd ed., 1996.
[90] J.C.F. de Winter, D. Dodou, "Preparing drivers for dangerous situations: A critical reflection of continuous shared control," 2011 *Proc. of the IEEE Int. Conf. SMC*, Alaska, U.S.A., pp. 1050-1056, Oct. 2011.
[91] J.C.F. de Winter, M. Mulder, M.M. van Paassen, D.A. Abbink, P.A. Wieringa, "A two-dimensional weighting function for a driver assistance system," *IEEE Trans. on SMC, Part B*, vol. 38, no. 1, pp. 189-195, Feb. 2008.
[92] J.C.F. de Winter, P.A. Wieringa, J. Kuipers, J.A. Mulder, M. Mulder, "Violations and errors during simulation-based driver training," *Ergonomics*, vol. 50, no. 1, pp. 138-158, Jan. 2007.
[93] J.C.F. de Winter, S. de Groot, M. Mulder, P.A. Wieringa, J. Dankelman, J.A. Mulder, "Relationships between driving simulator performance and driving test results," *Ergonomics*, vol. 52, no. 2, pp. 137-153, 2009.
[94] J.G. Proakis, D.G. Manolakis, *Digital Signal Processing*, Prentice Hall, 4th ed., April 2006, pp. 28-30.
[95] J.J. Breuer, "Analysis of Driver-Vehicle-Interaction in An Evasive Manoueuvre - Results of Moose Test Studies," *Proc. of the 16th ESV Conference*, 1998, paper no: 98-S2-W-35.
[96] J.J. Gibson, L.E. Crooks, "A theoretical field-analysis of automobile-driving," *American Journal of Psychology*, vol. 51, pp. 453-471, 1938.
[97] J.M. Chun, G. Park, S. Oh, J. Seo, S.H. Han, S. Choi, "Evaluating the Effectiveness of Haptic Feedback on a Steering Wheel for Forward Collision and Blind Spot Warnings," *Proc. of the 9th Pan-Pacific Conf. on Ergonomics* (PPCOE), Kaohsiung, Taiwan, 2010.
[98] J.P. Switkes, E.J. Rossetter, I.A. Coe, J.C., Gerdes, "Handwheel Force Feedback for Lanekeeping Assistance: Combined Dynamics and Stability," *Journal of Dynamic Systems, Measurement, and Control*, vol. 128, no. 3, pp. 532-542, 2006.
[99] J.P. Timings, D.J. Cole, "Efficient Minimum Manoeuvre Time Optimisation of an Oversteering Vehicle at Constant Forward Speed," *2011 Proc. of American Control Conf.*, pp. 5267 – 5272, 2011.
[100] J.S. Jermakian, "Crash Avoidance Potential of Four Passenger Vehicle Technologies," *Accident Analysis & Prevention*, vol. 43, no. 3, pp. 32-40, Nov. 2010.
[101] K. Kodaka, M. Otabe, Y. Urai, H. Koike, "Rear-End Collision Velocity Reduction System," SAE Technical paper 2003-01-0503, 2003, doi:10.4271/2003-01-0503, 2003.
[102] K. Rock, S. Beiker, S. Laws, J.C. Gerdes, "Validating GPS Based Measurements for Vehicle Control," *Proc. of the ASME IMECE2005*, Florida USA, 2005, paper no: IMECE2005-82212.

[103] K.A. Braitman, A.T. McCartt, D.S. Zuby, J. Singer, "Volvo and Infiniti Drivers' Experiences With Select Crash Avoidance Technologies," *Traffic Injury Prevention*, vol. 11, no. 3, pp. 270-278, 2010.
[104] K.D. Norman, "Objective Evaluation of On-Center Handling Performance," SAE Tec. paper: 840069, 1984.
[105] K.L.R. Talvala, K. Kritayakirana, J.C. Gerdes, "Pushing the Limits: From Lanekeeping to Autonomous Racing," *Annual Reviews in Control*, vol. 35, no.1 pp. 137-148, 2011.
[106] K.P. Tee, E. Burdet, C.M. Chew, T.E. Milner, "A model of force and impedance in human arm movements," *Biological cybernetics*, vol. 90, 2004, pp. 368-75.
[107] L. Ljung, Perspectives on system identification, online tutorial. Available: http://www.control.isy.liu.se/~ljung/seoul2dvinew/plenary2.pdf
[108] Live for Speed, Race Simulator, "Wheels," LFS Manual Wiki. Available: http://en.lfsmanual.net/wiki/Wheels
[109] M. Abdulrahim, "On the dynamics of automobile drifting," *in SAE World Congress*, Detroit, MI, April, pp. 3-6, 2006.
[110] M. Abe, W. Manning, *Vehicle Handling Dynamics: Theory and Application*, Elsevier Ltd., 2009.
[111] M. Alirezaei, M. Corno, A. Ghaffari, R. Kazemi, "Robust Road Departure Avoidance Based on Driver Decision Estimation," *Proc. of the 18th IFAC World Congress*, Milan, Italy, pp. 8427-8432, Sep. 2011.
[112] M. Alirezaei, M. Corno, D. Katzourakis, A. Ghaffari, R. Kazemi, "Robust Driver Steering Assistance for Road Departure Avoidance," *IEEE Trans. on Vehicular Technology*, in press 2012.
[113] M. Bröcker, "New control algorithms for steering feel improvements of an electric powered steering system with belt drive," *Vehicle System Dynamics*, vol. 44, no. 1, pp. 759-769, Jan. 2006.
[114] M. Hoedemaeker, K.A. Brookhuis, "Behavioural adaptation to driving with an adaptive cruise control (ACC)," *Transportation Research Part F*, vo. 1, no. 2, pp. 95-106, 1998.
[115] M. Itoh, T. Horikome, T. Inagaki, "Design and Evaluation of Situation-Adaptive Pedestrian-Vehicle Collision Avoidance System," *Proc. of the IEEE Int. Conf. SMC*, Alaska, U.S.A. 2011.
[116] M. Kondo, A. Ajimine, "Drivers' sight point and dynamics of the driver-vehicle-system related to it," SAE technical paper, Doc. no. 680104, Feb. 1968.
[117] M. Ljung, M. Blommer, R. Curry, B. Artz, J. Greenberg, D. Kochhar, L. Tijerina, M. Fagerstrom, L. Jakobsson, "The Influence of Study Design on Results in HMI Testing for Active Safety," *Proc. of the 20th ESV Conference*, 2007, paper no: 07-0383.
[118] M. Matosevic, Z. Salcic, S. Berber, "A Comparison of Accuracy Using a GPS and a Low-Cost DGPS," *IEEE Trans. On Instrumentation and Measurement*, vol. 55, no. 5, Oct. 2006, pp. 1677-1683.
[119] M. Mulder, D.A. Abbink, E.R. Boer, "The effect of haptic guidance on curve negotiation behavior of young, experienced drivers," *Proc. of the IEEE Int. Conf. on Systems, Man and Cybernetics*, SMC 2008, 12-15 Oct. 2008, pp. 804-809.
[120] M. Nuessle, R. Rutz, M. Leucht, M. Nonnenmacher, "Objective Test Methods to Asses Active Safety Benefits of ESP," *Proc. of the 20th ESV Conference*, 2007, paper no: 07-0230.
[121] M. Rothhamel, L. Drugge, J. Ijkema, "On a Method for Generating a Word Pool for the Description of Steering Feel," *Proc. of the 10th International Symposium on Advanced Vehicle Control*, AVEC10, pp. 693-698, 2010.
[122] M.D. Penna, M.M. van Paassen, D.A. Abbink, M. Mulder, M. Mulder, "Reducing steering wheel stiffness is beneficial in supporting evasive maneuvers," *Proc. of the IEEE Int. Conf. SMC*, Istanbul, Turkey, pp. 1628-1635, 2010.
[123] M.F. Land, D.N. Lee, "Where we look when we steer," *Nature*, vol. 369, pp. 742-744, 1994.
[124] M.V. Groll, S. Mueller, T. Meister, R. Tracht, "Disturbance compensation with a torque controllable steering system," *Vehicle System Dynamics*, vol. 44, no. 4, pp. 327-338, 2006.
[125] Mathworks, Data analysis: Removing outliers, Matlab help files, Version R2007b.
[126] N. Stanton, P. Marsden, "From fly-by-wire to drive-by-wire: Safety implications of automation in vehicles," *Safety Science*, vol. 24, no. 1, pp. 35-49, 2008.
[127] National Highway Traffic System Administrator, "Electronic Stability Control System," FMVSS no.126, March 2007.
[128] National Instruments, "Transitioning from Traditional NI-DAQ (Legacy) to NI-DAQmx Using ANSI C and NI LabWindows™/CVI." Available: http://zone.ni.com/devzone/cda/tut/p/id/5957
[129] O. Shechtman, S. Classen, K. Awadzi, W. Mann, "Comparison of driving errors between on-the-road and simulated driving assessment: a validation study," *Traffic Injury Prevention*, vol. 10, no. 4, pp. 379-385, 2009.
[130] Open Computer Vision Library (OpenCV). Available: http://opencvlibrary.sourceforge.net
[131] P. Griffiths, R.B. Gillespie, "Sharing Control Between Human and Automation Using Haptic Interface: Primary and Secondary Task Performance Benefits," *Human Factors*, vol. 47, no. 3, pp. 574-590, Fall 2005.

[132] P. Lugner, M. Plöchl, "Modelling in vehicle dynamics of automobiles," *Journal of Applied Mathematics and Mechanics*, no. 84, 219-236, 2004.
[133] P. Yih, J.C. Gerdes, "Modification of vehicle handling characteristics via steer-by-wire," *IEEE Trans. On Control Sys. Tech*, vol. 13, no. 6, Nov. 2005.
[134] P.E. Pfeffer, M. Harrer, D.N. Johnston, "Interaction of vehicle and steering system regarding on-centre handling," *Vehicle System Dynamics*, vol. 46, no. 5, pp. 413-428,2008.
[135] P.E. Uys, P.S. Els, M.J. Thoresson, "Criteria for handling measurement," *Journal of Terramechanics*, vol. 43, no.1, pp. 43-67, 2006.
[136] P.G. Griffiths, R.B. Gillespie, "Shared control between human and machine: Haptic display of automation during manual control of vehicle heading," *IEEE Proc. of the HAPTICS 2004 Symp*., 2004, pp. 358-366.
[137] Psychology world, "Within-Subjects Designs," Available: http://web.mst.edu/~psyworld/within_subjects.htm. Accessed, Apr. 2012.
[138] R. Corton, B. Cassoret, J. F. Brudny, "Characterization of three-phase harmonic systems generated by PWM inverter switching application to induction machine magnetic noise reduction," *IEEE Int. Conf. in Electric Machines and Drives*, IEMDC 2001, 2001, pp. 442-447.
[139] R. Hindiyeh, J.C. Gerdes, "Equilibrium analysis of drifting vehicles for control design," *Proc. of the ASME 2009 Dynamic Systems and Control Conference*, Hollywood, pp. 12-14, 2009.
[140] R. Pintelon, J. Schoukens, *System identification: A Frequency Domain Approach*, 2001, IEEE Press, New York.
[141] R. Rajamani, C. Zhu, L. Alexander, "Lateral control of a backward driven front-steering vehicle," *Control Engineering Practice J.*, vol. 11, no. 5, May 2003, pp. 531-540.
[142] R. Rajamani, *Vehicle Dynamics and Control*, Springer, 2006.
[143] R.D. Dorf, R.H. Bishop, *Modern Control Systems*, Prentice Hall, 2001, 9th ed. pp. 66-67.
[144] R.R. Mourant, P. Sadhu, "Evaluation of force feedback steering in a fixed based driving simulator," *Proc. of the Human Factors and Ergonomics Society 46th Annual Meeting*, pp. 2202-2205, 2002.
[145] R.S. Sharp, D. Casanova, P. Symonds, "A Mathematical Model for Driver Steering Control with Design Tuning and Performance Results," *Vehicle System Dynamics*, vol. 33, no. 5, pp. 289-326, May 2000.
[146] R.S. Sharp, M. Thommyppillai, S.A. Evangelou, "Towards a Model of a High-performance Driver for Circuit-racing Cars," *Proc. of the 10th International Symposium on Advanced Vehicle Control, AVEC2010*, 2010, pp. 713-718.
[147] R.S. Sharp, R. Granger, "On car steering torque at parking speeds," *Proc. of the IMECHE. Part D, J. of automobile engineering*, vol. 217, no 2, pp. 87-96. Available: http://www2.ee.ic.ac.uk/cap/publications/2003/parking_torques.pdf, 2003.
[148] Racelogic, RLVB20SL 20Hz Datalogger with Slip Angle, datasheet 2010. Available: http://www.racelogic.co.uk/?show=VBOX-Products-VBOX_IISX
[149] Race-technology, Sensors. Available: http://www.race-technology.com/sensors_8_922.html
[150] S. Arndt, M. Arndt, M. Rosenfield, "Effectiveness of Electronic Stability Control on Maintaining Yaw Stability When an SUV Has a Rear Tire Tread Separation," SAE paper no. 2009-01-0436.
[151] S. Data, F. Frigerio, "Objective evaluation of handling quality," *Proc. of the Institution of Mechanical Engineers, Part D: Journal of Automobile Engineering*, vol. 216, no. 4,pp. 297-305, 2002.
[152] S. de Groot, J.C.F. de Winter, J.M.L. García, M. Mulder, P.A. Wieringa, "The Effect of Concurrent Bandwidth Feedback on Learning the Lane-Keeping Task in a Driving Simulator," *Human Factors*, vol. 53, no. 1, pp. 50–62, Feb. 2011.
[153] S. Ishida, J. Tanaka, S. Kondo, M. Shingyoji, "Development of a Driver Assistance System," SAE Technical paper 2003-01-0279, doi:10.4271/2003-01-0279, 2003.
[154] S.G. Hart, L.E. Staveland, "Development of NASA-TLX (task load index): Results of empirical and theoretical research," in *Human Mental Workload*, P. A. Hancock and N. Meshkati, Eds. Amsterdam, The Netherlands: North Holland, pp. 139-183, 1988.
[155] SKF, "Hub Knuckle Module-Aluminium knuckle integration (Rolled first generation hub bearing unit) – HKM." Available: http://www.skf.com/portal/skf/home/industries?lang=en&contentId=867450&offerId=0.000336.516154.867394.867450.867525#, Accessed, Apr. 2012.
[156] Sparkfun Inc., IMU Sensors. Available: http://www.sparkfun.com/commerce/categories.php?c=160
[157] Steering support research TUDelft, SKF and Prodrive TU Delft. Available: http://www.youtube.com/watch?v=-m3KDv45d44
[158] T. Inagaki, "Adaptive automation: Sharing and trading of control," *Handbook of Cognitive Task Design*, ch. 8, pp. 147-170, 2003.

[159] T. Inagaki, T. Sheridan, "Authority and responsibility in human–machine systems: probability theoretic validation of machine-initiated trading of authority," *Cognition, Technology & Work*, pp. 1-9, 2001.
[160] T. Nagai, N. Cohen, Y. Moriguchi, Y, Murakami, "Dual-driver networked fire truck simulator with multimodal display including force feedback steering and rotating motion platform," *IEEE Proc. of the Int. Work. Enab. Tech.: Inf. Collab. Enterp.*, pp. 424-430, 2007.
[161] T.D. Gillespie, *Fundamental of Vehicle Dynamics*. SAE, 1992.
[162] TUDelft Video, http://www.youtube.com/watch?v=3lHV8jsXjIo
[163] V. Cerone, M. Milanese, D. Regruto, "Combined Automatic Lane-Keeping and Driver's Steering Through a 2-DOF Control Strategy," *IEEE Trans. on Control Systems Technology*, vol. 17, no.1, pp. 135-142, Jan. 2009.
[164] Vishay Micro-Measurements, Strain Gage Applications with M-Bond AE-10, AE-15 and GA-2 Adhesive Systems, Instruction Bulletin B-137-16. Available: http://www.intertechnology.com/Vishay/pdfs/Instruction_Bulletins/B-137-16.pdf
[165] Volkswagen AG, Wolfsburg, Service Training, Self-study programme 317, "The electro-mechanical power steering with dual pinion, Design and function." Available: http://tos.pp.fi/koukku/892403.pdf, 2010.
[166] W. Dick, M. Lannoije, J. Schller, M. Reuter, "Dynamic Steering in the Audi Q5," *ATZ and MTZ magazine*, Special ed, June 2008.
[167] W. Klier, G. Reimann, W. Reinelt, ZF Lenksysteme GmbH, Schwäbisch Gmünd, Germany, "Concept and Functionality of the Active Front Steering System," SAE 2004-21-0073.
[168] W. Mugge, D. Abbink, A.C. Schouten, J.P. DeWald, F.C.T. vd Helm, "A rigorous model of reflex function indicates that position and force feedback are flexibly tuned to position and force tasks," *Experimental brain research*, vol. 200, 2010, pp. 325-40.
[169] W. Tomaske, C. Breidenbach, T. Fortmüller, "A scientific and physiological research study with truck driving simulators in the army," *Proc. of the International Training & Education Conference (ITEC)*, Lille, France, 2001.
[170] W.J Conover, R.L. Iman, "Rank transformations as a bridge between parametric and nonparametric statistics," *American Statistician*, vol. 35, no.3, pp. 124-129, 1981.
[171] WinAVR. Available: http://winavr.sourceforge.net/
[172] Y. Shibahata, "Progress and future direction of Chassis control technology," *Annual Reviews in Control*, vol. 29, pp. 151-158, 2005.
[173] Y.H.J. Hsu, C. Gerdes, "The Predictive Nature of Pneumatic Trail: Tire Slip Angle and Peak Force Estimation using Steering Torque," *Proc. of AVEC08*, pp. 80-85, 2008.

Acknowledgment

“Δός μοι πά στώ καί ταν γάν κινάσω.”
Αρχιμήδης, 287-212 π.Χ.

“Give me a place to stand on and I shall move the earth.”
Archimedes, 287-212 B.C.

A great thank you to

my family, my mother Maria and my father Yannis for their invaluable support for many challenging years now; my brother Antonis (always supplying with his artistic designs, spread throughout this dissertation) and his fiancé Emmi.

my supervisors, Dr. Riender Happee, Dr. Frans van der Helm and Dr. Edward Holweg for their support and help throughout this long journey. I hope we continue working together.

my closest co-operators, Dr. Efstathios Velenis, Dr. David Abbink, Dr. Joost de Winter and Dr. Matteo Corno. We really did some nice work together.

graduate students I supervised, ir. Cas Drogendijk, ir. Joop van Gerwen, Jeroen Beerens, Joost de Haan, Richard Nefs, Timothy Schuit.

SKF and especially Dr. Edward Holweg and Igor Dorrestijn. The Automotive Development Center of SKF has supported this work financially as well as ethically.

Prodrive Automotive in UK and especially Oliver Jones, Dave Rollet, Mat Taylor, Chris Roberts, Ben Garrat, Scott Parton and Adrian Hall.

Circuit Park Zandvoort, for granting usage of their test facilities.

the Biomechanical Engineering Group, Johannes Dukker and Jan van Frankenhuyzen.

my friends, Dimitris Stafylarakis and Marja Illona Kolski, Dimitris Theodoropoulos, Petros Tsigkourakos, Aristeidis Katsiorchis, Nima Tolou, Apostolis Perdikakis, Antreas Loupasakis, Giorgos Vrontakis, Christos Strydis, Tasos Melemenis, Luai Jraisat, Achilleas Trakakis, Peter van Leeuwen, Sotiris Agapitos, Giorgos Krintiras, Panos Oikonomidis and more. Of course Elli; standing by me and supporting me for years.

Diomidis I. Katzourakis
June 2012

Ένα μεγάλο ευχαριστώ

στην οικογένεια μου, στον πατέρα μου Γιάννη και στην μητέρα μου Μαρία για την ανυπολόγιστη στήριξη και υπομονή τους. Στον αδελφό μου Αντώνη, τον καλλιτέχνη της οικογένειας (η διατριβή είναι διάσπαρτη με τα σχέδια του) και στην αρραβωνιαστικιά του Έμμη.

στους επιβλέποντες καθηγητές μου, Δρ. Riender Happee, Δρ. Frans van der Helm και Δρ. Edward Holweg για την στήριξη τους σε αυτό το μακρύ ταξίδι.

στους πιο στενούς συνεργάτες μου, Δρ. Στάθη Βελένη, Δρ. David Abbink, Δρ. Joost de Winter και Δρ. Matteo Corno.

στους αποφοιτήσαντες υπό την επίβλεψη μου, ir. Cas Drogendijk, ir. Joop van Gerwen, Jeroen Beerens, Joost de Haan, Richard Nefs, Timothy Schuit.

στην SKF και ειδικότερα στον Δρ. Edward Holweg και Igor Dorrestijn. Το Automotive Development Center της SKF που υποστήριξε το έργο αυτό οικονομικά και ηθικά.

στην Prodrive Automotive στο Ηνωμένο Βασίλειο και ειδικά στους Oliver Jones, Dave Rollet, Mat Taylor, Chris Roberts, Ben Garrat, Scott Parton και Adrian Hall.

στο Circuit Park Zandvoort, για την παραχώρηση των εγκαταστάσεων τους για δοκιμές.

το Τμήμα Biomechanical Engineering και ειδικά τους Johannes Dukker και Jan van Frankenhuyzen.

τους φίλους μου, Δημήτρη Σταφυλαράκη και Marja Illona Kolski, Δημήτρη Θεοδωρόπουλο, Πέτρο Τσιγκουράκο, Αριστείδη Κατσίοχη, Nima Tolou, Αποστόλη Περδικάκη, Αντρέα Λουπασάκη, Γιώργο Βροντάκη, Χρήστο Στρύδη, Τάσο Μελεμενή, Luai Jraisat, Αχιλλέα Τρακάκη, Peter van Leeuwen, Σωτήρη Αγαπητό, Γιώργο Κρηντήρα, Πάνο Οικονομίδη κ.α. Και φυσικά την Έλλη. Για χρόνια δίπλα μου.

Διομήδης Ι. Κατζουράκης
Ιούνιος 2012

(CV) Diomidis I. Katzourakis

was born at Chania on 1983, in the beautiful island of Crete in Greece. He graduated from lyceum on 2001 and was accepted at the University on the same year.

He loves advance engineering (in particularly cars) and enjoys to develop his own engineering concepts and evaluate them in a test-track (in high speed driving). His research interests focus on automotive vehicles (dynamics and control), electronic systems' integration and instrumentation and measurement. He wants to pursue a career as an automotive control-systems engineer-researcher.

He does sports since 10 years old, and has passed from volley ball, track & field sports, to martial arts etc. He was a member of the traditional dancing group "Psiloritis" and he loves (lives) to play beach-rackets (ρακέτες) in the Cretan summer (whole day long).

Contact: d.katzourakis@tudelft.nl, diomkatz@gmail.com

Education

Oct. 2008 – Jun. 2012	Ph.D.: "Driver Steering Support Interface Near the Vehicle's Handling Limits." Intelligent Automotive Systems (IAS) and the Biomechanical Engineering (BME) research groups, Mechanical, Maritime and Materials Engineering (3mE), Technical University of Delft (TUDelft), the Netherlands.
Oct. 2006 – Sept. 2008	M.Sc. on Electronics: "Test Bed for Automotive Experiments: Evaluation of Electronic Stability Control Schemes." Microprocessor & Hardware Lab., at the Department of Electronic and Computer Engineering (ECE), Technical University of Crete (TUC), Greece. GPA 10/10.
Sep. 2001 – Jul. 2006	Diploma of Engineering (B.Sc.-M.Sc., 5 years programme): "Autonomous Vehicle Guidance." Computer Engineering and Informatics Engineer Department (CEID), University of Patras (UPatras), Greece. GPA 8.01/10.
March 2001	Certificate of Proficiency in English, University of Michigan.

Work/Research Experience

Sep. 2011 – Nov. 2011	Research contractor under SKF's patronage: "Aggressive cornering negotiation with variable feedback torque." Prodrive automotive technology, UK.
Oct. 2008 – Oct. 2012	Ph.D. candidate for SKF: "Driver Steering Support Interface Near the Vehicle's Handling Limits." BME, 3mE, TUDelft, supported by the Automotive Development Center of SKF as part of the project Mobility Intelligence using Loadbased Lateral Stability (MILLS).
Jun. 2009 – Aug. 2009, Oct. 2009	Research assistant: "Stabilization of Steady-State Drifting for Rally vehicles." Brunel University, UK.
Jun. 2008 – Aug. 2008	Researcher: "Vision tracking system for a UAV helicopter." Intelligent Systems & Robotics Laboratory, Department of Production Engineering & Management, TUC.
Feb. 2008 – May 2008	Team Member of TUCER. Implementation of a prototype, low consumption urban vehicle for the Shell Eco-marathon, May 2008.
Oct. 2007 – Jun. 2008	Teacher, IEK, Chania: a) "Technologies and Services of Internet." b) "Wireless Transmission."
Oct. 2006 – Aug. 2008	Web Administrator, Systems' Division.
Oct. 2006 – Aug. 2008	Teacher under the P.D. 407, ECE, TUC: a) "Theory and Application of Automatic Control Systems." b) "Neural Networks and Applications." c) "Linear Systems."
Feb. 2005 – Jul. 2005	Lab Assistant: "Introduction to Computer Systems." CEID, UPatras.
Summers 2003, 2004, 2006	Electronic and Electrical engineer assistant at the Public Energy Corporation.
Summer 2001	Lifeguard, "Limnoupoli," Varypetro, Chania.

“Ξυνόν γαρ αρχή και πέρας επί κύκλου περιφερείας.”
Ηράκλειτος, 544-484 π.Χ.

“In a circle, every point is simultaneously the beginning and the end.”
Heraclitus, 544-484 B.C.

Τέλος.

The end.

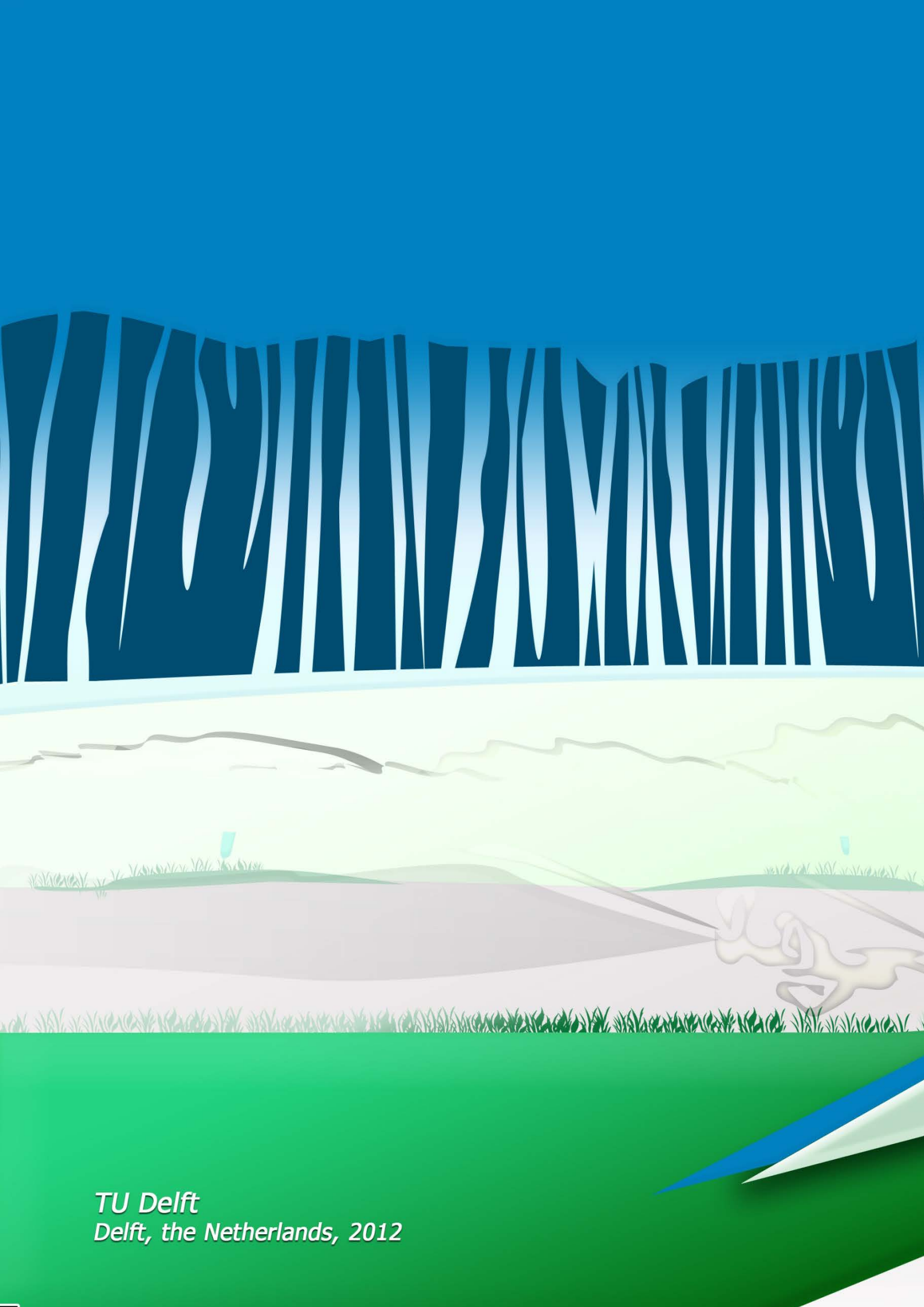

TU Delft
Delft, the Netherlands, 2012